PRECISION ENGINEERING CONSORTIUM

2018 ANNUAL REPORT
VOLUME XXXII
January 2019

Sponsors:	Facebook Los Alamos National Laboratory
Faculty:	Thomas Dow Victoria Miller David Muddiman Brendan O’Connor Mark Pankow Ronald Scattergood
Graduate Students:	Charan Bodlapti Sumit Gundyal Noa McNutt
Staff:	Kenneth Garrard Anthony Wong
Consultants:	Karl Falter Stephen Furst

Table of Contents

SUMMARY

The goals of the Precision Engineering Consortium (PEC) are: 1) to develop new technology in the areas of precision metrology, actuation, manufacturing and assembly; and 2) to train a new generation of engineers and scientists with the background and experience to transfer this technology to industry. Because the problems related to precision engineering originate from a variety of sources, significant progress can only be achieved by applying a multidisciplinary approach; one in which the faculty, students, staff and sponsors work together to identify important research issues and find the optimum solutions. Such an environment has been created and nurtured at the PEC for 34 years and the 100+ graduates attest to the quality of the results.

The 2018 Annual Report summarizes the progress over the past year by the faculty, students and staff in the Precision Engineering Consortium. During the past year, this group included 2 faculty, 3 graduate students, 2 technical staff members and 1 administrative staff member. This diverse group of scientists and engineers provides a wealth of experience to address precision engineering problems. The format of this Annual Report separates the research effort into individual projects but there is significant interaction that occurs among the faculty, staff and students. Weekly seminars by the students and faculty provide information exchange and feedback as well as practice in technical presentations. Teamwork and group interactions are a hallmark of research at the PEC and this contributes to both the quality of the results as well as the education of the graduates.

A brief abstract follows for each of the projects and the details of the progress in each is described in the remainder of the report.

1. **Development of a Surrogate System to Study the Dry Turning of Plutonium**
   To reduce time and costs associated with disposing of cutting fluids used to machine radioactive materials like plutonium, dry machining is being investigated at Los Alamos National Laboratory (LANL). However, such soft radioactive materials present machinability issues when a cutting fluid is not used. The main issue is chip seizure. This occurs when chip material adheres to the rake face of the tool and smears the machined surface, leading to poor surface finish. To safely study this phenomenon, soft, pure 1199 aluminum was chosen as a suitable surrogate material. By conducting machining experiments on 1199 aluminum, feeds, speeds, depths and tool parameters were optimized to reduce the effects of chip seizure and optimize surface roughness. High positive rake angled tools, larger feed rates and depths of cut, and moderate cutting speeds produce the best machined surfaces. Now an abbreviated series of test cuts should be devised and recommended to Los Alamos to quickly optimize parameters for plutonium.

2. **Diamond Turning of Plastics**

   Single point diamond turning is a common method to create plastic optics. The optics industry claims that tool wear is a major problem. The objective of this research is to optimize machining parameters (such as feed, depth of cut, cutting speed and rake angle) to produce optical surface quality (RMS Surface finish < 10 nm) while minimizing tool wear for Poly (methyl methacrylate) (PMMA) and Polycarbonate (PC). A wide range of experiments were performed on the two materials by varying machining parameters and measuring worn tools using the Electron Beam Induced Deposition (EBID) technique in the Scanning Electron Microscope (SEM). For the experimental conditions used, PMMA was found to have better surface finish than PC when machined with a diamond tool. Polycarbonate was found to wear the tool more than PMMA under similar cutting conditions. It was also found that Polycarbonate is more sensitive to chip management and chip geometry than PMMA. Built up edge on the tool and chip management were identified as the important reasons for poor surface finish on PC. Tribo-electric charging was found to be a major mode of tool wear when machining PC. Holes in the diamond tool were observed on the diamond tool when large depths of cut were used. Using Tap Magic Aqueous as cutting fluid during machining PC was found to minimize tool wear and improve surface finish. Detailed effects of all machining parameters for the two materials were reported

3. **Microscale Lens Array: FIB Milling and Indenting Microscale Features**

   This research investigates the fabrication of microscale features in glassy carbon that will be used as a die to stamp features into a mold for injection molding of plastic lenses. The concept is to FIB mill a die with multiple features (4-9) and then stamp those features at a high repetition rate (>100/second) to create a mold for a large lens array. The features are nominally spherical with radii on the order of 15.8 µm that would, with the parameters given above, create a mold with 3x106 lenses in an hour.

   The FIB characteristics such as material removal rate, angle of incidence sensitivity, and beam shape were measured. It was estimated that a single lens feature could be milled in a matter of minutes. A simulation tool was developed to assist in planning the FIB milling process. Glassy carbon dies with 4 and 9 features were FIB milled. The FIB process parameters were investigated to improve the form of the die. 1100 Aluminum was indented with the glassy carbon die and arrays of indents were successfully fabricated

4. **Microscale Lens Array: Modeling of the Microindentation Process**

   This report addresses the design of multi-indenter die and development of indentation strategies to create the negative features of a micro lens array on a mold. Initially, correlation of quasi-static nanoindentation results of FEA models to the experimental results is obtained to gain confidence in the models. A material parameter study is performed using commercial finite element analysis software Abaqus^{TM} to understand the effects of different material properties on the spring back amount, pile up and the maximum force required. Al 1100 is selected as the mold material based on this study. Glassy carbon is used as the die material. Possible drawbacks in the design of the multi-indenter die and the different indentation strategies are discussed.

5. **Evaluation of Digital Image Recognition Methods for Mass Spectrometry Imaging Data Analysis**

   Analyzing mass spectrometry imaging data can be laborious and time consuming, and as the size and complexity of datasets grow, so does the need for robust automated processing methods. We here present a method for comprehensive, semi-targeted discovery of molecular distributions of interest from mass spectrometry imaging data, using widely available image similarity scoring algorithms to rank images by spatial correlation. A fast and powerful batch search method using a MATLAB implementation of structural similarity (SSIM) index scoring with a pre-selected reference distribution is demonstrated for two sample imaging datasets, a plant metabolite study using *Artemisia annua* leaf, and a drug distribution study using maraviroc-dosed macaque tissue

1 DEVELOPMENT OF A SURROGATE SYSTEM TO STUDY THE DRY TURNING OF PLUTONIUM

Noa McNutt
Graduate Student
Thomas Dow
Professor
Mechanical and Aerospace Engineering

To reduce time and costs associated with disposing of cutting fluids used to machine radioactive materials like plutonium, dry machining is being investigated at Los Alamos National Laboratory (LANL). However, such soft radioactive materials present machinability issues when a cutting fluid is not used. The main issue is chip seizure. This occurs when chip material adheres to the rake face of the tool and smears the machined surface, leading to poor surface finish. To safely study this phenomenon, soft, pure 1199 aluminum was chosen as a suitable surrogate material. By conducting machining experiments on 1199 aluminum, feeds, speeds, depths and tool parameters were optimized to reduce the effects of chip seizure and optimize surface roughness. High positive rake angled tools, larger feed rates and depths of cut, and moderate cutting speeds produce the best machined surfaces. Now an abbreviated series of test cuts should be devised and recommended to Los Alamos to quickly optimize parameters for plutonium.

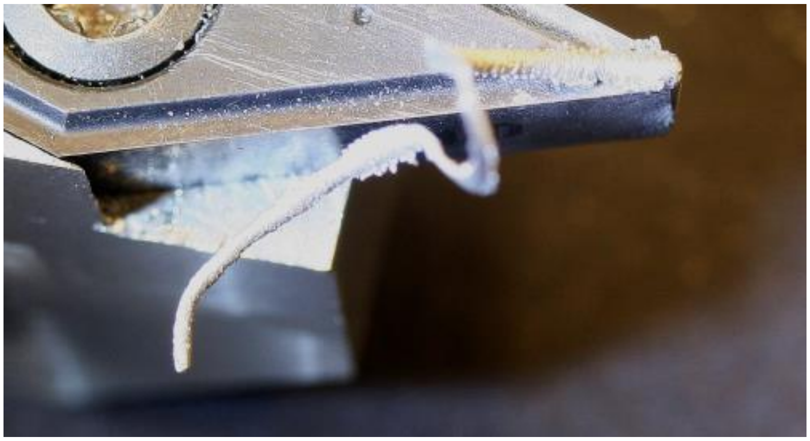

1.1 INTRODUCTION

This project investigates possible machining parameters to machine plutonium without the use of a cutting fluid. Dry machining presents Los Alamos with an opportunity to reduce time and costs associated with separating and disposing of radioactive cutting lubricant that is a byproduct of machining plutonium. Unfortunately, dry machining also presents a challenge: how to prevent soft materials such as plutonium from “sticking” to the rake face of the tool. This sticking behavior ultimately leads to formations on the tool such as built-up-edge (BUE) and/or chip seizure. These formations result in poor surface finish and figure error on the final plutonium part [1].

The project identified a non-radioactive surrogate material for plutonium that will behave similarly using standard LANL tooling, feeds and speeds. An ideal surrogate has similar density, hardness and “stickiness” to plutonium. Once the best surrogate material was identified, a series of turning experiments was conducted to maximize surface finish on the surrogate while minimizing the presence of BUE or chip seizure, all without the use of a cutting fluid.

Summary of Previous Work at the PEC

Before any machining parameters could be studied and optimized, three key questions had to be investigated. What sort of materials should be considered for plutonium surrogacy, which of these materials performs most similarly, and what are the fundamental problems that make plutonium and any surrogates so hard to machine? The large majority of 2017 was spent answering these three questions. For an in depth description of these investigations, see the 2017 PEC Annual Report [2].

Surrogate Identification

Rather than machine a large amount of materials with many of the results being unlike plutonium, a materials approach was taken to identify a small group of potential surrogate materials. Properties of the plutonium such as crystallographic structure, thermal diffusivity, tensile yield strength, and hardness characteristics were identified to find potential surrogates. Materials to be considered were soft ($H_v < 50$), Face Center Cubic (FCC) structure metals. A good surrogate should display chip seizure or BUE characteristics similar to plutonium during dry machining.

Four metals were identified using only these criteria; 1199 aluminum, 1100 aluminum, annealed OFHC copper, and lead based babbitt. Both species of aluminum and copper can be considered commercially pure. Next, a composite scoring system was devised to predict the machining performance of these four metals. This Machining Surrogate Score (MSS) is a single number to compare these materials similarity to plutonium on the basis of thermal diffusivity and tensile yield strength. Both of these properties are crucial to machining performance. Thermal diffusivity describes the materials ability to remove heat from the cutting zone. Thermal diffusivity (α) is a function of thermal conductivity, density and specific heat of the material. Equation (1) describes this relationship.

$$\alpha = \frac{k}{\rho c_p} \tag{1}$$

A good surrogate should have a low thermal diffusivity, similar to plutonium. This means that cutting zone temperatures should be relatively high. Tensile yield strength (σ) describes the amount of stress that is required to plastically deform the material. Energy required during chip formation is strongly dependent on the tensile yield strength of the material [3]. Equation (2) describes the relation between thermal diffusivity, yield strength and the MSS.

$$MSS_{\mathrm{x}} = \left(\frac{\sigma_{Pu}-\sigma_x}{\sigma_{Pu}}\right) * \left(\frac{\alpha_{Pu}-\alpha_x}{\alpha_{Pu}}\right) \tag{2}$$

The MSS of a material is essentially the product of the normalized differences between the yield strengths and thermal diffusivities of plutonium (Pu) and the potential surrogate (x). Note that a smaller MSS for a surrogate indicates that it is similar to plutonium with regards to these two properties. This means that a surrogate is predicted to be a suitable surrogate to study the machining of plutonium. The properties of interest for plutonium, 1199 aluminum, 1100 aluminum, OFHC copper and Babbitt are shown in Table 1.

Table 1. Material Properties of Potential Surrogates and Plutonium

Material	**σ (MPa)**	**k ($W/m°k$)**	**ρ (kg/m^3)**	**c_p ($J/kg°K$)**	**α (mm^2/s)**
1199 aluminum	110	240	2700	900	99
1100 aluminum	103	220	2710	904	90
OFHC copper	35	398	8930	385	116
lead babbitt	42	24	10200	163	14
Plutonium [4]	100	8.4	19800	130	3

It is shown in Table 1 that 1199 and 1100 aluminum are closest to plutonium with regards to yield strength, while lead babbitt is closest with respect to thermal diffusivity. Assuming that both of these material properties are equally important with respect to machining performance, the MSS will serve as a tie-breaker to determine which materials should be tested extensively. Figure 1 displays the MSSs for all four materials listed in Table 1.

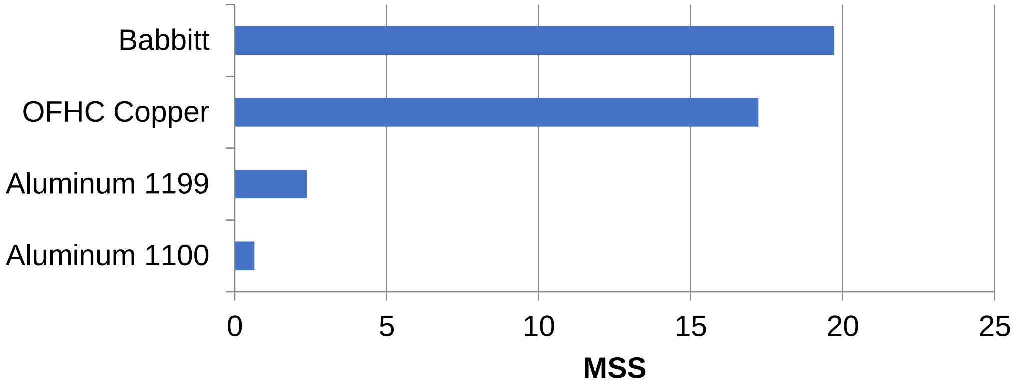

Figure 1. MSSs for the Four Metals Considered

Figure 1 indicates that 1199 and 1100 aluminum have much lower MSSs than babbitt or copper, indicating that they are good candidates for machining surrogates to plutonium. Note that if plutonium were plotted in Figure 1, it would have a perfect MSS of zero. In the following section both aluminum and copper will be tested to validate or disprove the MSS system and determine which metal should be used for the remainder of the project.

Surrogate Testing

While material properties are useful for identifying some potential surrogate materials, to ultimately determine which materials are best dry machining experiments must be conducted on each of the potential surrogates. Dry machining experiments were conducted with 1199 aluminum, 1100 aluminum and OFHC. Due to health concerns associated with lead, along with a lack of sticking behavior during sample preparation, babbitt eliminated from consideration.

The machining operation used for these experiments was a facing operation with a non-overlapping feed rate. An example of a surface created for these conditions is shown in Figure 2. Notice how the grooves in the machined surface are not in contact with the grooves on either side. This provides insight to the state of the tool and chip flow at the time each groove was cut. This surface will indicate the presence of any BUE or chip seizure occurring while the surface was machined. The dark area on Figure 2 indicates the presence of BUE, while any large peaks above the Z=0 line would indicate chip seizures. Either of these features on a workpiece would indicate that it is a promising surrogate to plutonium. After discussions with Los Alamos engineers, it was determined that seizure and smearing is a more significant problem when machining plutonium, so it will be the focus of this report.

After a potential surrogate was turned using the non-overlapping facing cut, the tool was examined in the scanning electron microscope (SEM) for evidence of BUE or chip seizures on the tool. These features should be fairly easy to recognize on the high magnification of the SEM.

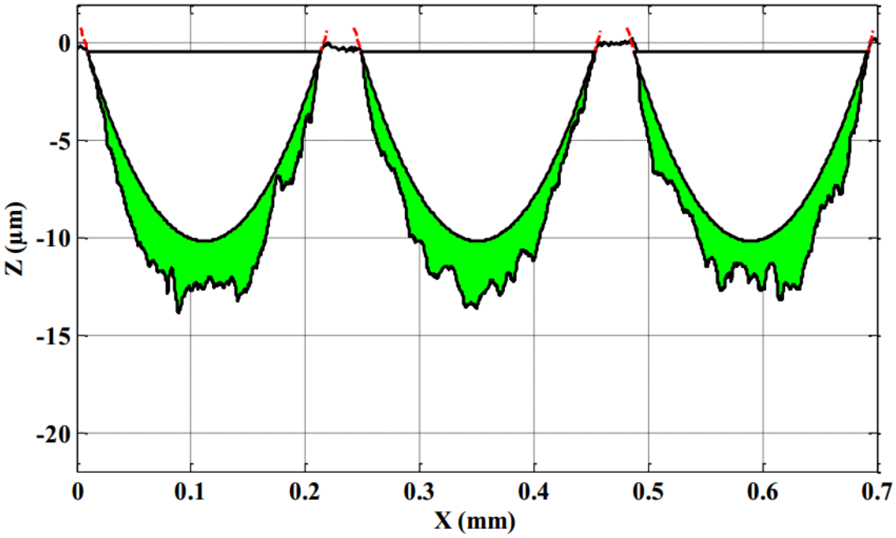

Figure 2. Example of a Machined Surface Created by a Non-Overlapping Feed, Facing Cut. Mild Steel [5]

Little evidence of BUE or chip seizure was observed on the surface or the tools when machining OFHC copper and 1100 aluminum. Little evidence of BUE was seen on 1199 aluminum, but a large chip seizure was suspected from the machined surface, and later confirmed on the SEM. Figure 3 shows 30-40 µm peaks above Z=0 for the depth of cut of 20µm. This is consistent with plowing due to chip seizures on the tool.

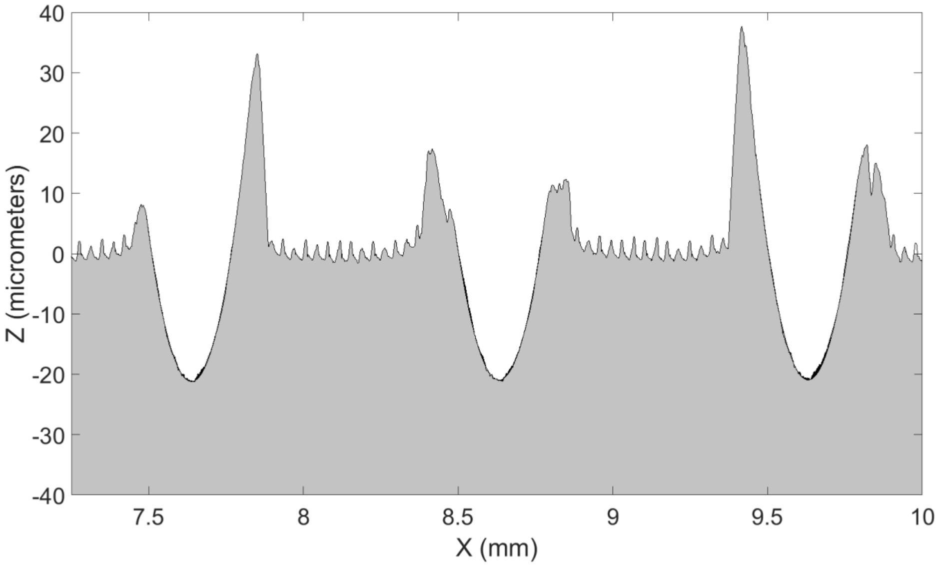

Figure 3. Three Grooves Machined in 1199 Aluminum Using a Non-Overlapping Feed, Facing Cut

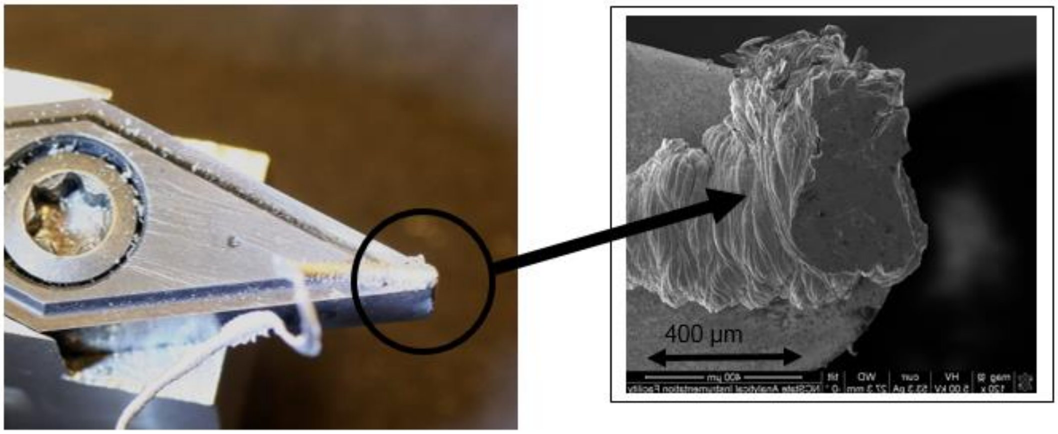

Figure 4. Photograph of Chip Seizure (L), SEM Micrograph of the Same Chip Seizure (R), Same Cut as Shown in Figure 3

Figure 4 shows evidence that corroborates the expected chip seizure from Figure 3. This large, prominent chip seizure indicated that 1199 aluminum is the closest surrogate material to study the dry turning of plutonium. Given the very similar chemistry between 1199 and 1100 aluminum, differences in machining performance were likely due to crystallographic features of the materials such as grain size and orientation. For the remainder of the project, this 1199 aluminum will be the emphasis of the machining experiments.

1.2 DETAILS OF THE PROJECT

Work performed in 2018 centered on optimizing machining parameters to reduce chip seizure during dry machining of 1199 aluminum. The hypothesis being that if 1199 aluminum behaves similarly to plutonium and the mechanism of chip seizure can be understood and eliminated on the aluminum, this knowledge could then be applied to produce the best machined surfaces for plutonium operations at LANL. Parameters of interest are rake angle, tool coating, depth of cut, cross-feed and cutting velocity.

Experimental Setup

To investigate surface finish, machining forces and how different machining parameters affect them, a Nanoform 600 Diamond Turning Machine (DTM) was used to face a 100 mm diameter disc of 1199 aluminum. The DTM used in this study is a high precision turning center. It features an air bearing spindle, vacuum chuck, hydrostatic axes slides, and interferometric axes control. This machine can be used to create high precision machined surfaces required for optical manufacturing applications. Using a high precision machine such as this reduces the amount of variability in the machined surface from machine errors and vibration, allowing for emphasis on effects such as BUE and chip seizure. Figure 5 shows a photograph of the machine setup during the experiments in 2018.

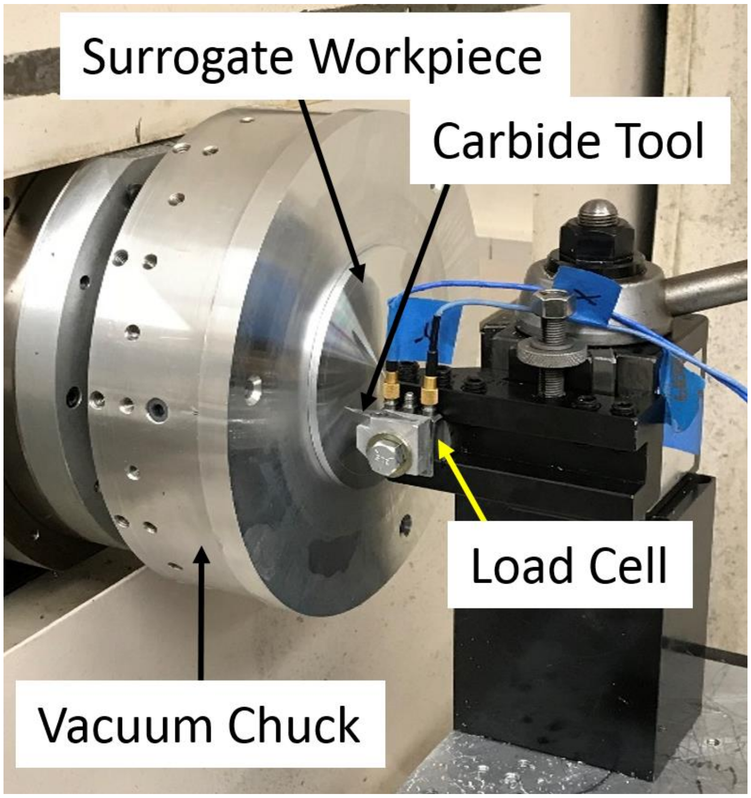

Figure 5. Nanoform 600 Diamond Turning Machine Equipped with an 1199 Aluminum Workpiece, a Kennametal Carbide Turning Insert, and a Kistler Piezoelectric Load Cell

During each experiment, the carbide turning insert fed from the outside radius of the surrogate disc, 50mm, and feed inward to a final radius of 20mm. Though each set of experiments varied a single machining parameter at a time, all parameters tested were be based off of a set of "control" parameters, based on those used on plutonium at LANL. These parameters is displayed in Table 2.

Table 2. Control Machining Parameters Used on 1199 Aluminum

Machining Parameter	Value
Rake Angle (degrees)	+15
Tool Coating	None
Depth of Cut (μm)	120
Cross-Feed (μm/rev)	40
Cutting Speed (m/s)	3-1.8
Tool Nose Radius (μm)	400

Note the range of cutting speed (3 m/s-1.8 m/s) is given in Table 2. This is because at a constant spindle speed of 573 rpm, the cutting speed drops from 3 m/s at the outer radius of the disc, to

1.8 m/s at the minimum radius of 20 mm. All turning inserts used in this experiment were Kennametal V-Series carbide inserts as shown in Figure 6.

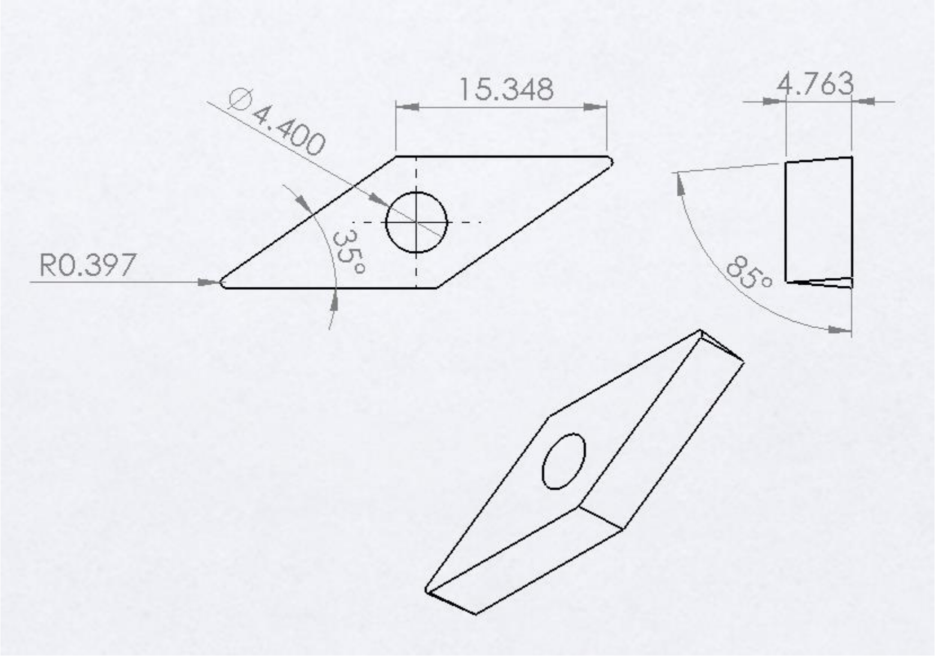

Figure 6. Multiview Drawing of a Kennametal V-Series Carbide Turning Insert, units are in mm, degrees. Drawing Courtesy of Kennametal Graphics Department

Analytical Approach

There were three principle methods to quantify the machining performance of a parameter set during a given experiment. These were force measurement, chip measurement and surface profilometry. These measurements indicate surface roughness as well as the presence of BUE or chip seizure during an experiment.

Force Measurement

A Kistler piezoelectric load cell was used to measure main cutting forces (Fc) and thrust forces (Ft) experienced by the tool. By using a piezoelectric load cell, small changes in machining forces can be measured as small charges in the piezoelectric material. These small charges can be converted to a load measurement by multiplying by a predetermined gain. The orientation of these forces with respect to the tool is shown in Figure 7.

While machining under constant conditions, spikes in measured forces can indicate sticking phenomena such as chip seizure or BUE on the tool. In addition to raw force data, parameters such as coefficient of friction (μ) can also be determined if the rake angle and both Fc and Ft are known.

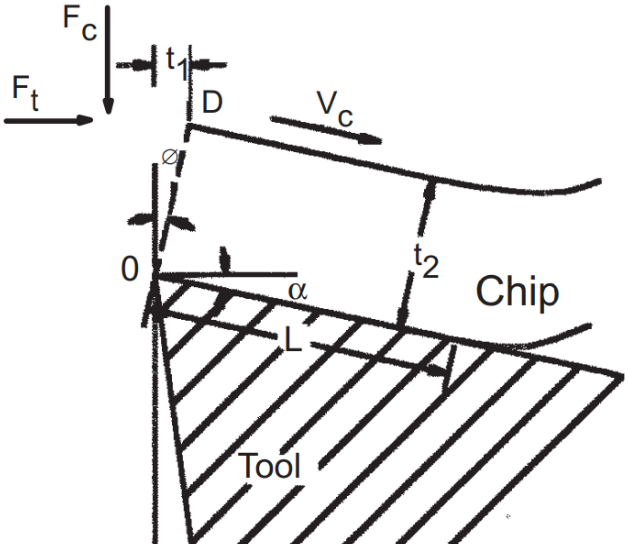

Figure 7. Orientation of Cutting Force (Fc) and Thrust Force (Ft) with Respect to the Tool [6]

An example of a graph of cutting and thrust forces as measured by the Kister load cell are shown in Figure 8.

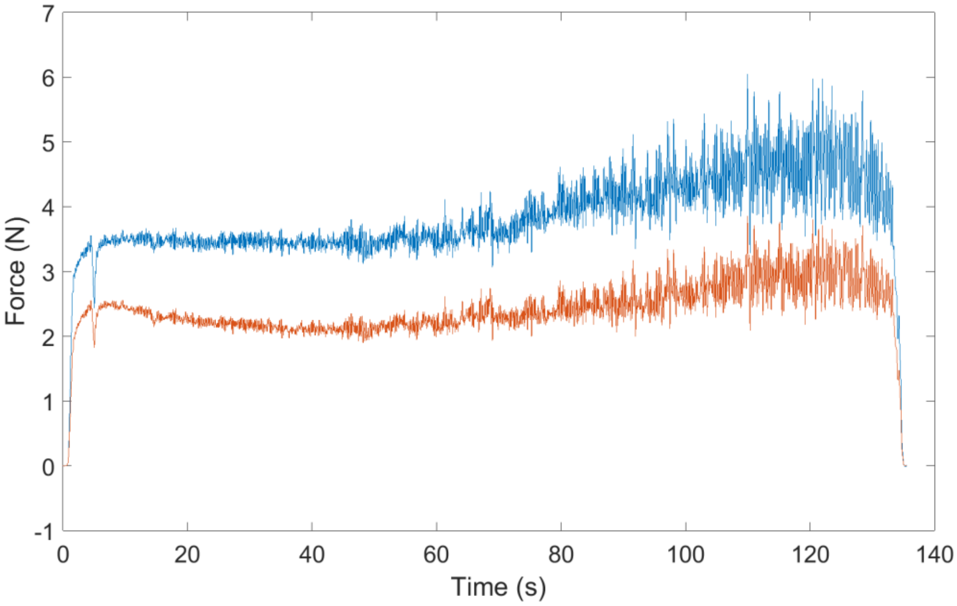

Figure 8. Cutting and Thrusting Forces and Measured by the Kistler Piezoelectric Load Cell

The blue (top) line shown in Figure 8 represent the cutting forces experienced by the tool. The orange (bottom) line shown in Figure 8 represent the thrusting forces. By using the Equation (3), the average coefficient of friction between the chip and the tool was determined to be 1.04 [6].

$$\mu = \frac{F_c \sin(\alpha) + F_t \cos(\alpha)}{F_c \cos(\alpha) - F_t \sin(\alpha)} \quad (3)$$

where Fc is the cutting force, Ft is thrusting force and α is the rake angle of the tool as defined above in Figure 7.

Surface Profilometry

After the face of the disc was machined, the surface was measured in the Talysurf stylus profilometer. For each surface, three radial measurements were conducted; each clocked 120° apart. From these three profiles, Rq (root mean square) surface roughness was calculated for the entire profile. Any features larger than 3 mm in wavelength were filtered out as form error and not considered for Rq measurements. The reported roughness for each experiment is the mean value for the three profiles.

Figure 9 shows how the Talysurf measures machined surfaces. While the stylus traverses over the surface in the X direction as defined in Figure 9, the stylus tip is moved in the Z direction by small features on the surface of the part. A laser interferometer then reads these Z displacements as a function of X, to form a 2-D profile.

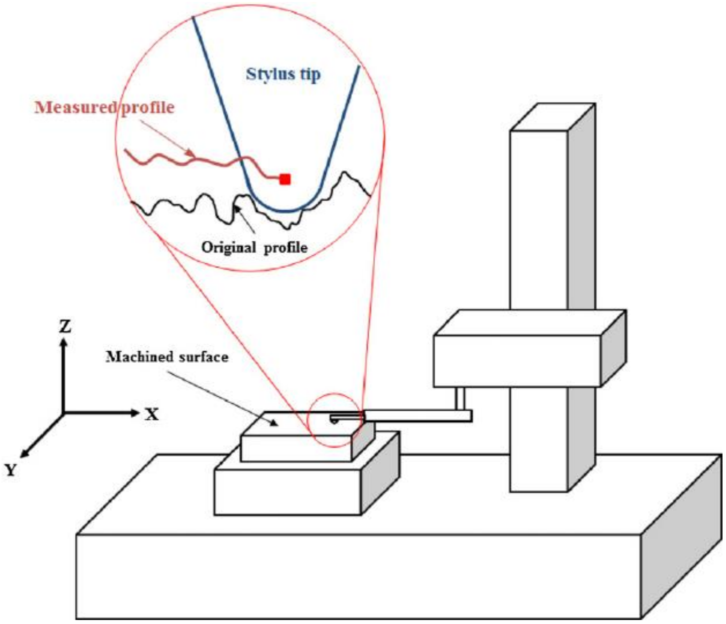

Figure 9. Schematic of a Stylus Profilometer Measuring a Machined Surface, Image Courtesy of AEP Technology

Since the nominal nose radius of the round-nosed tool and the cross-feed (length/revolution) are known quantities, a plot of the theoretical surface can be compared to the machined surface as measured by the Talysurf. Figure 10 shows an example of this comparison. The theoretical surface is shown as the dashed gray line. The solid black line represents the machined surface as measured by the Talysurf.

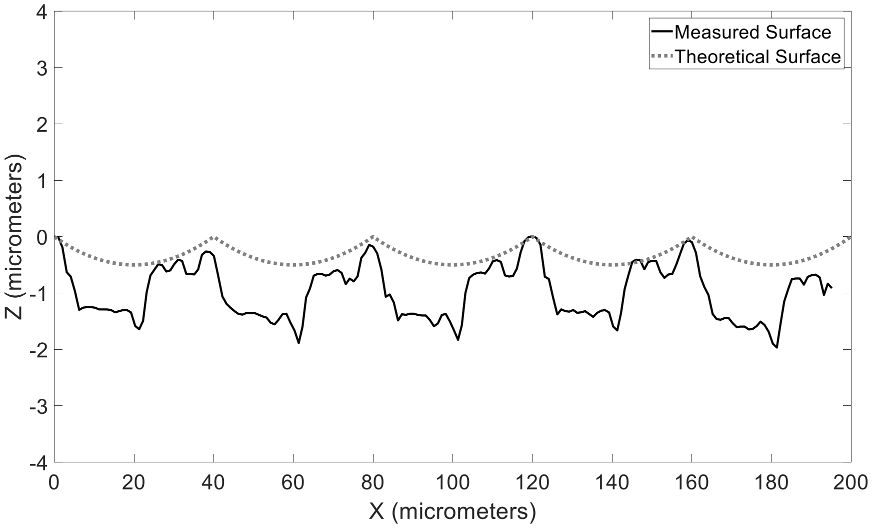

Figure 10. A Surface Profile Created with an Overlapping Feed Rate of 40 µm/rev, spindle rpm = 573, Depth of Cut = 80 µm.

Notice the vertical magnitude of the repeating features in Figure 10. The average of these magnitudes can be quantified for comparison as root-mean-square or Rq surface roughness. Rq surface roughness can be calculated using the formula in Equation (4).

$$Rq = \sqrt{\frac{\int_0^l Z^2(x)dx}{l}} \tag{4}$$

where l is the length of the entire profile and Z(x) is the vertical displacement function as measured by the Talysurf. By approximating the shape of the round nose tool as a parabola, a strictly geometric or “theoretical” value for Rq can be calculated using Equation (5). This is the dashed grey line in Figure 10

$$Rqt = f^2/26.6r \tag{5}$$

where f is the cross-feed, and r is the nose radius of the tool.

Equation (5) assumes no vibration, a perfect cutting edge, no friction, no chip seizure and no BUE. As a result, it acts as a lower bound for surface roughness. For the control parameters (nose radius of 400 µm and a cross-feed of 40 µm/rev), this theoretical roughness value is equal to 0.15 µm. For experiments where cross feed is the independent variable, a quantity called surface fidelity will be used for comparison rather than surface roughness. This "surface fidelity" value is defined as the ratio of theoretical Rq roughness to measured Rq roughness. A higher fidelity value would indicate that the measured surface is similar to the geometric surface.

Chip Measurement

After collecting over 50 chips during each facing operation, it was determined that the cross section of the chip was roughly semielliptical, with the chip width being about twice its thickness. The semielliptical cross section is shown in Figure 11. By monitoring chip geometry, process parameters such as shear plane angle and chip flow velocity can be evaluated. Changes in these parameters could potentially be symptomatic of chip formation issues such as BUE or chip seizure.

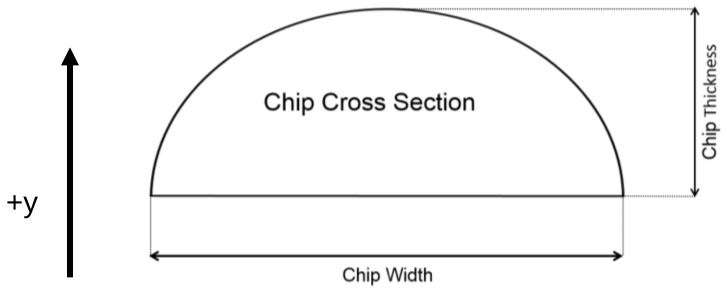

Figure 11. Semielliptical Chip Cross Section

$$A = \frac{\pi}{2}(\mathrm{CT})(\mathrm{CW}) \tag{6}$$

$$MRR = v_{surface} f d = v_{chip}\frac{\pi}{2}(\mathrm{CT})(\mathrm{CW}) \tag{7}$$

Equation (6) describes the relationship between chip thickness (CT), chip width (CW) and Chip Cross Sectional Area (A). The Material Removal Rate (MRR) is related to known input parameters, Surface Speed ($v_{surface}$), Crossfeed (f), and Depth of Cut (d). By assuming that chip volume is conserved during the chip formation process, Equation (7) can be derived. From Equation (7), Chip velocity (v_{chip}), can be calculated.

In addition to chip flow velocity, shear plane angle for the process can be calculated from chip thickness. Equation (8) describes the relationship between shear plane angle (ϕ), rake angle (α), depth of cut (t1) and chip thickness (t2).

$$\varphi = \tan^{-1}\left(\frac{rcos(\alpha)}{1-rsin(\alpha)}\right), r = \left(\frac{t_1}{t_2}\right) \tag{8}$$

Chip collection occurred at 2 points during each experiment, at the onset of the cut, and at the conclusion of the cut. The average of the two chips width and thickness are the reported values for each experiment. The maximum chip thickness measurements were done with micrometers, while width measurement was done via an optical microscope.

Spectral Analysis of Machined Surfaces

When examining the surface of a machined part, features occur on the surface at a wide range of spatial frequencies. Very low frequency ($f \ll crossfeed$) features are likely due to tool path straightness and squareness error, waviness filters should remove most of these types of features before analysis. Very high frequency ($f \gg crossfeed$) features are likely due to machine vibration or small imperfections in the cutting edge. These features are not the main focus of this project. Features of a similar frequencies (or integer multiples) to the cross feed are signs of healthy chip formation, even if surface finish is poor. This is due to the face that poor finish due to tool wear will still occur at the frequency of the cross-feed. Features created as a result of BUE or chip seizure will likely have frequencies lower than that of the cross feed. These frequency signatures are of the most interest to this project.

To identify these frequencies and determine their prevalence, a Fourier transform is performed on the data produced by the Talysurf. The output of the Fourier transform is a Fourier spectrum plot like is shown in Figure 12 and Figure 13.

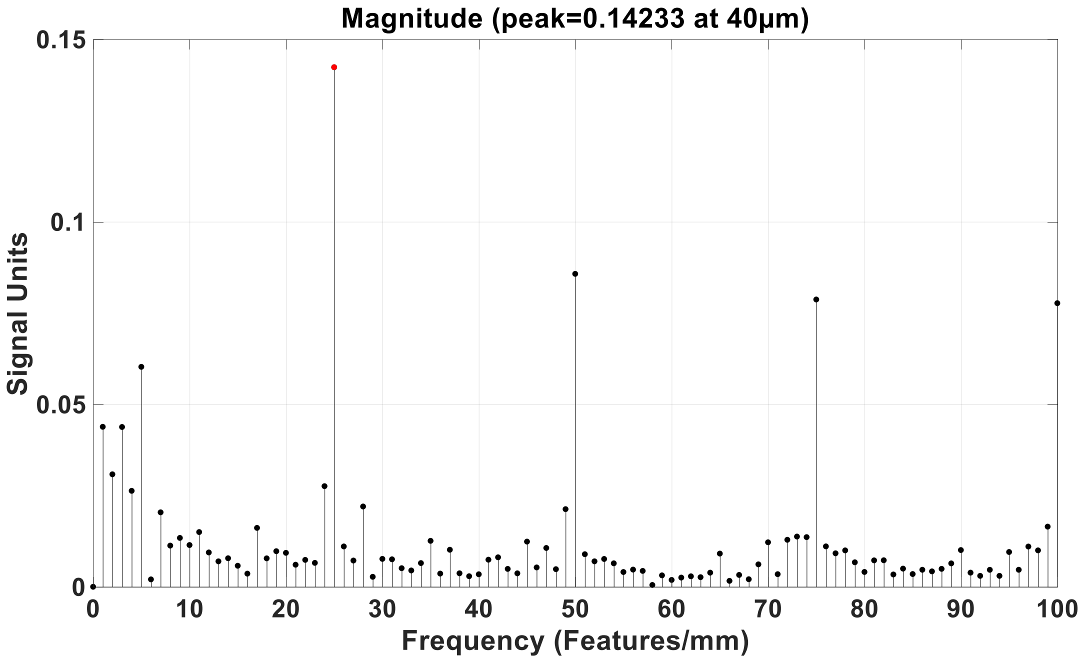

Figure 12. An Example of a Fourier Spectrum of a Machined Part with Good Surface Finish, 40μm Cross-Feed

A near ideal Fourier spectrum is shown in Figure 12. While some non-zero signals are detected in between the peaks seen at integer multiples of the cross-feed frequency, they are very small. It is clear that the three large peaks occur at 25, 50 and 75 features/mm. This means that the surface is largely characterized by the tool path and the geometry of the tool, rather than BUE, chip seizure, or machine error.

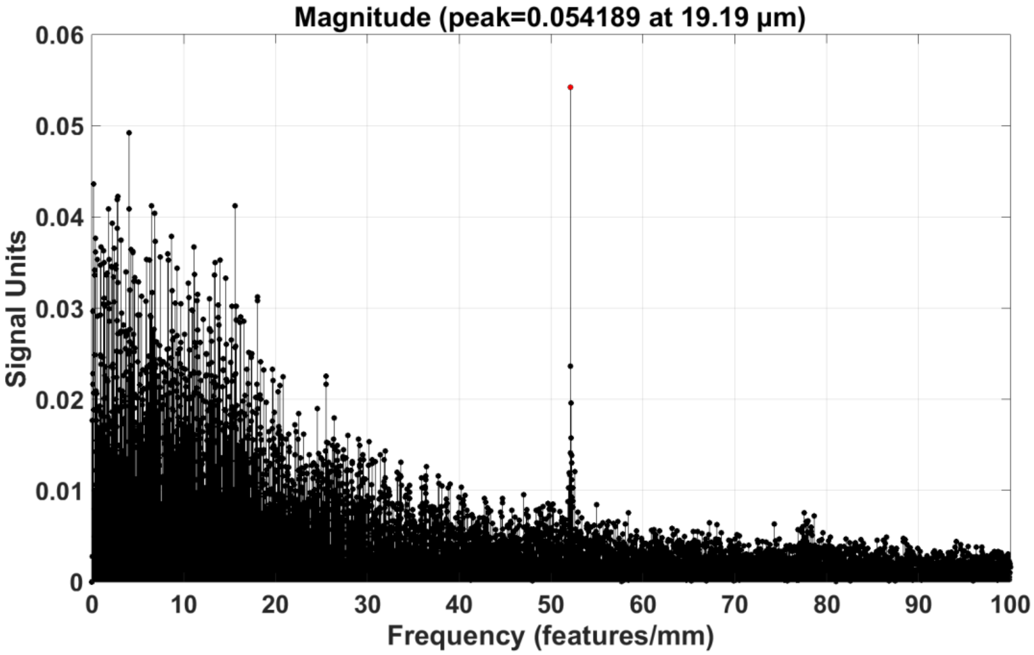

Figure 13. An Example of a Fourier Spectrum of a Machined Part with Poor Surface Finish, 20µm Cross-Feed

The Fourier spectrum shown in Figure 13 depicts a more realistic surface. While a strong peak is prevalent at 50 features/mm, there are many large, low frequency peaks (below 20 features/mm). Since much of the waviness of the surface has been filtered out, this large amount of low frequency features are likely evidence of chip seizure or BUE.

Cyclic Chip Seizure Considerations

During conversations with Los Alamos engineers in 2017, it was determined that chip seizure, not BUE was the principle concern with plutonium. This chip seizure, as described by LANL, is when a reactive chip of plutonium adheres to the rake face of the tool forming a piled up formation. This ball then contacts the already machined surface, smearing the soft plutonium surface and causing large streaks and poor surface finish.

During 2017 experiments, it was determined that this seizure behavior could be replicated using 1199 aluminum as a surrogate. By collecting chips and filming the cutting process, it was hypothesized that the seizure process occurs cyclically, this cycle has also been observed by [8]. The 5 steps of the process are detailed below:

Figure 14 shows the tool at the start of a cut where the depth is very small; too small to create a continuous chip - especially if the surface of the part has some runout. In this case, a short, thin slice of the workpiece is shaved off and sticks to the tool. The width of this sliver grows with the depth of cut on this round-nosed tool as shown in Figure 14. The initial contact at the narrow right-hand-side (RHS) of the pickup shown in Figure 14 would be a small depth of cut and a narrow chip. As the tool is fed into the moving workpiece, the pickup features get wider but remain thin slices.

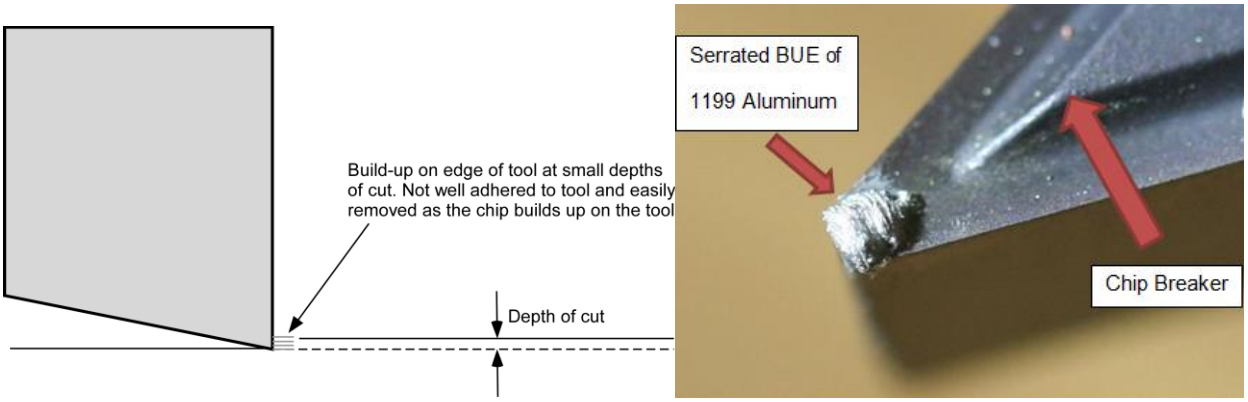

Figure 14. Geometry of the Pickup of Workpiece Material on the Carbide Tool at Small Depths of Cut

Figure 15 shows the cutting model for a deeper cut than Figure 1 with a fixed tool and a chip moving into it from the right to produce a chip. This figure describes Phase 1 of the cutting process where the sliding plane forms in the direction of the maximum combined stress. The chip slides over the rake face of the tool and the contact region is heated due to chip deformation and friction.

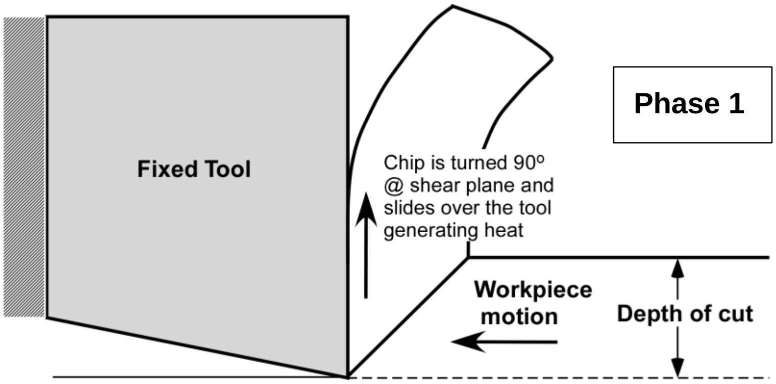

Figure 15. Geometry of the Cutting Process with a Fixed Tool – Phase 1. No Seizure of Chip to the Tool

When the contact temperature reaches a certain level (for a given workpiece and tool material), the force required for the chip to slide on the face of the tool becomes greater than that needed to plastically deform the workpiece ahead of the tool. Basically, the chip is welded to the tool. At this point the chip/tool is the "new cutting tool." It changes the "normal" chip formation process causing an increase in force to move the tool through the workpiece and poor surface finish.
As a result, the "new tool" shape", cutting force increases leading to an increase in the dimensions of the plastic zone in front of the tool and larger surface roughness on the machined part. (Phase 2 shown in Figure 16).

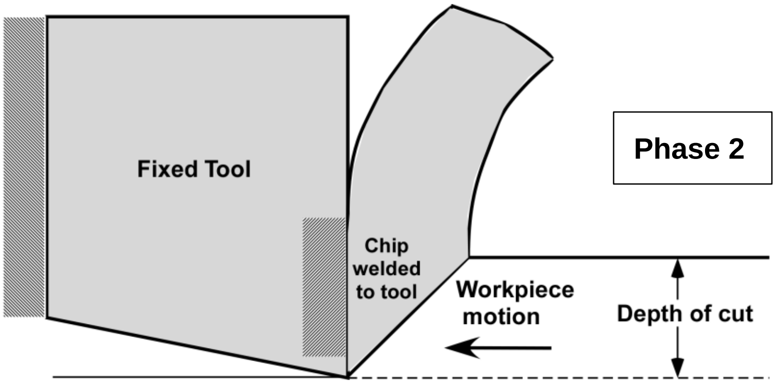

Figure 16. Due to Force/Temperature at the Chip/Tool Interface, the Chip Becomes Welded to the Tool. As a Result the Tool/Chip Becomes the "New" Tool and Forces/Part Roughness Will Increase.

In Phase 2(a), shown in Figure 17, the increase in size of the plastic zone leads to the formation of a growing deposit of the workpiece material on the tool. Here zone ***acd*** is the current plastic zone formed after the chip sliding over the tool face seizes to it. The boundary ***ac*** separates the plastic zone and the motionless chip while its boundary ***ad*** separates this zone from the un-deformed layer being removed. As the workpiece approaches the tool, the material in the plastic zone is compressed and squeezed in the direction of its only free surface ***cd*** so that zone ***acd*** expands. As the chip is motionless and has already been severely deformed, the plastic zone expands into the workpiece; that is, γ_1 gets larger.

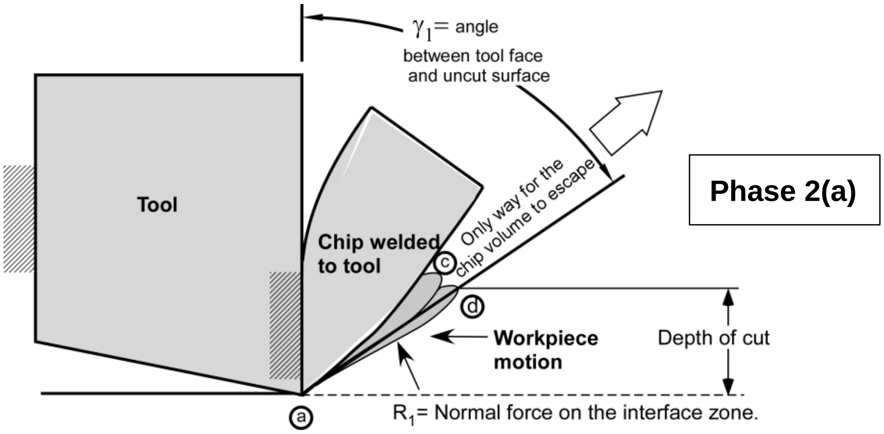

Figure 17. After the Chip is Welded to the Tool, a New Flow Process Begins with the Workpiece Coming in from the Right

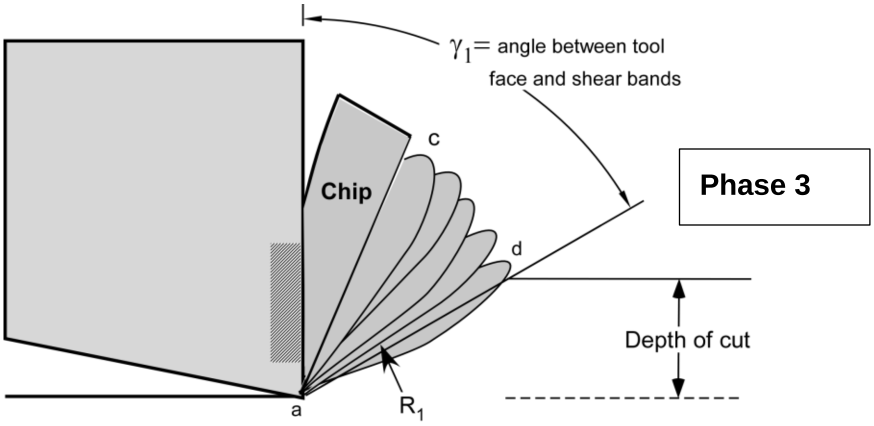

R_1 is the resultant force from creating the shear bands (in region ***acd***) that rotates toward vertical as γ_1 increases and breaks the chip tool connection.

Figure 18. In Phase 3, the Chip is Stuck to the Tool and Plastic Shearing of the Incoming Workpiece Increase γ_1 and Turns R_1 Vertical to Push the Chip off the Tool and Restart the Chip Flow.

During this transformation shown in Figure 18, the angle γ_1 gradually increases up to 90º which leads to a change in the mode of deformation from compression to the shear. When γ_1 approaches 90º, the reaction force R1 (from elastically deformed part of layer being removed) has changed its direction to become parallel to the tool rake face leading to Phase 4, shown in Figure 19. When the cutting force reaches a certain value, the reaction force R1 becomes great enough to shear the chip fragment and the shear bands from the tool and they become part of the chip as shown in Figure 6. Once the built-up edge has been removed, the normal chip formation returns until the contact temperature becomes high enough to start the formation of a new built up edge.

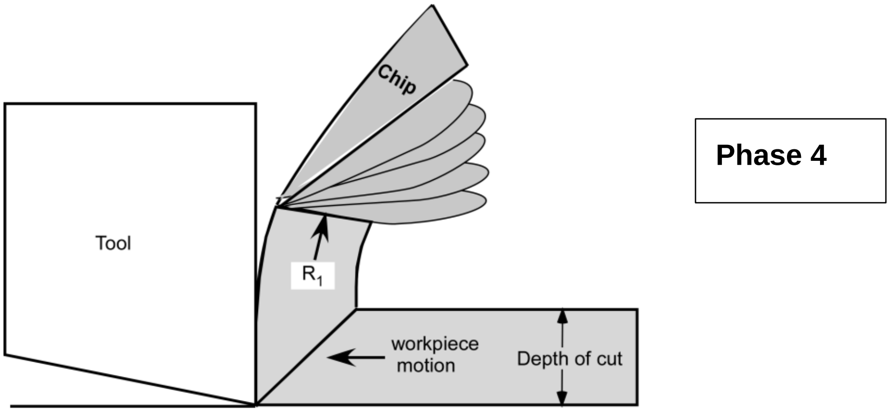

Figure 19. The Motion of the Incoming Workpiece Rotates and Ejects the Built-up Region and Starts a New Chip that Can Again Stick to the Tool and Start the Cycle Over Again. Depending on the Conditions, the Chip Can be Continuous for Some Time before Welding Again.

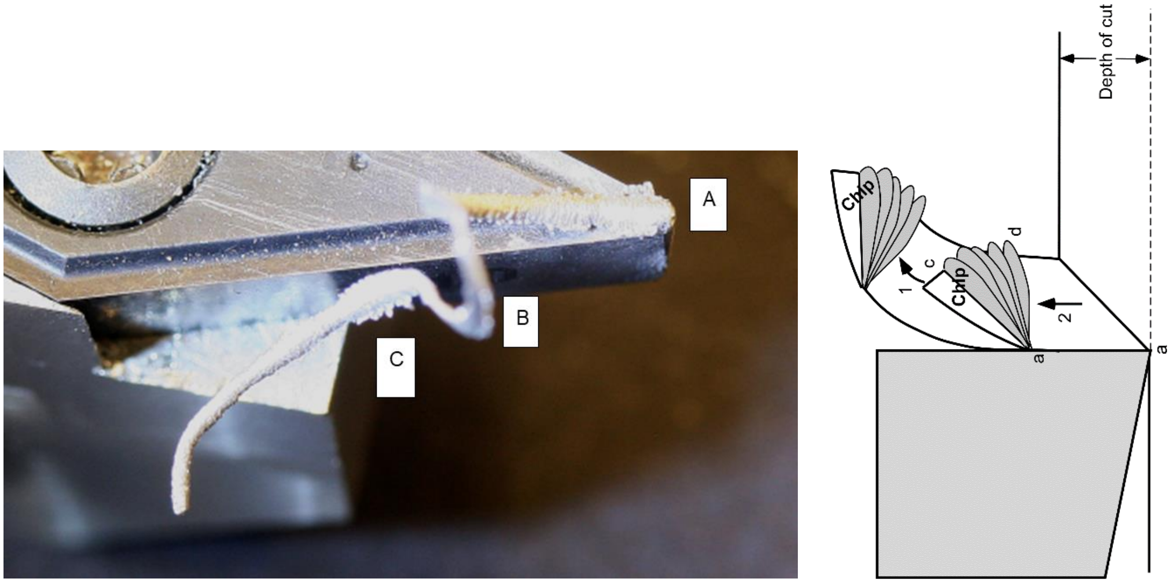

Figure 20. The Image of a Chip Generated Cutting 1199 Al. The Photo Shows a Chip that was stuck to the Cutting Edge during Machining and the Force Became Large Enough to Stall the Motor. The Image on the Right is the same as Figure 19 but Two Broken-off Chips are Shown and It is Turned 90 Degrees to Match the Point of View on the Photo.

The chip in Figure 19 was collected as a result of luck when the motor stalled with the chip still attached to the tool. It started as a normal chip at the left, C is a region where the chip stuck to the tool, B is a normal chip but with a twist probably caused by interaction with the chip breaker design of this tool and A is another stuck region that took more torque that the motor could produce and ended the experiment. Observation during the experiment showed at A and C the chip seem to stop (it was probably moving slowly) and moving much faster at B and the beginning of the cut to the left of C.

The cartoon on the right in Figure 19 shows how the chip may have been created and the reason for the slow speed and the features of the chip observed in the photograph. As explained in Phase 3 and 4 of the intermittent chip generation, the sticking of the workpiece material to the tool begins with the soft, hot aluminum chip welding to the tool. It stops the normal material flow until the chip get pushed out of the way and a new chip is formed. The cartoon and the chip features appear similar and may reveal a way to improve the chip flow and the surface finish when machining this soft material.

Evidence to show how chip seizure effects surface roughness is displayed in Figure 21.

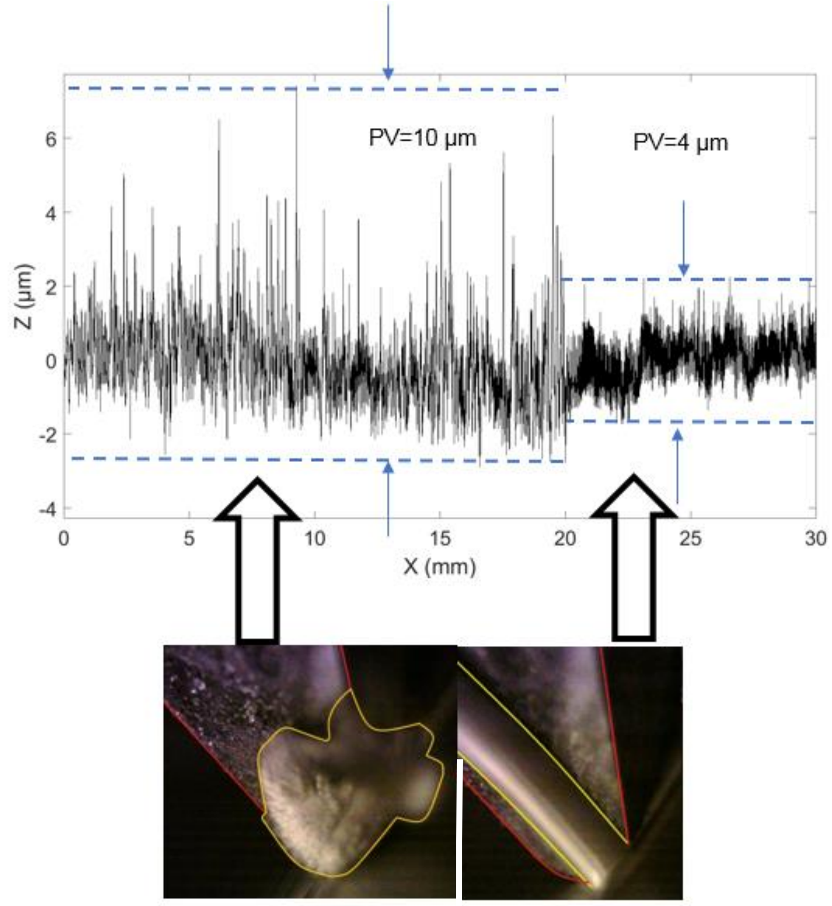

Figure 21. Surface Profile of 1199 Aluminum Turned with Tool 2 at 80 µm Depth of Cut, Turned at 550 RPM at a Feed Rate of 22 mm/min

Figure 21 shows an interesting trend on the surface of a machined part. This surface can be divided into two regimes. To the right of x=20 mm, the surface is consistent, smooth, and contains no features taller than 2 µm. This correlates with the formation of a smooth, continuous chip, which was recorded by a high magnification video camera. This smooth, continuous chip can be seen in the bottom right.

To the left of the 20 mm line, the surface contains many tall, irregular features. This correlates with poor chip flow across the tool. Video evidence of this poor chip flow is shown in the bottom left. This poor chip flow is characterized by slow moving, massive chips periodically seizing to the tool's rake face like photographed **Figure 20**.

This change across the machined surface is due to the cutting speed decreasing as the tool feeds towards the center of the disc. Higher cutting speeds resulted in continuous chip flow and improved surface finish, while low surface speeds resulted in intermittent, seized chip flow and bad surface finish.

Figure 22 is a high-magnification view of a 200 µm region of the machined surface measured in the right (smoother) side of Figure 21. While the measured surface in Figure 21 does deviate from the theoretical surface, 5 distinct feeds of the tool can be seen at the prescribed cross feed of 40 µm. This is in agreement with the smooth chip flow shown in the bottom right of Figure 21.

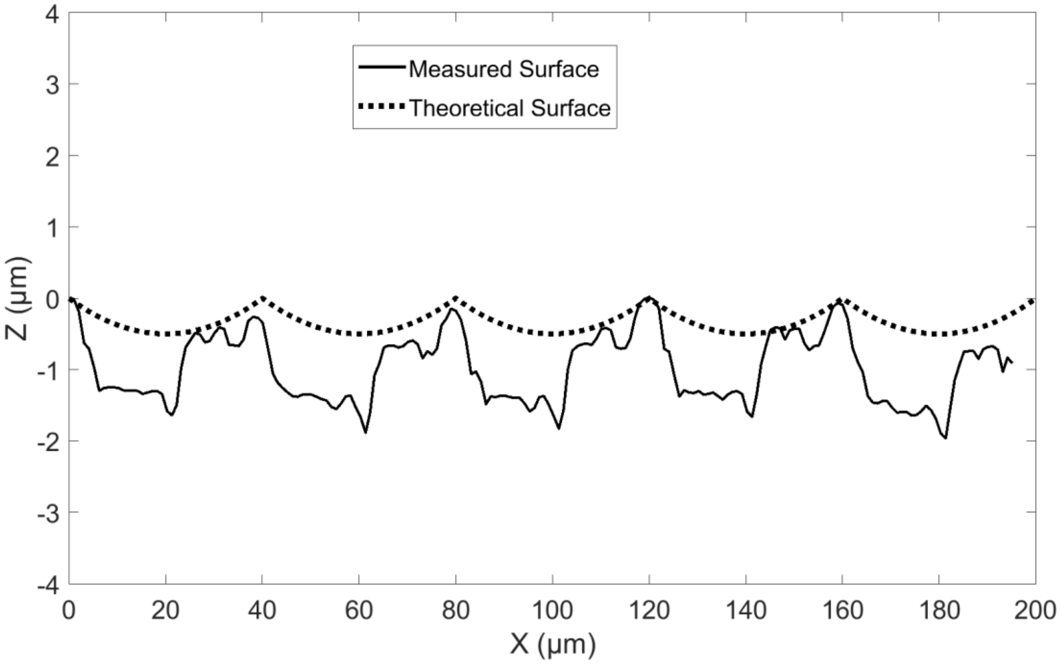

Figure 22. Comparison of Surface Created at 80 µm Depth of Cut to the Theoretical Surface, Tool 2, Turned at 550 RPM at a Feed Rate of 40 µm per Revolution. Above 1.77 m/s Cutting Speed. This is a zoomed in version of the same data displayed on the right side of Figure 21.

Figure 23 is a frequency-magnitude plot of the machined surface measured in Figure 21 (smooth side of Figure 21), to the right of the x=20 mark. This correlates to the region where cutting speed was above 1.77 m/s. The largest peak present on the plot can be seen at a spatial frequency of 25 features/mm. This reflects the 40 µm/rev cross feed of the tool. This strong peak in combination with the lack of low frequency (<25 features/mm) indicates smooth chip formation.

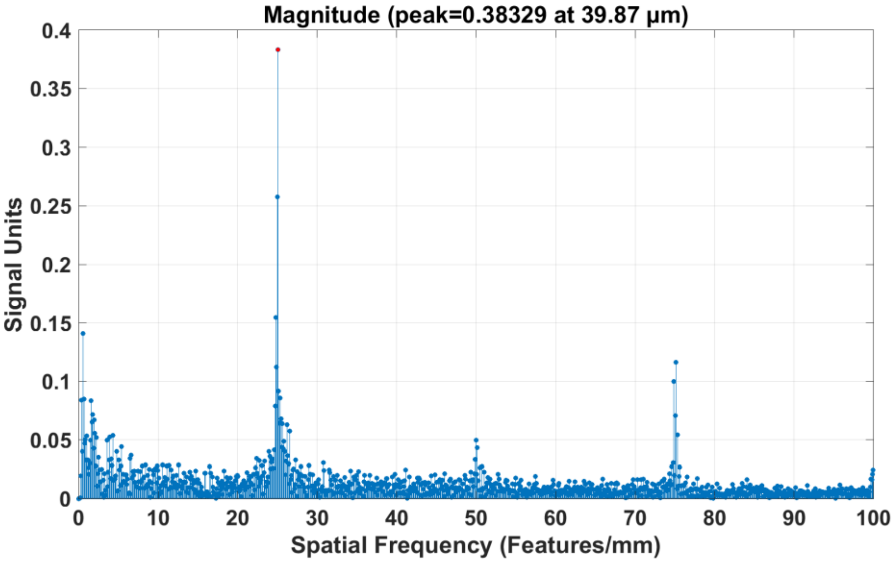

Figure 23. Frequency-Magnitude Spectrum of the Machined Surface Shown in the Right Side of Figure 21, 1199 Aluminum Turned with Tool 2 at 80 µm Depth of Cut, Turned at 550 RPM at a Feed Rate of 40 µm/rev, above 1.77 m/s

Figure 24 is a high-magnification view of a 200 µm band of the machined surface measured in the left side Figure 21. Since repeated features can be seen, few similarities to the theoretical surface exist. This indicates chip flow issues such as seizure.

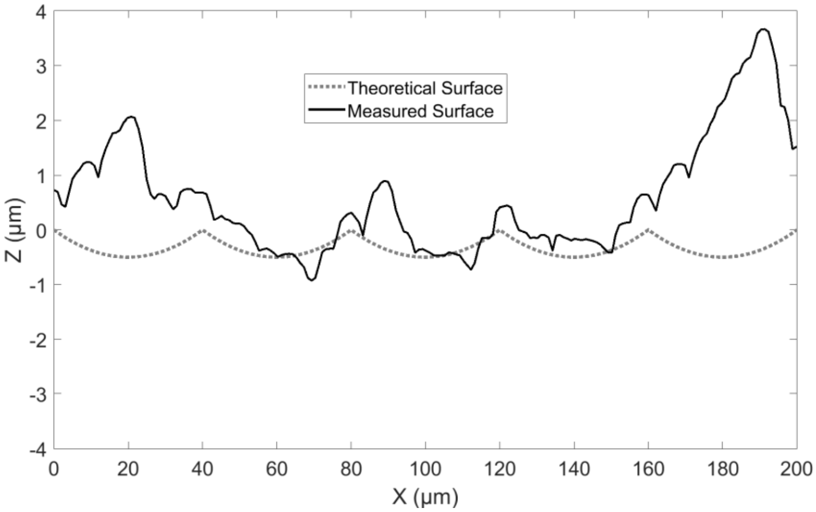

Figure 24. Comparison of Surface Created at 80 µm Depth of Cut to Theoretical Surface, Tool 2, Turned at 550 RPM at a Feed Rate of 40 µm per Revolution. Below 1.77 m/s cutting speed. This is a zoomed in version of the same data displayed on the left side of Figure 21.

Figure 25 is a frequency-magnitude plot of the machined surface measured in Figure 21, to the left of the x=20 mark. This correlates to the region where cutting speed was below 1.77 m/s. The largest peaks present on the plot can be seen at a spatial frequency of below 15 features/mm. Since the wavelength of these strong features is lower than the frequency of the cross feed (25 features/mm), they indicate poor chip flow such as shown at the bottom left of Figure 21. In addition to these low frequency features, strong peaks are also present at 25, 50 and 75 features/mm. These are integer multiples of the cross feed frequency, meaning that some smooth chip flow did occur. This is evidence to the cyclic nature of the chip seizure shown in **Figure 20**

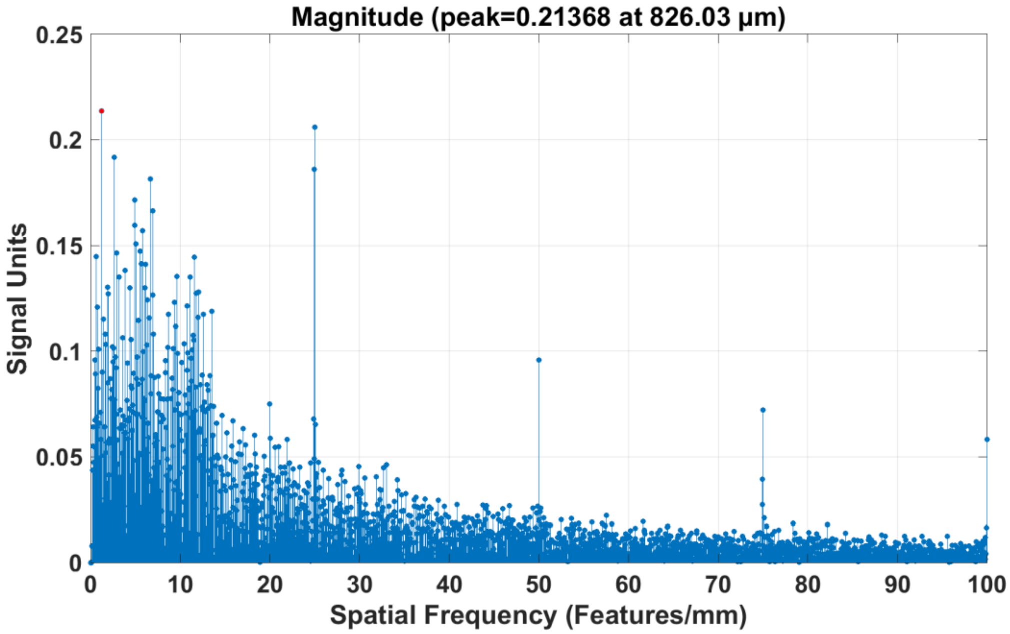

Figure 25. Frequency-Magnitude Spectrum of the Machined Surface Shown in the Left Side of Figure 21, 1199 Aluminum Turned with Tool 2 at 80 µm Depth of Cut, Turned at 550 RPM at a Feed Rate of 40 µm/rev, below 1.77 m/s

Table 3 quantifies the change in surface roughness as a function of speed witnessed at 80 µm depth of cut. The line at 20 mm on the x axis on Figure 21 equates to 1.77 m/s surface speed at 550 rev/min. RMS surface finish is significantly improved when cutting speed is above 1.77 m/s.

Table 3. Surface Finish Above and Below 1.77m/s (Figure 21). Tool 2. Aluminum 1199, 80 µm Depth of Cut

	Tool 2 (<1.77m/s)	Tool 2 (>1.77 m/s)
Theoretical RMS Surface Finish (µm)	0.16	0.16
RMS Surface Finish (µm)	0.62	1.16

1.2.3 Experimental Results of Parameter Study on 1199 Aluminum

Using the machine and tool path described in section 1.2 and the analytic methods described, the control parameters were altered one at a time, a single factor study. The parameters varied were rake angle (1), tool coating (2), depth of cut (3), cross-feed (4) and cutting speed (5).

Effects of Rake Angle on Dry Machining of 1199 Aluminum

Using the 50 mm diameter disc of 1199 aluminum disc, 5 different rake angles of Kennametal V-Series carbide inserts were studied. **Table 4** displays the machining parameters used for the 5 experiments. During preliminary experiments in 2017, it was determined that negative rake angles are not feasible for use on 1199 aluminum due to excessive machining forces and poor surface finish. Geometric theoretical roughness for all four of these experiments is 0.15 µm.

Table 4. Parameters Used for Rake Angle Experiments

Machining Parameter	Value
Rake Angle (degrees)	+15,+12,+9,+6,+3
Tool Coating	None
Depth of Cut (µm)	120
Cross-Feed (µm/rev)	40
Cutting Speed (m/s)	3-1.8
Tool Nose Radius (µm)	400

Figure 26 displays the surface roughness of the aluminum disc, as well as the shear plane angle of the 1199 aluminum disc as a function of tool rake angle.

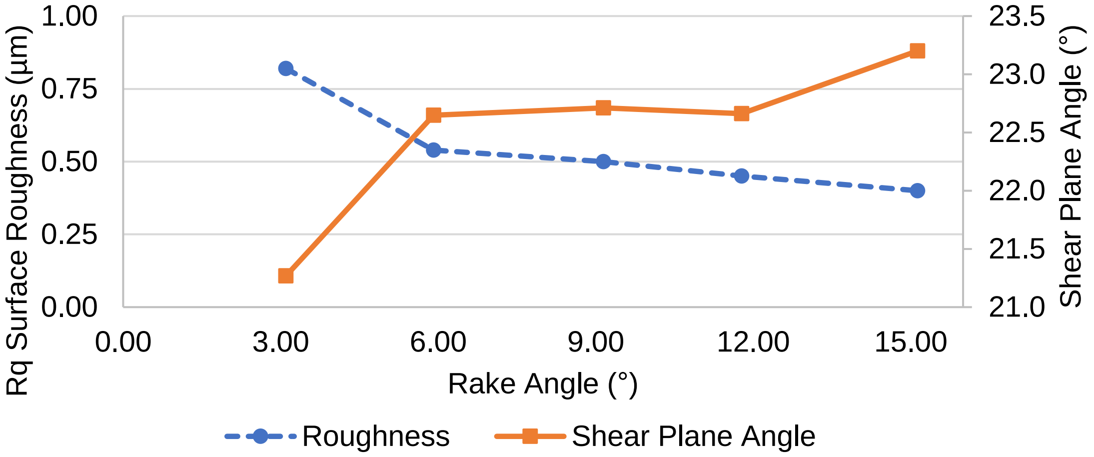

Figure 26. Surface Roughness and Shear Plane Angle as a Function of Rake Angle

As shown in Figure 26, surface roughness improved monotonically from the smallest rake angle of +3° to the highest rake angle of +15°. Surface finish improved from 0.82µm to 0.40 µm across the band. This represents a 49% improvement. This is due to improved chip flow that resulted in reduced chip seizures and smearing on the machined surface. Shear plane angle, as described as ϕ in Figure 7, was highest at +15° and lowest at +3° with a plateau on the three intermediate rake angles. A higher shear plane angle is associated with better chip flow [7]. Shear plane angle increased 9% from 21.27° to 23.20° across the band of rake angles tested.

Figure 27 shows cutting force (Fc), thrust force (Ft), and total (resultant) force as a function of rake angle.

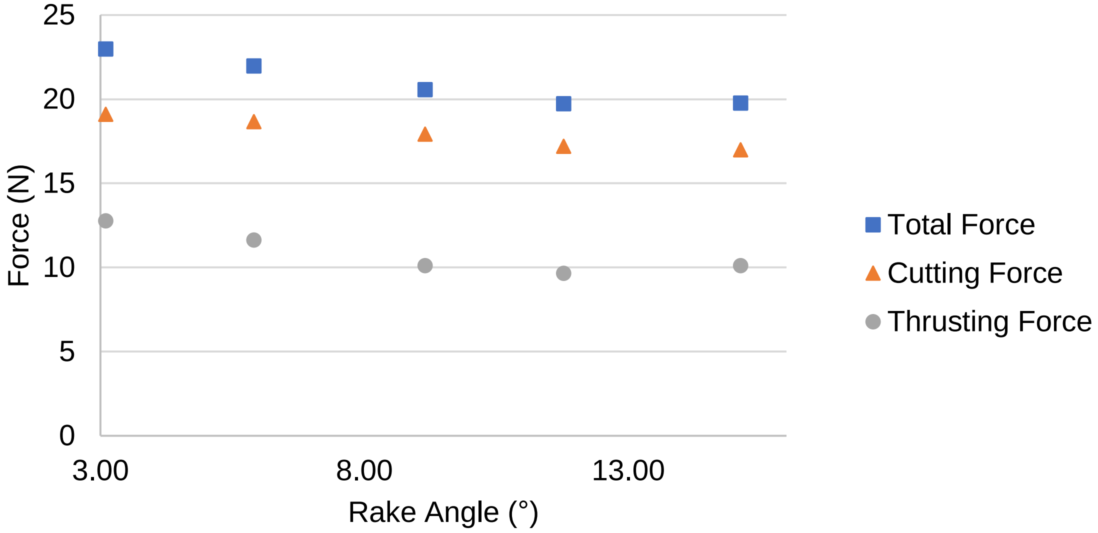

Figure 27. Machining Forces as a Function of Rake Angle

Figure 27 cutting force decreased 11% from a rake angle of +3° to +15°, while thrust force decreased 21% and total force decreased 14%. This change is on the same order of magnitude as seen in rake angle research on other metals [7], and is likely due to the more concentrated stress field projected ahead of the tool as a result of higher rake angles [7]. Figure 28 and Figure 29 display the frequency spectra as measured on the machined surfaces at +3° and +15° degrees, the roughest and smoothest surfaces, respectively.

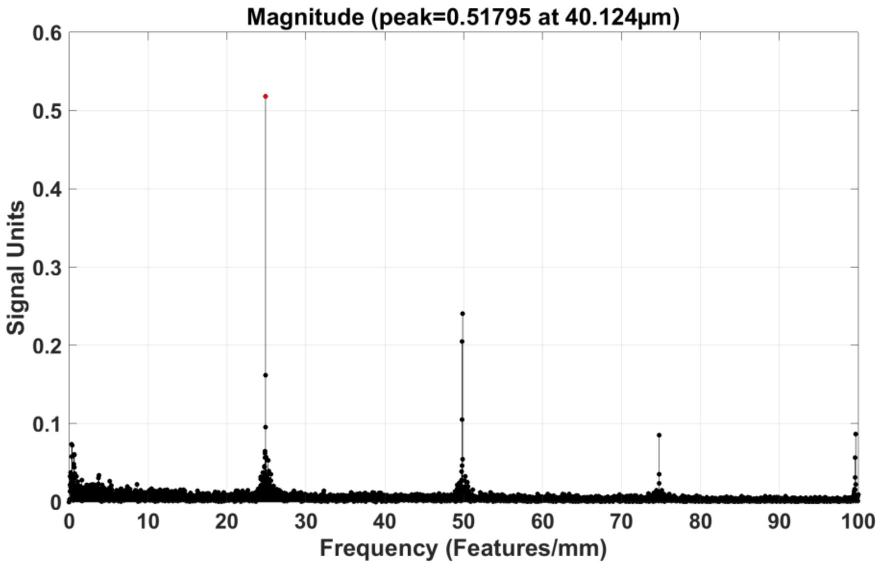

Figure 28. Fourier Spectrum for the Surface Machined with a +3° Rake Angle

As shown in Figure 28, strong peaks are present at 25, 50 and 75 features per millimeter. These are integer multiples of the cross-feed of 40μm per revolution. These strong peaks indicate that chip seizure and smearing were not prevalent on these surfaces machined by positive rake angles. Negative rake and zero rake tools were tested in previous experiments on 1199 aluminum, and deemed to be inappropriate for ductile materials due to extreme chip seizure and high machining forces.

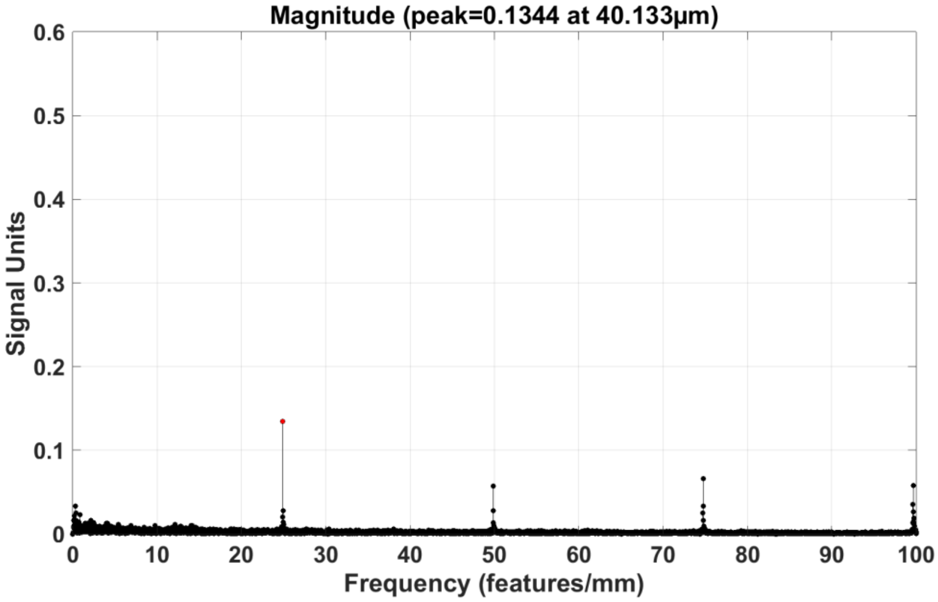

Figure 29. Fourier Spectrum for the Surface Machined with a +15° Rake Angle

Figure 29, which is shown on the same scale as Figure 28, shows defined peaks at the same integer multiples of 25 features per millimeter. This indicates strong chip flow, void of seizure events. However, the magnitude of these peaks is about 33% of the peaks seen on Figure 28, which indicates improved surface roughness, in agreement with the measured Rq values in Figure 26 which indicated better surface finish.

Effects of Tool Coatings on Dry Machining of 1199 Aluminum

Using the 50 mm diameter disc of 1199 aluminum, 6 different PVD (physical vapor deposition) tool coatings on Kennametal V-Series carbide inserts were studied. Table 5 shows the machining parameters used for the 6 experiments. The Kennametal descriptions for each of the coatings tested are in Table 5. All tool coatings tested are available off the shelf from Kennametal and are recommended for use on non-ferrous metals. Geometric theoretical roughness for all four of these experiments is 0.15 µm.

Table 5. Parameters Used for Tool Coating Experiments

Machining Parameter	Value
Rake Angle (degrees)	+15
Tool Coating	None (K313), KC730, KC5410, KC5020, KC5010, KCU25
Depth of Cut (µm)	120
Cross-Feed (µm/rev)	40
Cutting Speed (m/s)	3-1.8
Tool Nose Radius (µm)	400

KC730: A PVD TiN coating over a very wear-resistant unalloyed substrate. Application: For general purpose machining of high-temperature alloys, aerospace materials, refractory metals and 200 or 300 series stainless steels. The thin, uniformly dense, smooth coating increases wear resistance and reduces problems with built-up edge. It also provides an unusually good combination of properties for machining difficult-to-machine materials and aluminum. The substrate offers superior thermal deformation resistance, depth of cut notch resistance, and edge strength. Run at higher speeds than uncoated grades. Most ground periphery inserts have a sharp edge.

KC5410: An extremely hard TiB2-PVD-coated grade that provides very good wear characteristics at high cutting speeds and is best suited for machining aluminum with <10% silicon and other non-ferrous materials. KC5410 resists built-up edge, can help reduce the burring effect, and will generate excellent surface finish.

K313: A hard, low binder content, unalloyed WC/Co fine-grained grade. Application: Exceptional edge wear resistance combined with very high strength for machining titanium, cast irons, austenitic stainless steels, non-ferrous metals, nonmetals, and most high-temperature alloys. Superior thermal deformation and depth of cut notch resistance. The grain size is well controlled for minimal pits and flaws which contributes to long, reliable service.

KC5010: This grade is ideal for finishing to general machining of most workpiece materials at higher speeds. Excellent for machining most steels, stainless steels, cast irons, non-ferrous materials and super alloys under stable conditions. It also performs well machining hardened and short chipping materials.

KCU25: An advanced PVD TiAlN coated grade with a tough, ultra-fine grain unalloyed substrate. Application: For general purpose machining of most steels, stainless steels, high-temperature alloys, titanium, irons, and non-ferrous materials. Speeds may vary from low to medium and will handle interruptions and high feed rates.

KC5025: For general purpose machining of most steels, stainless steels, high-temperature alloys, titanium, irons, and non-ferrous materials. Speeds may vary from low to medium, and will handle interruptions and high feed rates.

Figure 30 shows the shear plane angle and surface finish values for all 5 coatings and the uncoated (K313) tools.

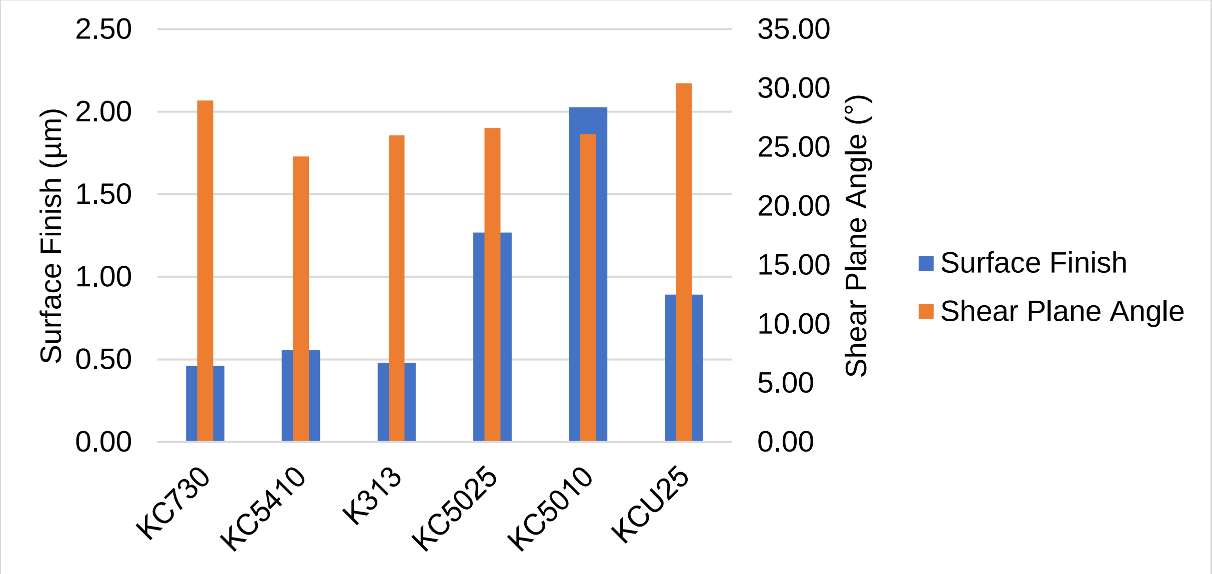

Figure 30. Surface Roughness and Shear Plane Angle for all 6 Tool Coatings

Figure 30 shows that surface finish changed drastically depending on the coating applied to the tool. The best surface finish of 0.46 µm is only 23% as rough as the worst surface roughness of 2.03 µm. KC5025, KC5010 and KCU25 coatings resulted in the worst surface roughness. These coatings all contained aluminum, while the three best performing coatings (KC730, KC5410 and uncoated) do not contain aluminum. This poor surface finish could be a result of chip seizure and smearing due to reactivity between the aluminum in the coating and the aluminum work piece. While the KC730 and KC5410 produced better surfaces than the other coatings, they did not yield an improved surface when compared to the uncoated tool. Shear plane angle measurements were inconclusive with respect to tool coatings.

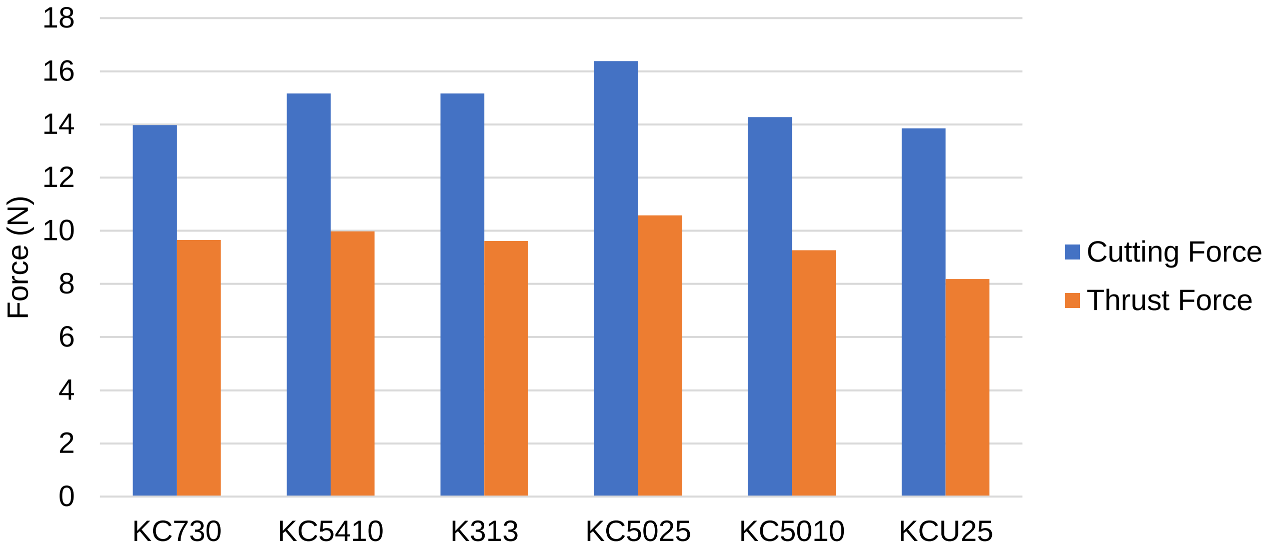

Figure 31. Machining Forces for all 6 Tool Coatings

Figure 31 displays average cutting and thrust forces for all tool coating tested. KC5025 had the highest cutting and thrust forces, while KCU25 had the lowest. However, the difference between these was only about 2 N (~15%) for cutting and thrust (~20%). The three coatings that yielded the best surface finishes (KC730, KC5410 and uncoated (k313)) have cutting and thrust forces within 1 N of each other.

Figure 32 and Figure 33 display the frequency spectra of the features as measured on the machined surfaces with KC5010 and KC5410, the roughest and smoothest surfaces, respectively.

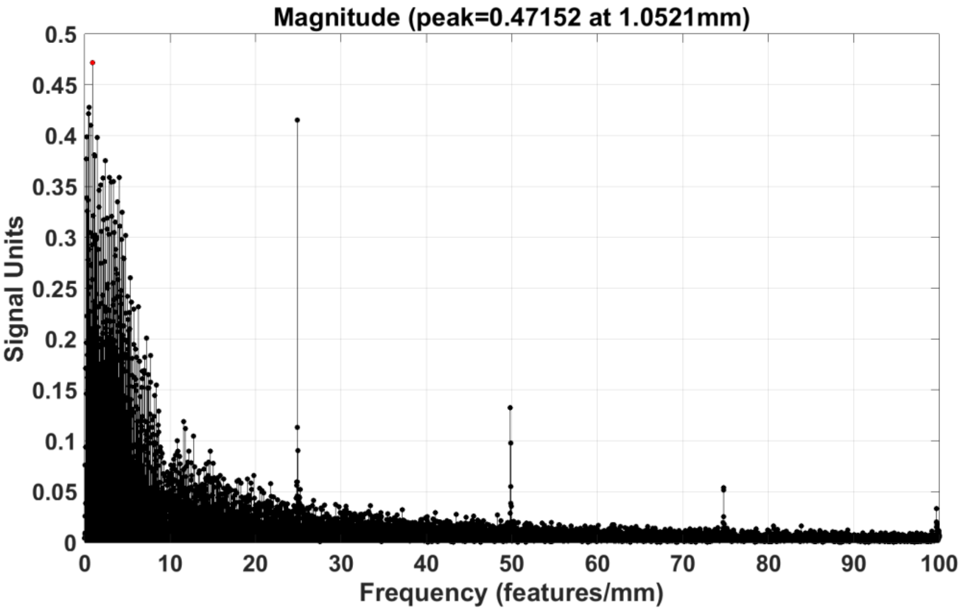

Figure 32. Fourier Spectrum for the Surface Machined with a KC5010 Coating

Figure 32 shows the Fourier spectrum for the surface machined with the KC5010 tool. While strong peaks are seen at integer multiples of the cross-feed frequency (25, 50 and 75 features per mm), many strong peaks are also present below 10 features per mm. These peaks are indicative of features on the surface created by low frequency phenomena such as chip seizure and the resulting smearing.

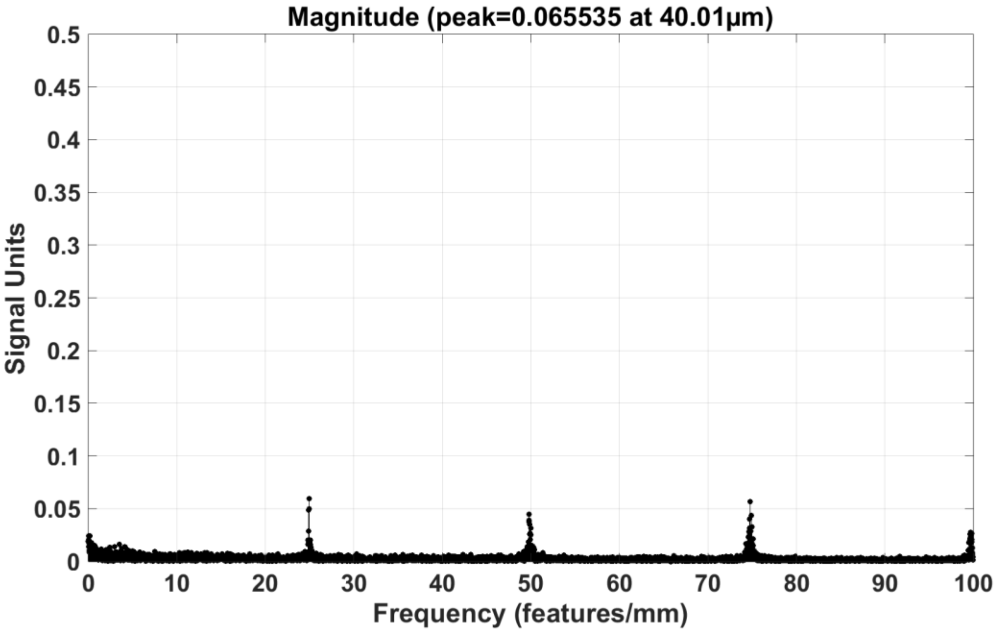

Figure 33. Fourier Spectrum for the Surface Machined with a KC5410 Coating

Figure 33 describes the surface machined with the KC5410 tool. It shows a very different machined surface than the one shown in Figure 32. The peaks are much smaller, and occur at integer multiples of the cross-feed frequency. This indicates a smooth surface, void of low frequency features caused by chip seizure and smearing on the machined surface.

Effects of Depth of Cut on Dry Machining of 1199 Aluminum

Using the 50 mm diameter disc of 1199 aluminum disc, 5 different depths of cut were tested using Kennametal V-Series carbide inserts. Table 6 displays the machining parameters used for the 5 experiments.

Table 6. Parameters Used for Depth of Cut Experiments

Machining Parameter	Value
Rake Angle (degrees)	+15
Tool Coating	None
Depth of Cut (µm)	20, 40, 60, 80, 100, 120
Cross-Feed (µm/rev)	40
Cutting Speed (m/s)	3-1.8
Tool Nose Radius (µm)	400

Figure 34 displays surface roughness and shear plane angle as a function of depth of cut.

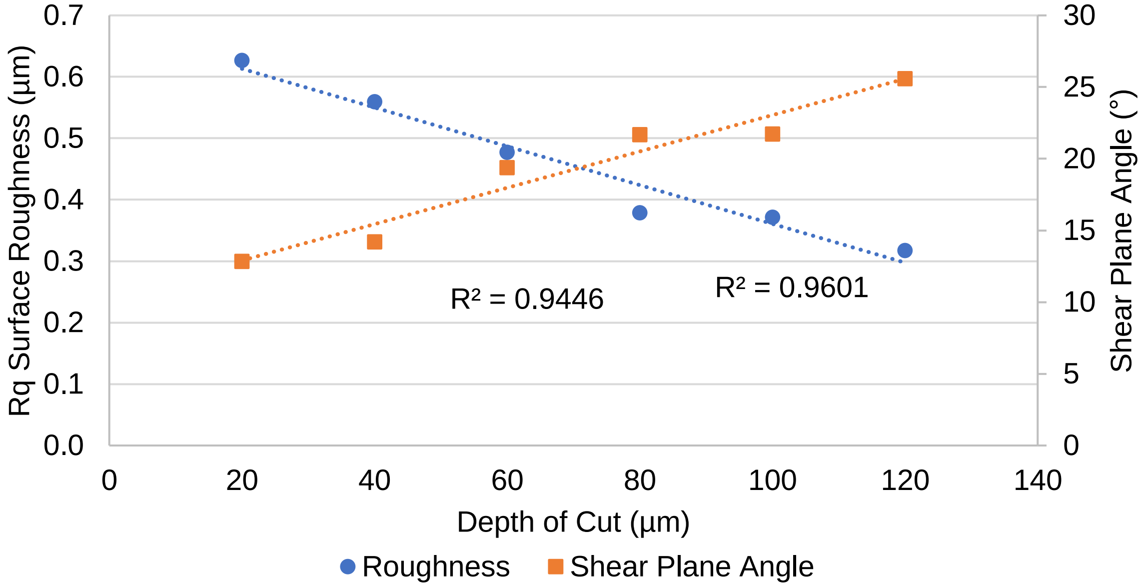

Figure 34. Surface Roughness and Shear Plane Angle as a Function of Depth of Cut

As shown in Figure 34, surface roughness and shear plane angle showed strong linear correlation with depth of cut, one positive, one negative. Surface roughness improved monotonically from 0.63 µm to 0.32 µm as depth of cut was increased from 20 µm to 120 µm. Shear plane angle increase from 12.84° to 25.60° across the same band. This correlation between shear plane angle and surface roughness is in agreement with Cohen and was also evident in the rake angle experiments [9].

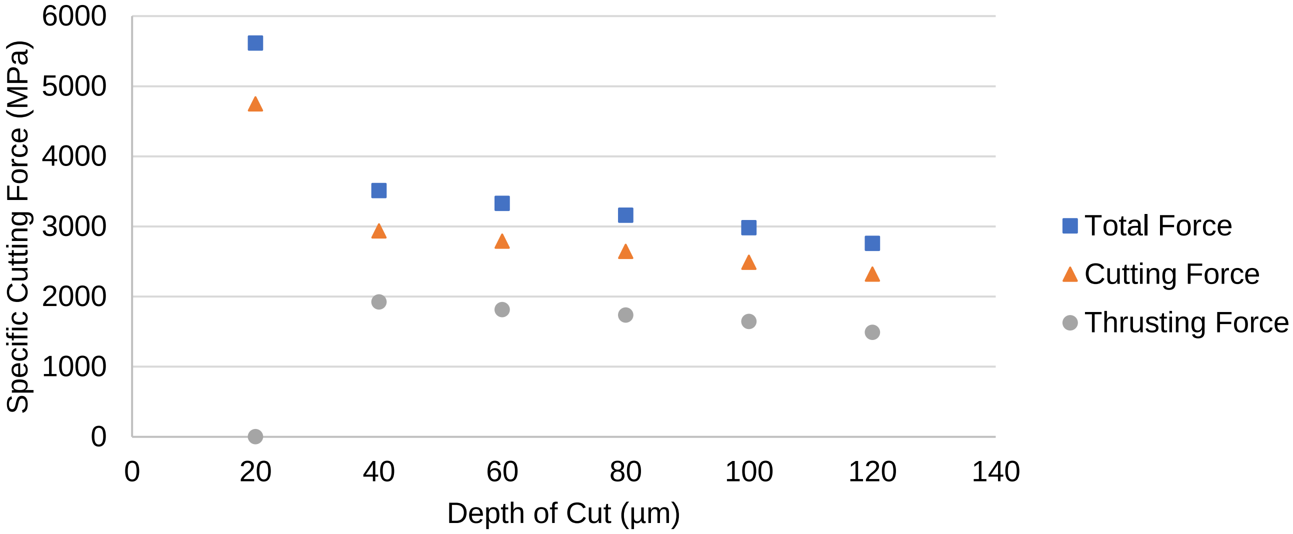

Figure 35. Machining Forces as a Function of Depth of Cut

Since the chip load increased as depth of cut increased, it is not appropriate to compare the magnitude of the machining forces as a function of depth of cut. Instead, force per unit chip area should be used as a basis for comparison. Figure 35 displays machining forces per unit chip area in MegaPascals (N/mm^2). Total (resultant), cutting and thrust specific forces decreased linearly from a depth of cut of 40 µm up. This is likely due to the decreasing effects of the imperfect cutting edge since it is smaller in comparison to the entire chip.

The high forces seen at the 20 µm depth of cut are due to the drastic onset of chip seizure events. Depths of cut larger than 40 µm resulted in fewer and less severe chip seizure events.

Figure 36 and Figure 37 display the frequency spectra of the features as measured on the machined surfaces with 20 µm and 120 µm depths of cut, the roughest and smoothest surfaces, respectively.

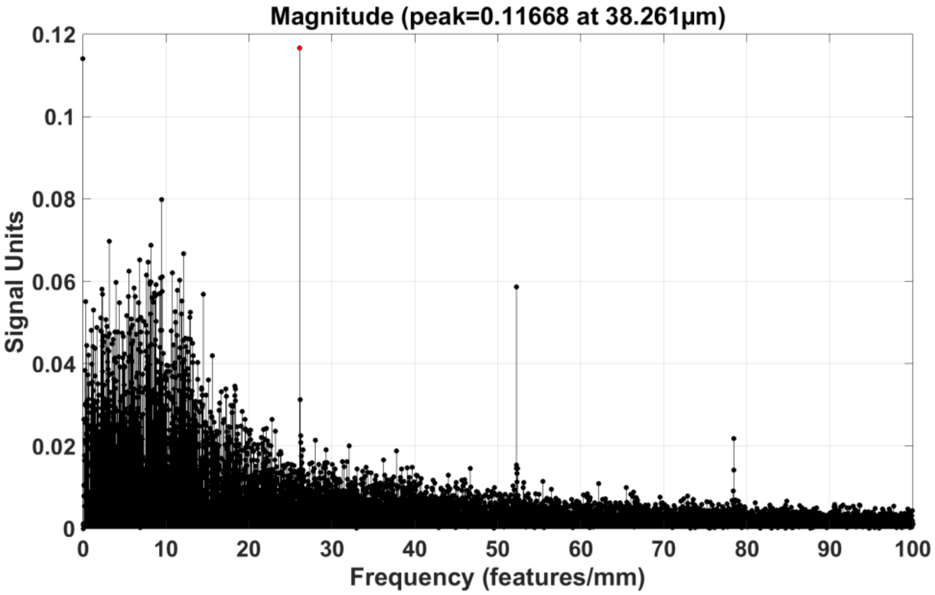

Figure 36. Fourier Spectrum for the Surface Machined with a 20μm Depth of Cut

Figure 36 shows the frequency spectrum for the surface machined at a 20 μm depth of cut. While strong peaks are seen at integer multiples of the cross-feed frequency (25, 50 and 75 features per mm), many strong peaks are also present below 10 features per mm. These peaks are indicative of features on the surface created by low frequency phenomena such as chip seizure and smearing.

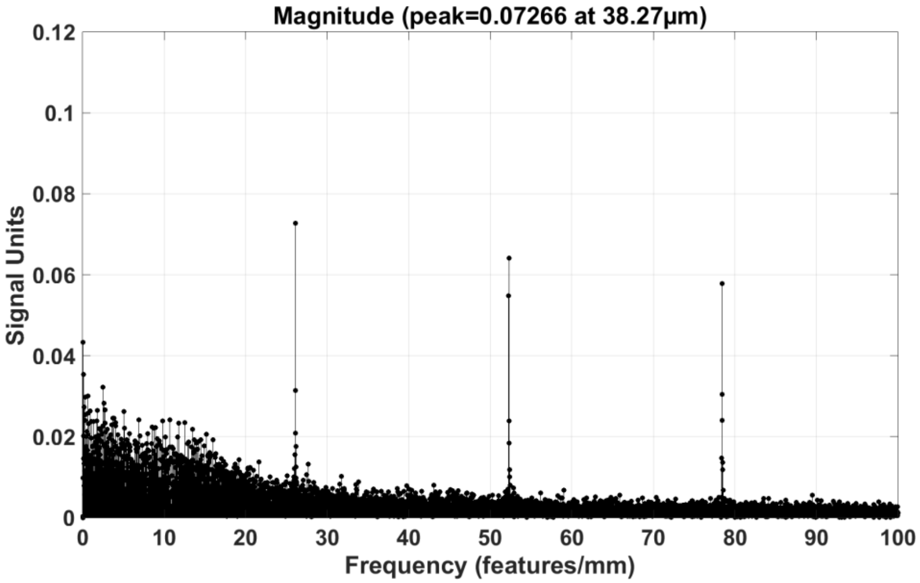

Figure 37. Fourier Spectrum for the Surface Machined with a 120 μm Depth of Cut

Figure 37 shows the frequency spectrum for the surface machined at 120 µm depth of cut. The peaks are smaller, and the dominant peaks occur at integer multiples of the cross-feed frequency. This indicates a smooth surface, void of low frequency features caused by chip seizure and the resultant smearing on the machined surface.

Effects of Cross Feed on Dry Machining of 1199 Aluminum

Using the 50 mm diameter disc of 1199 aluminum, 5 different cross-feeds were tested using Kennametal V-Series carbide inserts. Table 7 displays the machining parameters used for the 5 experiments. Theoretical roughness changes with the square of the cross feed. At 20 µm/rev the theoretical roughness is equal to 0.04 µm. At 60 µm/rev the theoretical roughness is equal to 0.34 µm.

In accordance with Equation (5), the theoretical surface roughness of the machined part is dependent on the cross-feed of the tool path. This means that in these experiments, measured surface roughness is not a valid criterion for comparison. Instead, surface fidelity, defined as the ratio of the theoretical roughness to the measured roughness, will be used. A surface fidelity closer to 1indicates a surface that is closer to the theoretical surface for the given cross-feed.

Table 7. Parameters Used for Cross Feed Experiments

Machining Parameter	Value
Rake Angle (degrees)	+15
Tool Coating	None
Depth of Cut (µm)	120
Cross-Feed (µm/rev)	20, 30, 40, 50, 60
Cutting Speed (m/s)	3-1.8
Tool Nose Radius (µm)	400

Figure 38 shows shear plane angle and surface fidelity as a function of cross-feed.

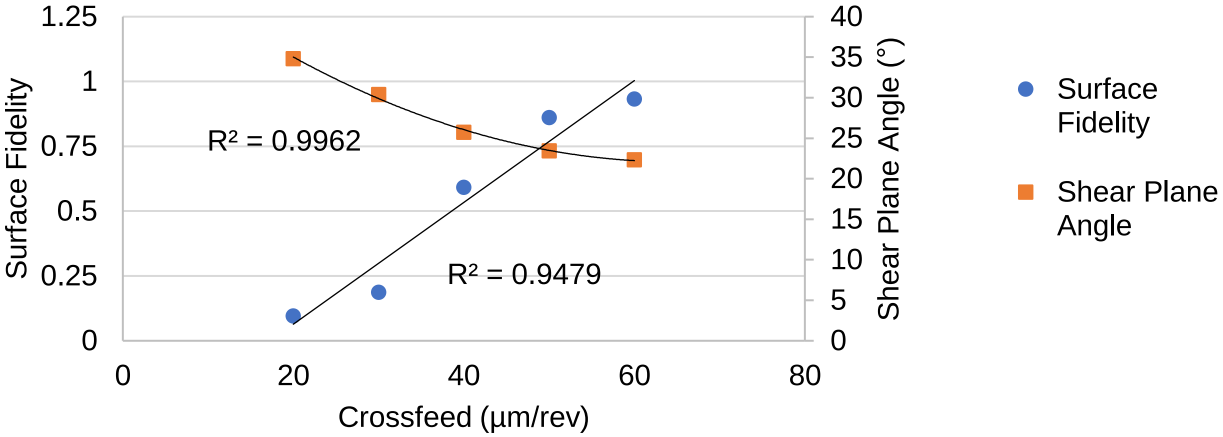

Figure 38. Surface Fidelity and Shear Plane Angle as a Function of Cross Feed

Figure 38 shows shear plane angle decreased quadratically from 35° to 22° as cross-feed increased from 20 µm to 60 µm. This decreasing shear plane angle is not expected, since higher shear plane angles are generally associated with smoother surfaces [7]. Surface fidelity increased linearly from 0.095 to .933 across the range of cross-feeds tested. It should be noted that the best surface finish achieved was 0.25 µm, which occurred at a 40 µm/rev cross-feed.

To explain the improved surface fidelity despite the decreasing shear plane angle, the stiffness of the chips was investigated. This trend of improved fidelity despite lowering shear angle is contrary to past research [6]. The theory is that a stiffer chip will result in one that is more capable of overcoming high interface friction and chip seizures, it will have a higher area moment of inertia. Figure 39 shows the relationship between chip stiffness (area moment of inertia, Y direction as defined in Figure 11), and surface fidelity.

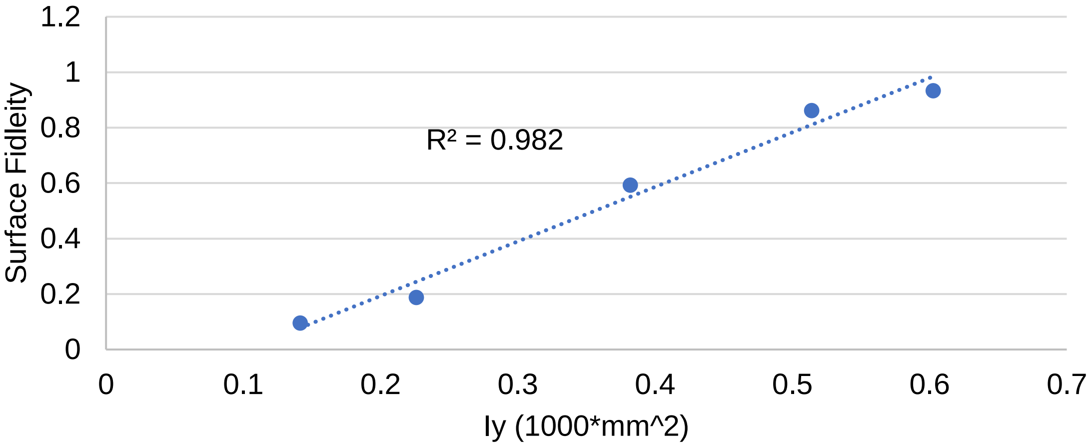

Figure 39. Surface Finish as a Function of Chip-Area Moment of Inertia

Figure 39 shows that chip fidelity increases linearly as the chip's stiffness increases. This is a possible explanation for how the surface fidelity increases despite the decreasing shear plane angles. Figure 40 displays the relationship between cross-feed and specific machining forces. Specific machining forces need to be used for comparison since chip load is variable with cross-feed.

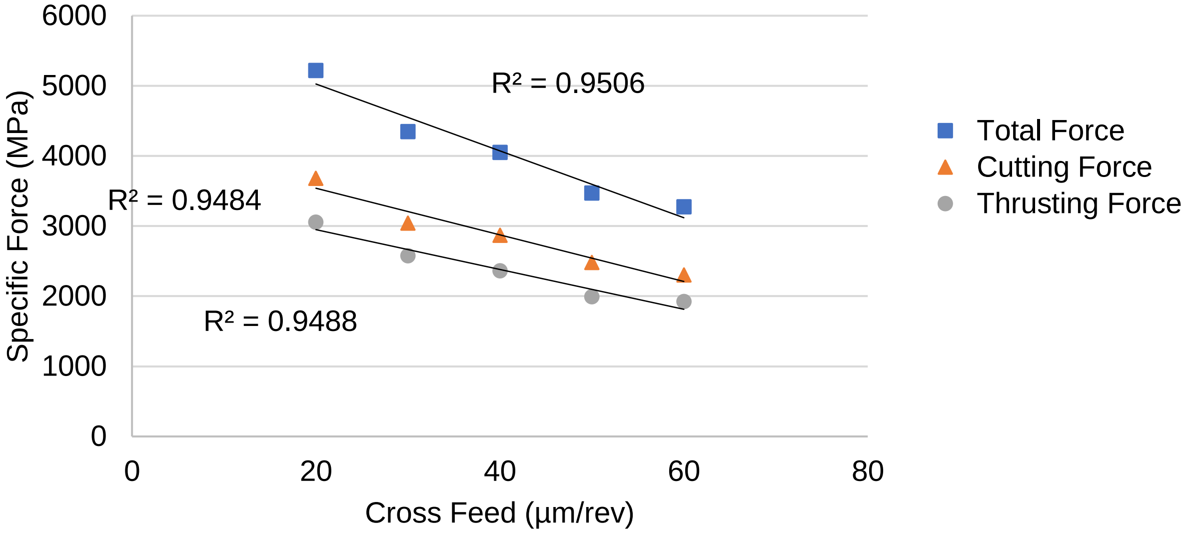

Figure 40. Machining Forces as a Function of Cross Feed

As shown in Figure 40, cutting, thrust and total (resultant) specific forces all decreased linearly as cross-feed increased from 20 to 60 µm/rev. This is due to the decreasing effect of the imperfections in the tooling, similar to what happened in the depth of cut experiments.

Figure 41 and Figure 42 display the frequency spectra as measured on the machined surfaces with 20 µm/rev and 60 µm/rev cross-feeds, the lowest and highest fidelity surfaces, respectively.

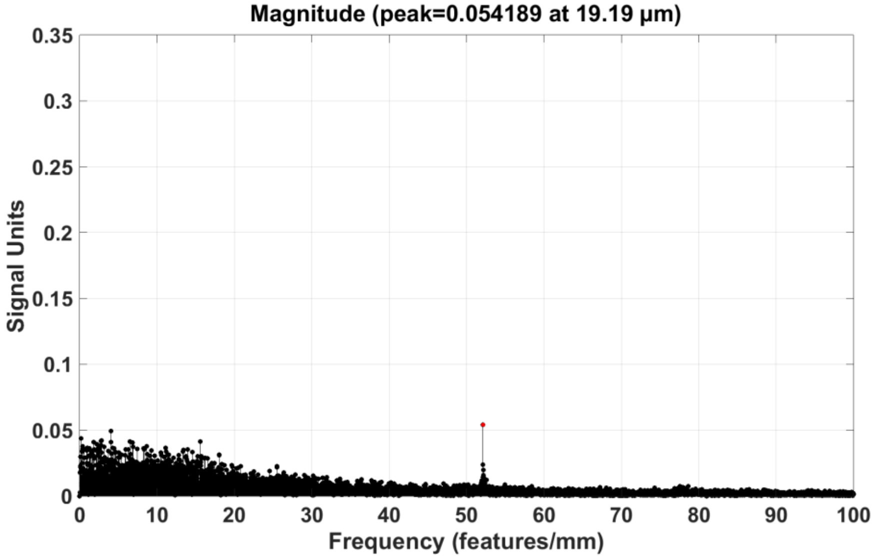

Figure 41. Fourier Spectrum for the Surface Machined with a 20µm/rev Cross Feed

While Figure 41 does have a peak at the cross-feed (50 features/mm), many of the dominant features on the surface are present below 20 features/mm. This presence of low frequency features indicates that chip seizure was a problem when the surface was machined. This also explains the low surface fidelity.

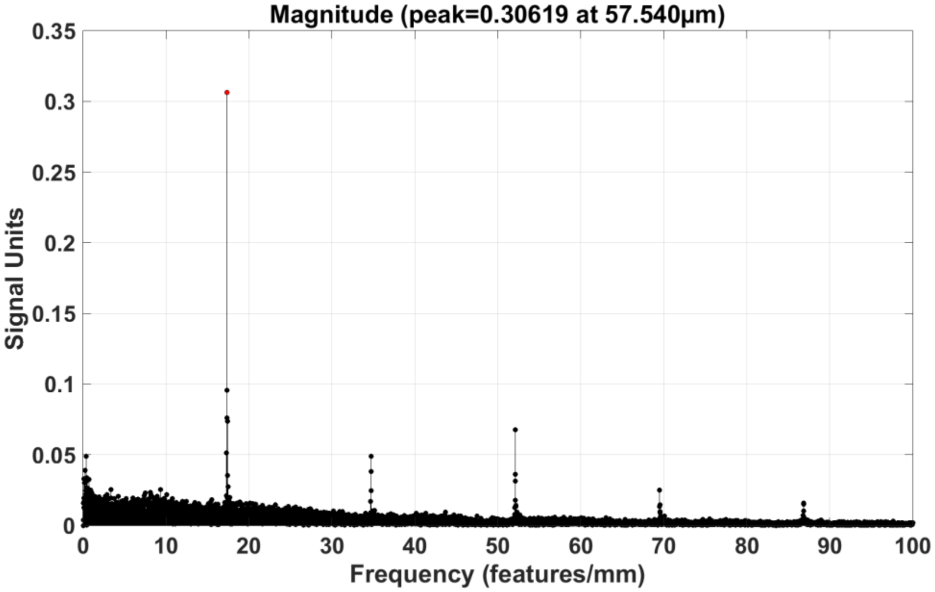

Figure 42. Fourier Spectrum for the Surface Machined with 60µm/rev Cross Feed

Figure 42 displays a very different story than Figure 41. While the magnitude of the peak at the cross-feed (17 features/mm) is much larger, this is expected since the theoretical roughness is higher for the larger cross-feed. Strong peaks are also present at the multiples of the cross-feed frequency. The features lower in frequency than the cross-feed are relatively very small compared to the peaks. This indicates that chip seizure was not an issue during machining.

Effects of Cutting Speed on Dry Machining of 1199 Aluminum

Using the 50 mm diameter disc of 1199 aluminum, 5 different cutting speeds were studied using Kennametal V-Series carbide inserts. Table 8 displays the machining parameters used for the 5 experiments. Both cutting speed and cross-feed were held constant for these experiments. This was achieved by increasing the spindle speed continuously as the cutting radius decreased as the tool fed inward. To prevent the cross-feed from decreasing as the spindle speed increased, the feed was increased every 75 µm to compensate. Due to torque limitations of the spindle motor, depth of cut was limited to 20 µm.

Table 8. Parameters Used for Cutting Speed Experiments

Machining Parameter	Value
Rake Angle (degrees)	+15
Tool Coating	None
Depth of Cut (µm)	20
Cross-Feed (µm/rev)	40
Cutting Speed (m/s)	0.5, 1, 1.5, 2, 2.5 ,3
Tool Nose Radius (µm)	400

Figure 43 shows surface roughness as a function of cross-feed. Due to small, discontinuous chips, chip thickness and therefore shear plane angle, as defined in Figure 11, couldn't be measured.

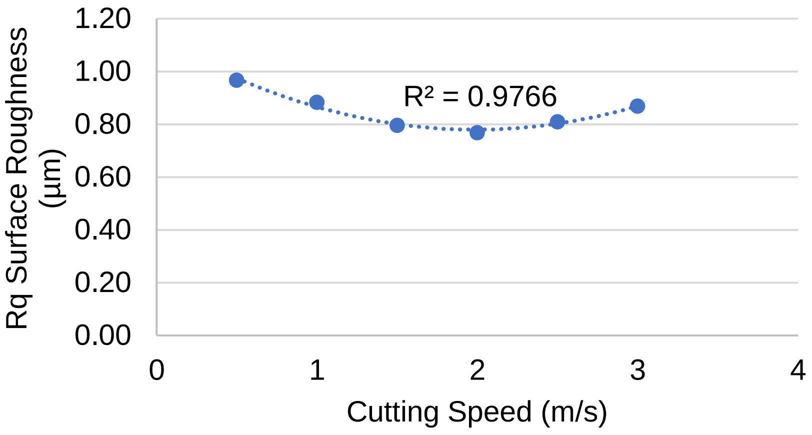

Figure 43. Surface Roughness as a Function of Cutting Speed

Figure 43 shows that surface roughness had a parabolic relationship with cutting speed. At low cutting speeds (<1.5 m/s), discontinuous chip flow and smearing due to chip seizure resulted in higher surface roughness. At higher cutting speeds (>2 m/s), it is possible that vibration caused increased surface roughness since chip seizure was not an issue. This vibration effect will vary from machine to machine.

Figure 44 shows the main cutting, thrust and total (resultant) forces as a function of cutting speed. All three machining forces in Figure 44 decreased as cutting speed increased from 0.5 m/s to 3 m/s. Main cutting force decreased from 5.73 N to 3.15 N, while thrusting force decreased from 4.3 N to 2.11 N. Total (resultant) force decreased from 7.16 N to 3.78 N. These decreases in force are in agreement with traditional machining research, which states that decreasing friction and increasing temperature cause forces to lower as speed increases [9].

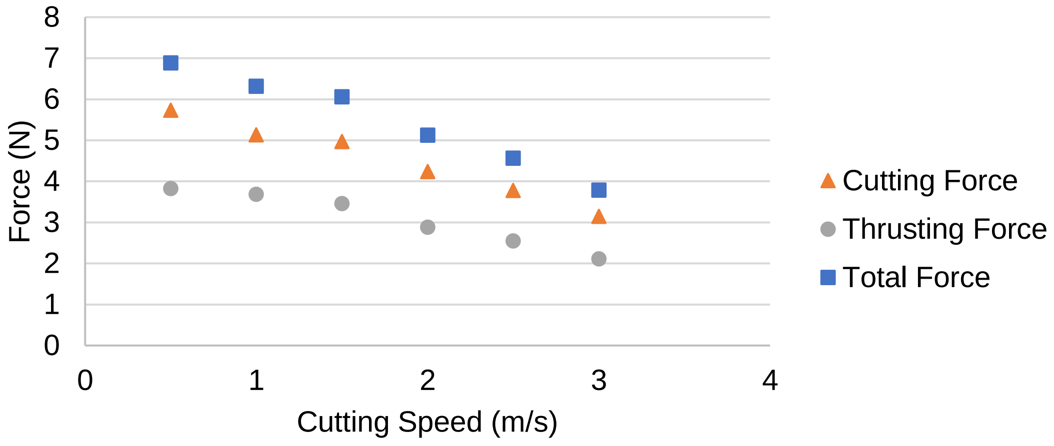

Figure 44. Machining Forces as a Function of Cutting Speed

Figure 45 and Figure 46 display the frequency spectra of the features as measured on the machined surfaces at 0.5 m/s and 2 m/s cutting speeds, the roughest and smoothest surfaces, respectively.

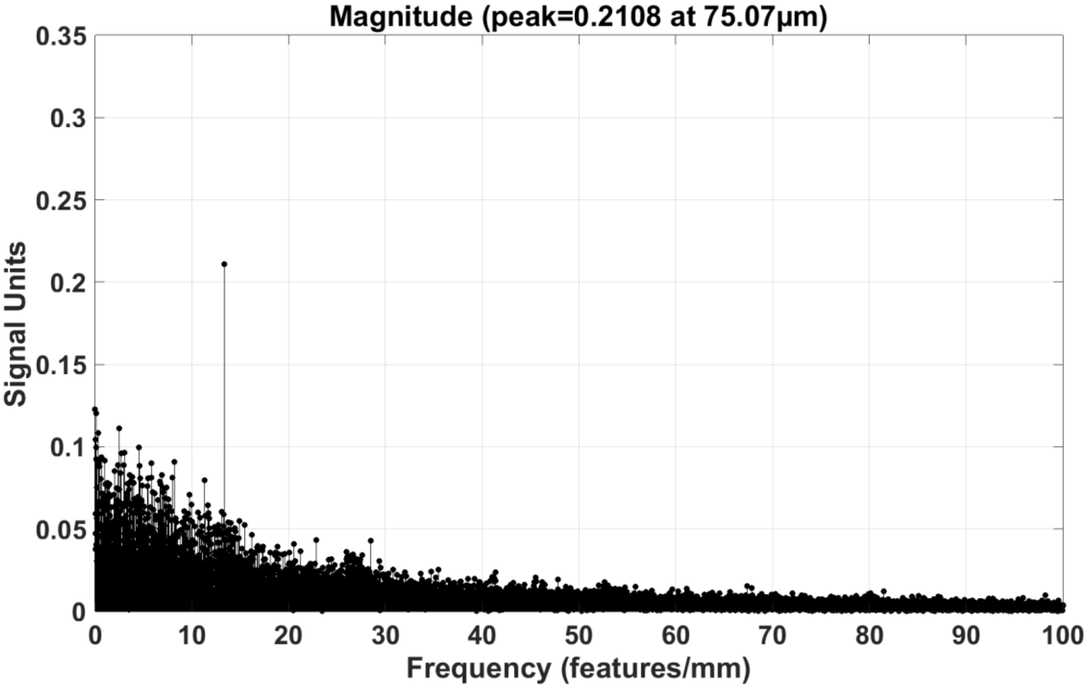

Figure 45. Fourier Spectrum for the Surface Machined with a 0.5 m/s Cutting Speed

The Fourier spectrum in Figure 45 shows one dominant peak at 75 μm, and then lots of smaller peaks below 10 features/mm. The peak at 75 μm is due to the cross-feed adjustments to compensate for the increasing spindle speed. Notice how there is not a discernable feature at 25 features/mm (the cross-feed), this indicates very poor chip formation. The large amount of low frequency peaks is due to smearing caused by chip seizure.

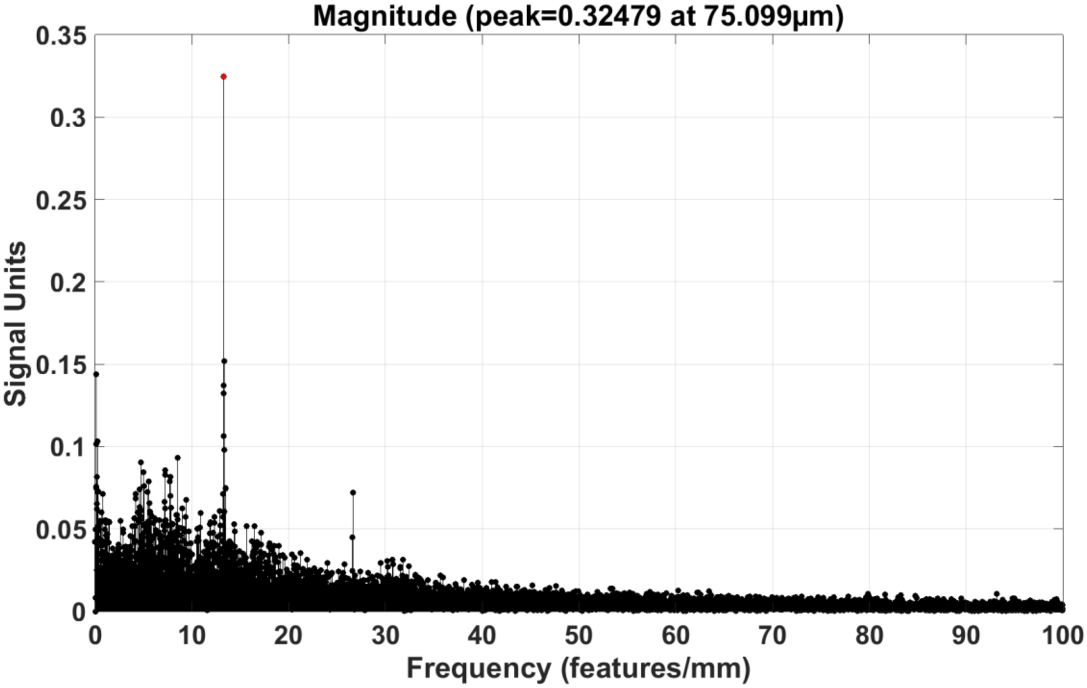

Figure 46. Fourier Spectrum for the Surface Machined with a 2 m/s Cutting Speed

Figure 46 shows the same low frequency features caused by seizure, and the same spike at 75 µm as Figure 45. The key difference is the discernable peak at the cross-feed frequency (25 features/mm). This indicates healthier chip flow, and is in agreement with the surface finish measurements.

1.3 CONCLUSIONS

Previous Work

Beginning in 2017, experiments were conducted to find a suitable machining surrogate to plutonium. It was determined that due to its tendency to seize to the tool, and then the work-piece, it was determined that 1199 aluminum presents an opportunity to study the dry machining of plutonium without health and safety concerns.

Through camera observation and chip collection, it was determined that the chip seizure phenomenon occurs in a cyclic nature. It goes through periods of seizure, and periods of smooth chip flow. To learn how to eliminate this cycle and produce a high fidelity machined surface, experiments were conducted to optimize machining parameters.

Optimized Machining Parameters for Dry Machining of 1199 Aluminum

Using Kennametal V-series carbide tools with a 400 µm nose radius, a single factor study was conducted by machining faces on 1199 aluminum using different machining parameters. The parameters considered were: rake angle, tool coatings, depth of cut, cross-feed and cutting speed.

First 5 different positive rake angles were tested, +3, +6, +9, +12 and +15 degrees. It was determined that surface finish improved and cutting forces decreased as rake angle increased. The +15 degree tool machined a surface of 0.40µm Rq surface roughness and showed little tendency to produce chip seizure issues. In agreement with Los Alamos engineers, it is agreed that high positive rake angled tools should be used in the future when machining plutonium.

5 tool coatings and one uncoated tool were tested. All coatings were PVD ceramics deposited on Kennametal's 2% cobalt K313 carbide grade. The uncoated tool was also K313 grade. The three coatings that contained aluminum provided higher forces and poor surface finish due to increased chip seizure frequency. While the two non-aluminum based coatings did perform better than the other coatings, neither performed significantly better than the uncoated tool. For this reason along with concerns over coatings chipping off during machining, it was determined with Los Alamos engineers that uncoated carbide is the best option on plutonium as well.

6 depths of cut were tested: 20, 40, 60, 80, 100 and 120 µm. It was found that specific cutting forces decreased as well as seizure incidents as depth of cut was increased. 120 µm provided the smoothest surface roughness as well as the lowest specific machining forces. While higher depths of cut might have yielded even better results, the Nanoform diamond turning machine lacked the torque to test depths above 120 µm. While the exact depth that would perform best for finishing passes on plutonium is still unknown, this data suggests that a smaller depth of cut is not necessarily better. This is in contradiction with traditional machining thought.

Cross-feeds of 20, 30, 40, 50 and 60 µm were tested. Each time cross-feed was increased, specific machining forces decreased and surface fidelity improved, meaning that the machined surface was closer to the theoretical (geometric) surface. Since fidelity and surface finish are not equivalent, the 60 µm cross-feed didn't necessarily produce the best surface finish. The 40 µm cross-feed produced the best finish of 0.25 µm Rq. This is the same cross-feed currently being used at Los Alamos. Further optimization on plutonium may be required.

Constant cutting speed was the last parameter tested. Speeds tested were 0.5, 1, 1.5, 2, 2.5 and 3 m/s. Chip seizure was a predominant issue at cutting speeds below 1.5 m/s, while vibration was likely the problem at 2.5 and 3 m/s. The best surface finish was achieved at 2 m/s, the same speed that is currently being used at Los Alamos. This result is likely very machine and material dependent, meaning that further optimization may be required at Los Alamos to determine the best cutting speed for plutonium on their machine tools.

Future Work

Up to now, traditional carbide turning inserts have been studied. The next step should address the performance of diamond turning inserts. Diamond tools may improve chip seizure by reducing rake face temperatures and reactivity with the chip.

Since the machining parameters have been optimized in a single factor study (meaning secondary effects are assumed to be negligible), the parameters should all be combined for a single experiment and compared to the control parameters provided by Los Alamos.

Finally, an abbreviated process should be devised for the engineers at Los Alamos to determine how well the results from the surrogate machining carries over to actual plutonium parts. This should involve far fewer experiments than were conducted in this study.

REFERENCES

1. Balog J, Gonzales T, Harwood S, Stout S, Lopez O, Lucero R. Dry Machining of Plutonium Metal: Insert Selection for Machinability and Meeting Surface Finish Criteria. LANL Engineering Week Poster. 2013.
2. Dow T, Wong A, Garrard K, McNutt T, Bodlapati C. 2017 Precision Engineering Consortium Annual Report. 2017.
3. Trent E, Wright P. Metal Cutting: 4th Edition. Butterworth-Heinemann. 2000; 58-65.
4. Wick O. Plutonium Handbook: A Guide to the Technology, Volumes I and II. American Nuclear Society. 1980; 82.
5. Suit B. Analysis of Accelerated Tool Wear and Built Up Edge When Diamond Turning Ferrous Metals. Master's Thesis, Precision Engineering Center, North Carolina State University. 2016; 136-138.
6. Cohen P. ISE 589: Advanced Machining: Mechanics: Strain, Strain Rate, Energy, Shear Stress. North Carolina State University. 2018.
7. Pradeesh A, Mubeer M, Nandakishore, Muhammed A, Mohammed Manzoor, Muhammed Raees M. Effect of Rake Angles on Cutting Forces for A Single Point Cutting Tool. IRJET. 2016.
8. Ashoktov V. Generalized Model for Chip Formation. Journal of Tribology for Metal Cutting. 2006. 37-38.
9. Altin A, The Effect of the Cutting Speed on the Cutting Forces and Surface Finish When Milling Chromioum 210 Cr12 Steel Hardfacings with Uncoated Cutting Tools. 2013.

2 DIAMOND TURNING OF PLASTICS

Charan Bodlapati
Graduate Student
Anthony Wong
Research Associate, PEC
Ken Garrard
Senior Research Associate, PEC
Thomas Dow
Professor
Mechanical and Aerospace Engineering

Single point diamond turning is a common method to create plastic optics. The optics industry claims that tool wear is a major problem. The objective of this research is to optimize machining parameters (such as feed, depth of cut, cutting speed and rake angle) to produce optical surface quality (RMS Surface finish < 10 nm) while minimizing tool wear for Poly (methyl methacrylate) (PMMA) and Polycarbonate (PC). A wide range of experiments were performed on the two materials by varying machining parameters and measuring worn tools using the Electron Beam Induced Deposition (EBID) technique in the Scanning Electron Microscope (SEM). For the experimental conditions used, PMMA was found to have better surface finish than PC when machined with a diamond tool. Polycarbonate was found to wear the tool more than PMMA under similar cutting conditions. It was also found that Polycarbonate is more sensitive to chip management and chip geometry than PMMA. Built up edge on the tool and chip management were identified as the important reasons for poor surface finish on PC. Tribo-electric charging was found to be a major mode of tool wear when machining PC. Holes in the diamond tool were observed on the diamond tool when large depths of cut were used. Using Tap Magic Aqueous as cutting fluid during machining PC was found to minimize tool wear and improve surface finish. Detailed effects of all machining parameters for the two materials were reported.

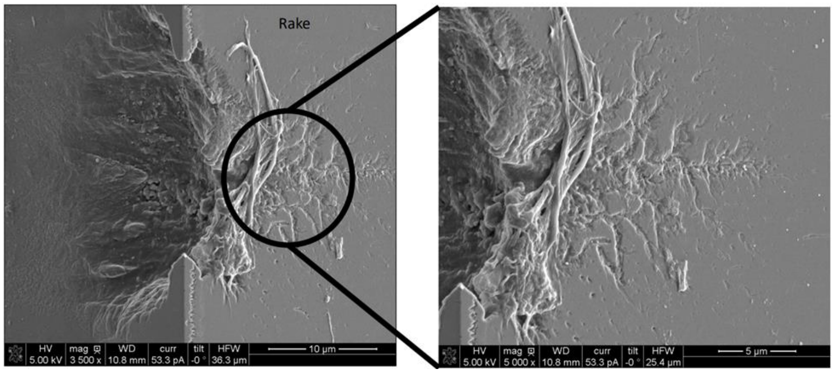

2.1 INTRODUCTION

Diamond turning (DT) of plastics is an efficient method to create versatile optical surfaces. Their performance is influenced by a wide variety of factors such as glass transition temperature of the polymer, material properties and operator controlled cutting conditions. Diamond turning is a precision lathe operation where workpiece material is removed by a single crystal diamond tool. The DT process is typically performed on a machine with precise hydrostatic bearings and axis displacement control using interferometric measurements or linear encoders. DT allows for the creation of optical surfaces. Current non-diamond turned production of lenses is done using two main methods. The first involves compression molding of the polymer followed by multi-step grinding to achieve the desired surface finish. Finally, the workpiece is beveled to prevent surface damage from the sharp edges of the workpiece [1]. The second method involves high pressure injection into a mold of the desired geometry. After the mold is filled, the liquid polymer is allowed to cool and solidify. The workpiece is then polished to the desired surface finish [2]. While these two methods are effective for mass production, the DT process enables flexibility in the production process. This allows cost effective production of small batches of asymmetric and off axis optics with excellent form and finish. Single point diamond turning (SPDT) is one of the common methods to create plastic optics.

2.2 DETAILS OF THE PROJECT

The two polymers used in this research are Polymethyl methacrylate (PMMA) and Polycarbonate (PC). PMMA is a transparent thermoplastic with refractive index of 1.49 and capable of light transmission up to 92% within a wavelength of 300 nm to 900 nm making it one of the most important materials in the optical industry. Polycarbonate is a thermoplastic with refractive index of 1.60 and capable of light transmission up to 89% within a wavelength of 300 nm to 900 nm. PC is high yield strength material and is used by 35% of lens industry in USA. Detailed list of properties of the two plastics are shown in Table 1.

Table 1. Material properties

Material / Property	PMMA	PC
Refractive index	1.49	1.6
Abbe Number *	58	27.86
Light transmission (%)	92	89
Density (g/cm^3)	1.18	1.20
Glass transition temperature (°C)	105	147
Critical entanglement molecular wt, (g/mole)	29,500	6,000
Coefficient of linear expansion (10^{-5} °C)	5.9	7.0
Specific heat (Cal/g-°C)	0.35	0.36
Dielectric breakdown strength (KV/mm)	15.8-19.7	15-67
Youngs modulus (MPa)	1800-3100	2100-2900
Thermal conductivity at 23°C (W/m-K)	0.167	0.19-0.22
Thermal diffusivity (mm^2/s)	0.121	0.147
Yield Strength (MPa)	55.5	89.6
Hardness ASTM D785 (metric)	94	108-120

Most of the optical industry uses Polymethyl methacrylate (PMMA) and Polycarbonate (PC) for creating optics. Prior work on diamond turning of plastics was performed by Gubbels [3] and others [4-6], but information on parameters that can optimize the surface finish and minimize diamond tool wear is lacking. The objective of this research is to optimize machining parameters (such as feed, tool radius, depth of cut, cutting speed and rake angle) to produce optical quality surface while minimizing tool wear while cutting PMMA and PC. This research builds on previous work on surface finish and diamond tool wear when machining polymers [3-6]. This research is aimed at 1) finding the relationship between the machining conditions (tool orientation, surface speed, depth of cut, tool radius, chip management and lubricants) and the surface finish and 2) identify critical parameters that effects diamond tool wear. The work will address the issue of:

3) What are the best conditions to produce optical finishes (RMS < 10 nm) while minimizing tool wear.

2.3 EXPERIMENTAL SETUP AND MEASUREMENT METHODS

2.3.1. SURFACE FINISH EXPERIMENTS

Experiments were conducted on a Pneumo ASG 2500 Diamond Turning Machine (DTM). A DTM is a precision, computer numeric controlled (CNC) lathe using a lapped single point diamond tool. Single point tools are tools with a single cutting edge. The ASG supports the two orthogonal linear hydrostatic bearing slides: the first holds the diamond tool and the second holds the air bearing spindle and therefore the part. Figure 1 shows a front view with the cylindrical plastic part attached with a vacuum chuck to the spindle that moves into/out of the picture. The second slide (on the left) supports the diamond tool and moves left/right to change the depth of cut. As arranged in Figure 1, the spindle holds the counter clockwise rotating part and moves into the page while being machined by a stationary diamond tool to study surface finish and tool wear using a round nose tool. The workpiece is a 50 mm diameter rod which is readily available in PMMA and PC. The rod is 80 mm long.

One of the important issues is the potential of the machined chips to contact and damage the finished surface. This issue of chips damaging the surface is discussed in Section 1.5. The spindle rotates counter-clock-wise and, with the tool on the left side of the part, will make the chip exit to the left. Two additional components were added to the system to help capture the chip as it leaves the part. The first is a suction system above the tool that pulls the air (and the chip) upward into the vacuum. The second is an Electrostatics, Inc HPN AC ionizer nozzle with an adjustable pressure source powered using a Herbert static high voltage unit. This adds a second vertical flow of air past the chip exiting from the machining process with the ability to increase the flow rate and charge the air flow. The result is as the chip leaves the cutting interface horizontally, it is immediately entrained in the vacuum/pressure flow and removed from the cutting region. The specifications of air ionizer are shown in Table 2.

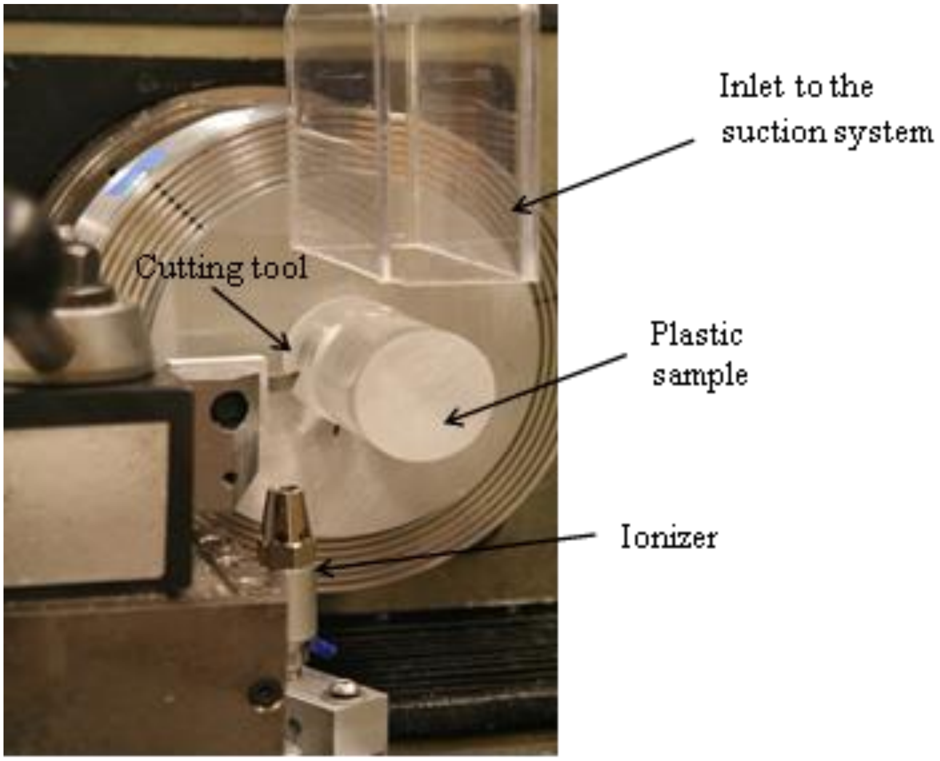

Figure 1. Experimental setup for surface finish experiments.

Table 2. Ionizer specifications

Ionizer	Electrostatics,Inc HPN (AC)
Power Unit	Herbert Static Control, 50 Hz
Max. air pressure (psi)	15-30 psi
Input Voltage (v)	120
Output Voltage (KV)	4
Current Limited (mA)	5

2.3.2 TOOL WEAR EXPERIMENTS

Tool wear experiments were performed using two different experimental setups. When round nose tools were used, the setup used is like the one shown in Figure 1. The tool wear experiments performed using a round nose radius tool and a plastic cylinder made it difficult to estimate the tool wear, as the tool geometry is different across the edge due to the variable chip thickness along the cutting edge. Therefore, to make the chip thickness constant across the cutting edge, plunge cutting setup is used.

To understand tool wear, plunging experiments were performed. A 3.5 mm wide square nose (infinite radius) diamond tool was plunged into the outer diameter of 1.5 mm thick plastic disk. The setup used for plunge cutting is shown in Figure 2. A vacuum and air ionizer system were used to manage chips, like the setup shown in Figure 1. This series of experiments were believed to give an idea of tool wear as uncut chip thickness is constant across the entire width of the chip.

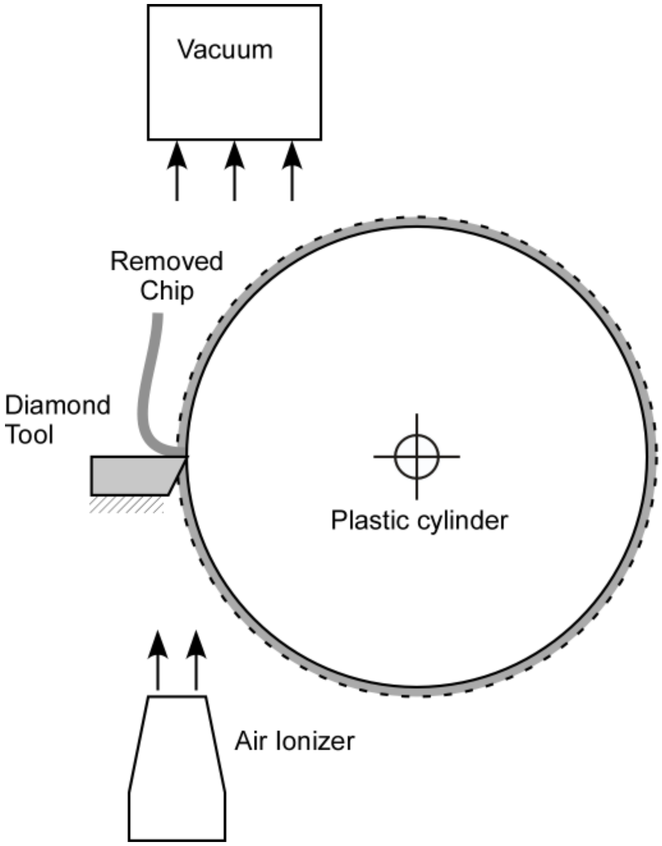

Figure 2. Schematic of plunge cutting setup for tool wear experiments.

2.3.3 DATA AQUISITION

Force Measurements

Forces were measured using a KISTLER 9251A 3-component force transducer. The tool was attached to the tool post via the load cell. A 10 ft-lb preload on the bolt was used. Figure 3 shows the load cell and axes of measurements. The technical data of the load cell is shown in Table 3.

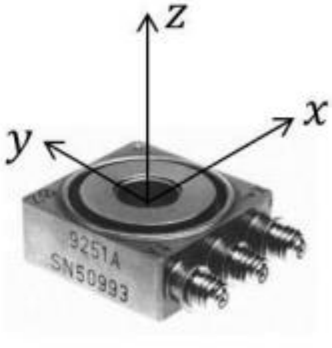

Figure 3. KISTLER load cell used for measurements [3].

Table 3. Technical specifications of KISTLER load cell

Compression Range (Z – axis) [N]	+5000 to -5000
Shear Range (X, Y axis) [N]	+2500 to -2500
Rigidity (Z – direction)	1000
Rigidity (X, Y axis)	300
Natural Frequency (Y- direction) [KHz]	11
Weight [grams]	32
Sensitivity (F_Z) [pC/N]	-4.1
Sensitivity (F_X, F_Y) [pC/N]	-7.5
Noise Floor (N)	0.01

In the experiments performed, orthogonal cutting was employed and thus the forces in Z direction were irrelevant. F_Y is the cutting force and F_X is the thrust force. Figure 4 shows the load cell placement in the experimental setup. The forces measured, and the axes are shown in Figure 5.

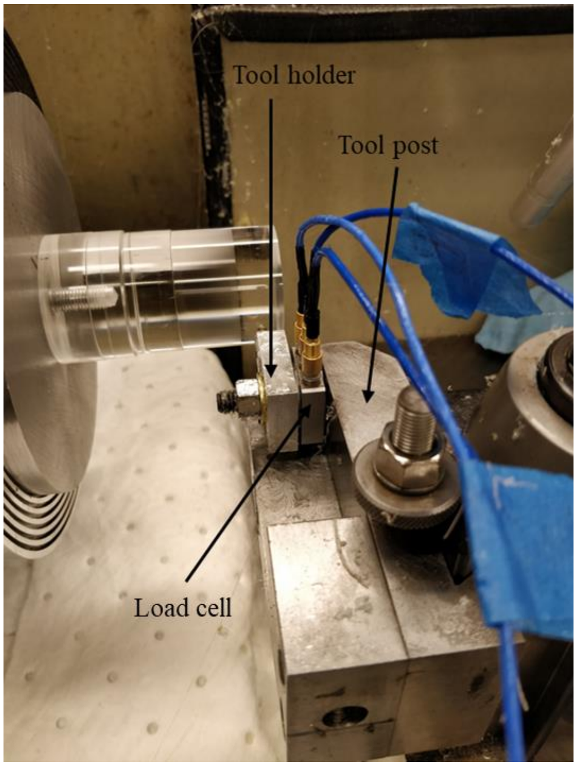

Figure 4. Orientation of load cell in the experimental setup

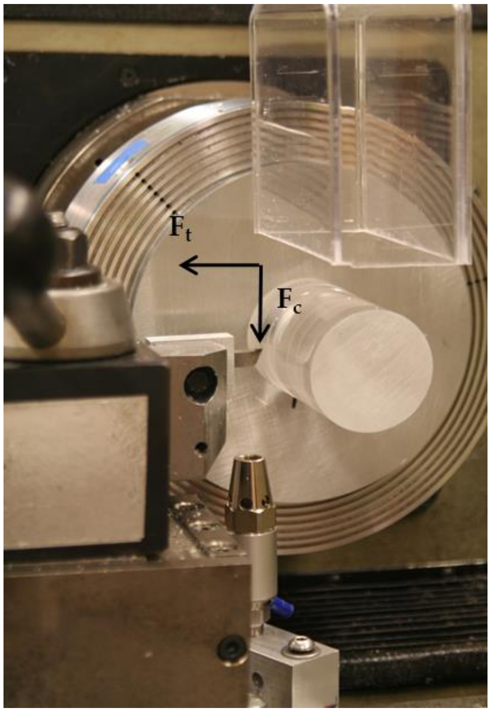

Figure 5. Forces measured using the load cell

Two charge amplifier settings were used during cutting experiments named setting I and setting II based on the sensitivity required during the cutting process. The charge amplifier settings used in the cutting experiments are shown in Table 4.

Table 4. Load cell amplifier settings

Setting I		
	Cutting Force	Thrust Force
Sensitivity settings	6.76	6.76
Capacitor decay	Long	Long
Scale (Mech units/volt)	10	10
Setting II		
	Cutting Force	Thrust Force
Sensitivity settings	8.76	8.76
Capacitor decay	Long	Long
Scale (Mech units/volt)	5	5

A 3 channel KISTLER 5004 charge amplifier was used to condition the signal. The amplifier can produce voltages up to 10 V. The voltages V_X and V_Y were recorded using National Instruments LABVIEW software. Data was acquired at 2.5 kHz. Then the forces were calculated using the scale value showed in Table 4 as shown in Equation (1).

$$F = \text{Scale value of the axis } \left(\frac{N}{V}\right) * \text{Voltage} \qquad (1)$$

Video System

A Supereyes B011 digital microscope was employed for recording videos and taking snapshots of the cutting process. The microscope is connected to a computer using USB 2.0 and saved to the computer using the Supereyes user interface. The digital microscope has a 5-megapixel resolution and 100-2000X magnification depending on the lens used for recording. The data acquisition rate of the camera was 30 fps. The microscope also has a replaceable light source and touch adjustment illumination which gives ample light for a clear image. The Supereyes microscope is focused on the tool tip so that it gives a top-view of the cutting process. Figure 6 shows the microscope in the experimental setup.

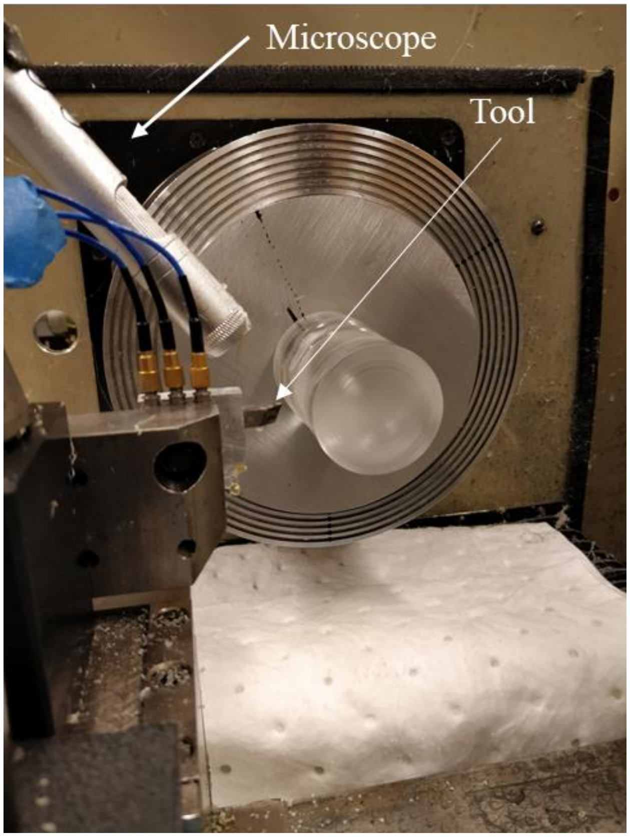

Figure 6. Supereyes digital microscope in the setup

2.3.4 SURFACE FINISH MEASUREMENTS

Surface finish of the machined parts was measured using a Zygo Newview 5000 scanning white light interferometer and a Keyence VKX 1100 laser confocal microscope. The following sections describe the process of surface finish measurements and analysis of the workpiece surfaces.

Zygo Newview 5000 white light interferometer

Zygo Newview 5000 white light interferometry is a non-contact optical method used to measure surface profile. Zygo Newview 5000 has a vertical resolution of 1 nm and 0.7 µm horizontal resolution. Interferometers use the principle of superposition by measuring interference fringes from the combination of a fixed beam path and beam that is reflected from the specimen [7].
Four areal roughness measurements were taken at different regions on the plastic workpiece that are 90^0 apart and the roughness values were averaged to get a roughness number. 50X objective lens and 1.3X focus were used to take measurements over an area of 109 µm by 89 µm. It is a common practice in the optical industry to quantify surface finish as Root mean square deviation called RMS surface finish [8], which gives an idea about Raleigh scattering on the surface.

Figure 7 shows an example of Newview measurement of diamond turned PMMA surface. The camera had a resolution of 640 X 480 with 640 being used in the feed per revolution direction and 480 used in the upfeed direction. Figure 8 shows the example of measured areas on the surface to estimate the surface roughness of the machined surface. Four areal surface finish measurements (90^0 apart) were taken on the plastic cylinder and measurements are averaged to quantify RMS surface finish of the machined surface.

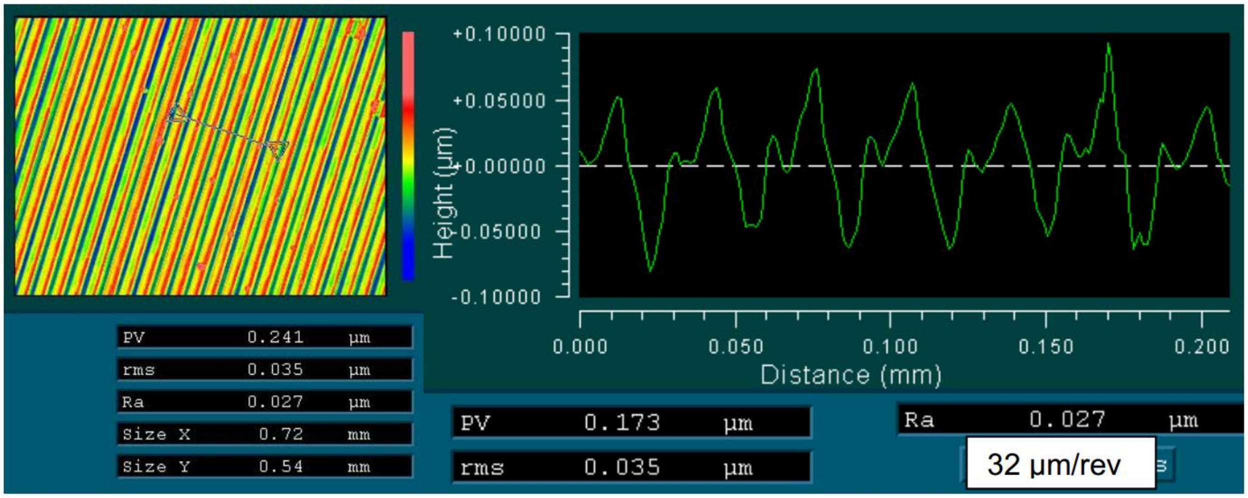
PV 0.241 µm
rms 0.035 µm
Ra 0.027 µm
Size X 0.72 mm
Size Y 0.54 mm

PV 0.173 µm
rms 0.035 µm
Ra 0.027 µm

Figure 7. Newview measurement of diamond turned PMMA surface. 300 RPM spindle speed, 32 µm/rev feed per rev, 10 µm depth of cut and 3 m/s cutting speed.

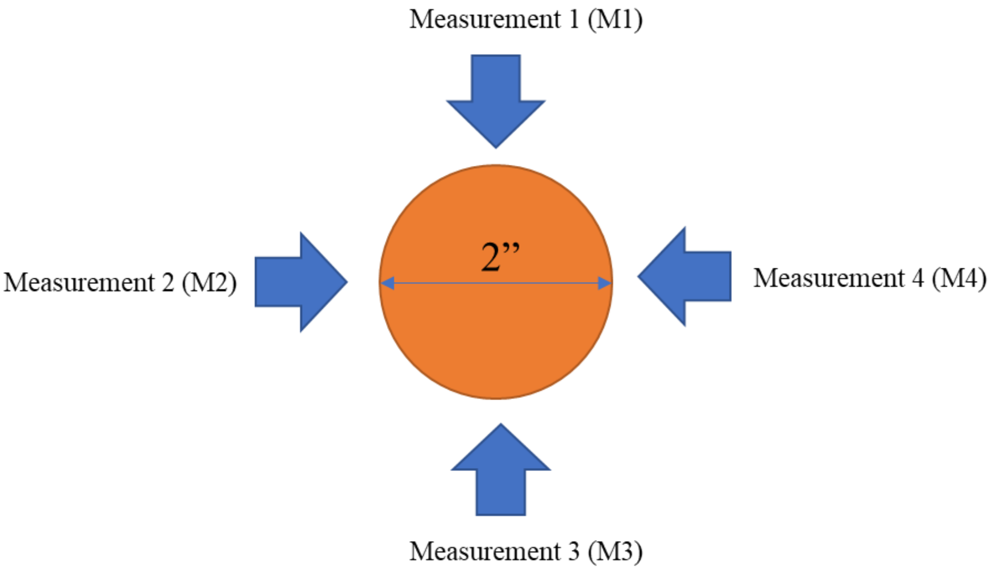

Figure 8. Schematic setup of surface finish measurements on the workpiece (feed direction is into the plane of the page)

Keyence laser confocal VKX 1100 measurements

The Zygo Newview 5000 has difficulty measuring steep sloped grooves (slopes greater than 18^0). To overcome the issue of measuring steep slopes and to validate surface roughness measurements obtained from the Zygo Newview, a Keyence laser confocal microscope was employed. A laser confocal microscope captures multiple images at different depths and reconstructs all the images at their best focus to give a 3D image. Confocal microscope uses a point illumination and a pinhole to remove out of focus noise and therefore increases resolution in the depth direction.

The VKX 1100 has a total magnification up to 28,800X and a field of view of from 11 µm to 7398 µm. According to manufacturer, the vertical resolution is 0.5 nm and resolution in the horizontal direction is 1 nm. The area and procedure of surface finish measurement using VKX 1100 was the same as that of Newview as discussed before.

2.3.5 TOOL WEAR MEASUREMENTS

After machining, the diamond tools are cleaned and imaged in the Scanning Electron Microscope to analyze wear. Electron Beam Induced Deposition (EBID) [7, 9] was used to quantify and analyze worn tools. The following sections explain the process employed for tool wear measurements.

Tool Cleaning

After the tool was used for machining, plastic material was found to stick onto the tool. To clean the tools, the tools were ultrasonicated in di-chloromethane for 20 minutes, followed by 40 minutes of ultrasonication in acetone. Ultrasonication is a cleaning process where the sample is vibrated using ultrasound transmitted through liquid, generally water. The tool was then imaged in an Olympus optical microscope. At 500X, if no plastic material was stuck to the diamond it was measured in the SEM. Before measuring in the SEM, the tool was coated with Au-Pd to make the tool conductive. In case any material is left after ultrasonication, clean room wipes dipped in acetone were used to rub and clean off the material. After this step, tool was taken to the SEM and imaged.

Based on the experiments, it was found that the tool after machining PMMA was easier to clean than the tool used for machining PC. Di-chloromethane is a solvent for polycarbonate and was found to be best one for cleaning PC from the cutting edge. The rake face of uncleaned and cleaned tools is shown in Figure 9. The tool in Figure 9 was used to cut PC for 66 km and the tool has a radius of 0.537 mm.

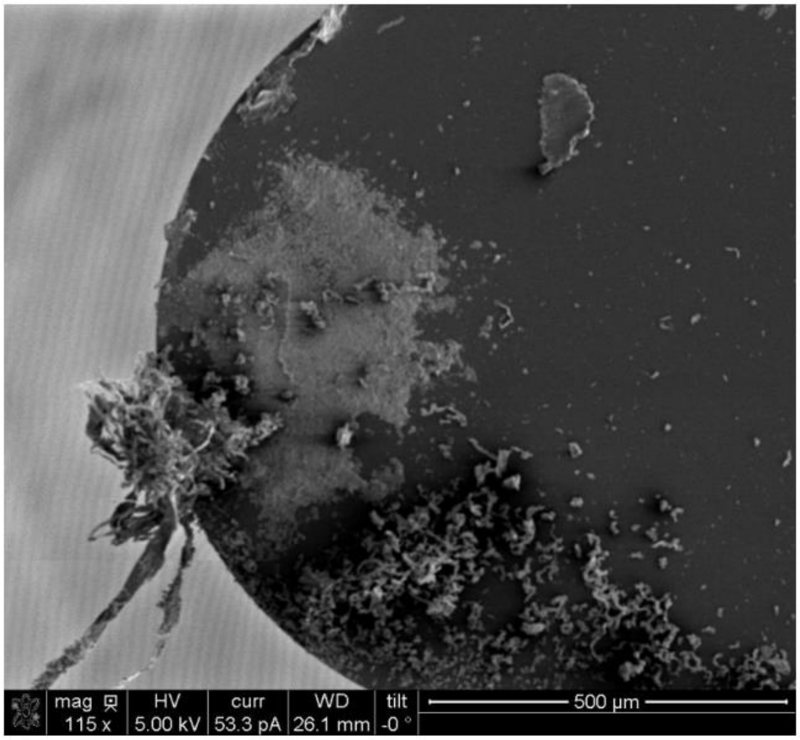

(a)

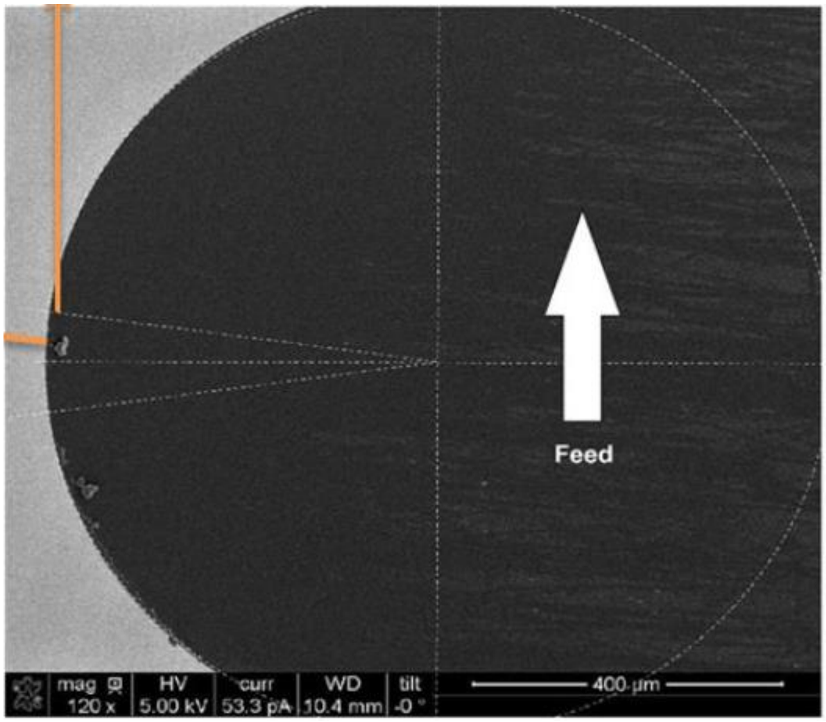

(b)

Figure 9. (a) Tool before cleaning and (b) Tool after cleaning

EBID Technique

The PEC uses a unique measurement method using a Scanning Electron Microscope with a focused ion beam to provide a reference line on the tool that can be used to image the edge of the tool. The EBID technique writes a hydrocarbon contamination line on the tool. When an electron beam scans across the contamination, hydrocarbons polymerize and leave a line on the surface which acts a reference line described above. Figure 10 shows the EBID line on a freshly re-lapped tool. Once the SEM image is captured, EBID line is taken as reference and 2D cross sectional wear area was created using image processing software in MATLAB.

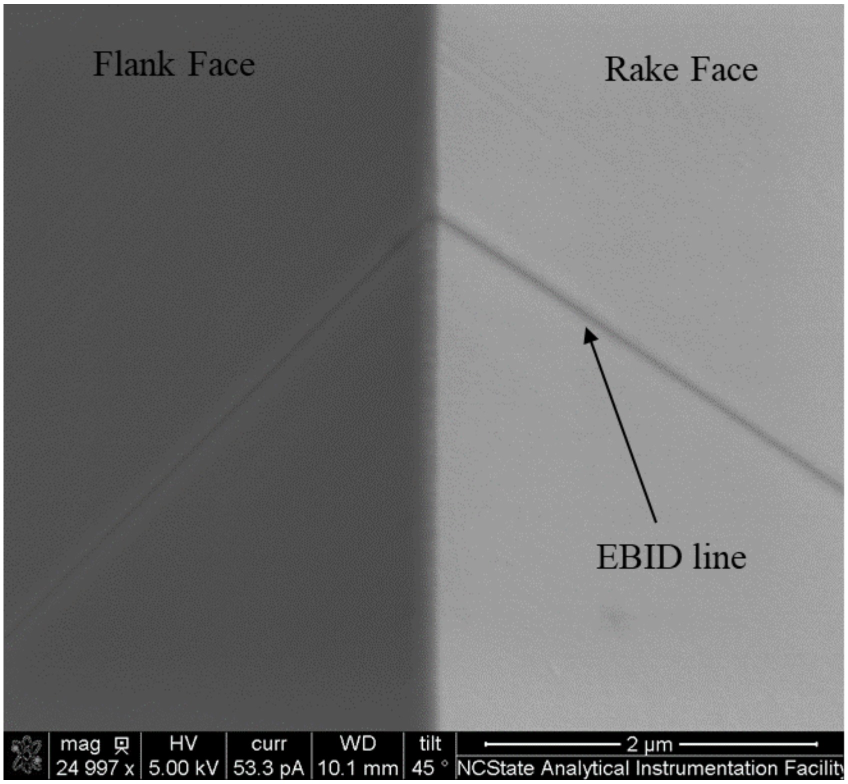

Figure 10. EBID line on the cutting edge.

The Quanta 3D FEG Dual Beam SEM at the Analytical Instrumentation Facility of North Carolina State University was used for wear measurements. The SEM parameters used for measurements are shown in Table 5.

Table 5. SEM parameters used for tool wear measurements.

Beam Energy (KV)	5
Beam Current (pA)	53.3
Aperture (µm)	30
Chamber Pressure (Torr)	$<5x10^{-5}$
Working Distance (mm)	10.5
Image Dwell Time (µs)	10
Image Size (pixels)	1024x943

2.4 MACHINING PMMA

2.4.1 SURFACE FINISH

It was found from the literature [3-6] that PMMA is easily machined and initial testing on PMMA during this research indicated the same. It will be discussed in the future sections, how chip management have no effect on surface finish when machining PMMA. However, chip management was found to have profound impact when machining PC which will be discussed in Section 1.5. Therefore, to compare both the materials and draw conclusions, the setup shown in Figure 1 was employed for experiments on both the materials.

A series of experiments were conducted on PMMA to study the effect of machining parameters, namely feed per revolution, cutting speed, depth of cut, tool radius and rake angle on the surface finish generated.

Effect of feed per revolution

Figure 11 shows the effect of cross feed on RMS surface finish for a 0.5 mm nose radius diamond tool. The results at smaller feed rates in Figure 12 illustrates a lower limit for surface finish which is limited by minimum chip thickness (cannot be zero) and machine vibration. Surface finish and feed rate are geometrically related using a parabolic approximation [10] as shown in Equation (2).

$$\text{Theoretical RMS roughness} = \frac{f^2}{26.6R} \qquad (2)$$

Where f is feed rate in µm/rev and R is nose radius of the tool in µm. RMS finish is in µm.

According to Equation (2), the relation between the feed rate and surface finish is parabolic for a given tool radius, but this relation was found not to hold at very small feed rates or small theoretical roughness. Figure 12 shows the variation of RMS roughness with feed rate. According to Lucas Lamonds [11], the surface finish at finer feeds also depends on asynchronous spindle rotation and machine vibration. When the amplitude of machine vibration is more than the height of grooves created due to the feed rate, then the geometric relation between surface finish and feed rate (Equation (2)) will not be valid.

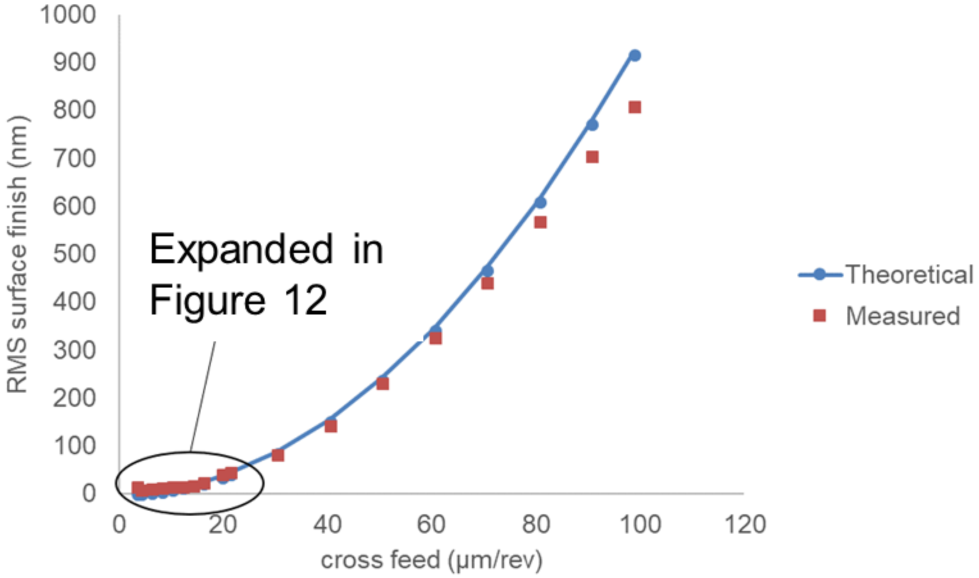

Figure 11. Effect of cross feed on RMS roughness of PMMA when machined with a 100 µm nose radius tool at 1450 rpm and 10 µm depth of cut (DOC).

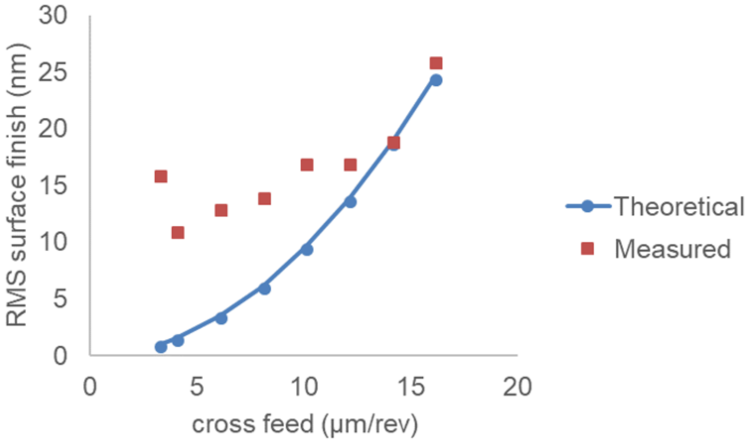

Figure 12. Effect of cross feed vs RMS roughness at finer feed rates.

Effect of cutting speed

Figures 13 and 14 shows the effects of cutting speed on the RMS roughness of the PMMA surface. It was found that there is no variation in surface roughness with cutting speed which was in contrast with Gubbels data [3], where increasing cutting speed resulted in better surface finish. However, no effect of cutting speed on RMS roughness indicates that the temperature at the cutting zone has not affected the surface finish generated in the experimental conditions used, which will strengthen the arguments made by Gubbels [3].

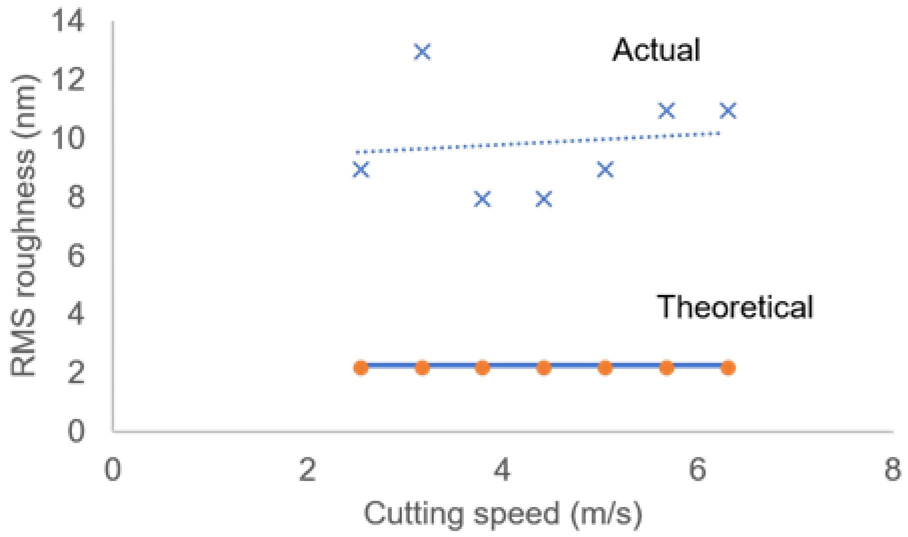

Figure 13. Effect of cutting speed on RMS roughness of PMMA at a cross feed of 4.6 µm/rev feed per rev and 10 µm depth of cut.

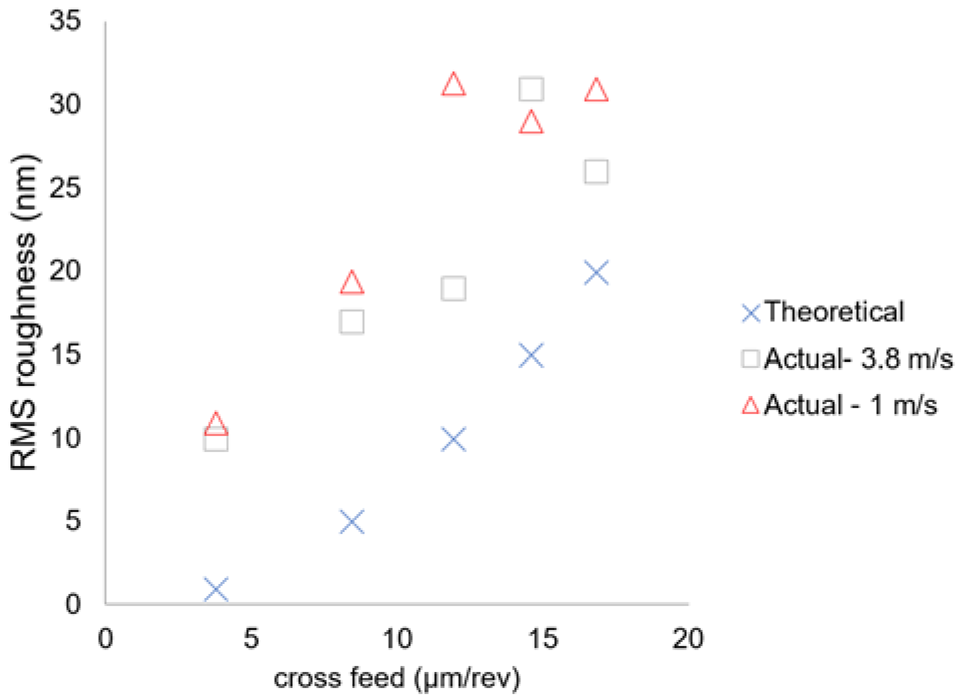

Figure 14. RMS roughness vs cross feed at different cutting speeds for PMMA at 10 µm depth of cut.

Effect of depth of cut

Figure 15 shows the effect of depth of cut on the RMS roughness of PMMA when machined using a 0.5 mm nose radius diamond tool. No trend was observed in the RMS surface finish with change in depth of cut.

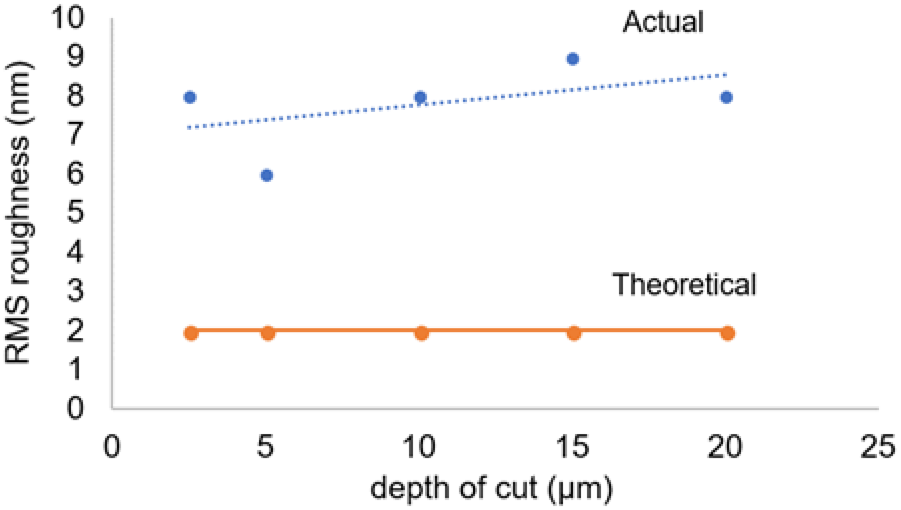

Figure 15. RMS roughness vs depth of cut at a cross feed of 4.6 µm/rev feed rate

Effect of rake angle

Figure 16 shows the effect of rake angle on the surface finish. The 250 µm nose radius diamond tool had a 50-degree included angle and 12-degree conical clearance. The tool was rotated to get different rake angles. RMS surface finish for +5, 0 and -5-degree rake angles were measured. Figure 16 shows that negative rake angle is better than zero or positive in terms of RMS roughness. A similar trend of rake angle vs surface finish was also found by Gubbels [3]. The surface generated from negative rake angle did not show consistent chip formation and looked random in terms of the shape of the grooves generated on the surface as shown in Figure 17 (a).

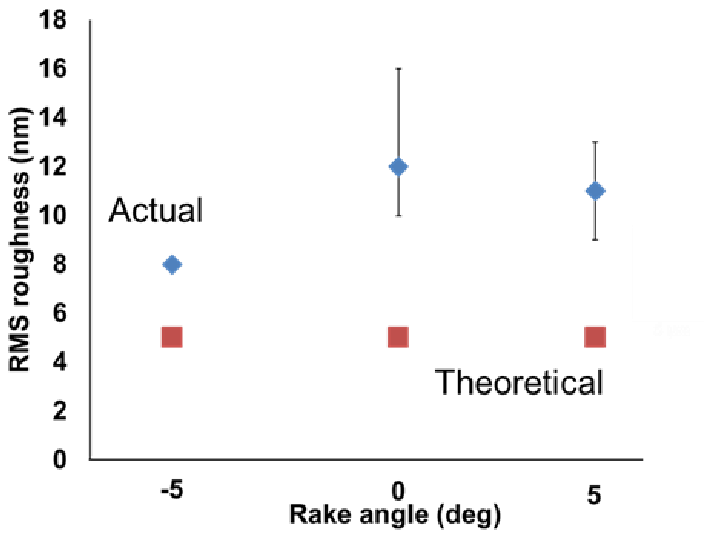

Figure 16. Effect of rake angle on RMS roughness on PMMA when machined with a 250 µm and nose radius tool at 1450 rpm and 10 µm depth of cut (DOC)

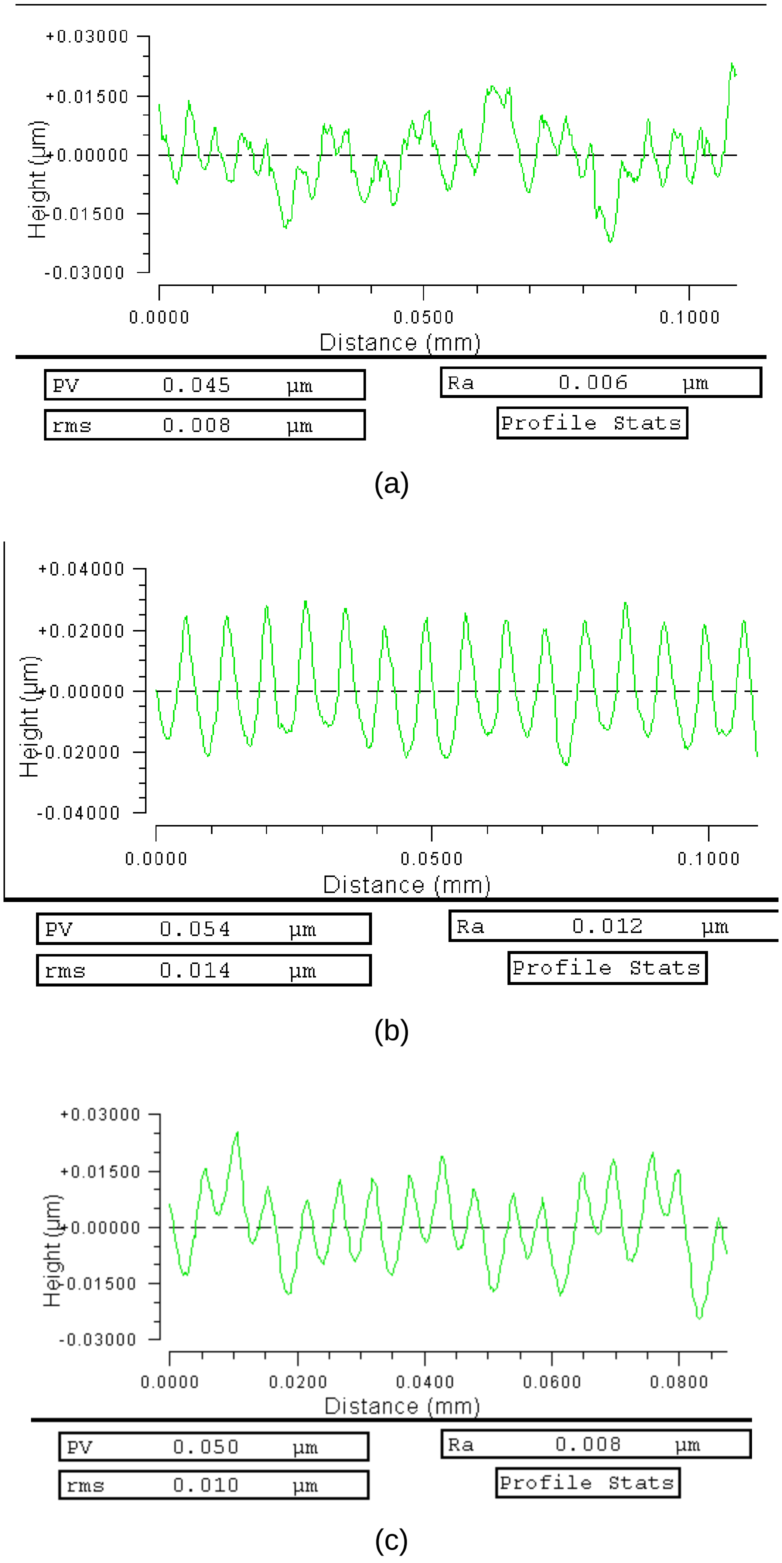

PV 0.045 µm
rms 0.008 µm
Ra 0.006 µm

(a)

PV 0.054 µm
rms 0.014 µm
Ra 0.012 µm

(b)

PV 0.050 µm
rms 0.010 µm
Ra 0.008 µm

(c)

Figure 17. Surface profiles at rake angles (a) -5^0 (b) 0^0 and (c) +5^0

Effect of tool radius

Details of the chip geometry are shown in Figure 18 which shows 3 passes of the tool. One observation is that the geometry of the chip is dependent on the radius of the tool and its cross feed. For the same cross feed, a smaller tool radius makes a shorter, thicker chip. Because the theoretical surface finish requires the chip thickness to become zero, the angle of the chip as it approaches the edge of the cut may be an important parameter. This chip angle is defined in Figure 18. This chip angle is same as the included angle of the tool across a chord equal to the feed per revolution in a circle.

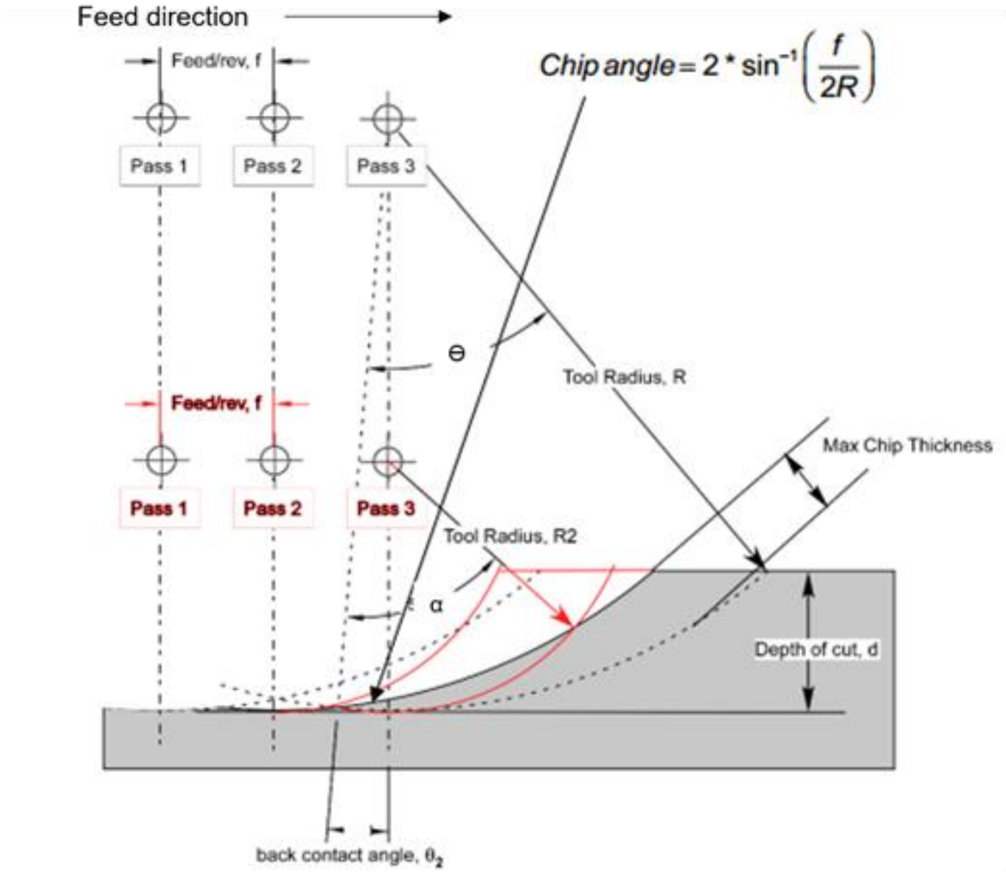

Figure 18. Theoretical geometry of the chip. Decreasing the tool radius while keeping other parameters constant makes the included angle of the chip larger and may result in better surface finish.

Figure 19 shows the effect of tool radius on RMS surface roughness. A smaller tool nose radius generated better actual surface finish for a larger radius tool. Note that the cross feed was compensated to ensure that the theoretical roughness was the same for both nose radii tested. The data in Figure 19 suggests that machining at a smaller crossfeed (1µm/rev) could achieve the same 6 nm RMS finish as that of running at relatively larger crossfeed (10 µm/rev) when using a small radius tool, this could be attributed to the vibration of machine which becomes more prevalent at very low cross feeds. For the smaller cross feeds there are many periods of the vibration within the measurement field of view.

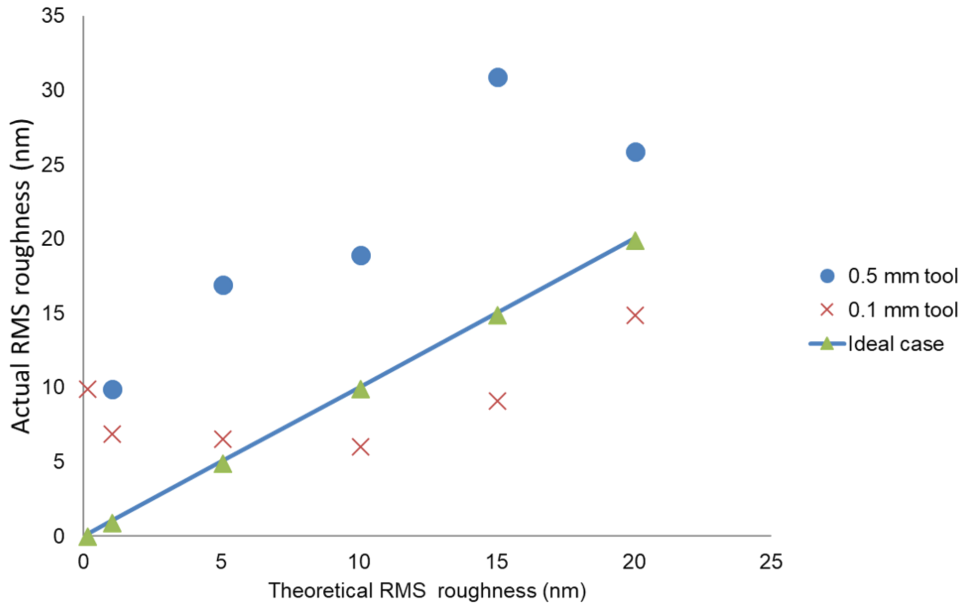

Figure 19. Effect of tool radius on RMS roughness of PMMA when machined with a 100 μm and 500 μm nose radius tools at 1450 rpm and 10 μm depth of cut (DOC).

Effect of chip management

To determine the effect of chip management on surface finish in PMMA, a series of experiments were performed with and without the chip management system. It was found that using an ionizer and removing chips from the cutting zone had no significant impact on surface finish generated on PMMA. Figure 20 shows the PMMA surfaces machined under cutting conditions with and without chip management system.

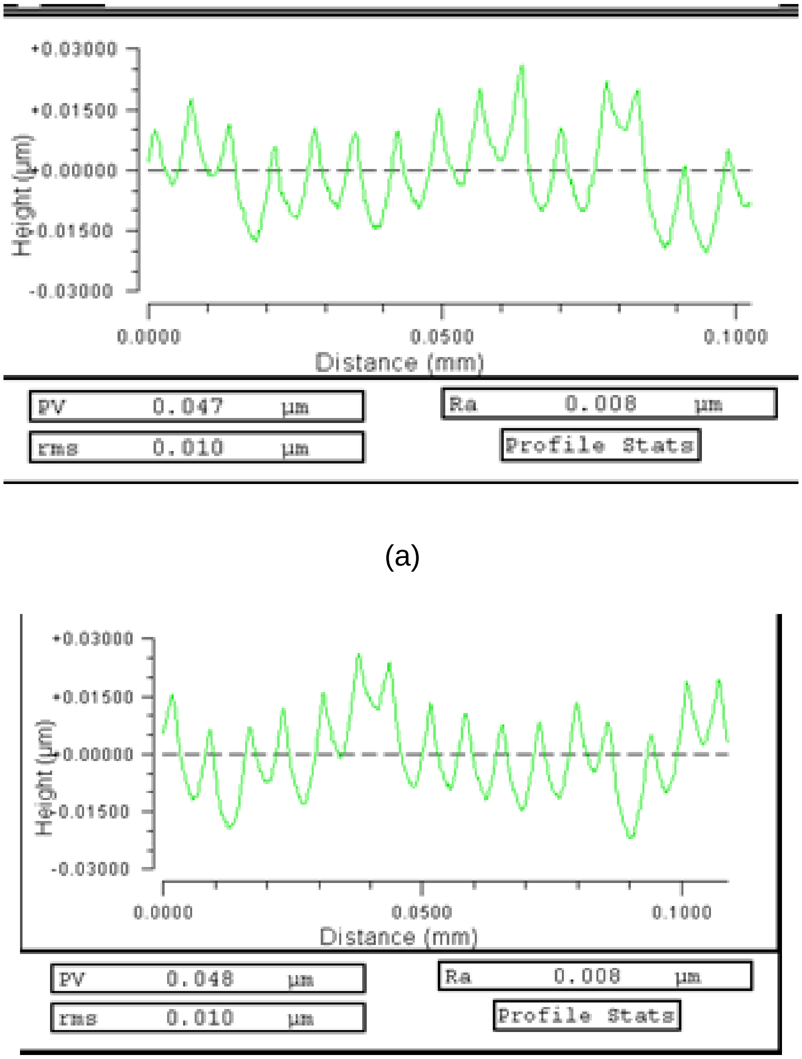

PV 0.047 µm
rms 0.010 µm
Ra 0.008 µm

(a)

PV 0.048 µm
rms 0.010 µm
Ra 0.008 µm

(b)

Figure 20. 2D profiles of surface generated in PMMA, (a) with and (b) without the use of the chip management system.

Figure 21 shows the surface roughness of PMMA with and without chip management under similar cutting conditions. The graph in Figure 21 is generated by repeating experiments five times on PMMA with and without chip management.

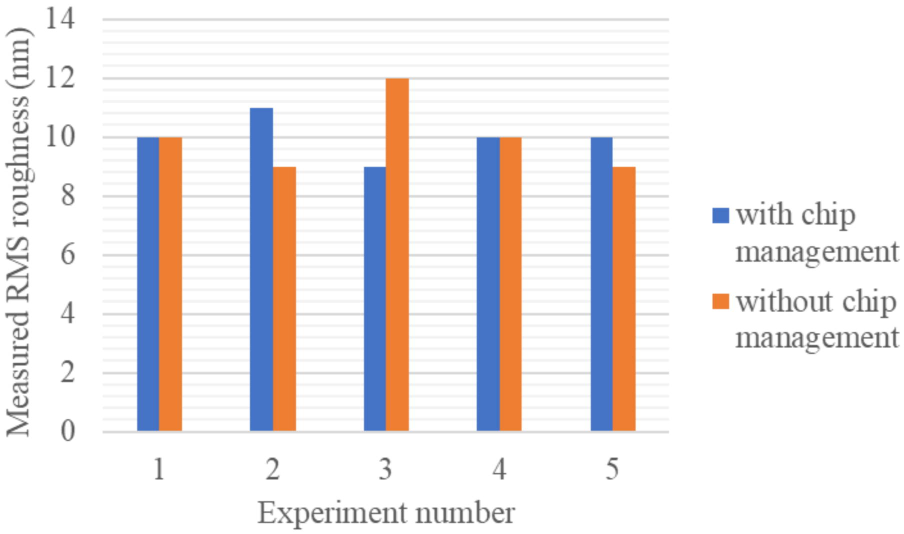

Figure 21. Measured RMS roughness on PMMA with and without chip management system. 0.5 mm nose radius tool, 10 µm depth of cut and theoretical RMS of 5 nm.

Effect of Lubricants

Research is not available in terms of lubricants and their effect on surface finish machining PMMA. Based on the viscosities and inertness to PMMA, several cutting fluids were used to study the effect on surface finish. Odorless mineral spirits (ODM), WD-40, and glycerin were used as coolants. While cutting PMMA, these coolants were dripped on the tool using transfer pipette for every 200 µm tool travel across the part. 1450 RPM spindle speed, 0.45 µm feed per rev at 5 µm depth of cut was used for the experiments. However, it was observed that the use of coolants did not significantly improve RMS surface finish. Figure 22 shows the effect of lubricants on surface finish.

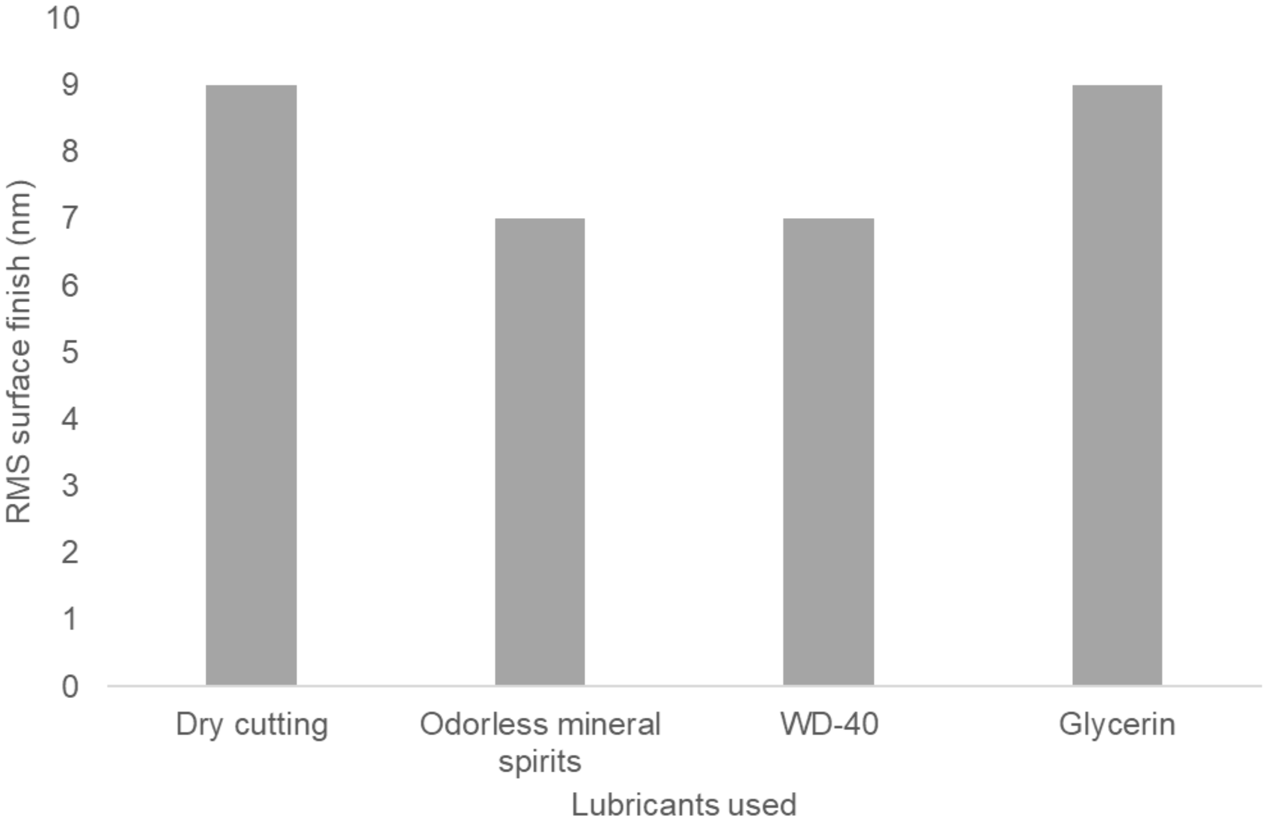

Figure 22. Coolants effect on surface finish for PMMA.

2.4.2 TOOL WEAR

According to Gubbels [3], tool wear on PMMA was seen after 80 km of cutting at larger feed rates and 1 mm nose radius diamond tools. This indicates that the tool wear in PMMA is not a problem, as tools in optical industry were generally re-lapped after 10 km of cutting [8]. A series of dry overlapping feed experiments were performed on PMMA using 0.5 mm round nose diamond tool for a cutting distance of 8 km. The diamond tool looks sharp and no measurable wear was seen after imaging the tool in the SEM. Figure 13 shows one of the diamond tools that was used for cutting PMMA for 8 km.

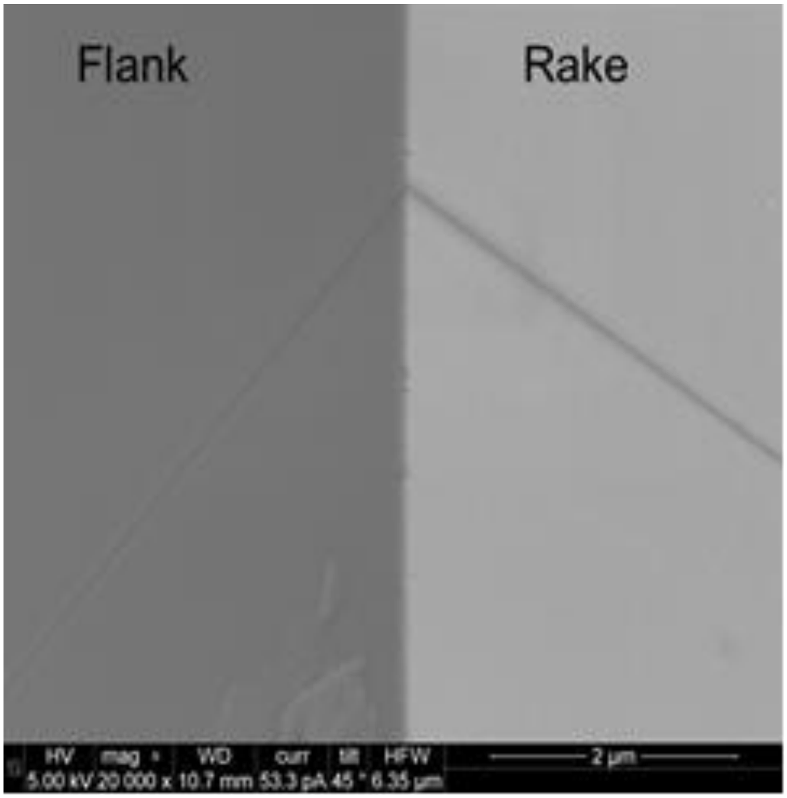

Figure 23. Diamond tool after cutting PMMA for 8 km (20,000X magnification in the SEM).

Figure 24 shows the diamond tool that was used to cut PMMA for 16 km. However, no measurable wear was seen on the diamond tool after 16 km of cutting. 1450 rpm, 20 μm depth of cut and 1 m/s of cutting speed was used for the experiment. The cutting speed was then increased to 4 m/s using the same cutting conditions, a small amount of wear was seen after 16 km of cutting. Figure 25 shows the tool after cutting 22 km. Note that the images in Figure 25 and 26 are at same magnification.

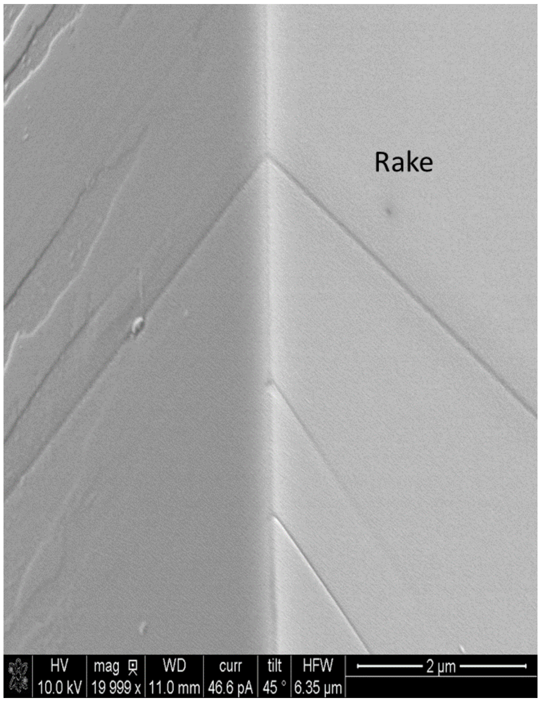

Figure 24. Diamond tool after cutting PMMA for 16 km at 1 m/s.

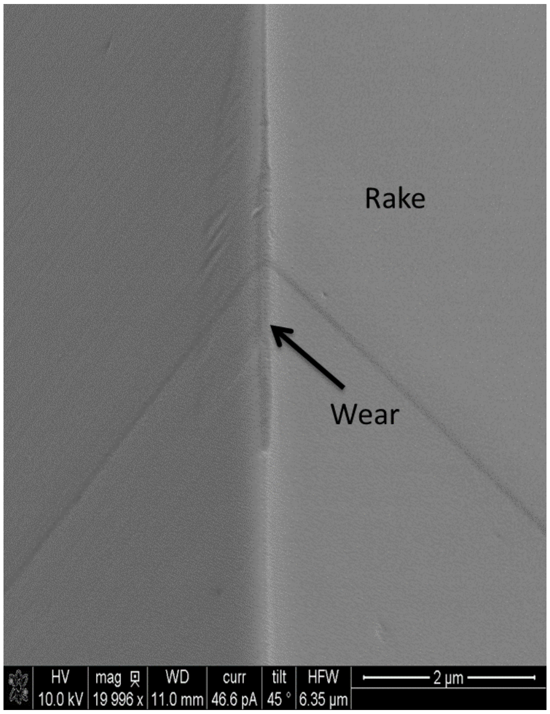

Figure 25. Diamond tool after cutting PMMA for 16 km at 4 m/s.

The comparison in Figure 26 shows the diamond tools that has not been used for cutting and the edge that was used for cutting 16 km at 4 m/s. In the case of PMMA, tool wear was found only when cutting for distances greater than 16 km and higher cutting speeds.

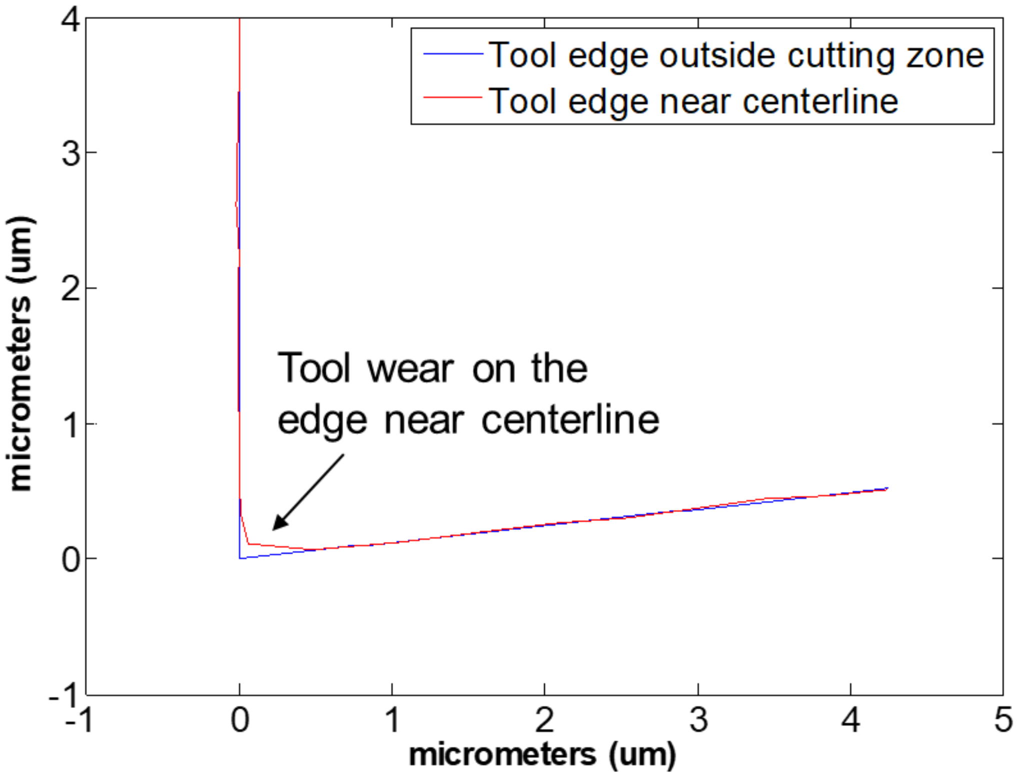

Figure 26. Wear on diamond tool that cut PMMA for 16 km at 4 m/s.

2.5 MACHINING POLYCARBONATE

2.5.1 SURFACE FINISH

Polycarbonate is a transparent thermoplastic with high impact strength. Dry turning of polycarbonate to obtain optical quality surface finishes was found to be difficult. Polycarbonate chips ball up on the diamond tool during cutting and strike the machined surface. Figure 27 shows streakiness on the surface of polycarbonate sample after diamond turning.

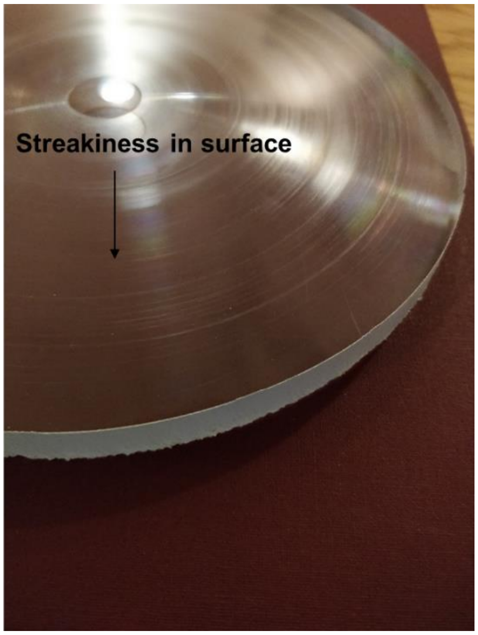

Figure 27. Polycarbonate after dry facing operation

It was difficult to measure the surface shown in Figure 27 on the Newview 5000. Measurements showed that the data points on the surface profile were missing and thus resulted in higher RMS surface finish. The reason for this was identified to be steep slopes at the side of the grooves that could not be imaged. Figure 28 shows the surface profile as measured by Zygo Newview 5000 white light interferometer.

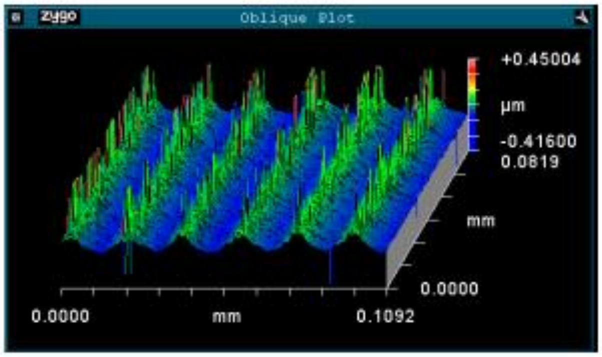

Figure 28. Newview 5000 measuring polycarbonate after dry facing.

Dis-continuous chips were produced when dry turning PC. To remove chips from the cutting zone, an air ionizer and a vacuum system were employed. Figure 29 shows the chip management system developed for cutting experiments. This system was used for all the machining experiments unless it is explicitly stated otherwise. The setup shown in Figure 29 was the same as that of setup shown in Figure 1.

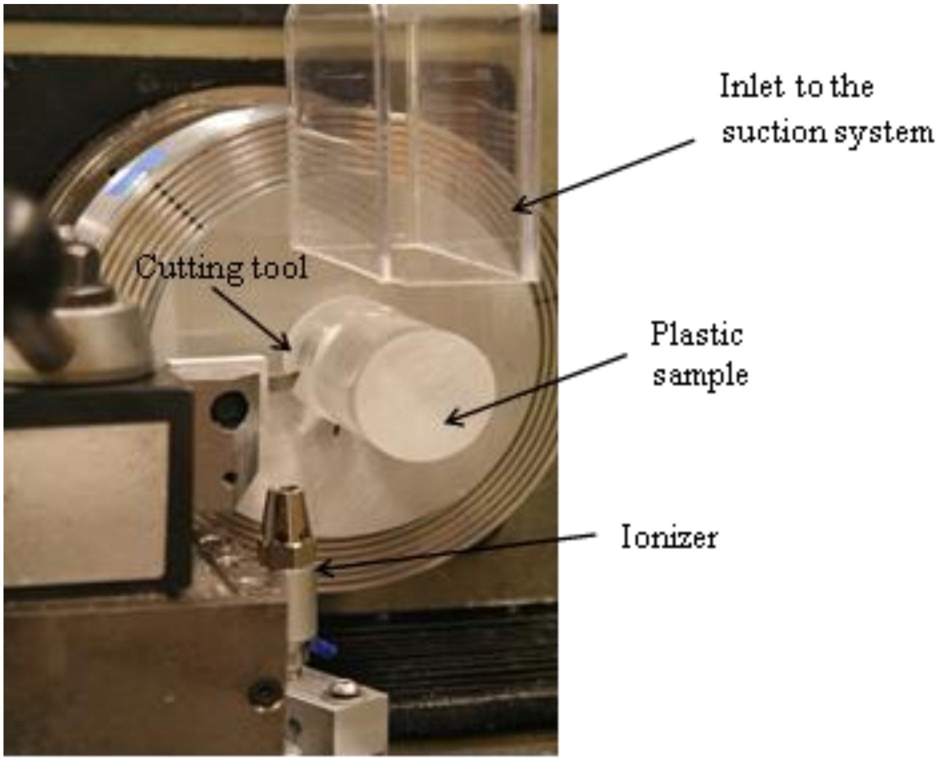

Figure 29. Setup developed for cutting experiments.

This chip management setup has a pressure adjustable air ionizing nozzle and an inlet to the vacuum system. High pressure (> 0.7 psi) from the air nozzle resulted in a turbulent flow, where the chip wobbles sideways, as shown in Figure 30, instead of being entrained in the flow created by air from nozzle and the suction system.

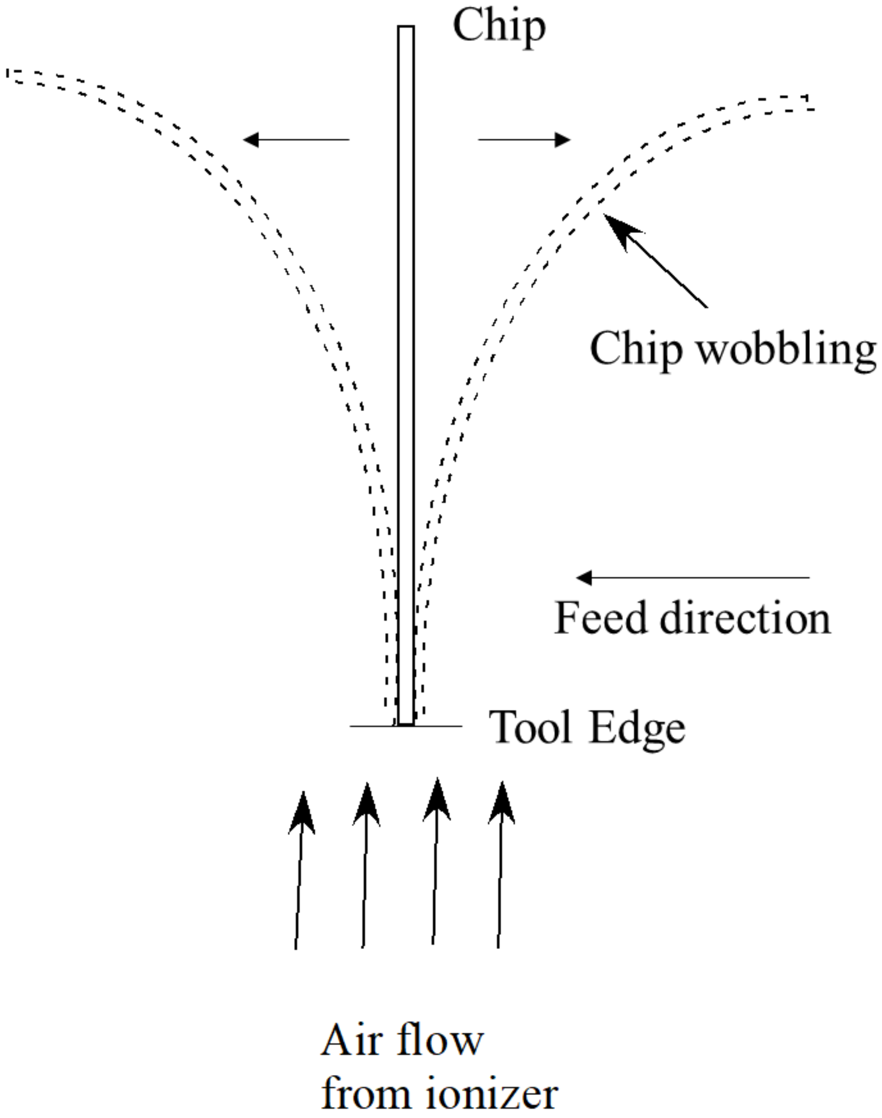

Figure 30. Chip wobbling due to turbulent flow generated when pressure > 0.7 psi was used.

A continuous free flowing chip was observed when higher feed rates were used or when larger depths of cut were used or both. When appropriate feed rate and depth of cut were used, the chip would continuously be entrained in the flow and removed from the cutting zone. This suggested that the chip flow in the setup is dependent on the stiffness of the chip. Experimental flow analysis was performed, and optimum pressure and velocity of air towards the clearance face of the tool required to generate a continuous chip were identified. The air pressure and velocity were measured using an Extech digital manometer. Optimum air pressure and velocities are tabulated below. However, it was found that keeping the velocity at the cutting zone close to the cutting sped is advantageous.

Table 6. Optimum flow parameters to generate continuous PC chips.

Air pressure (psi)	0.4 to 0.6
Velocity of air from air ionizer (m/s) [Location A in Figure 4-5]	5.5
Velocity of air at inlet of the suction system (m/s) [Location B in Figure 4-5]	2.8
Velocity at the cutting zone due to both ionizer and suction (m/s) [Location C in Figure 4-5]	4

Location A, B and C in Table 6 are marked in the Figure 31. Based on the experimental flow analysis, the air pressure from the nozzle is set to 0.5 psi for all the cutting experiments where the chip management system is used.

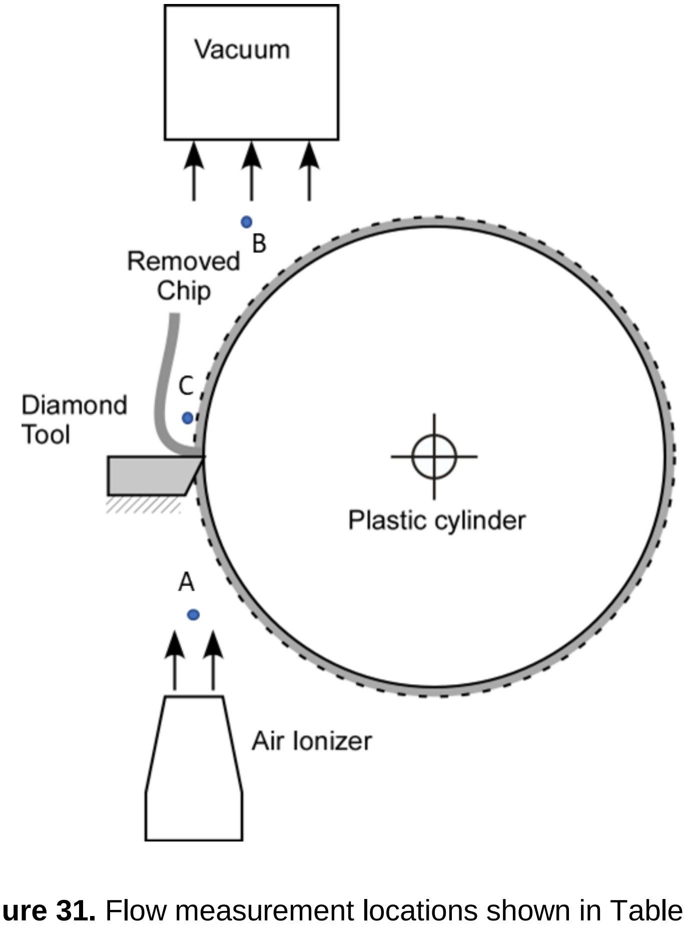

Figure 31. Flow measurement locations shown in Table 4-1.

In a demonstration of the robustness of the system, the rectangular vacuum inlet was removed and the 2” diameter vacuum tube was located on the ceiling about 5 feet above the workpiece. The cutting is started with the ionizer blowing from below and the ceiling vacuum pulling from the top and within a few seconds the chip finds the ceiling vacuum and stays connected through out one pass of the tool. The optimum feed rates and depths for cutting PC and the effect of this chip management system on surface finish will be discussed in the following sections.

Effect of feed per revolution

Figure 32 shows the variation of RMS surface roughness generated as a function of cross feed on PMMA and PC when machined with a 0.4 mm nose radius diamond tool and surface finish was measured using 150X objective on Keyence VKX-1100 microscope. Increase in feed per revolution increased the surface finish as expected for PC, but surface finish on PMMA was better than PC under same cutting conditions.

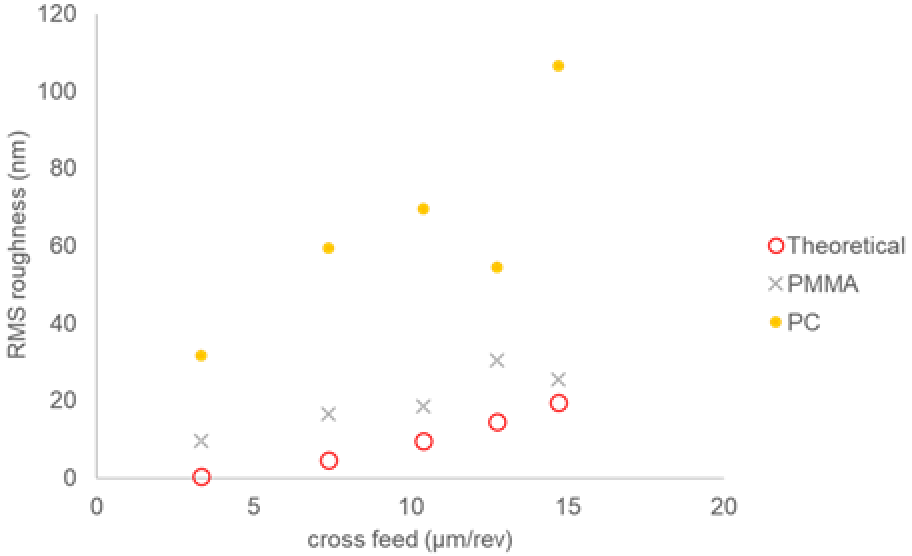

Figure 32. RMS roughness vs feed per revolution. 1450 RPM spindle speed. 4 m/s cutting speed and 20 µm depth of cut.

Effect of cutting speed

No effect of cutting speed on surface finish was observed in PC. Figure 33 shows the results from a cutting experiment where spindle speed was varied to get different cutting speeds. For a theoretical RMS of 1 nm, the RMS values for all the cutting speeds were approximately 35 nm RMS.

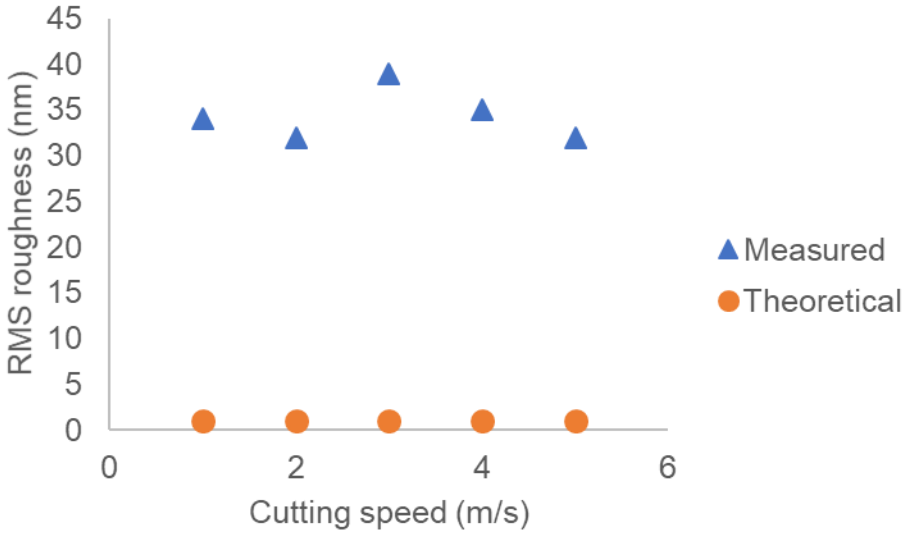

Figure 33. Effect of cutting speed on RMS roughness in PC. 0.5 mm nose tool radius.

A similar lack of trend for RMS roughness with cutting speed was also observed by Gubbels [3] with a larger radius (1 mm) tools.

Effect of depth of cut

Figure 34 shows the effect of changing the depth of cut on the RMS roughness for PC when machined with a 100 µm tool and expected 0.07 nm theoretical RMS roughness. It was observed that chips generated for larger depths of cut were easier to remove from the cutting zone. One hypothesis is the chips are relatively stiffer, larger in size and can be more efficiently removed. This improves the surface finish and can be seen in Figure 34. Continuous and larger chips were found to give better surface finish.

Chip dimensions can be controlled using feed rate or depth of cut or both for a given tool radius. Increasing feed rate would increase the groove size and would increase the achievable theoretical RMS finish. Moreover, increase in depth of cut would not affect theoretical RMS surface finish.

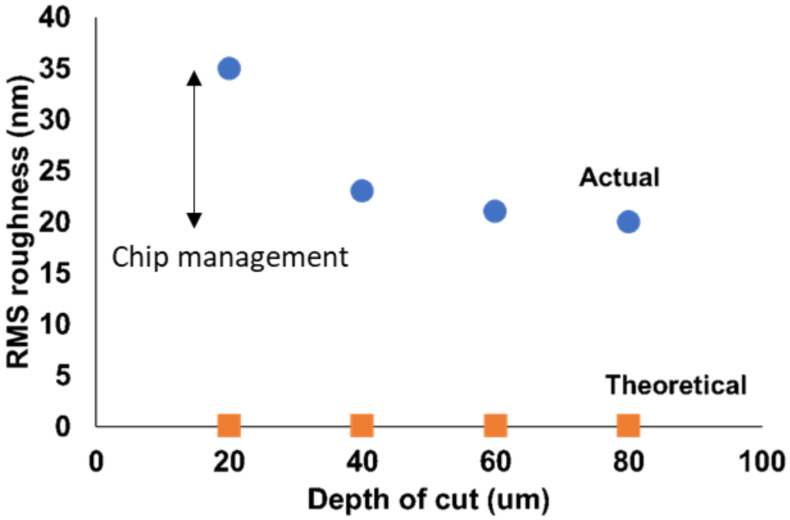

Figure 34. Effect of depth on RMS surface finish of PC when machined with a 100 µm nose radius tool at 1450 RPM and 0.45 µm/rev feed rate.

Therefore, a series of experiments were conducted on PC that relates the principle moment of inertia of the chip in the air flow direction (into the page) and the achievable surface finish in the experimental conditions investigated. Figure 35 shows the half crescent shaped chip that is generated from overlapping cuts.

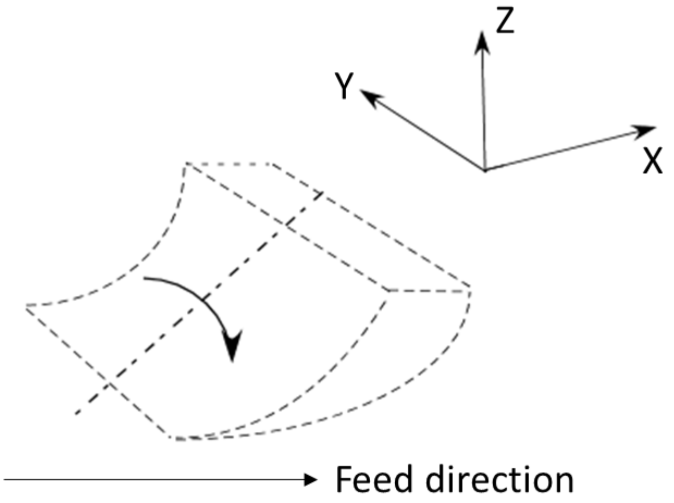

Figure 35. Half crescent shaped chip generated during overlapping feed rates.

The moment of inertia for the chip is calculated and the optimum depth of cut for a tool radius was identified. Figure 36 shows the plot where principle moment of inertia in the Y- direction of the chip is plotted against depth of cut. Moment of inertia directly scales with the depth of cut. The plot shown in Figure 36 resulted after cutting PC using a 100 µm nose radius tool and 0.45 µm/rev.

It was identified that 80 μm depth of cut and principle moment of inertia in Y-direction > 770 μm^4 gave a better surface finish in the experimental conditions used.

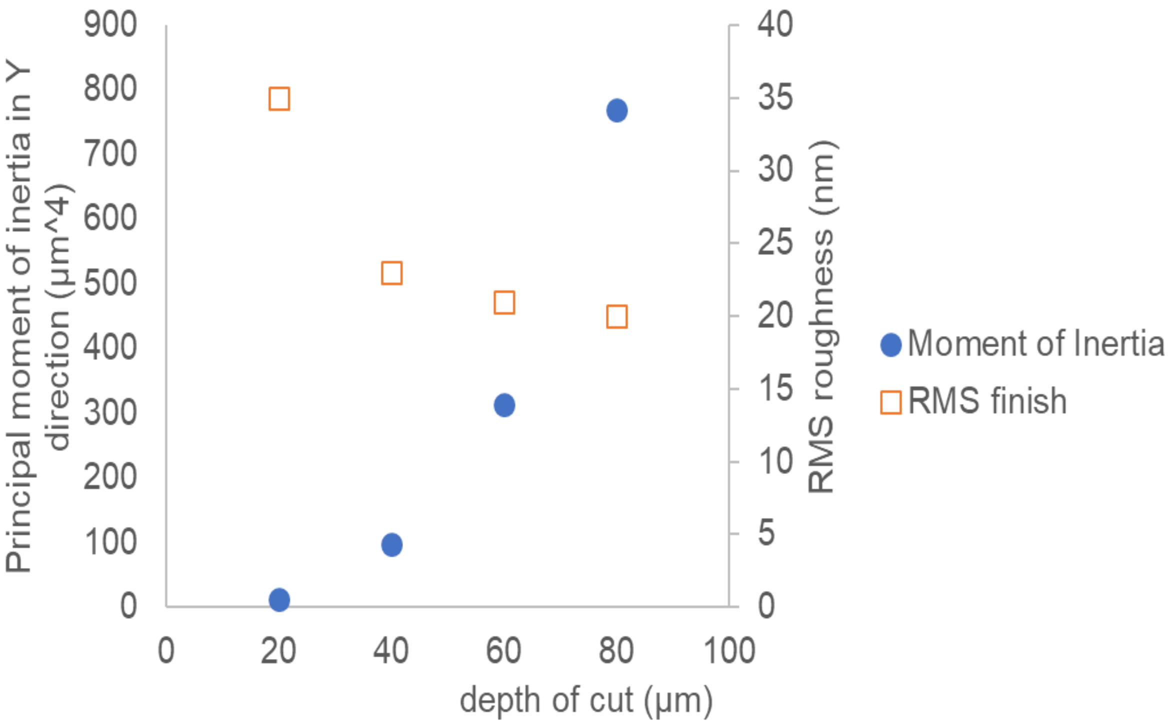

Figure 36. Moment of inertia of chip and RMS roughness variation with depth of cut.

In the Figure 36, the reduction of RMS roughness from 35 nm to 20 nm is due to efficient management of chips. The optimum depth of cut and chip removal for PC in the experimental conditions used are tabulated in Table 7.

Table 7. Optimum depths of cut when machining with chip collection system at theoretical RMS of 0.07 nm RMS.

Tool Radius (mm)	Depth of cut (μm)
1	>20
0.5	>30
0.1	>60

It was interesting that even when the chips are effectively removed from the cutting zone, the best RMS roughness on PC was 20 nm and is 285 times that of the theoretical RMS of 0.07 nm. It was found that the surface finish is also affected by plastic build up on the tool. Effect of build up on surface finish will be discussed in the following section.

Build up on the tool

Figure 37 shows the PC surface and the theoretical tool profile after machining with a 0.4 mm nose radius tool at 20 µm depth of cut and 14 µm/rev cross feed. Theoretical grooves in Figure 37 are smaller than the actual measured grooves. This can be attributed to the buildup of PC on the tool while cutting; thus, increasing depth of the groove and degrading the surface finish. The RMS finish of the surface shown in Figure 37 was found to be 100 nm RMS for a theoretical of 20 nm RMS. It was also found that the cutting edge with acetone dipped q-tip after every pass improved surface finish by 15%. Figure 38 shows the plastic left on the tool after every pass

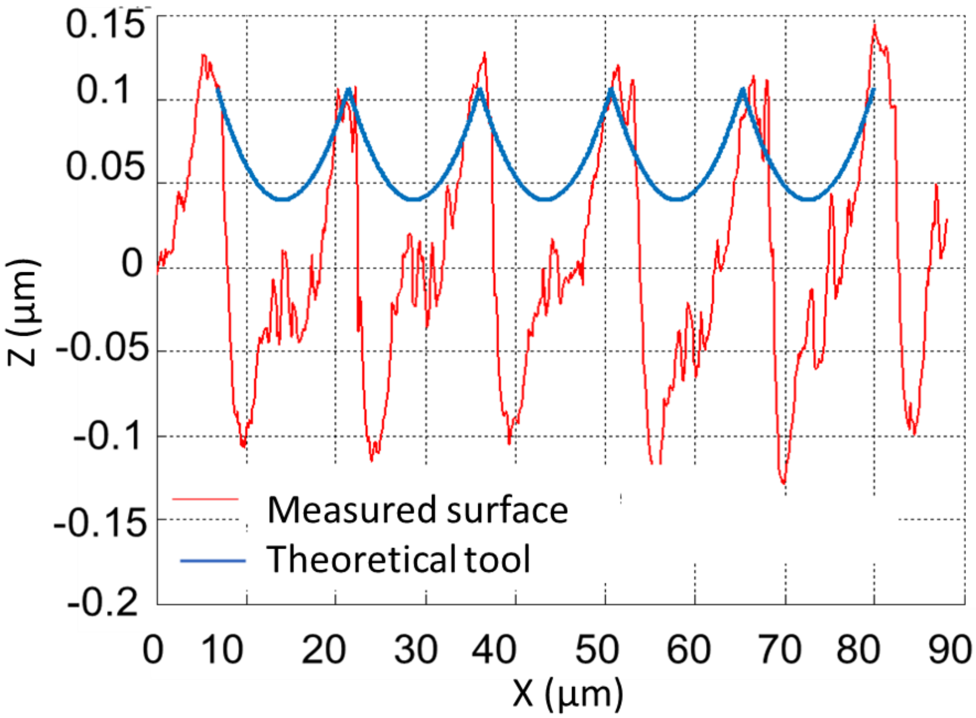

Figure 37. Evidence of Build up edge (BUE) on the PC surface.

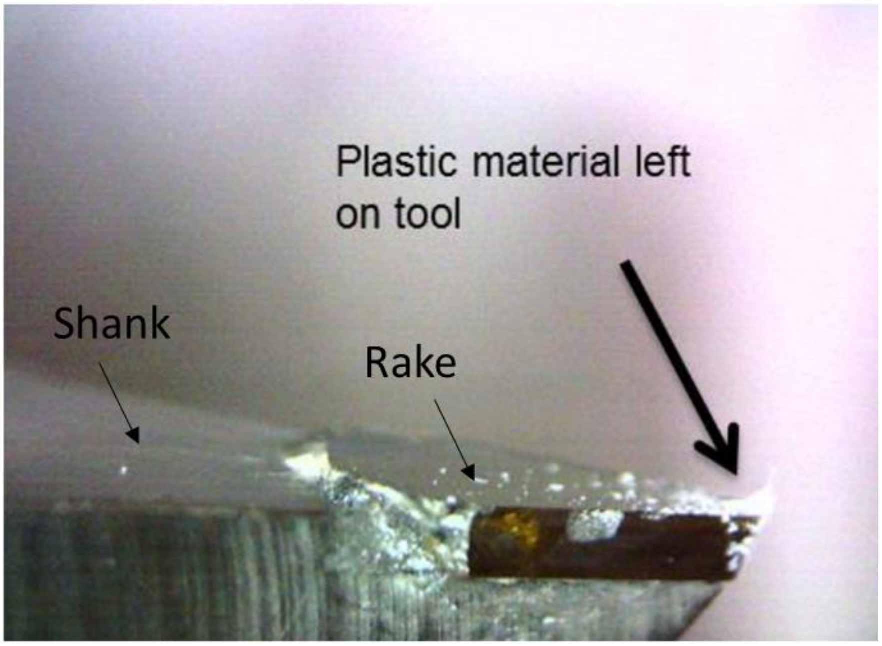

Figure 38. Tool after machining PC [34].

It was found that at lower feed rates, as the chip thickness would be lower, and the thickness would be less than 70 nm. With the developed chip management system, it was very difficult to remove chips from the cutting zone at very fine feed rates on PC. Chips tend to ball up on the tool edge and plastic builds up on the tool thus making the surface finish larger than the theoretical value.

Figure 39 and 40 shows the force plots from two experiments, where high frequency in the cutting force can be seen at lower cross feeds which faded away at larger cross feeds and this high frequency in the force plot can be directly related to the measured surface finish.

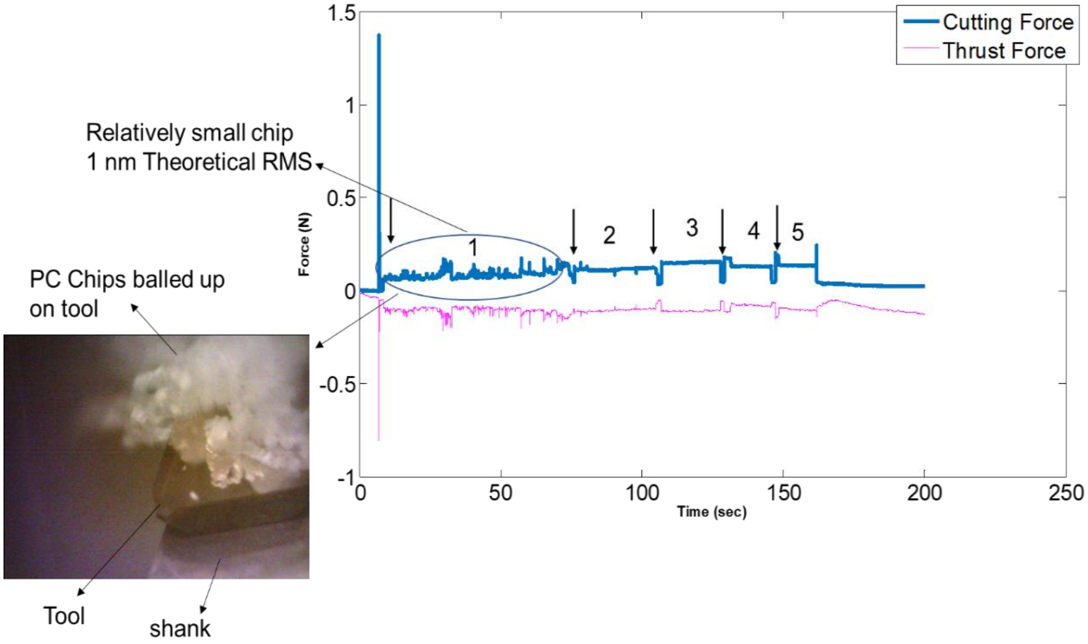

Figure 39. Force plot at different cross feeds in PC.

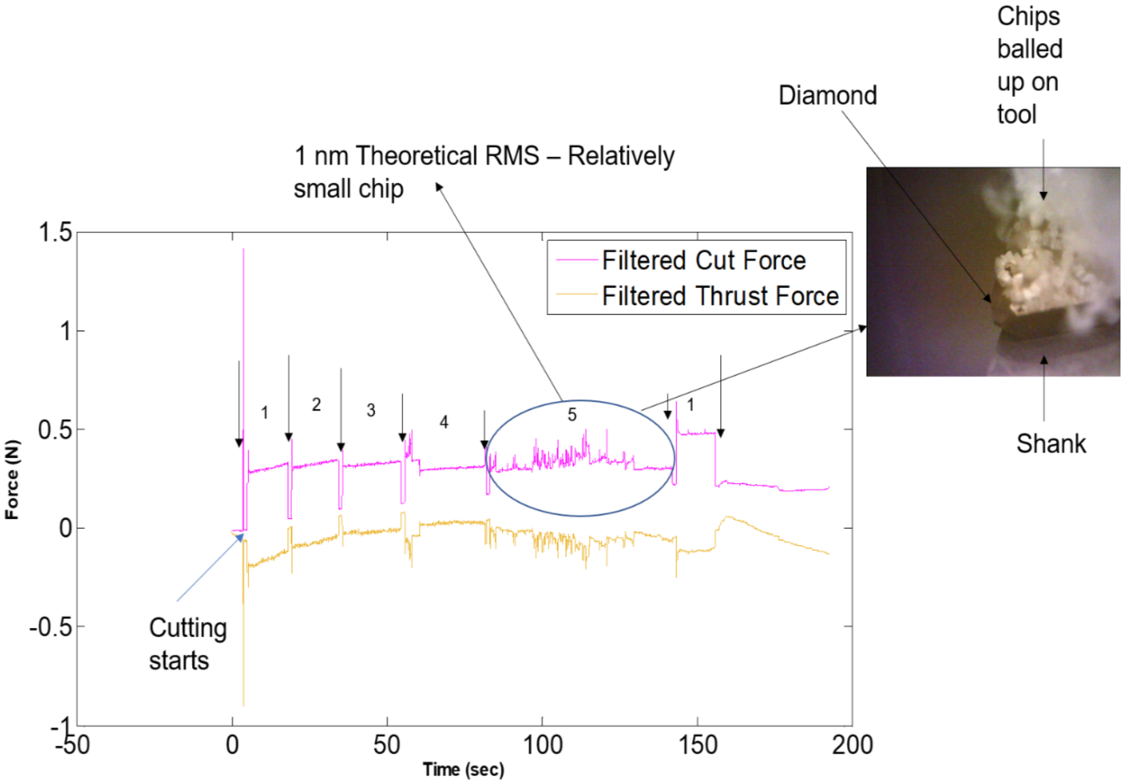

Figure 40. Force (low pass filtered) plot at 6 different cross feeds in PC.

Figures 39 shows the force plot where the part is cut at different feed rates and the cross feeds used were tabulated in Table 8. A downward pointing arrow indicates start and stop of a crossfeed.

Table 8. Cross feeds shown in Figure 39

Number	Feed rate (µm/rev)	Theoretical RMS (nm)
1	3.76	1
2	8.41	5
3	11.89	10
4	14.56	15
5	16.82	20

Figure 40 shows the force plot where cross feeds were inverted from that of Figure 39. Cross feeds in Figure 40 are tabulated in Table 9.

Table 9. Cross feeds shown in Figure 9

Number	Feed rate (µm/rev)	Theoretical RMS (nm)
1	16.82	20
2	14.56	15
3	11.89	10
4	8.41	5
5	3.41	1

In Figures 39 and 40, when machined at finer feed rates and small chip, the chips balled up on the tool and high frequency in force data can be observed. At higher feed rates, the frequency is significantly lower, and the chip is continuously removed from the cutting zone. This can be directly related to the ratio of actual RMS roughness measured to the theoretical RMS roughness, shown in Figure 41.

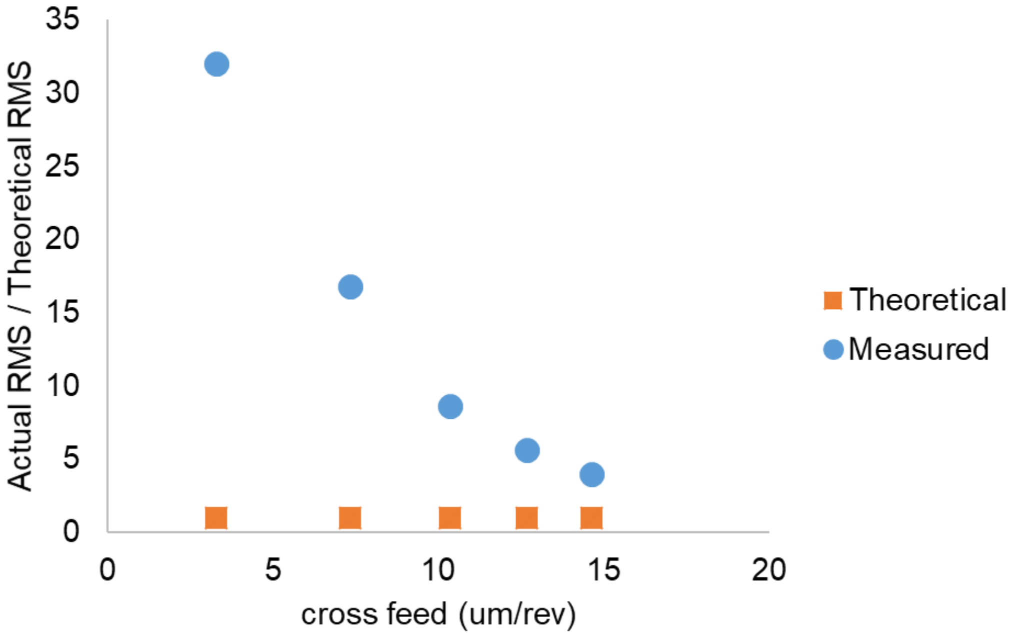

Figure 41. Actual/theoretical RMS ratio vs feed rate for PC

Looking at the surface profile in Figure 42, a repeatable pattern of good surface finish region and a region of bad surface finish was found on the plastic sample after machining, which could be due to both build up on the tool and the inefficient chip management at finer feed rates. Having good and bad surface finish on the part will increase the areal RMS surface finish. Figure 42 shows the surface on a machined part, which has both good and bad regions. In Figure 42, the line RMS finish on the left is 18 nm RMS vs 85 nm RMS on the right.

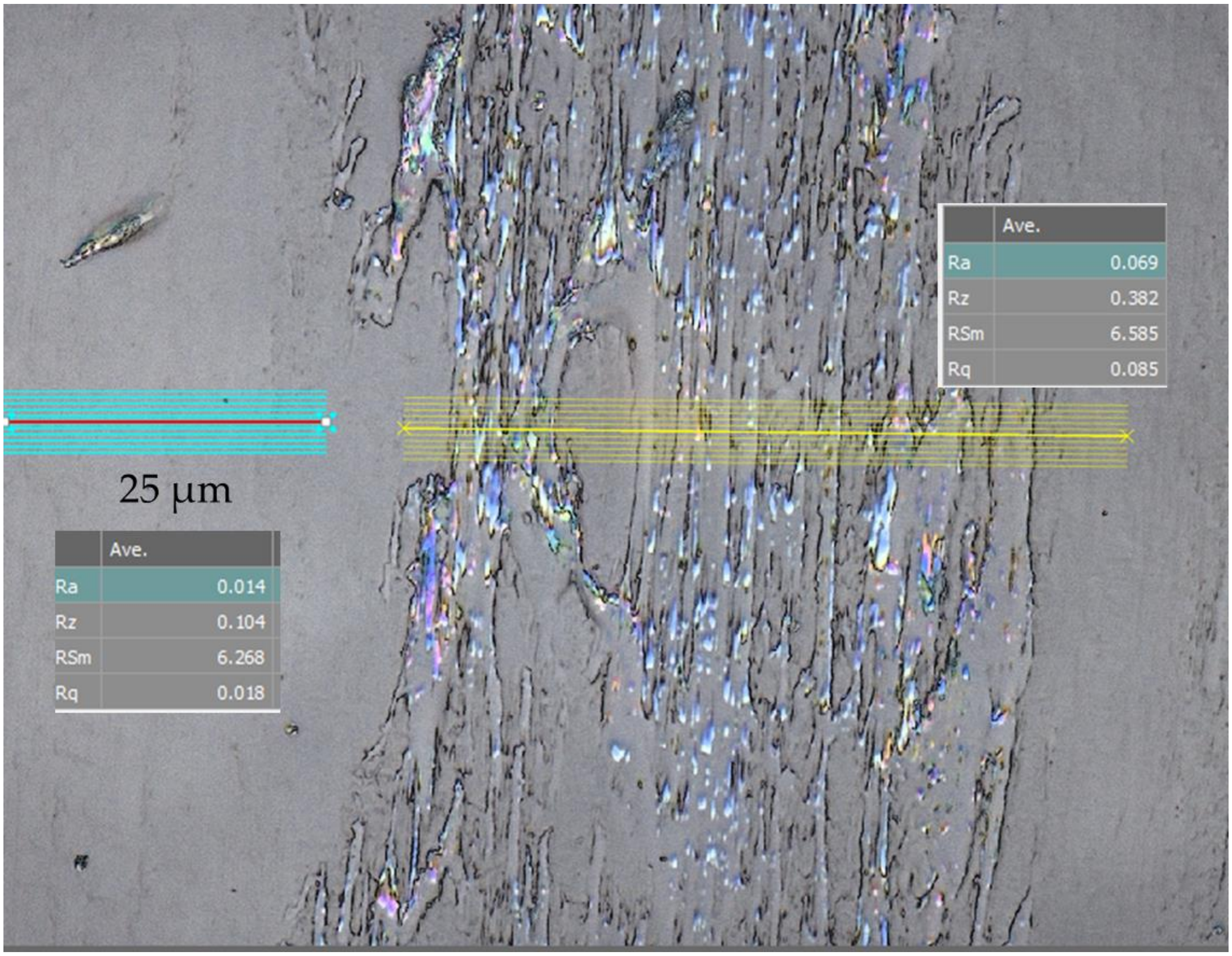

	Ave.
Ra	0.069
Rz	0.382
RSm	6.585
Rq	0.085

	Ave.
Ra	0.014
Rz	0.104
RSm	6.268
Rq	0.018

Figure 42. RMS surface finish of PC at different regions on the same part (The lines show the region of surface finish measurements).

Effect of Rake Angle

Figure 43 shows the effect of rake angle on PC surface finish. $+5^0$ rake angle was found to be better than zero. The surface finish data generated by $+5^0$ rake angle was found to have a relatively small standard deviation compared to zero rake. +5 degrees is found to be better for PC, this could be attributed to the fact that PC is a ductile material unlike PMMA.

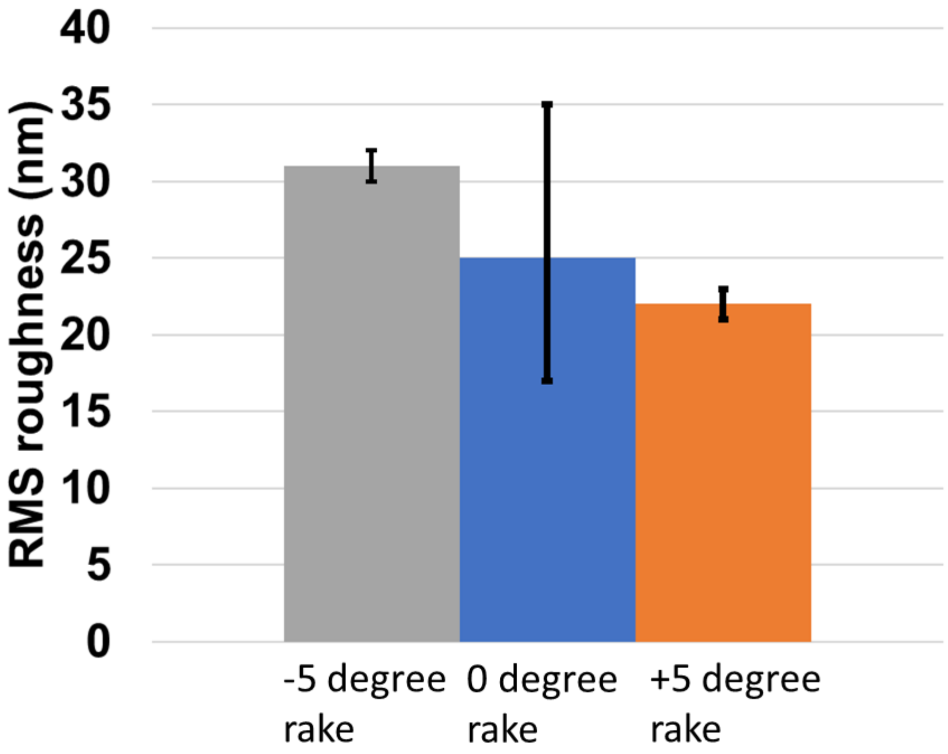

Figure 43. Effect of rake angle on RMS surface finish on PC when machined with a 250 µm nose radius tool at 20 µm depth of cut.

Effect of Chip Management

Dry turning polycarbonate with no chip management system yielded streaks on the machined surface and thus gave bad surface finish like Figure 42. It was found that using the chip management system without lubrication described in this research decreases RMS finish by 28%. Figure 44 (a) shows the surface when PC was machined using a 0.5 mm nose radius diamond tool. Chips generated from machining PC are statically charged and ball up on the tool and scratch the machined surface. Figure 44 (b) shows the surface when the chip management system was employed.

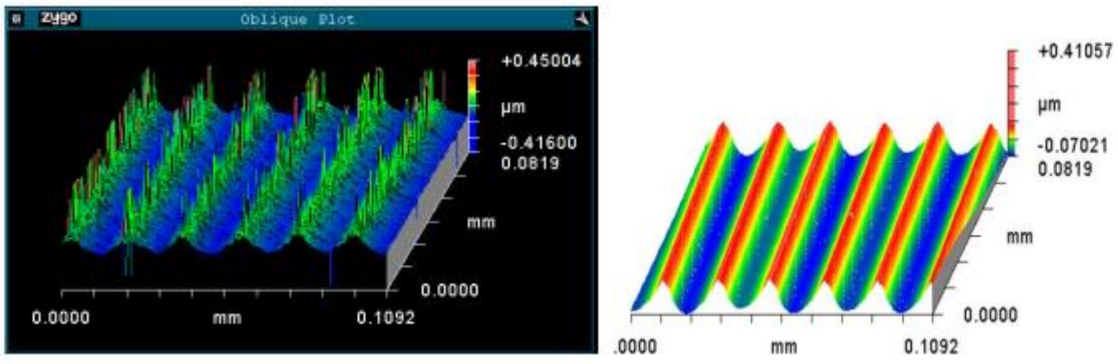

(a) (b)

Figure 44. Machined PC surface (a)without chip management (b) with chip management system

Effect of Lubricants

Using the chip management system reduced the RMS roughness by 28%, but it was still not anywhere close to the theoretical RMS roughness. To solve the problem of build up and chip management. A wide range of coolants were used for cutting experiments. Selection of lubricants was primarily based on their non-reactivity with PC. The lubricants were picked from hydrocarbon-based oils, glycerin-based oils, silicone-based oils and other miscellaneous oils.
The coolants used for testing on PC were

- Hydrocarbon based oils
  - Kerosene
  - WD 40
  - Motor oil
  - Odorless mineral spirits (ODM)
- Silicone oil
  - 3 in 1 silicone oil for high temperatures
- Glycerol based oil
  - Medical grade glycerin
- Miscellaneous
  - DI water
  - Renoform oil OL1814
  - Tap magic aqueous

The coolant was dripped using a transfer pipette for every second onto the tool while cutting the part. 100 µm nose radius tool was used for cutting at 1450 RPM spindle speed, 5 µm depth of cut and 0.65 mm/min, resulting in 0.07 nm theoretical RMS finish. Experiments with above mentioned conditions were repeated 3 times and showed similar RMS finish values. Figure 45 shows the effect of coolants on the surface finish generated.

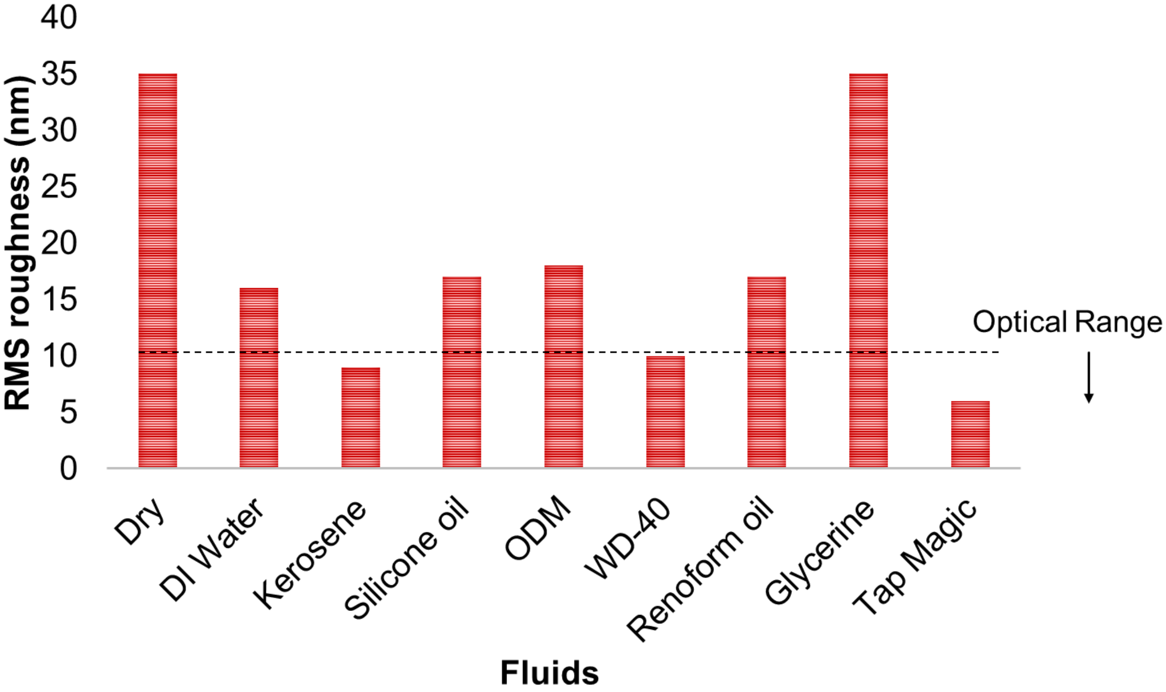

Figure 45. RMS roughness achieved after using different lubricants

Kerosene, WD 40 and Tap magic aqueous gave optical range surface finish (RMS < 10 nm) on PC. DI water, silicone oil, odorless mineral spirits and Renoform oil gave surface finish around 17 nm RMS. Tap magic aqueous gave best surface finish. Kerosene and WD 40 have similar composition and viscosities [12-15], which might be one of the reasons for achieving similar RMS surface roughness. Tap magic aqueous was primarily used for two reasons – electrical conductivity and low viscosity. Achieving best surface finish by using Tap magic aqueous can be attributed to two possibilities. Firstly, the electrical conductivity which helps in removing static electricity at the cutting zone. Secondly, it has low viscosity and its kinematic viscosity decreases with increased temperature. The electrical resistance of Tap magic aqueous was measured using a multimeter and resulted in 250 KΩ.

Table 10 shows the viscosity and chemical composition of WD-40, Tap magic aqueous and kerosene [12-15]. The surface profiles achieved on PC after machining with kerosene, WD-40 and Tap magic aqueous are shown in Figures 46, 47 and 48 respectively. To check if Tap magic Aqueous has any impact on mechanical properties of PC. A Vickers hardness test was performed with a 1 kg load on a PC sheet of 1.5” thickness. Three hardness measurements were taken on the sample and then the sample was soaked in Tap Magic Aqueous for 24 hours at room temperature. Vickers hardness test was performed again on the PC sheet after soaking. The

Vickers hardness value was same before and after soaking the PC sheet inside Tap magic Aqueous. The hardness value obtained was 5.3 kgf/mm^2. Surface in Figure 47 have P-V roughness of 400 nm and RMS of 10 nm, which is unusual, this can be attributed to WD-40 still stuck to the surface after cleaning with DI water.

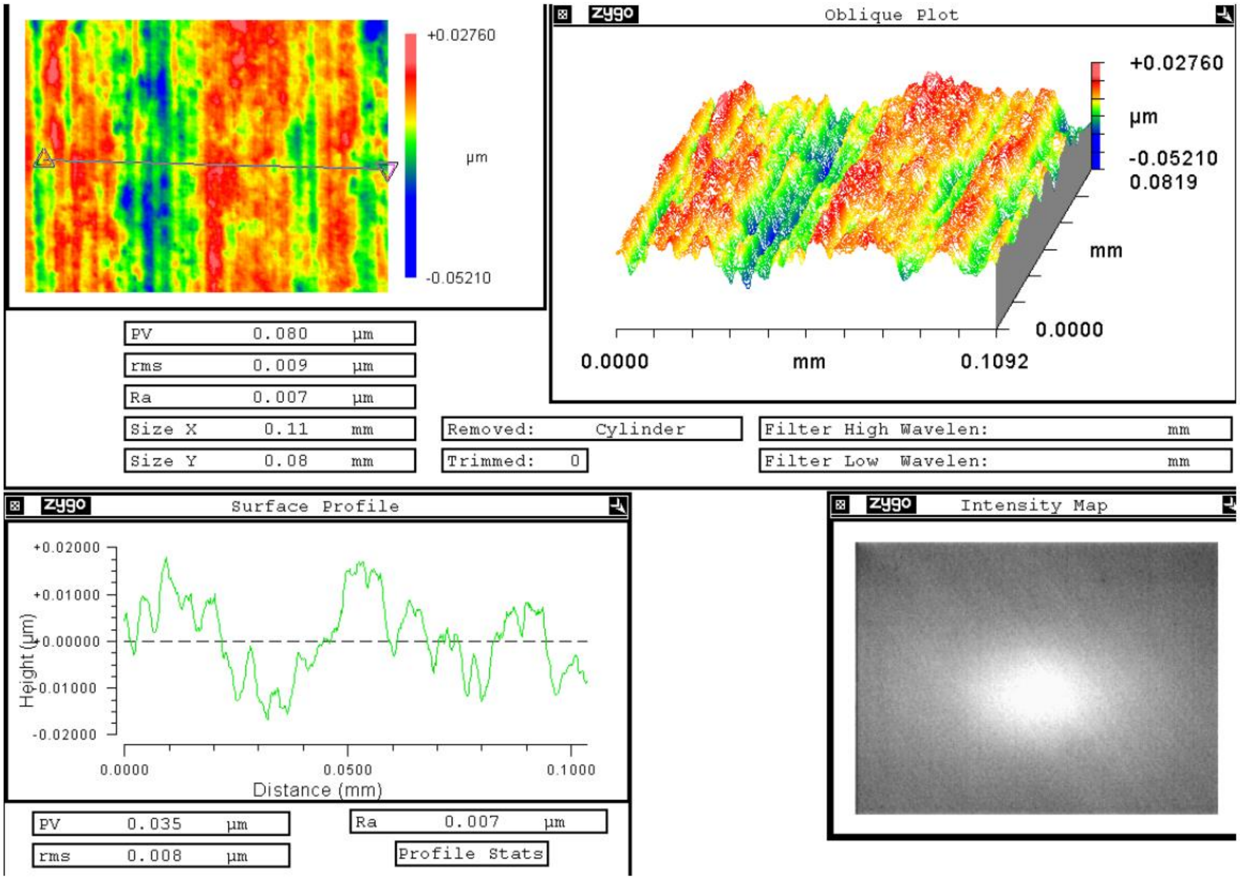

PV 0.080 µm
rms 0.009 µm
Ra 0.007 µm
Size X 0.11 mm
Size Y 0.08 mm
Removed: Cylinder
Trimmed: 0
Filter High Wavelen: mm
Filter Low Wavelen: mm

PV 0.035 µm
rms 0.008 µm
Ra 0.007 µm
Profile Stats

Figure 46. Surface profile of PC after machining with kerosene.

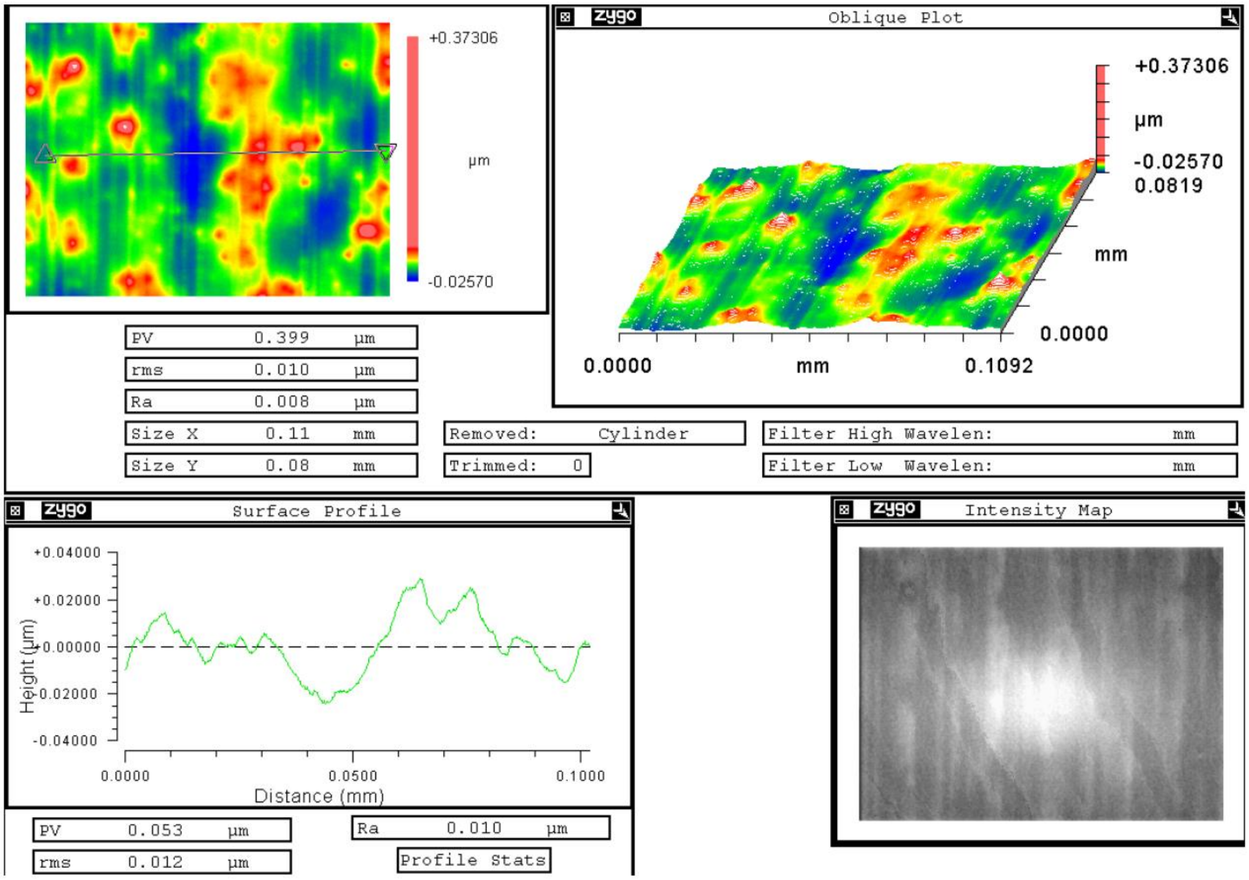

PV 0.399 µm
rms 0.010 µm
Ra 0.008 µm
Size X 0.11 mm
Size Y 0.08 mm
Removed: Cylinder
Trimmed: 0
Filter High Wavelen: mm
Filter Low Wavelen: mm

PV 0.053 µm
rms 0.012 µm
Ra 0.010 µm
Profile Stats

Figure 47. Surface profile of PC after machining with WD 40.

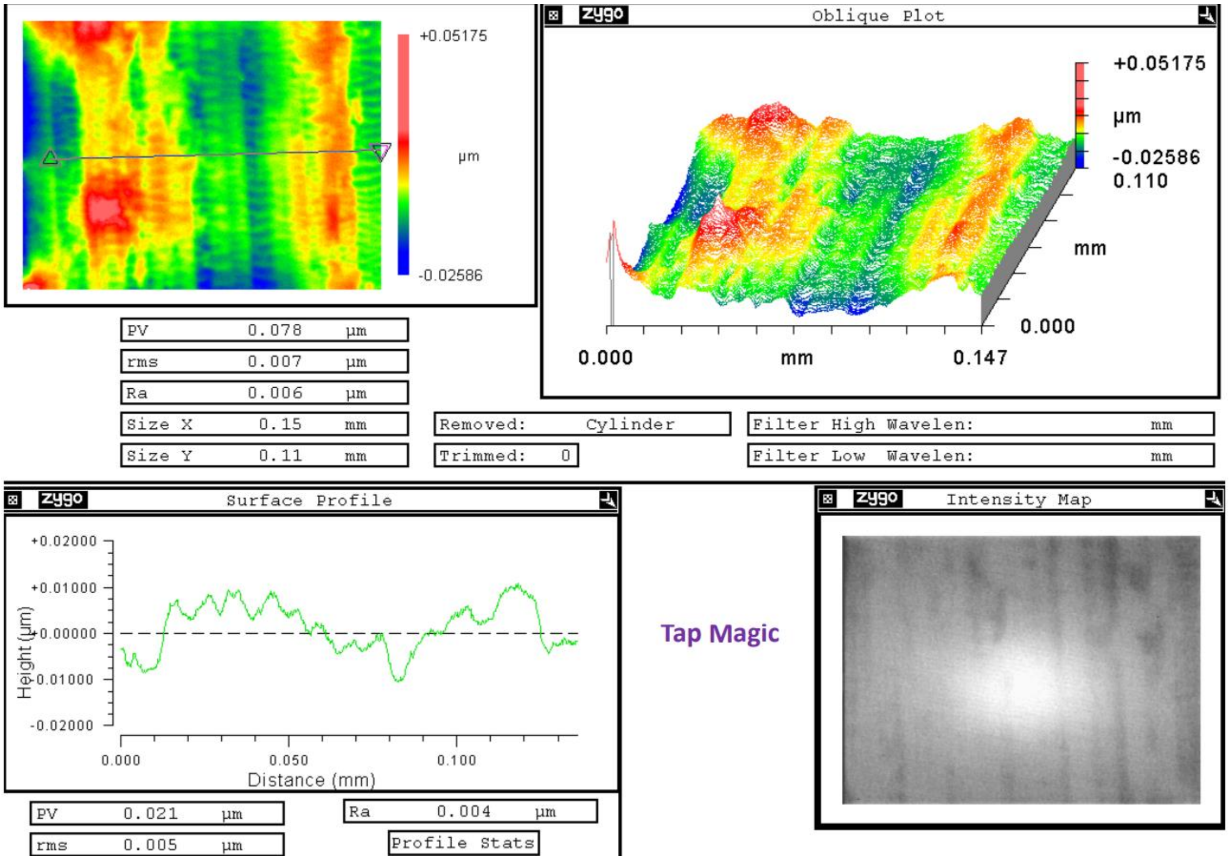

PV 0.078 µm
rms 0.007 µm
Ra 0.006 µm
Size X 0.15 mm
Size Y 0.11 mm
Removed: Cylinder
Trimmed: 0
Filter High Wavelen: mm
Filter Low Wavelen: mm

PV 0.021 µm
rms 0.005 µm
Ra 0.004 µm
Profile Stats

Figure 48. Surface profile of PC after machining with Tap magic aqueous.

Table 10. Kerosene, WD 40 and Tap magic aqueous composition and viscosities at 40^0 F.

	Composition	Kinematic viscosity (CSt)
Kerosene	Petroleum – Alkanes, Naphthenes, Aromatics and Asphaltics Ethyl Benzene Naphthalene	2.71
WD-40	Aliphatic hydrocarbons, Petroleum base oil, LVP aliphatic hydrocarbons, Carbon dioxide, Di-methyl naphthalene, alkane hydrocarbons, Cyclo-hexane	2.79
Tap magic aqueous	Polyethylene glycol phenyl ether phosphate, Triethanolamine, Amine trade secret, Alcohols, C12-15, ethoxylated propoxylated	6.5

2.5.2 TOOL WEAR

Tool wear on a 0.5 mm radius round nose tool with 6.5 µm/rev feed rate was too small to measure after machining PMMA for 8 km of cutting distance. Figure 49 (a) shows the tool after 8 km of cutting on PMMA. Polycarbonate was also machined under similar cutting conditions for 3 km. This tool is shown in Figure 49 (b). Figure 50 shows that the diamond tool after cutting PC was worn quicker than the tool used on PMMA.

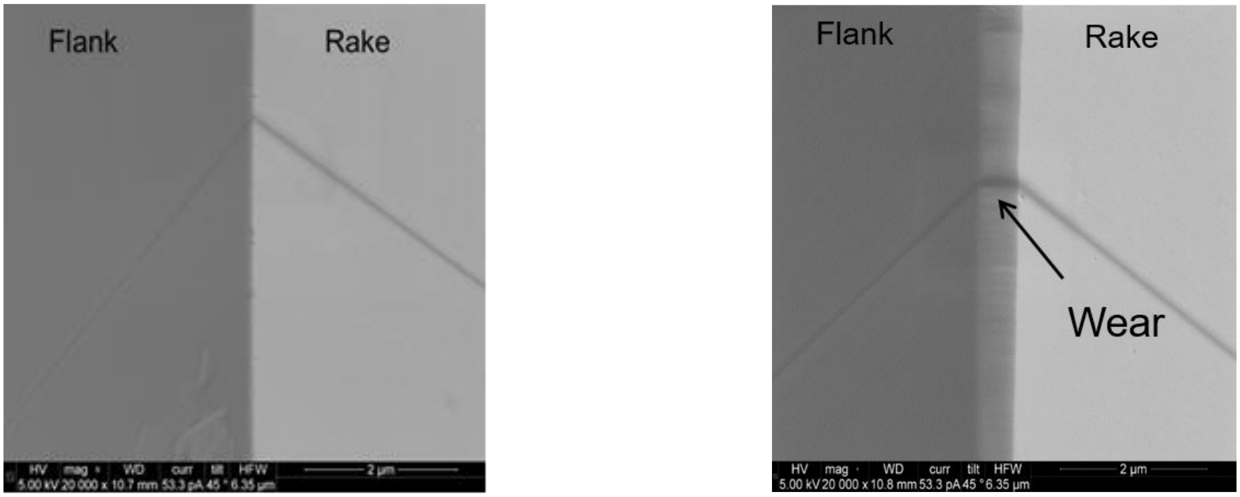

(a) PMMA, 8 Km (20000X mag)

(b) PC, 3 Km (20000X mag)

Figure 49. Tool after cutting (a) PMMA and (b) PC

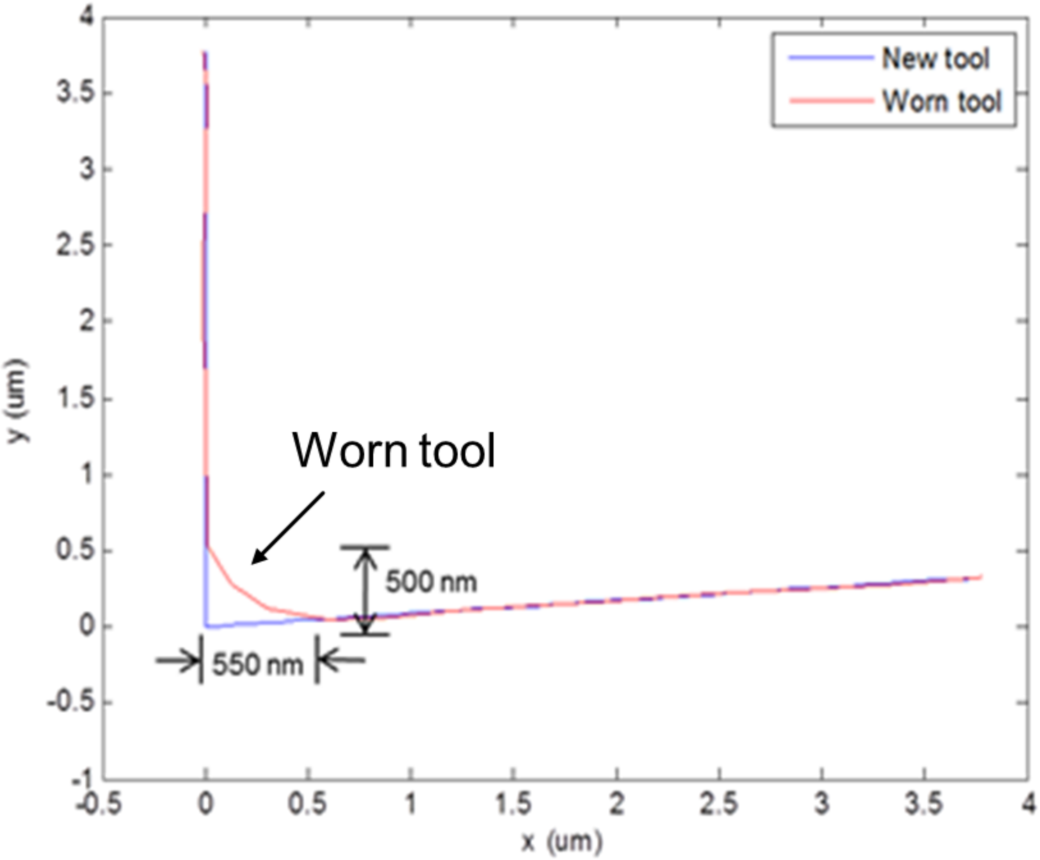

Figure 50. Tool after cutting PC for 3 km

PC was machined using a round nose tool for 66 km at a 5 µm depth of cut with a 0.5 mm radius tool, it was observed that the amount of wear on the edge changed across the width of the cutting edge as shown in Locations E, F and G in Figure 51 (b). This can be attributed to change in chip thickness during cutting for a round nose overlapping feed cut.

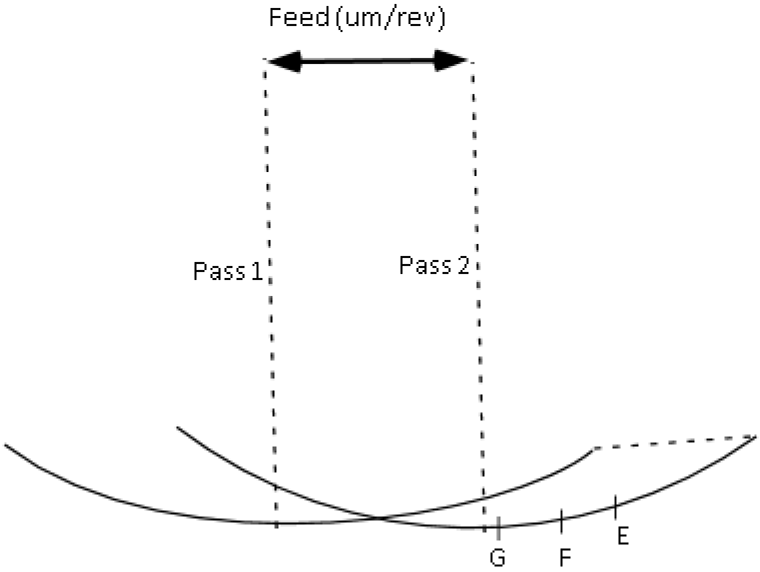

(a) Schematic of chip geometry of cut.

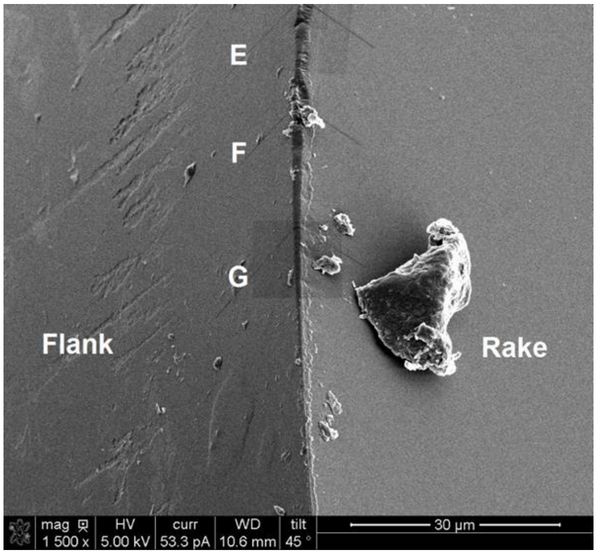

(b) SEM image of diamond tool

Figure 51. Tool after cutting PC for 66 km.

To understand tool wear, plunging experiments were performed. A 3.5 mm wide square diamond tool was plunged into the outer diameter of a (1/16)” thick plastic disk. This series of experiments give an idea of tool wear as uncut chip thickness is constant across the entire width of the chip. The experimental setup is discussed in Section 1.3.

PC disks were cut from outside diameter at different depths of cut – 2 µm/rev, 3 µm/rev, 5 µm/rev and 10 µm/rev to study tool wear with a constant 4m/s cutting speed. The images of tools were shown in Figure 52. Different diamond tools in Figure 52 machined PC at different in-feed rates for 4 km. An AC ionizer and a vacuum were used to manage chips during cutting. In Figure 52 (a), a layer of unknown material was observed on the rake face of tool. Solvents such as chloroform, methylene chloride, acetone and Keller’s reagent (mixture of nitric acid, hydrofluoric and hydrochloric acid) were not able to remove the material from rake face of the tool. In Figure 52 (b), an area of material was eroded from the clearance face of the tool, while the tool edge remained sharp.

In Figure 52 (c), Lichtenberg Figures were observed on the rake face of the tool due to electric discharge through air. In Figure 52 (d), 10 µm/rev feed rate created holes through the diamond. Every hole on rake face of tool had a corresponding hole on clearance face of the diamond. There were also holes on the clearance face without a matching hole on the rake face. This suggested that the holes started on the clearance face of the diamond. Since both PC and diamond are electrical insulators, growing static electric field could develop in the cutting zone. This could be linked with some electric field strength. The AC ionizer generates both positive and negative charges. The ionized air was directed on to the clearance face of the diamond. The ions acquire energy from the static electric field developed in the cutting zone. If the energy acquired by the ion is greater than 7.4 eV (which is bond dissociation energy of the carbon-carbon bond in the diamond [3]) then the ions are expected to drill through the diamond to reach the oppositely charged ions on the rake/chip interface.

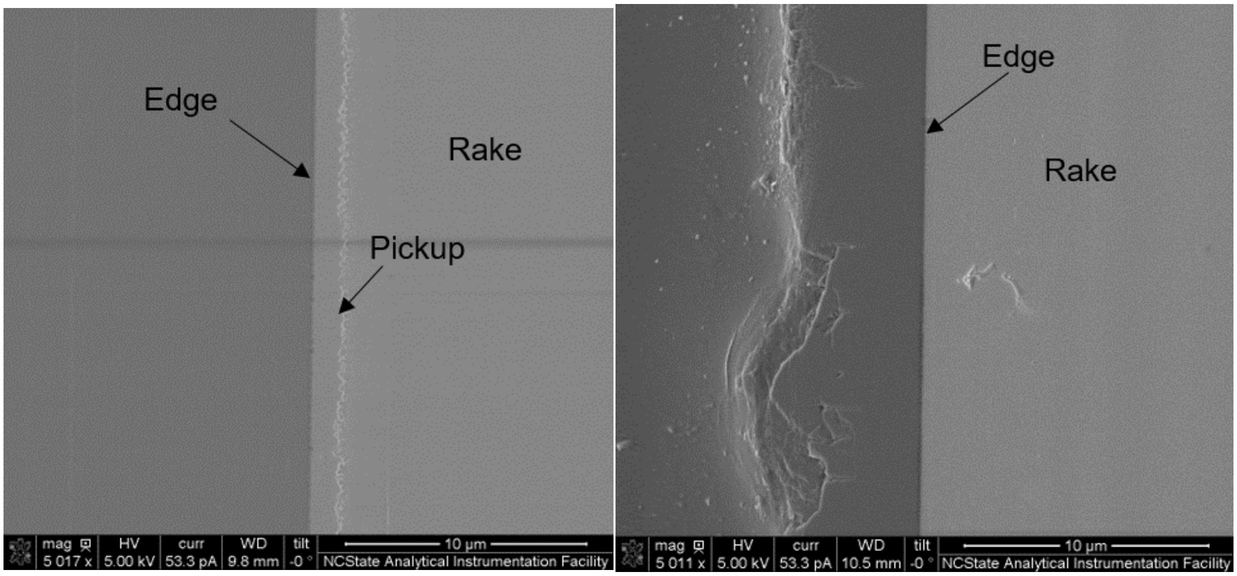

(a) 2 µm/rev (b) 3 µm/rev

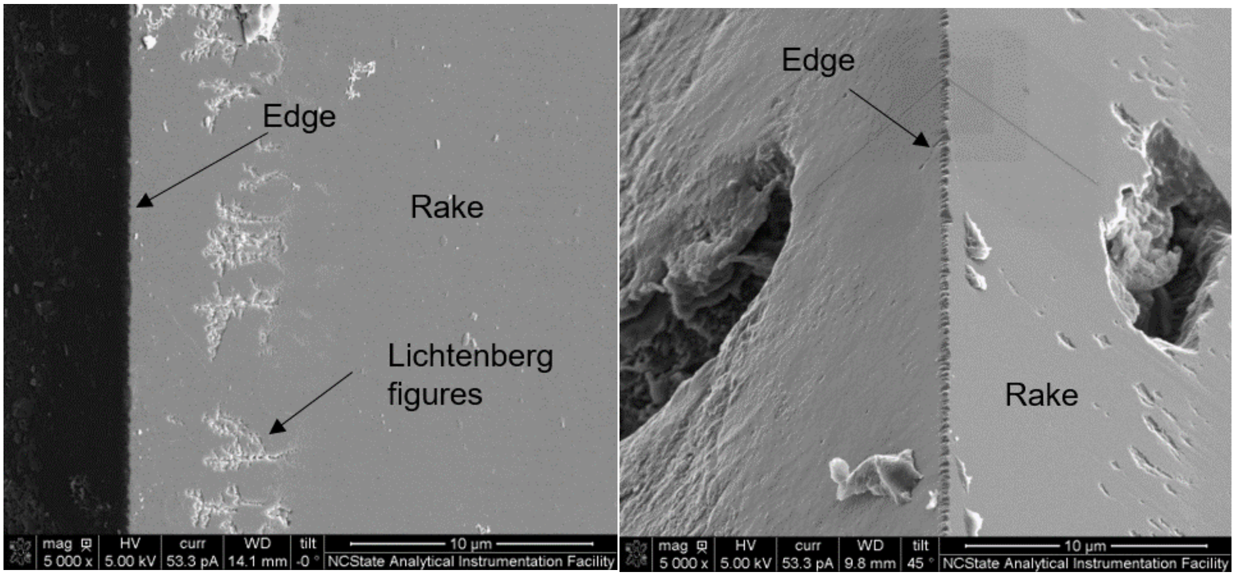

(c) 5 µm/rev (d) 10 µm/rev (rotated 45^0 for the best possible view)

Figure 52. Diamond tools after cutting PC for 4 km at various in-feed rates.

Figure 53 shows one of the possible static charge configurations developed on the machined surface and chip side. Increase in static electric effects with depth of cut when machining polymers was identified by Gubbels [3].

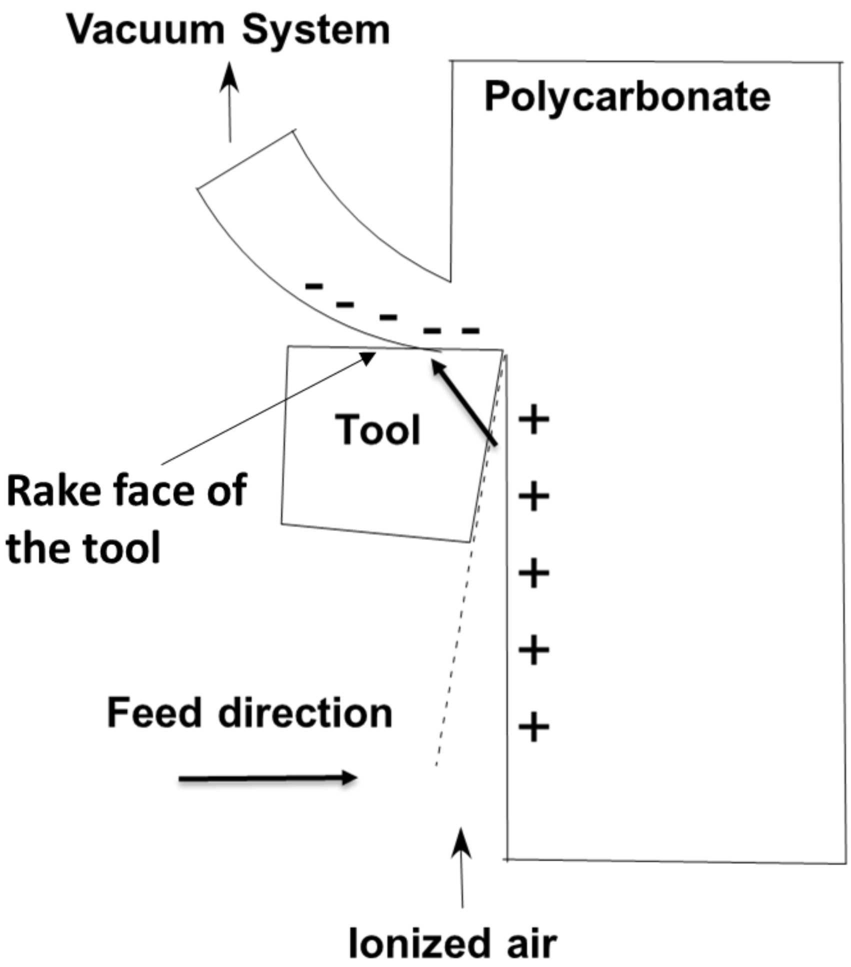

Figure 53. Schematic showing possible charge configuration during cutting [9].

To reduce the number of ions in the cutting zone, the ionizer was turned off and another plunge cutting experiment at 3 µm/rev on PC was conducted. Less tool damage was observed when the ionizer was switched off. Figure 54 shows images of tool– with and without ionizer.

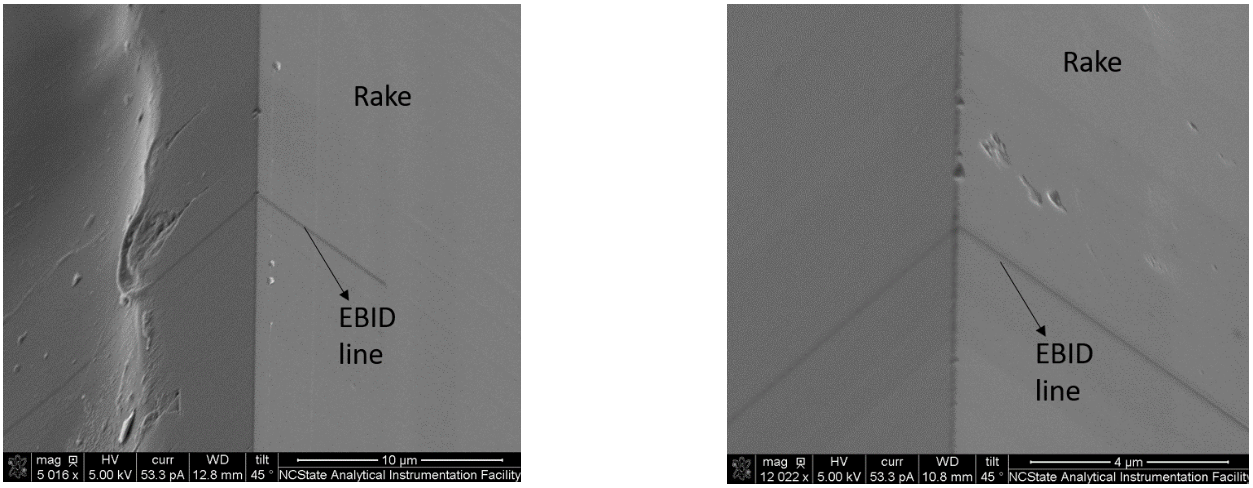

(a) with ionizer (6000X) (b) without ionizer (12000X)

Figure 54. Tools after machining PC for 2 km.

To test the effect of cutting speed on diamond tool wear after cutting polycarbonate, a series of plunge cutting experiments were performed at two different cutting speeds (– 4 m/s and 10 m/s) keeping all other cutting parameters constant. Figure 55 (a) shows the tool after cutting PC for 2 km at 4 m/s and Figure 55 (b) shows the tool after cutting PC for 2 km at 10 m/s. Figure 55 (b) shows that a small portion of the edge is lost due to cutting and a Lichtenberg figure can be seen on the rake face. This shows that the magnitude of triboelectric tool wear is larger at higher cutting speeds.

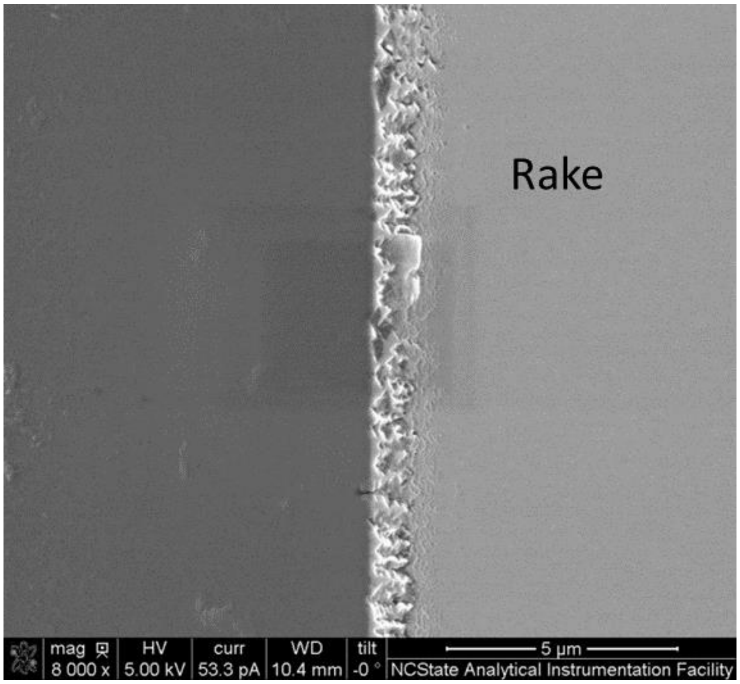

(a) 4 m/s

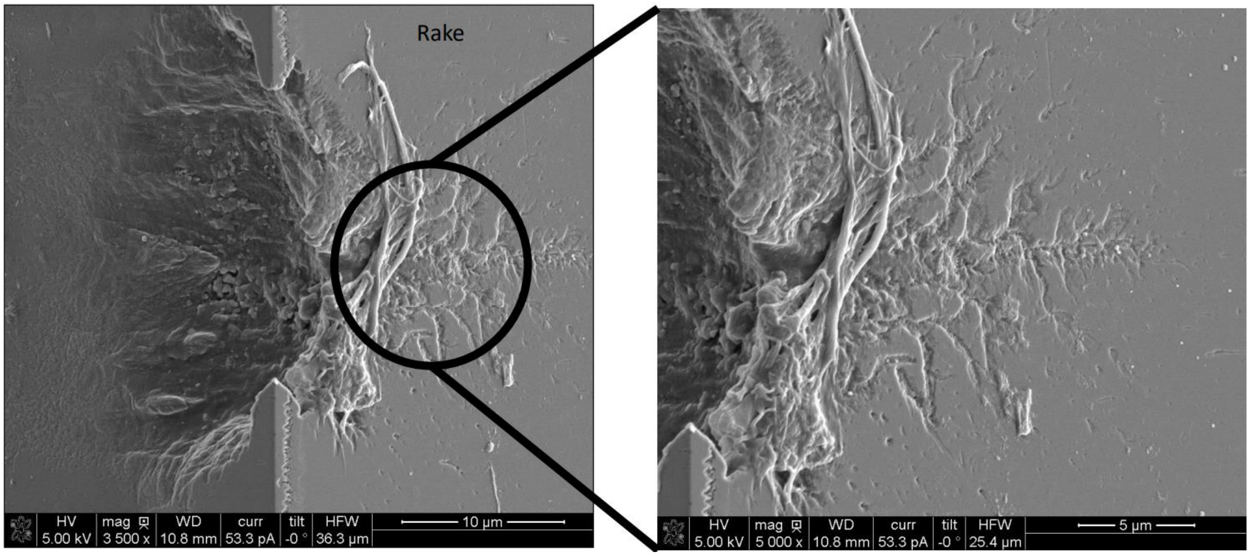

(b) 10 m/s

Figure 55. Diamond tool wear after cutting PC for 2 km at different cutting speeds

To study the effect of coolants on the wear in tools machining PC, WD-40 was used to machine PC. Although all isoparaffinic oils are insulators, their conductivity increases with temperature and pressure. Plunge cutting experiments were performed on PC disks at 1 µm/rev in-feed rate and

800 RPM. The total cutting distance in each experiment is 2 km. Figure 56 shows the effect of WD-40 on tool wear in PC. Figure 56 (b) shows the tool after machining PC without WD-40.

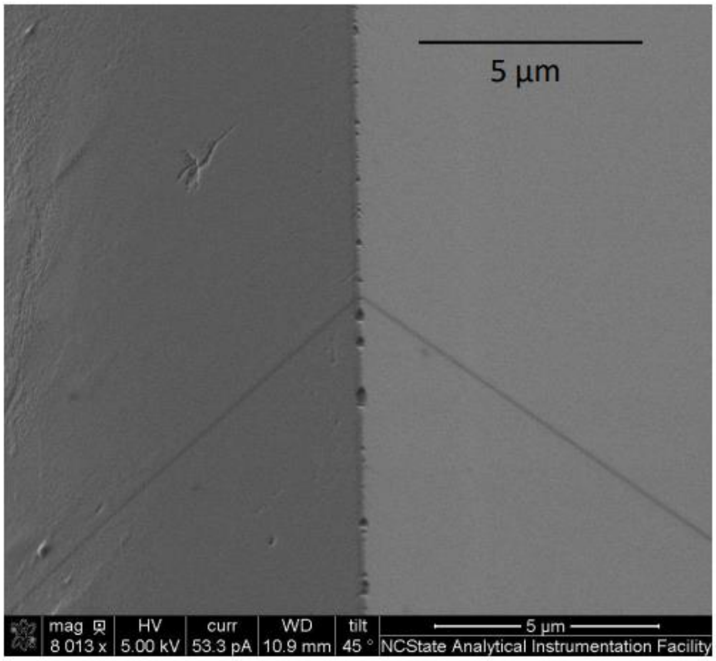

(a) With WD-40.

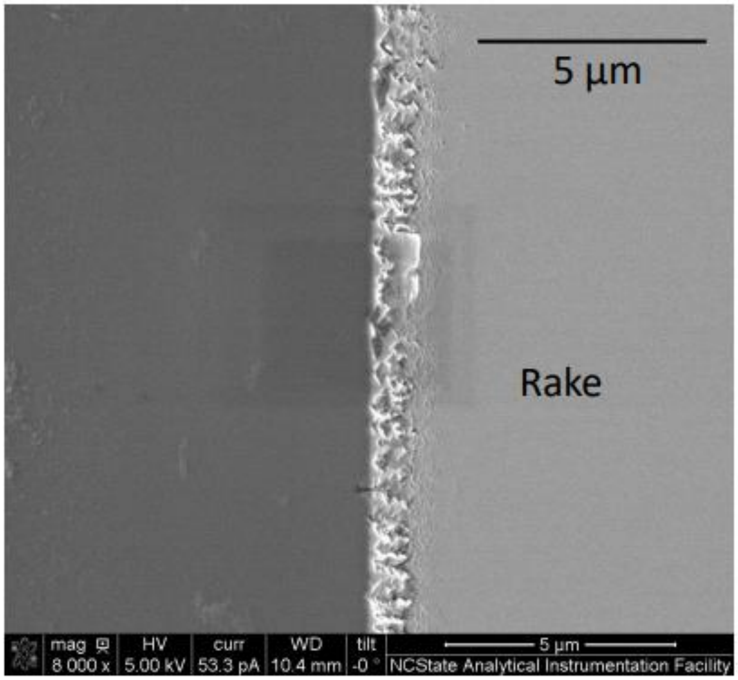

(b) Without WD-40

Figure 56. Tool wear on PC after 2 km of cutting at 4 m/s cutting speed.

The next coolant to be studied was Tap Magic Aqueous on PC, a plunge experiment was performed at 1 µm/rev in-feed rate and 4 m/s cutting speed. The diamond tool after cutting is shown in Figure 57 (a). Figure 57 (b) shows image of the tool after dry cutting under similar cutting conditions. Because Tap magic aqueous is conductive, it should help to remove triboelectric charge generated during the cutting process.

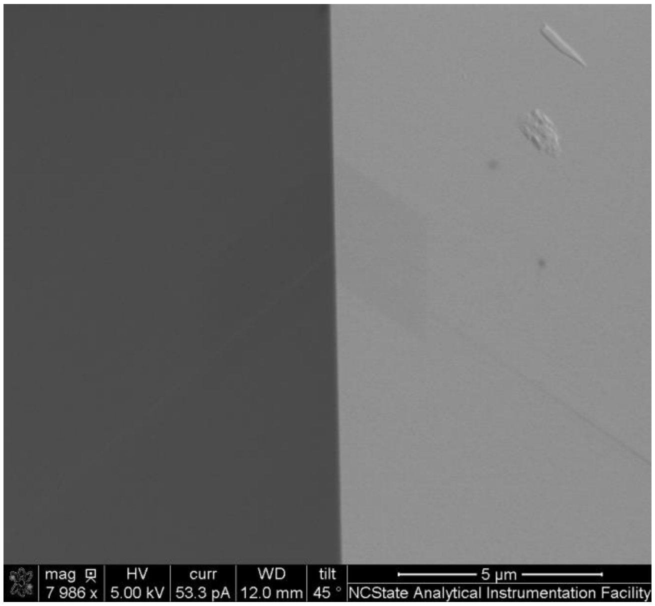

(a) Tap magic (rotated 45^0 for better view)

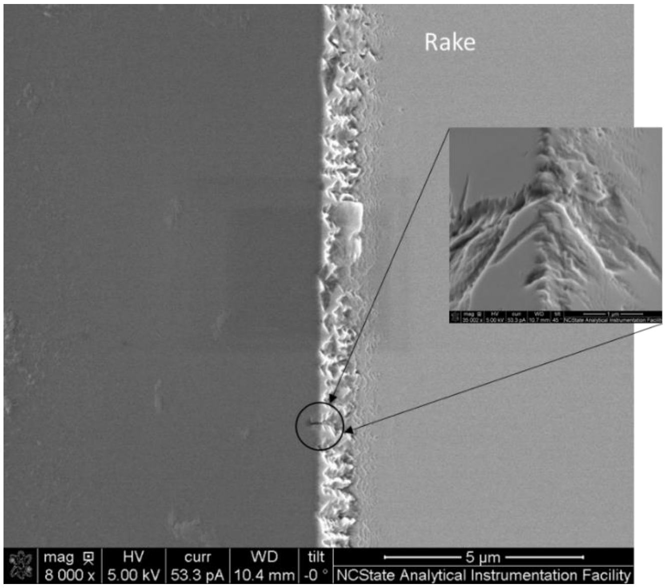

(b) Dry

Figure 57. Diamond tool wear after cutting PC for 2 km

2.6 CONCLUSIONS

2.6.1 PMMA

For the experimental conditions studied, a smaller nose radius tools generated better surface finish when machining PMMA. Very low cross feeds did not generate theoretical surface finish because motion of the tool at the fine crossfeed was dominated by machine tool vibration [8]. No effect of static chips on surface finish was found. Slightly negative rake angle tools generated best RMS surface finish. No effects of cutting speed and depth of cut were found. PMMA wears diamond tools less than PC. From the experimental conditions and results, the best conditions to machine PMMA with the ASG 2500 are given in Table 11.

Table 11. Best conditions to machine PMMA

.

Tool Radius (mm)	0.1
Feed rate (µm/rev)	2-3
Depth of cut (µm)	5
Rake angle (degrees)	-5
Cutting Speed (m/s)	1 - 5
Type of machining	Dry
Best RMS surface finish achieved (nm)	3

2.6.2 PC

For the experimental conditions used, chip management was found to be crucial for obtaining good surface finish when machining polycarbonate. PC build up on the tool due to statically charged chips will lead to poor surface finish. Larger depths of cut and feeds would help manage chips from the cutting zone, thus generating better surface finish. No effect of cutting speed was found. Lower chip thickness was found to be better to avoid tool damage. Tool wear on round nose diamond tools varied with chip thickness. The ionizer should not be used with PC because it increased the potential for triboelectric damage to the tool. However, ionizer could be used to assist the initial entrainment of the chip into the vacuum and can be turned off to get good surface finish while minimizing tool wear with PC. Kerosene, WD 40 and Tap magic aqueous were identified to generate optical range surface finish on PC and helps in minimizing electric effects on the tool. From the experimental conditions and results, the best conditions to machine PC with the ASG 2500 are given in Table 12.

Table 12. Best conditions to machine PC.

Tool Radius (mm)	0.1
Feed rate (µm/rev)	0.5
Depth of cut (µm)	< 5
Rake angle (degrees)	5
Cutting Speed (m/s)	1 - 5
Type of machining	Coolant - Tap magic aqueous
Best RMS surface finish achieved (nm)	5-7

2.7 FUTURE WORK

Chip entrainment and chip geometry were identified to be critical to achieve good surface finish on PC. Aerodynamic simulation of the setup may give other possible explorations of factors like drag coefficient, chip integration and dynamics of chip flapping. This would be useful to develop a model that could help in development of more sophisticated chip management setup.

High frequency in cutting and thrust force data was found to indicate balling up of chips and build up on the tool which resulted in poor surface finish on PC. A highly sensitive load cell (noise threshold < 0.01 N) can be used to dynamically measure surface finish and predict when poor surface finish will be generated.

Electrical conductivity and viscosity of the cutting fluid was found to effect surface finish generated on PC. Detailed chemical analysis on Tap magic aqueous and WD-40 would help to identify other factors that influence surface finish generated on PC.

Tool wear tests at lower cross feeds with chip management system resulted in deposition of unknown thin layer on the rake face of the tool near the cutting edge. X-ray diffraction, EDX analysis in an SEM did not result in significant information as the layer was very thin. Elemental analysis on the thin layer would help in prediction of chemical reaction at the cutting edge.

2.8 REFERENCES

1. Gerhard, Christoph. *Optics Manufacturing*. 1st ed. Milton: CRC Press, 2017. Print. Optical Sciences and Applications of Light.
2. Jaluria, Yogesh. *Advanced Materials Processing and Manufacturing*. Cham: Springer, 2018. Print. Mechanical Engineering Series.
3. Gubbels, G. P. H. "*Diamond Turning of Amorphous Polymers.*" Eindhoven University, 2006. Print.
4. Kobayashi, Akira. *Machining of Plastics*. New York [u.a.]: McGraw-Hill, 1967. Print.
5. Smith, Elizabeth. "*Single Point Diamond Turning of Amorphous Thermoplastic Polymers*." North Carolina State University, 1989. Print.
6. Carr, Jeffrey W., and Claudius Feger. "*Ultraprecision Machining of Polymers.*" *Precision Engineering* 15.4 (1993): 221-37. *CrossRef.* Web.
7. Suit, Brandon. "*Analysis of Accelerated Tool Wear and Built Up Edge when Diamond Turning Ferrous Materials.* ." North Carolina State University, 2016. Print
8. Sohn, Alex. Diamond Turning of Polymers. Ed. Bodlapati Charan., 2017. Print.
9. Shi, Meirong. "*Thermo-Chemical Tool Wear in Orthogonal Diamond Cutting Steel and Stainless Steel.*" North Carolina State University, Print.
10. Boothroyd, G. 1932. Fundamentals of Metal Machining and Machine Tools. United States:, 1975. Web.
11. Lamonds, Lucas. "*Surface Finish and Form Fidelity in Diamond Turning.*" North Carolina State University, 2008. Print.
12. Andeavor. "Kerosene - safety data sheet." Web. <http://www.andeavor.com/media/1094/kerosene.pdf>.
13. WD-40 Company. "WD-40 - Safety data sheet." Web. <https://www.wd40company.com/files/pdf/sds/mup/wd-40-multi-use-product-aerosol-sds-us-ghs-7-20-14.pdf>.
14. Wired Staff. "WHAT'S INSIDE WD-40." Apr 20, 2009. Web. <https://www.wired.com/2009/04/st-whatsinside-6/>.
15. Tapmagic. "Tapmagic Aqueous - Safety data sheet." Web. <http://www.tapmagic.com/assets/uploads/2016/02/20160217161143-tap-magic-formula-1-aqueous-sdspdf.pdf>.

3 FOCUSED ION BEAM MILLING OF MICROSCALE FEATURES

Anthony Wong
Research Associate

This research investigates the fabrication of microscale features in glassy carbon that will be used as a die to stamp features into a mold for injection molding of plastic lenses. The concept is to FIB mill a die with multiple features (4-9) and then stamp those features at a high repetition rate (>100/second) to create a mold for a large lens array. The features are nominally spherical with radii on the order of 15.8 µm that would, with the parameters given above, create a mold with 3x10^{6} *lenses in an hour.*

The FIB characteristics such as material removal rate, angle of incidence sensitivity, and beam shape were measured. It was estimated that a single lens feature could be milled in a matter of minutes. A simulation tool was developed to assist in planning the FIB milling process. Glassy carbon dies with 4 and 9 features were FIB milled. The FIB process parameters were investigated to improve the form of the die. 1100 Aluminum was indented with the glassy carbon die and arrays of indents were successfully fabricated.

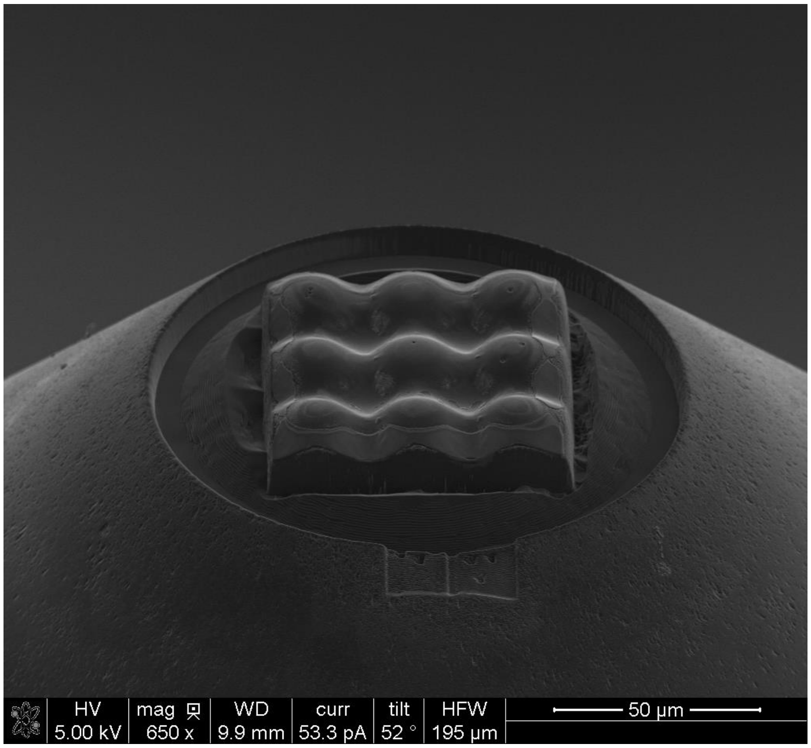

3.1 INTRODUCTION

As modern electronics have continued to shrink in size, the need for smaller and smaller optics has increased. For instance, a typical smartphone display can have pixels tens of micrometers in size. Some digital camera sensors now have pixels with single digit micrometer dimensions. Matching microscale optics are needed for each pixel to collimate light from a display or focus light onto a sensor. For a display, such optics would produce higher output intensity, while lowering the power consumption.

Figure 1 shows what the cross section of an array might look like, as well as a ray trace through a single lens for collimated light a lower index medium to a point behind the lens. In this day and age of portable, high-volume electronic devices, low-cost and light-weight microscale lens arrays need to be developed for applications such as this.

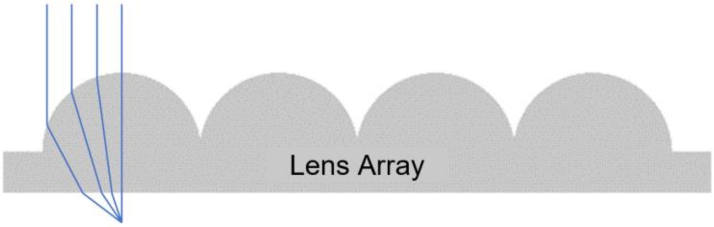

Figure 1. An array of lenses to enhance the brightness of a pixel array

To make an array of over a million lenses as required for these applications, a technique to increase the replication rate must be developed. The multi-step process under development is as follows:

1. Make a male die with 4-9 lens features using a hard material that can be used as an indenter which would look similar to that in Figure 2. This could be made using a focused ion beam, or a FIB. This task will be the focus of this section.

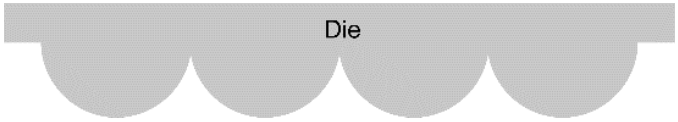

Figure 2. Die with lens features

2. Place this die on an actuator that can rapidly push the die into a workpiece to plastically deform the surface and replicate the features. This replication process will create a mold with millions of copies of the lens feature. The die shape may need to deviate from the lens shape in Figure 1 to control the plastic flow of the displaced material. The design of the actuator will be another significant part of this project but has not been started at this time as the focus of the project has been on a slow speed proof of principle.

3. The final step will be to use the mold from step 2 in a conventional plastic manufacturing process such as compression or injection molding to create the lens array that will look like

3.2 BACKGROUND

This concept is similar to a previous project at NC State in which nanoscale features were replicated through an indenting process [1, 2]. The mold will be used with a conventional plastic manufacturing process, such as compression molding or injection molding, to make a microlens array with millions of convex features. This work focuses on the first step of making the indenting die with convex features.

In the previous work at NC State, nanoscale features were milled into an indenting die with a focused ion beam (FIB). A FIB is able to precisely accelerate gallium ions at a target with spot sizes as small as tens of nanometers in diameter. When the gallium ions impact the target, atoms from the target will sputter off leaving a new shape. The FIB milling process is controlled by only a handful of parameters. First, the beam current determines the shape of the ion intensity distribution. The beam current does not change after the milling process begins, as it is related to the optics in the FIB. The focus and stigmation would need to be adjusted for a new beam current setting. The maximum dwell time, map of relative dwell times and number of passes are the parameters used to setup the equivalent of a toolpath in conventional milling. The maximum dwell time is the longest amount of time an area would be exposed to the ion beam. The longer the dwell time, the more material will be sputtered. A map of locations and relative dwell times for each (x, y) coordinate tells the machine where to turn the beam on and approximately what percentage of the maximum dwell time to expose that area. The number of passes is the number of times the “toolpath” will be repeated.

In practice the map of relative dwell times is described by a bitmap image. A bitmap consists of three 24-bit values for each pixel. Each pixel represents an (x,y) location in the viewing window of the FIB. Each value can range from 0-255 and represents a color – red, green, and blue. In the FIB control software, the red value is not used. The green value determines if the beam is on. 0 values turn the beam off. Non zero values turn the beam on. The blue value determines the dwell time for the pixel. Zero corresponds to .1 µs dwell time. 255 corresponds to the user specified maximum dwell time. Values in between 0 and 255 are linearly interpolated and rounded to a fixed table of allowable dwell times. The dwell time table consists of 124 approximately logarithmically spaced values ranging from .1 µs to 4624.8 µs.

Many researchers have examined the fabrication of concave molds with a focused ion beam. Yoshida et al. [3] made a press mold out of glassy carbon for an array of 20 µm diameter lenses by machining the form with a Nd-YAG, 300 mW laser, followed by FIB milling to improve the surface finish and to remove debris from the laser machining process. Langridge et al. explored fabricating 1 to 10 µm diameter parabolic concave features in silicon with the FIB for molding glass [4]. Youn et al. used a FIB to mill glassy carbon molds for microfluidic devices [5].

In addition to optical mold fabrication, there is a significant body of research on milling arbitrary 3D shapes with the FIB. In particular, Adams et al. describe a method of combining the beam intensity distribution with the sputtering yield to predict the material removal and final shape [6].

In this paper, FIB milling of glassy carbon is investigated for the purpose of producing an indenting die. Glassy carbon has high hardness and compressive strength, which are needed for the die which will be plastically deforming the mold. It also is amorphous, which means it will FIB mill more uniformly than a material with grain structure. Finally, it has a relatively high material removal rate, about 5 times that of diamond.

3.2.1 Geometry of the Lens Array

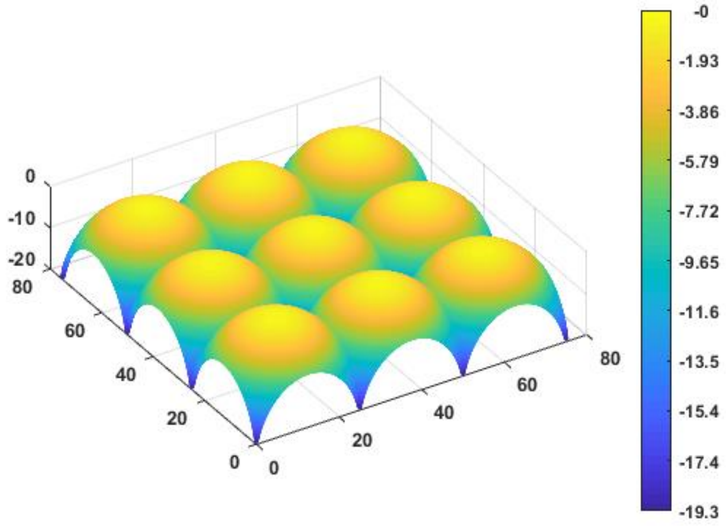

Figure 3. 3x3 array of elliptical lenses

The target geometry for the lenses is a f/1 lens shape on a square grid pattern with a 25 µm pitch. This yielded a prolate ellipsoid (k=-0.44) with a 13.5 µm radius of curvature and focal length of 40 µm for PMMA. Figure 3 shows what a closed packed 3x3 array would look like. In Figure 4 a single lens is shown (left) along with diagonal and side-to-side cross-sections of the lens surface.

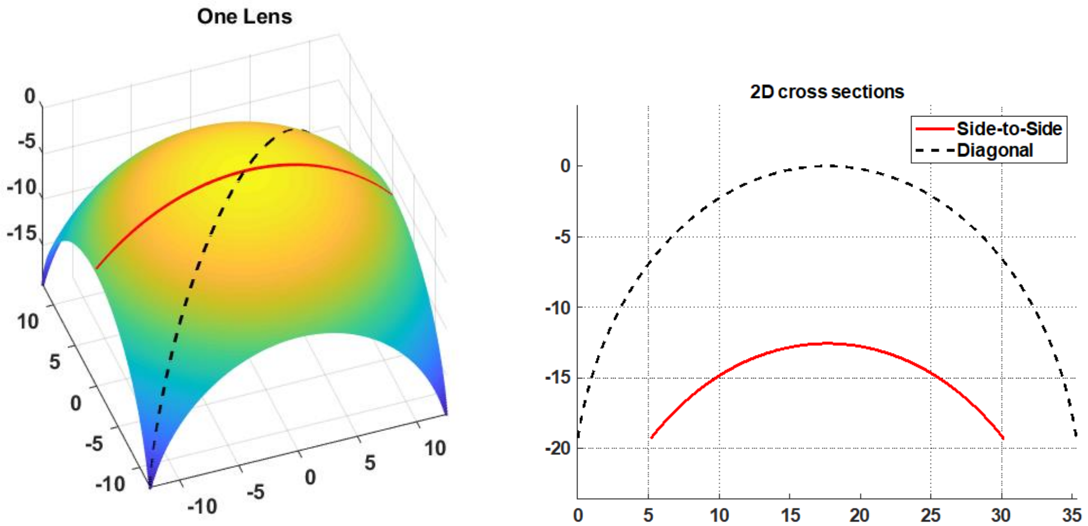

Figure 4. A single close-packed ellipsoidal lens (left) and 2D cross-sections (right).

A Matlab program for designing aspheric Fresnel lenses was adapted for ray tracing a single lens and used to confirm that each lens focuses collimated light to a point 40 µm to the right of its apex. This is shown in Figure 5 for the two cross-sections in Figure 4. For the ray traces the medium of the collimated light is air (N=1.0002926) and the lens is PMMA (N=1.4906). The code allows for a back surface to also be present with an index change at the interface. As shown the medium behind the lens is also PPMA. If this medium was air the best focus would be closer to the lens apex (~33.9) due to refraction at the high-to-low index interface. The ray trace code is general in that each surface is represented as a closely-spaced sequence of data points and normal vectors are calculated using balanced finite differencing. This allows it to be used for evaluating the potential performance of a fabricated lens given metrology data for its surfaces. The code can also be easily extended to trace multiple refractive or reflective surfaces.

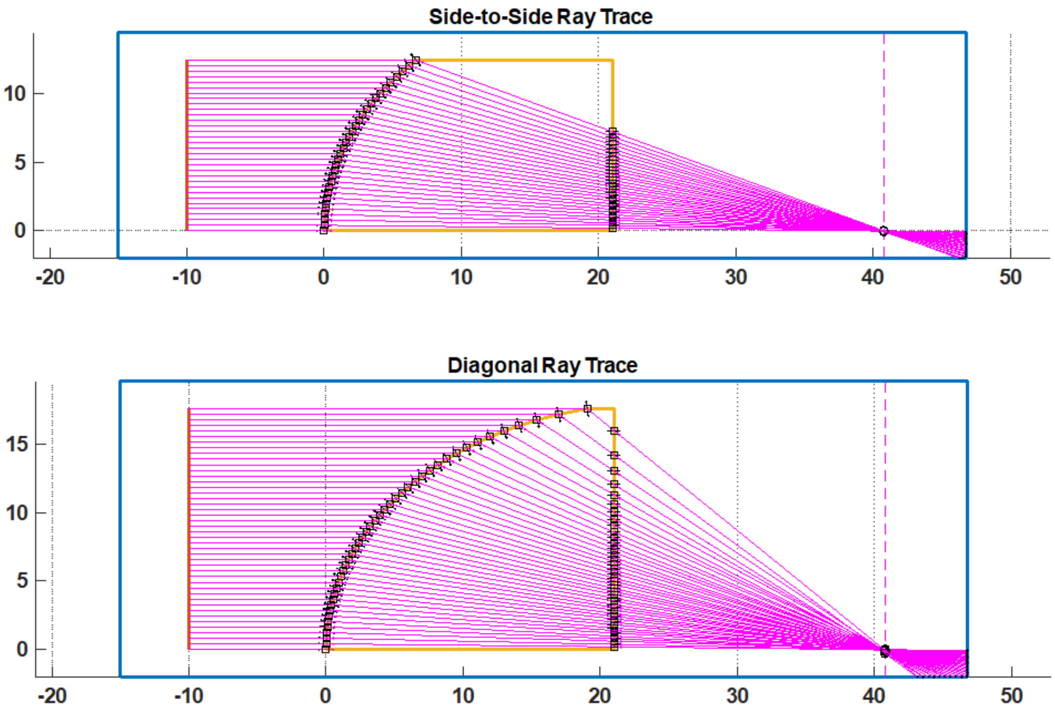

Figure 5. Side-to-side (top) and diagonal (bottom) ray tracing through the lens.

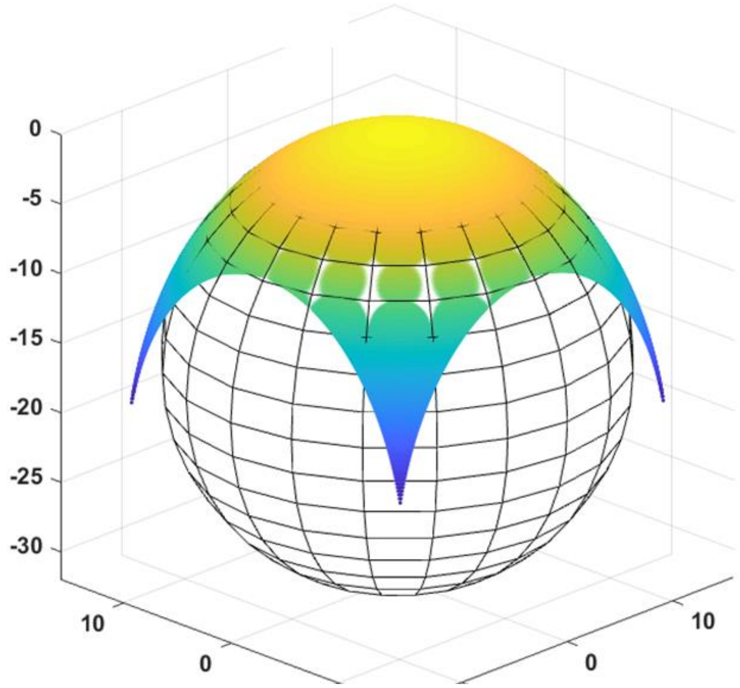

Figure 6. Best fit spherical shape to the lens. Radius of curvature is 15.84 µm

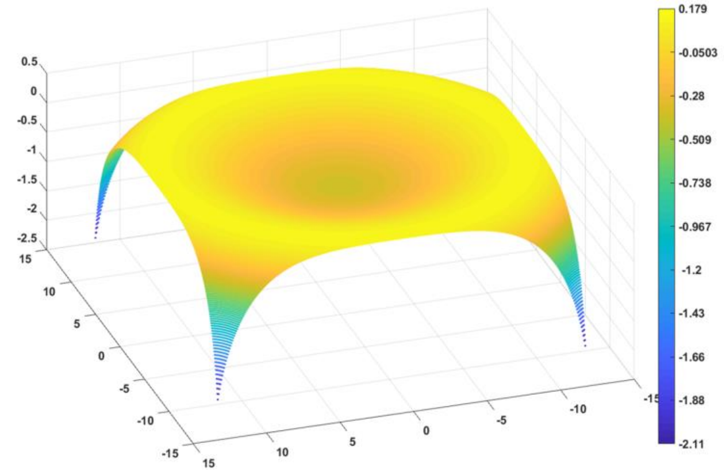

Figure 7. Residual of the sphere fit

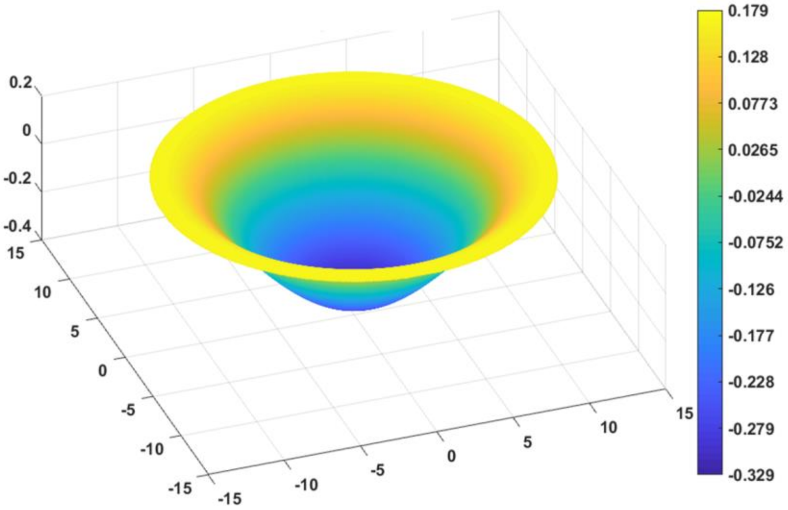

Figure 8. Residual trimmed to a Ø25 µm aperture

The least-squares best fit sphere to the elliptical lens surface has a radius of curvature of 15.84 µm. Figure 6 shows the elliptical lens shape and the best fit sphere in wireframe. Figure 7 and Figure 8 show the residual of the best fit sphere over a 25 µm square and circular aperture, respectively. For simplicity, this project will target spherical lens shape with a radius of curvature of 15.84 µm.

3.3 FIB BEAM CHARACTERISTICS

The FIB is able to remove material with high accuracy. One of the first steps in exploring FIB milling was to characterize the ion beam.

3.3.1 FIB Experimental Setup

For the FIB experiments, a FEI Quanta 3D FEG was used at the NC State Analytical Instrumentation Facility (AIF). The Quanta has an electron beam in addition to an ion beam to aid in imaging. A 25 mm X 25 mm X 3 mm SPI Glas 11 grade glassy carbon plate from SPI Supplies (Part Number 4375GCP-AB) was used as the sample material for the experiments. Table 1 shows the properties of this grade of glassy carbon. Glassy carbon was chosen because it is hard and has higher material removal rates than diamond which was used as a die in the previous nanoscale coining work [1, 2]. Also Yoshida was able to make similarly sized microscale indentions in glassy carbon with a combination of laser machining and FIB milling [3]. The glassy carbon plate was prepared by applying conductive carbon tape that covered the top surface and wrapped around to the bottom and also adhered the sample to a pin mount. Initially the entire top surface and the conductive tape were coated with Au-Pd to prevent any charging effects in the SEM-FIB. Charging occurs when the SEM sample is an insulator. The insulator builds up charge due to the incident electrons and develops its own electric field which distorts the electron beam causing what appears to be drift in the image. The Au-Pd coating creates a conductive layer connected to the grounded pin mount to prevent any charge from building up. Later it was determined that the glassy carbon is conductive and without the Au-Pd coating does not exhibit charging. Sometimes the glassy carbon sample was purposely contaminated with oil to measure features using electron beam induced deposition (EBID). The Electron beam is used to generate a visible line on the workpiece by polymerizing the hydrocarbons. The sample is rotated 45°, and an image is taken. The image is stretched with software by 1/cos(45°), or 141%, which simulates rotated the part an additional 45°. The contamination line then describes the profile of the feature to the correct scale. More about the EBID technique can be found in [7]. An example of a prepared sample is shown in Figure 9.

Table 1. Properties of SPI Glas 11

Property	**Value**
Bulk density	1.54 g/cm^3
Vickers Hardness	340
Compressive strength	580 GPa
Young’s Modulus	35 GPa
Coefficient of Thermal Expansion	2.5 x 10^{-6} m/m·K

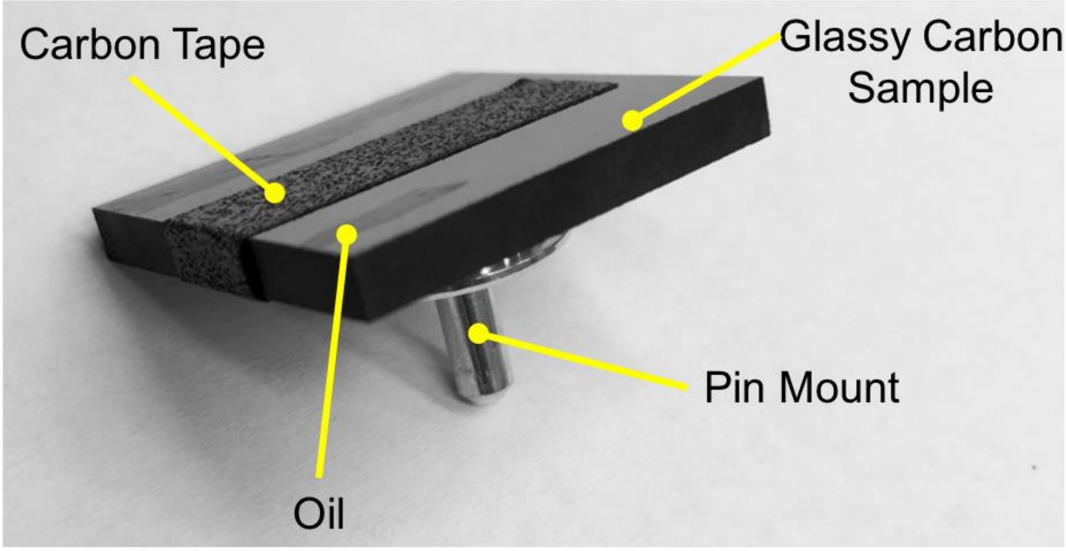

Figure 9. Glassy carbon sample prepared for the FIB

3.3.2 Material Removal Rate

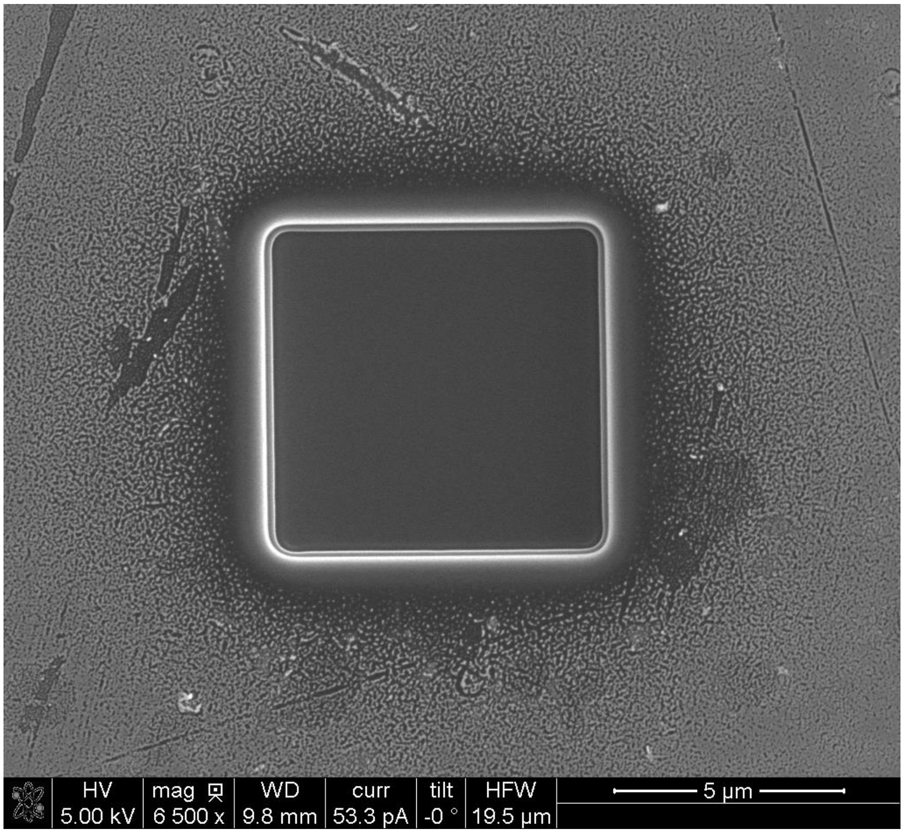

Figure 10. 7x7 µm square FIB milled into glassy carbon with a 15 nA beam.

To determine the material removal rate of the FIB with glassy carbon, a simple experiment was devised. The ion beam of the FIB executed a square milling pattern on the top of the glassy carbon sample. Based on Adams' work [6], it was recommended to keep the depth of the feature less than half the width of the feature to minimize redeposition. This means that as the material sputters, it can land back on the material and redeposit, reducing the effective sputtering rate and shape fidelity. This effect can be significant, particularly for deep narrow features where the sputtered material cannot escape. For this experiment a 7 x 7 µm square pattern was used. The total exposure time was adjusted to achieve the desired ion dose. Figure 10 shows the results of a 15 nA beam. The depressed surface was measured with a Zygo New View 5000, so that the volume of removed material could be calculated This volume was divided by the milling time to yield a material removal rate.

For a 15 nA current, a maximum dwell time of 100 µs was used. Then the number of passes was adjusted to 3962 to set the total milling time 24 seconds to control the dose. The surface was measured and the volume removed was calculated to be 73 µm^3. This yields a material removal rate of 3 µm^3/s. The experiment was repeated for a 65 nA current. The total milling time needed to be reduced to 6 seconds to attempt to keep the dose equivalent. The maximum dwell time was reduced to 1 µs, and the number of passes was adjusted to 4615 passes to get the total time down to 6 seconds. The 65 nA beam removed 165 µm^3 of material and achieved a material removal rate of 27 µm^3/s.

The material removal rate allows the time to mill a single feature to be estimated. The volume that must be removed to achieve the desired shape is estimated to be on the order of 2,500 µm^3. Removal rates of 3 µm^3/s and 27 µm^3/s correspond to machining times for a single feature of 14 minutes and 1.5 minutes respectively. This material removal rate study indicates that the FIB can mill glassy carbon fast enough to make a die with 4-9 features in a reasonable amount of time, as in minutes or hours, as opposed to days.

3.3.3 Angle of Incidence

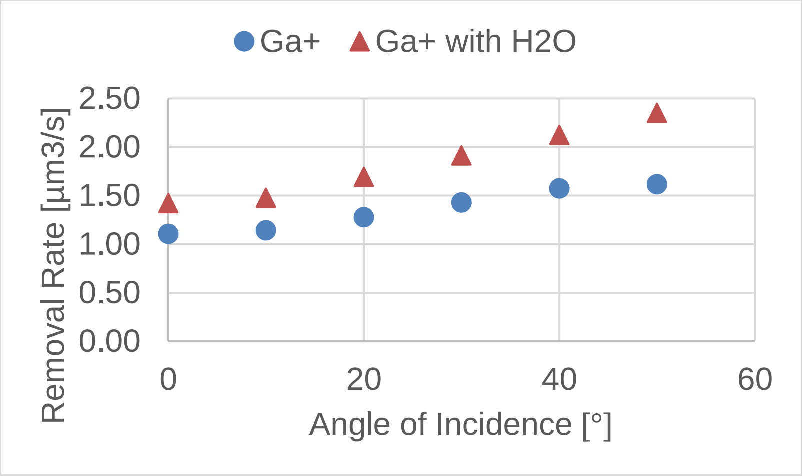

Figure 11. Removal rate dependence on angle of incidence for a 5 nA beam

From literature it is known that the angle of incidence, the angle between the beam and the surface normal, changes the material removal rate [6]. This dependence was investigated for glassy carbon. 10 µm square patterns were FIB milled with a 5 nA beam. The stage was tilted in 10° increments from 0° to 50° and the square pattern was repeated for each angle. This experiment was repeated with a H_2O gas assist as well. The volume of material removed was measured with a laser confocal microscope. This volume was divided by the time required for the FIB milling operation to yield a volumetric removal rate. The results are plotted in Figure 11. Similar to other materials reported in literature the removal rate increases with increasing angle of incidence. Also the removal rate increases by about 30% with the H_2O gas assist.

3.3.4 Beam Shape

The beam intensity distribution is difficult to directly measure. In literature, the beam intensity distribution is often modeled with a Gaussian profile [6]. However, to begin investigating the beam shape the material removed is used as a surrogate for the beam intensity. The assumption here is that the material removed will scale linearly with the ion dose for shallow depths.

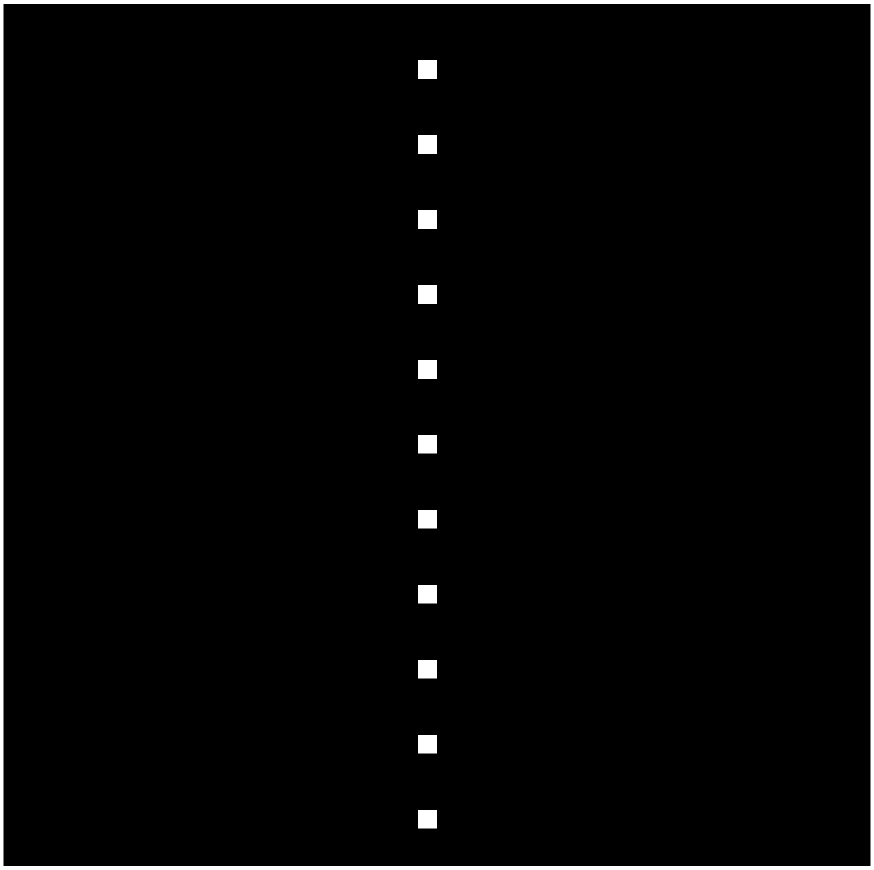

Figure 12. Bitmap for the beam shape experiment

A bitmap was generated with a single line of pixels to mill a thin line the width of the beam. Figure 12 shows the bitmap used to command the FIB. For this bitmap, the pixels are 8 nm. The white pixels are spaced 32 nm apart. The experiment was conducted with a 1 µs maximum dwell time and repeated with 1000, 2000, 3000, 4000 and 5000 passes which increases the depth of the line. The lines were then measured with the EBID technique [7]. Figure 13 shows a representative line measured with this method. This line was milled with a 15 nA beam current and 3000 passes.

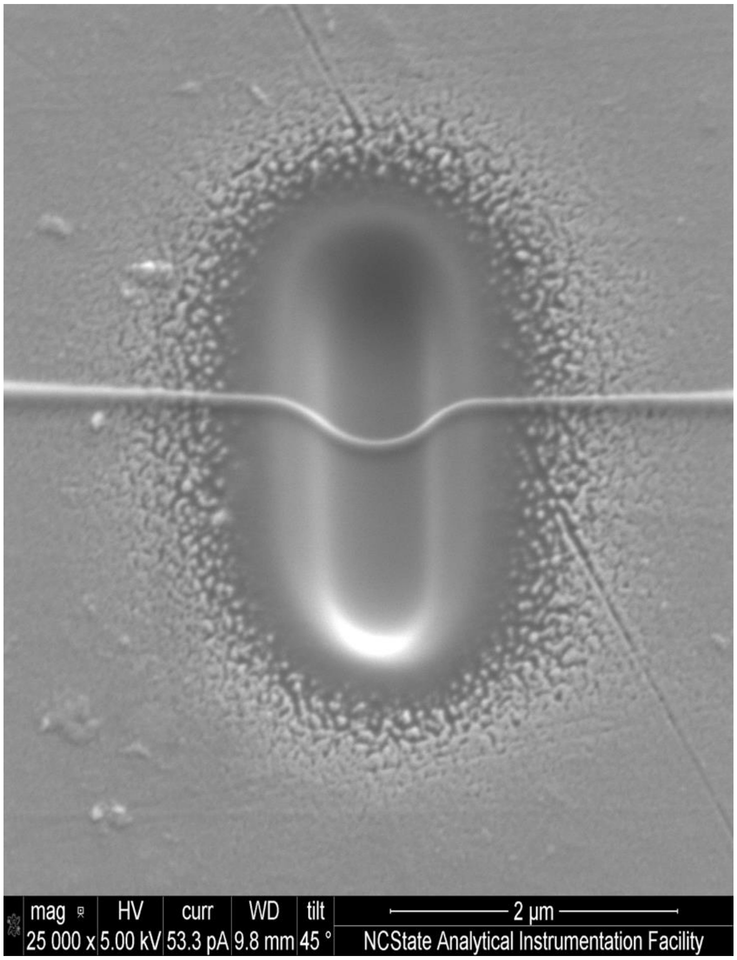

Figure 13. Line FIB milled in glassy carbon with a 15 nA beam. The image has been stretched by 141.42% in preparation for image analysis

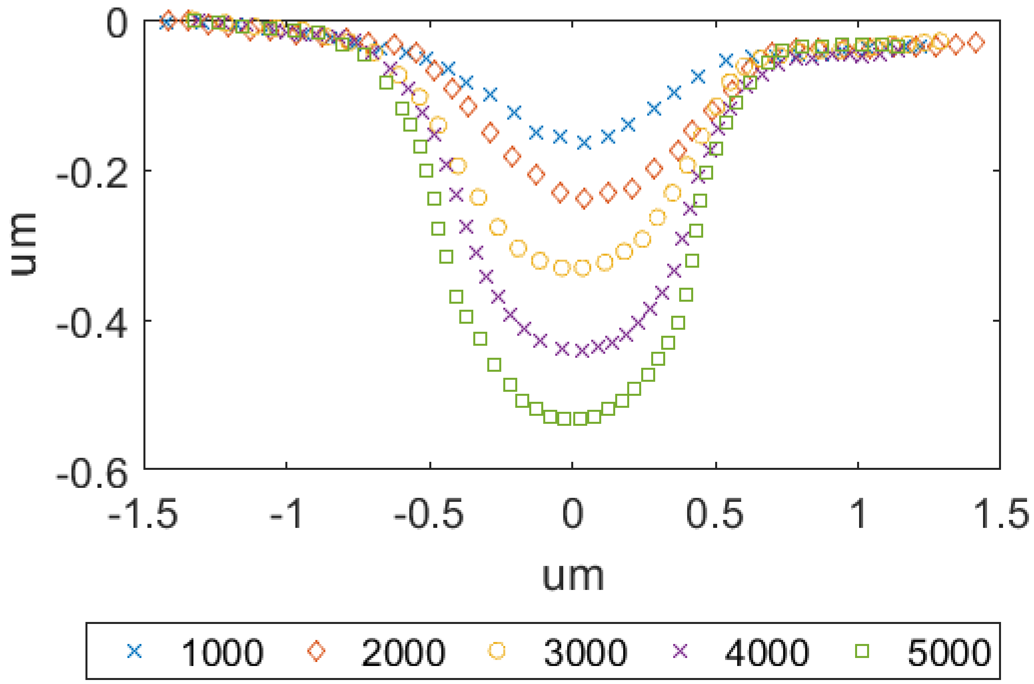

Figure 14. Profiles of lines produced by a 15 nA ion beam after n passes.

Figure 14 shows the resulting data for a 15 nA beam current. As can be seen from the figure, increasing the number of passes increases the depth as expected. However, the width stays roughly the same. The data was fit with a Gaussian equation of the following form:

$$y = a1 \cdot e^{-\left(\frac{x-b1}{c1}\right)^2} \tag{1}$$

In Equation (1) a1, b1, and c1 are constants, where a1 controls the amplitude, b1 the x shift, and c1 the width of the curve. For the purposes of the beam shape model, the constant c1 is the main parameter of interest. A1 should be proportional to the dwell time, and b1 will be related to how well the data is centered in the measurement coordinate system.

Table 2. Summary of the significant Gaussian fit parameter.

Number of passes	c1
1000	.5241
2000	.5003
3000	.4984
4000	.4918
5000	.5094

Table 2 shows the value of c1 for each experiment. The average of c1 across all the experiment is .5048 with a standard deviation of .0125. The low standard deviation indicates that the beam shape is stable and not changing with the depth.

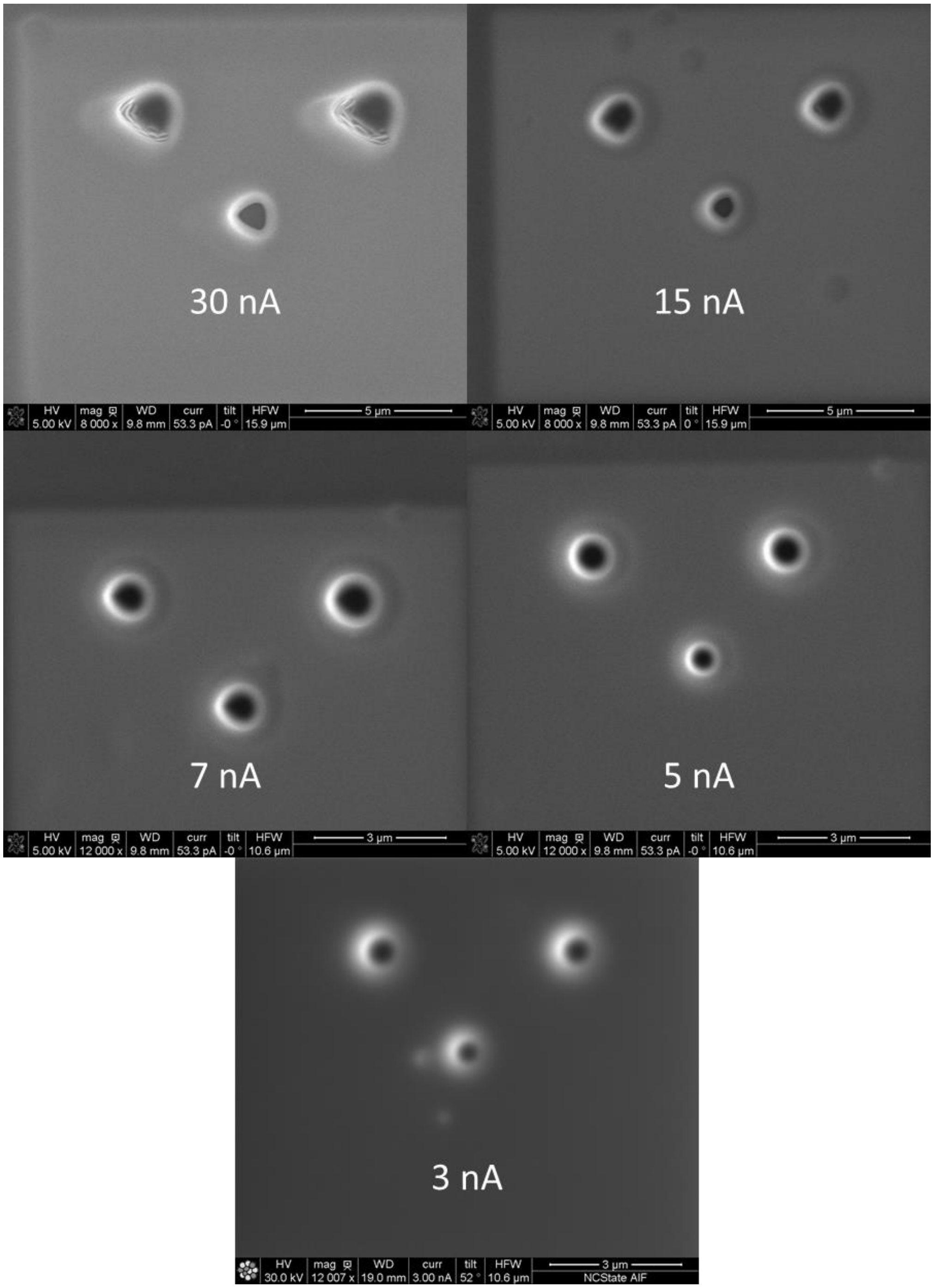

Figure 15. Spots milled with the FIB at various currents

It was also observed that sometimes the beam was not circular when the FIB was put in spot mode. In spot mode, the FIB will expose only a single pixel location to the incident gallium ions. As can be seen from Figure 15, the 30 nA beam is not very circular. The 15 nA beam is better, but 5 nA and lower is where the beam starts to appear circular. It is unknown whether this is a problem specific to the AIF's FIB or if it is present on all similar machines. Since the higher currents are mostly used for roughing operations, it is possible that most users find this beam asymmetry to be acceptable. The effect of the beam asymmetry has not been quantified in this work, but it is thought that a more circular beam would be better for the accuracy of the final surface.

3.3.5 Simulation Tool

FIB milling is typically used for preparing samples for a transmission electron microscope or to prototype 2D structures that would otherwise be made with a photolithography process. In these techniques, the FIB will mill down to a discrete number of depths similar to 2.5-axis CNC milling in the conventional manufacturing world. The desired lens shape has a smooth contour and requires variable depth control just like full 3-axis conventional machining. One significant challenge to FIB milling this 3D shape is that no commercial software exists to plan the 3D "toolpath". In previous work [1], the PEC used the FIB to mill diamond dies for coining nanoscale features. In collaboration with Smart Material Solutions (SMS), a local startup that licensed technology [2] developed by the Consortium, the PEC developed a Matlab function to simulate the FIB and how it removes material. This simulation tool is an important step to using the FIB to produce a finished surface just as a CAM software package is critical to conventionally milling a 3D shape with a 3-axis CNC machining center. The original code developed by SMS was optimized and its runtime reduced by 99.5% (i.e., 60 sec to 0.3 sec). Using the Matlab's parallel processing toolbox provides a further reduction of 47% for a 4 core processor.

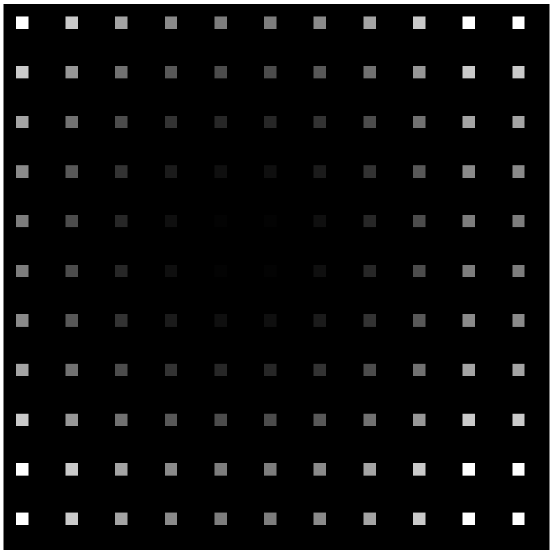

Figure 16. Example bitmap pattern for the FIB.

The simulation follows the method described by Adams [6]. It begins with a bitmap file. The blue value of the bitmap is converted to an array. Each array value represents a location in the FIB's field of view. The array values are converted to the table of available dwell times described by the FIB manufacturer. Figure 16 shows an example pattern.

The simulation uses a model for the beam intensity distribution to determine the dose applied to the surface at and around each pixel commanded to turn on the ion beam. Typically, in literature a Gaussian distribution is used for the beam [8]. A removal factor is calculated based on the angle of incidence and the sputtering dependence on the angle of incidence. The beam shape is then convolved with the removal rate to determine the surface. This process is repeated for each pixel and again for the number of passes specified to determine the final shape of the surface. Figure 17 shows an example output of the FIB milling simulation. It should be noted that this simulation does not account for redeposition; however it does account for the discretization of dwell times imposed by the FEI Quanta. The simulation can also be run in reverse by giving the desired final surface as input and adding material until it becomes flat. This is done by simply changing the sign of the slope dependent removal rate.

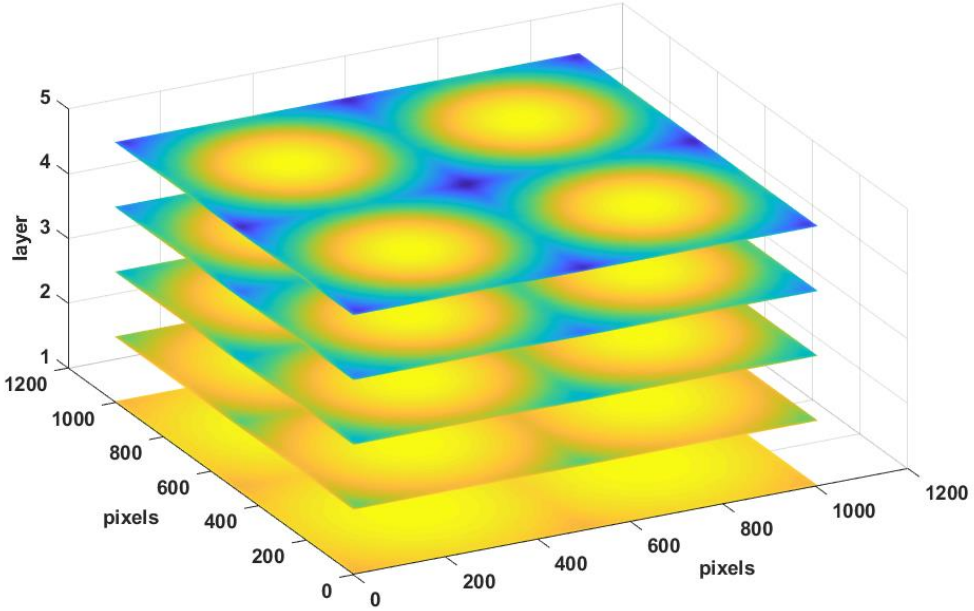

Figure 17. Example FIB simulation output. The five layers show the surface as material is removed from a initial flat surface (bottom layer) to a 2x2 array of parabolic features (top layer).

3.4 FEASIBILITY TRIAL

A Matlab script was developed to generate bitmaps to command the FIB. As described in Section 3.2, the color of each pixel in the bitmap is interpreted by the FIB as the relative dwell time of the ion beam. A plot of the relative dwell times is shown in Figure 18. A bitmap was generated which contained a dwell time distribution to create a 2 by 2 array of convex, smooth features, as well as a 5 μm border around the array. Each pixel represents a 40 x 40 nm area. A parabolic distribution of dwell times was used to command the FIB to mill the bumps. The dwell time goes to a minimum value at the center of the feature where little material should be removed. At the base of the feature, the dwell time is 100% where the maximum amount of material is to be removed. Figure 19 shows the results of this pattern of dwell times. The recessed area is approximately 50 x 50 μm and 6 μm at its deepest point.

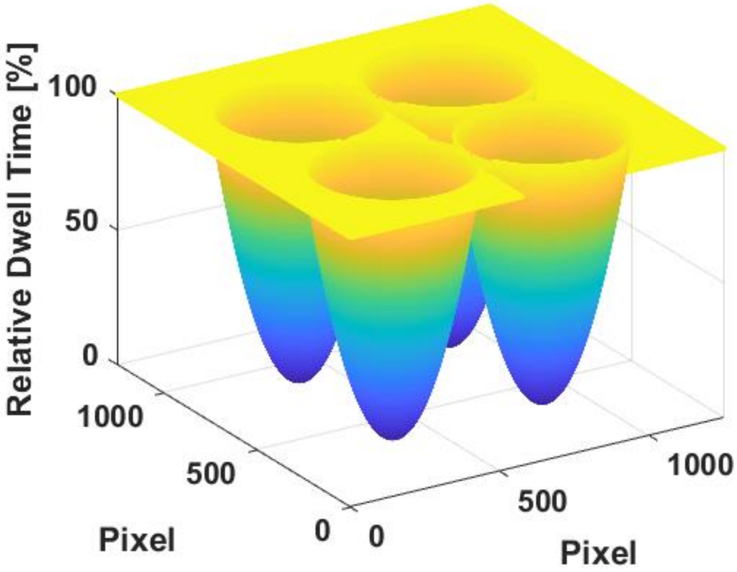

Figure 18. Representation of the relative dwell times assigned to each pixel (Zero values were removed for clarity.)

3.5 METROLOGY

After demonstrating that small convex features of the desired length scale could be FIB milled, methods to measure the features were investigated. While the features could easily be imaged with the SEM, quantitative measurement presented a challenge because of the sloped surfaces and small size.

The New View 5000 scanning white light interferometer was used on the features but was not able to measure the sloped surfaces. As a result data would only be returned for the roughly horizontal peaks and valleys. 3D digital microscopes such as a Hirox K7700 and Keyence VH-X

6000 also had issues with the slope of the features and would only return data at the relatively flat peaks and valleys.

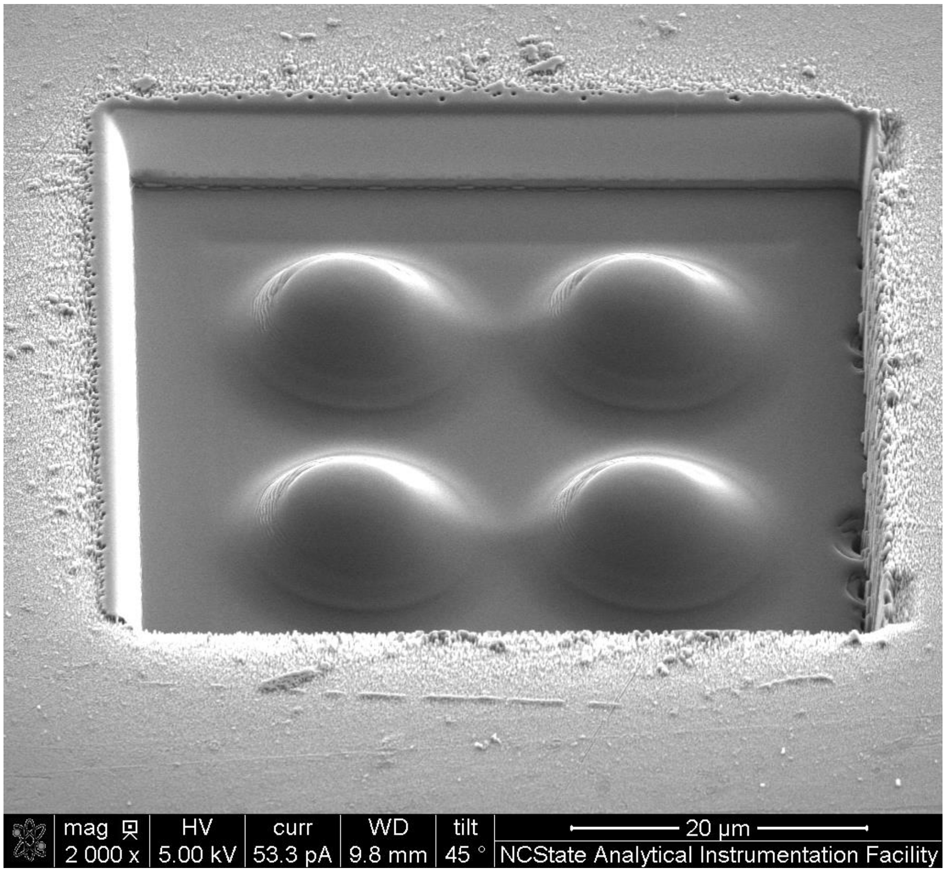

Figure 19. SEM image of FIB milled bumps in glassy carbon

Continuing to use the EBID was also considered but would only give a line measurement. This would make it difficult to quantify the three dimensional form of the features. Figure 20 shows an example of the features with an EBID line. These features are the same as the ones shown in Figure 19.

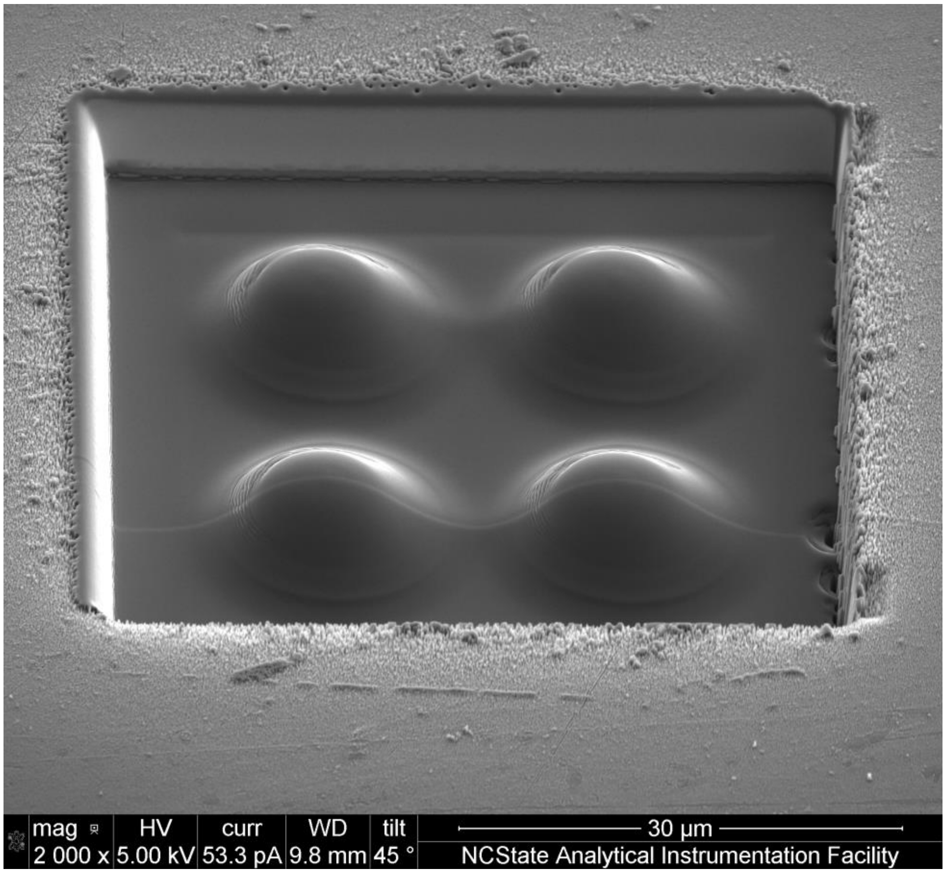

Figure 20. FIB milled bumps with EBID

Measurement with the Polaris, a custom made spherical coordinate measuring machine at the PEC, was investigated. The Polaris utilizes a chromatic aberration optical probe with 60 nm resolution. However, the machine axes of the Polaris are setup for spherical measurements, so the FIB milled features would need to be centered on the spindle of the Polaris. Given that the features are small and were cut near the edge of a 25x 25 x 3mm glassy carbon plate, finding and centering on the features was determined to be prohibitive.

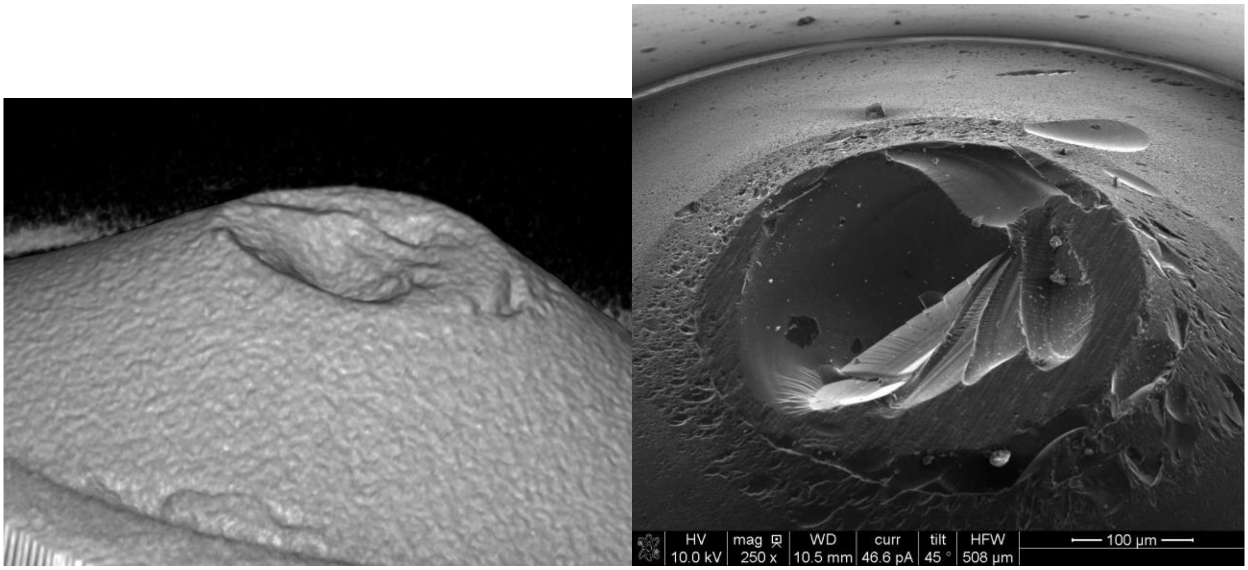

Figure 21. X-ray CT image (left) and SEM image (right) of a glassy carbon sample

X-ray computed tomography (CT) was also investigated. Since these instruments sends x-rays through the part, the slope of the features should not be a problem. A glassy carbon sample was sent to the Shared Materials Instrumentation Facility (SMIF) at Duke University, which has a Nikon XTH 225 ST. The SMIF staff imaged a glassy carbon sample, but as seen in Figure 21 the voxel size was not adequate for resolving the details. In an X-ray CT the sample needs to be rotated capture the volumetric data while also being as close as possible to the X-ray source for the best resolution. This requirement made it unsuitable for measuring the test features made on a 25 x 25 x 3 mm plate.

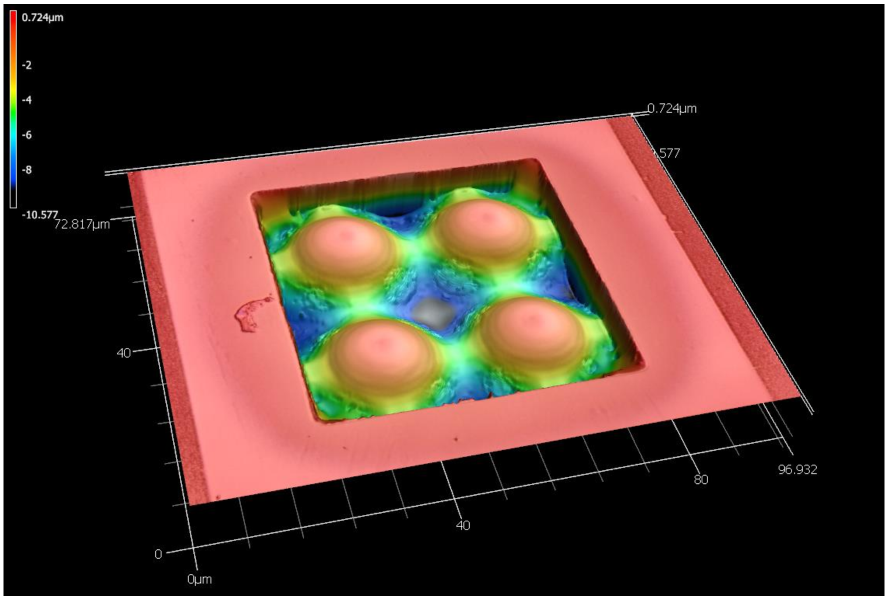

Figure 22. Laser confocal microscope measurement

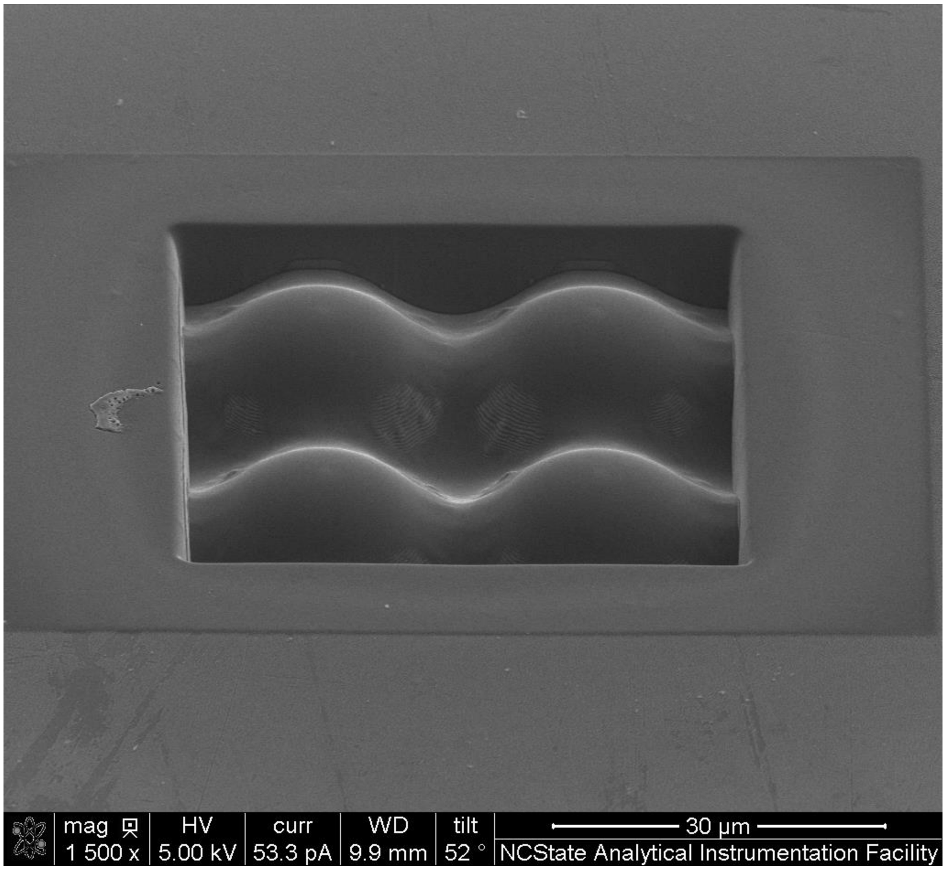

Figure 23. SEM image of the same features as Figure 22

A Keyence VK-X 1100 laser confocal microscope was found to adequately measure the features glassy carbon sample. Figure 22 and

Figure 23 show a comparison of a laser confocal measurement and an SEM image. The laser confocal microscope creates artifacts in the corners but measures the sloped surfaces of the convex features well. Unless otherwise specified, the Keyence VK-X 1100 was used for measuring the FIB milled features in the rest of this report.

3.6 FIB PROCESS PARAMETERS

Now that a metrology solution had been identified and the FIB had been proven to be able to make smooth convex features, the process parameters were investigated to achieve the best form.

3.6.1 Overlap

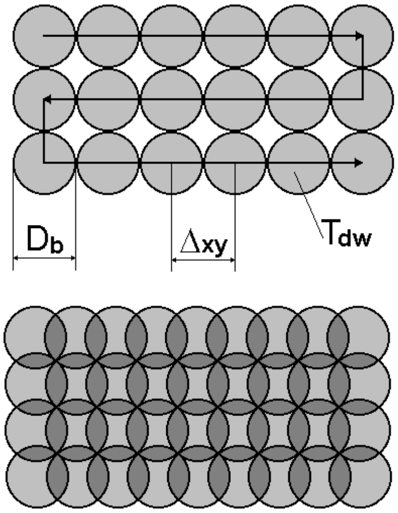

Figure 24. Cartoon of the FIB exposure pattern

The parameters which affect the form and finish of the FIB milled surface were investigated to determine how to fabricate the best die. A significant parameter when FIB milling features is the amount of overlap. Overlap is similar to stepover in CNC milling. It is the distance between the pixels where the beam turns on. Figure 24 illustrates this concept by showing a top down view of the surface being FIB milled. Each circle represents a location where the FIB dwells. D_b is the beam diameter, Δxy is the overlap, and T_{dw} is the dwell time. In the upper image there is no overlap. In the lower image the circles overlap as the pixel spacing is smaller than the beam diameter.

Similar bitmap patterns were created with overlap of 100 nm, 200 nm and 500 nm. The pattern was FIB milled with a 1 µs maximum dwell time and 15 nA beam. The number of passes was adjusted to try to keep the total dose approximately constant.

Figure 25, Figure 26, and Figure 27 show microscope images of the resulting surfaces. The FIB appeared to be having an issue that day which caused random holes in the features. The significant result though is the grid pattern that appears in Figure 27. This indicated that the pixels are spaced too far apart and the overlap needs to be decreased. The grid pattern while able to be discerned from the optical images, does not appear in the Keyence measurements and is likely very low amplitude. The manual for the FIB reports that the 15 nA beam has a diameter of 182 nm. It is not certain how the manufacturer is defining or measuring the diameter, but from these results overlap greater than twice the beam diameter appears to cause optical quality issues. For future experiments, an overlap of close to the manufacturer reported diameter was used.

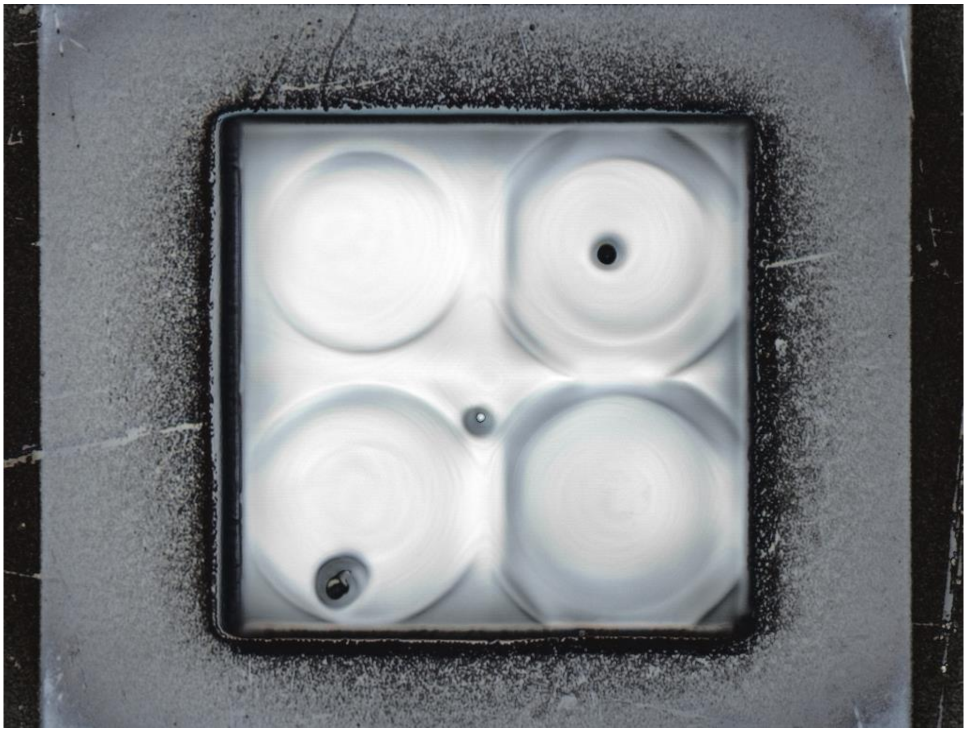

Figure 25. Feature FIB milled with a 100 nm overlap

Figure 26. Features FIB milled with a 200 nm overlap

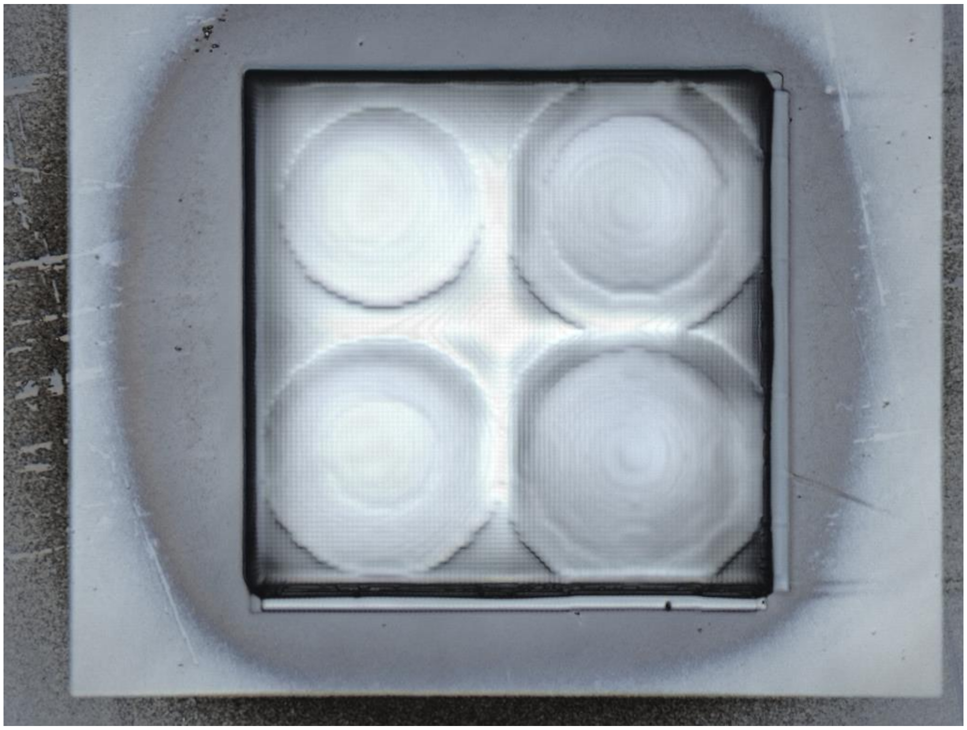

Figure 27. Features FIB milled with a 500 nm overlap

3.6.2 Maximum Dwell Time

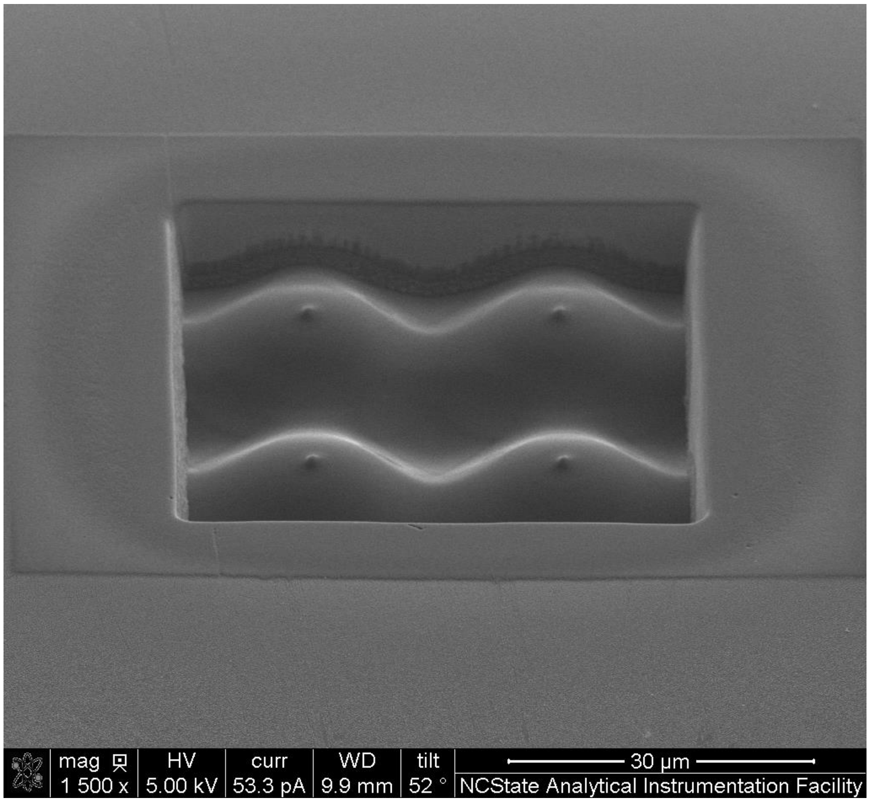

Figure 28. Features FIB milled with a 1 µs maximum dwell time

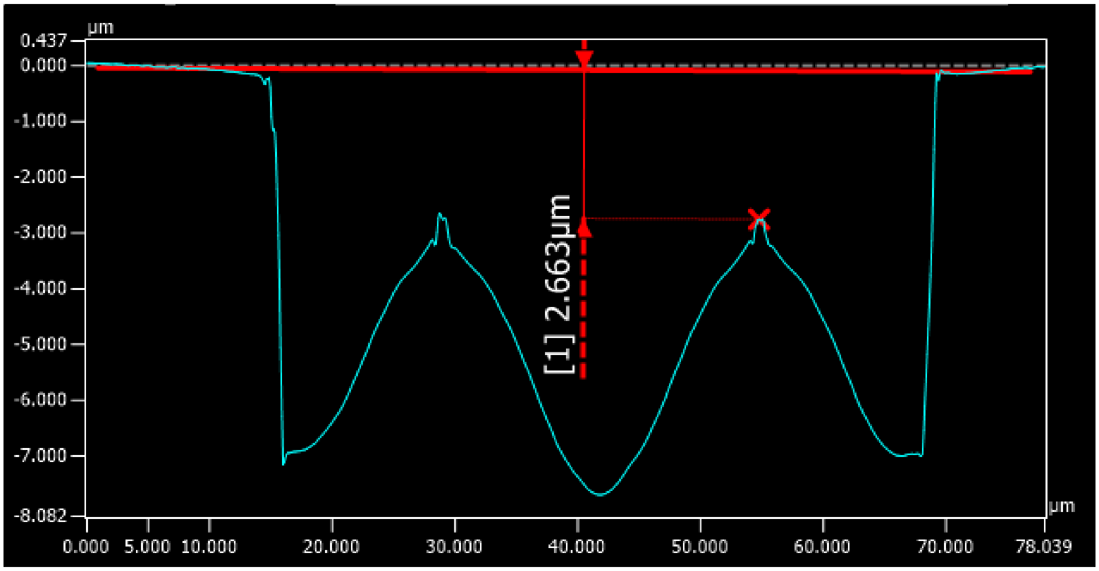

Figure 29. Profile of the features from Figure 11

One issue encountered was the entire features depressed below the original surface despite the FIB not being commanded to dwell at the apex of the bumps. Figure 28 shows features FIB milled in glassy carbon with a 1 µs maximum dwell time. The laser confocal microscope measurement shown in Figure 29 shows that the entire bump was 2.6 µm below the original surface. Also there is a small protrusion on the top of the bumps.

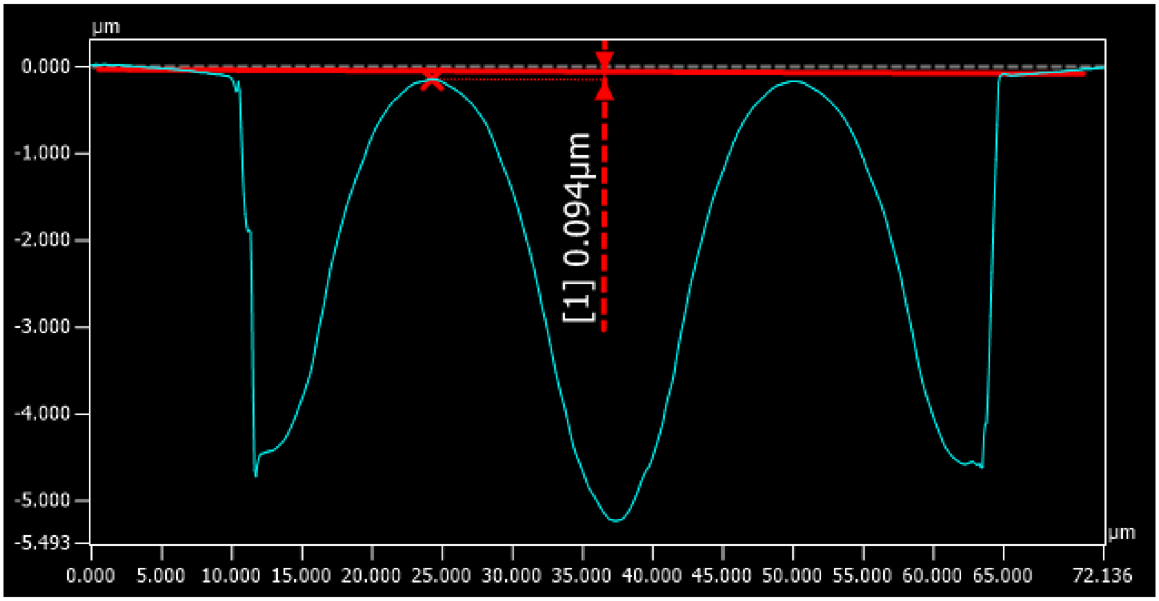

Figure 30. Profile of features from Figure 13

The fixed table of allowable dwell times only has 9 values below 1 µs, so the pattern is only able to use 10 distinct dwell times. It was hypothesized that increasing the maximum dwell time would improve the fidelity of the FIB milled surfaces as more dwell times would be available. The same pattern was used with a 100 µs dwell time and the number of passes was reduced by a factor of 100 to try to keep the total dose approximately the same. The resulting surface is shown in Figure 23. The lump at the top of the bumps disappears with the additional allowable dwell times. Also the profile shown in Figure 30 quantitatively shows that less material is removed at the peak of the bumps as intended by the bitmap.

These results indicate that short maximum dwell times (such as 1 µs) should be avoided. For the rest of this work dwell times of 100 µs were typically used.

3.6.3 Bitmap Error Correction

The FIB sputtering yield is dependent on the angle of incidence of the beam on the surface, so the previous pass influences the current pass. A simulation tool has been developed using Adam's model [6], but it has not yet proven useful for planning the command file for the FIB.

Rather, a rudimentary method of correcting an initial guess was used to FIB mill the desired shape. An initial relative dwell time map was created based on parabolically distributed dwell times used in the feasibility trial described in Section 3.4, but the features were more tightly spaced. No border was included, and the features were enlarged slightly to meet the project goals. The modified pattern is shown in Figure 31, where each pixel is 50 nm. A glassy carbon surface was FIB milled with this pattern to approach the correct depth. An SEM image of the surface is shown in

Figure 23.

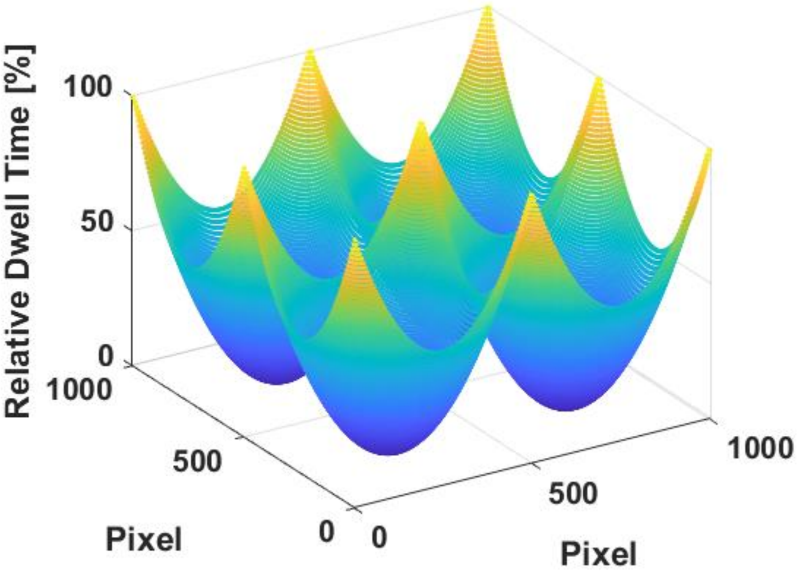

Figure 31. Modified relative dwell time map (Zero values removed for clarity)

The surface topography of the FIB milled surface was measured with a Keyence VK-X1100 laser confocal microscope. The data was first imported into Matlab, and a script was used to extract a user defined region of interest containing the lens feature and some of the surrounding area. A sphere was fit to the data. The data was trimmed to a Ø25 µm aperture centered on the best fit sphere center to remove data from the neighboring lens features which might have been included in the user defined region of interest. The best fit sphere was calculated for the new trimmed data set. The data was adjusted once again to a Ø25 µm aperture centered on the new best fit sphere center. The best fit sphere center was then considered the center of the lens feature. The measured surface was then compared to the desired shape, which in this case was a hemisphere over a circular aperture. A spheroid of the desired radius was calculated for each (x,y) measured data point. The desired spheroid was shifted so that the apex of the spheroid matched the measured data a (x,y) = (0,0). This forces the error to be zero at the center of the lens feature. The z-direction difference between the desired and measured was calculated for each data point. Representative data is shown in Figure 32, where the measured data is the colored surface and the wireframe surface is the desired R15.84 µm spherical surface. The error of the surface was calculated with respect to the beam direction and converted to a percentage of the maximum FIB milled depth. An example of this error map is shown in Figure 33. The large values at the edges indicate influence of the neighboring features. The command file was then adjusted by this percentage. For instance if a location were 5% too tall, the beam would be commanded to dwell 5% longer and remove more material there.

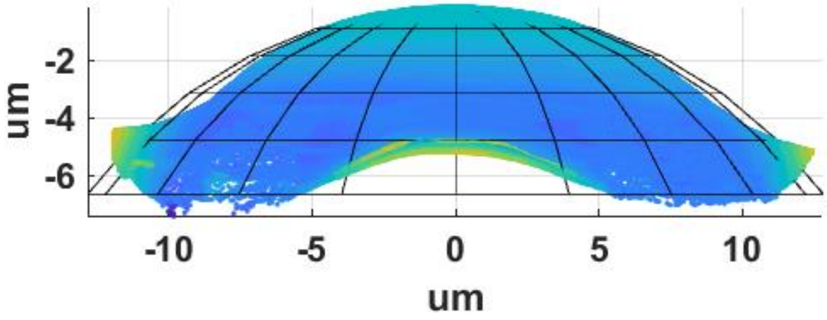

Figure 32. Measured surface data with the desired spherical shape overlaid

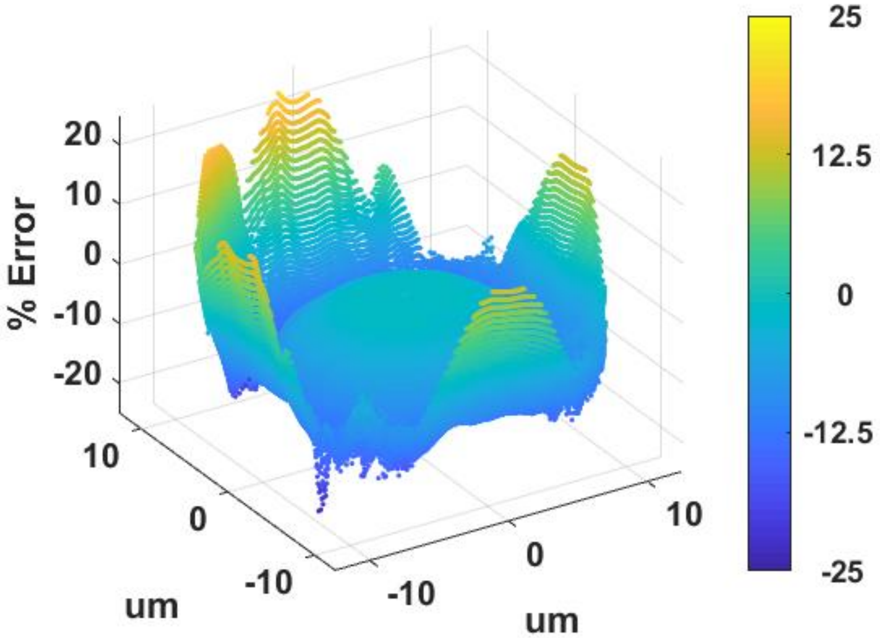

Figure 33. The deviation from the desired spherical surface converted to a percentage of the maximum FIB milled depth

This method was able to correct some of the error in the features. Figure 34 shows the average height error of the horizontal and vertical meridians of four bumps. In this visualization, a perfect surface would be a flat line representing zero error. The "original" four features were made with the parabolically distributed dwell times. Four more features were made with the dwell times adjusted by the previously described error compensation scheme. Within a 15 μm diameter aperture, the measured surface is within 250 nm of the desired shape. However, this method was not able to correct the errors outside the 15 μm aperture. Further investigation needs to be conducted to determine the reason for this.

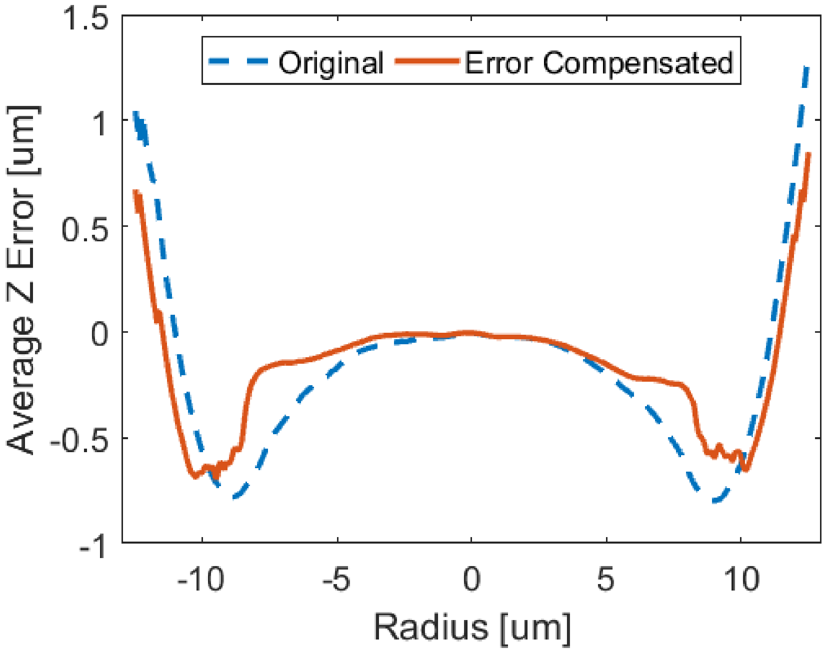

Figure 34. Comparison of the average error of 4 features FIB milled with and without error compensation

3.6.4 Other FIB Errors

Besides errors caused by the bitmap command files, other errors were found in the FIB milling process. For instance, the order of operations in the FIB milling process is important due to redeposition. In Figure 19 both the bumps and border were milled at the same time. If the border is FIB milled first, redeposition spoils the surface that the lens features will be FIB milled on. Figure 35a shows the surface after FIB milling the border. The square in the center has an unevenly distributed layer of redeposition on it. When the lens shapes are FIB milled, the uneven layer of redeposition prints through. Figure 35b shows the lens features 25% complete, while Figure 35c shows them completed. The final lens features are obviously unacceptable, and the border should not be FIB milled prior to the lens features.

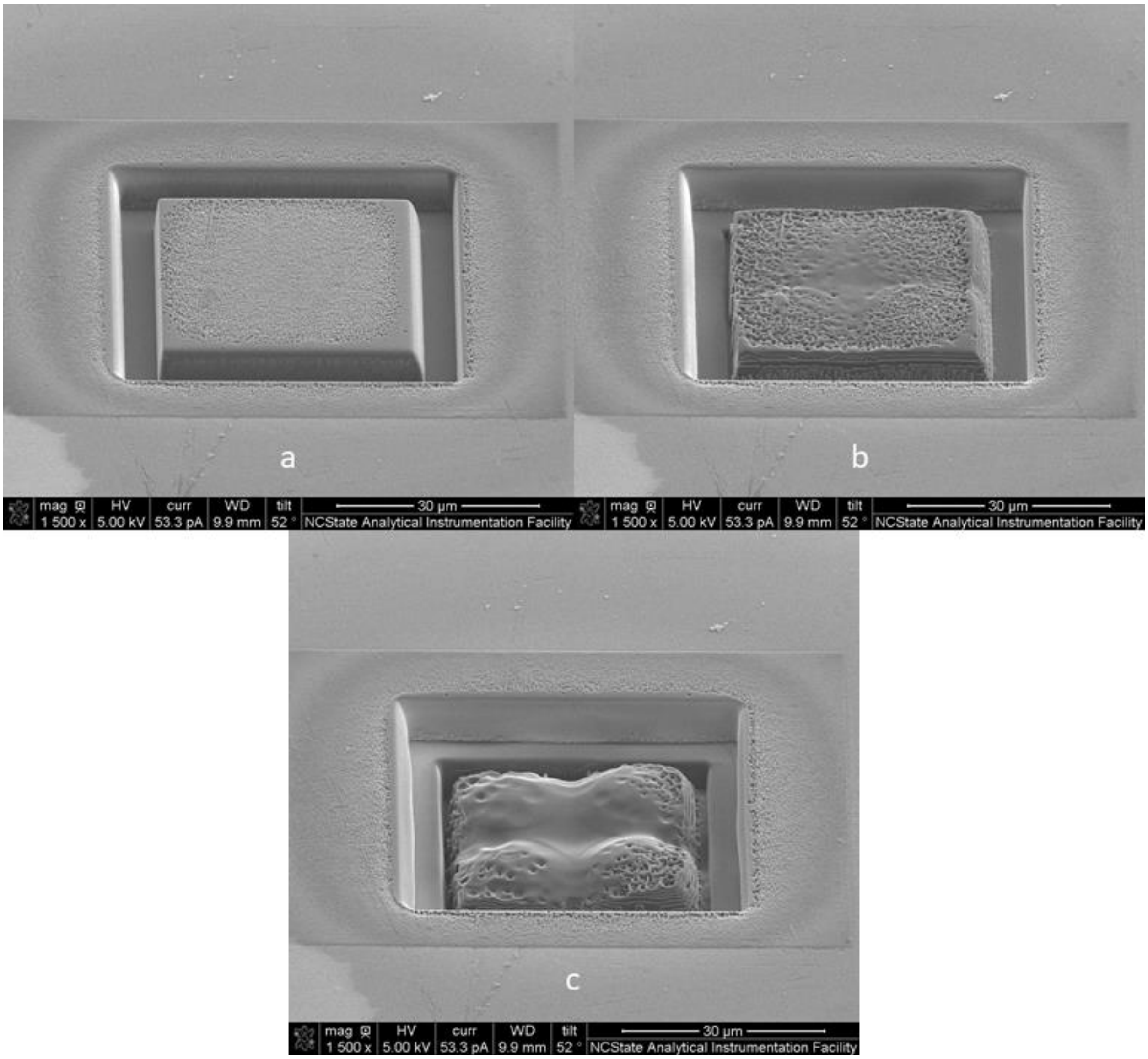

Figure 35. Border FIB milled (a), beginning of FIB milling of the bumps (b), final bumps (c)

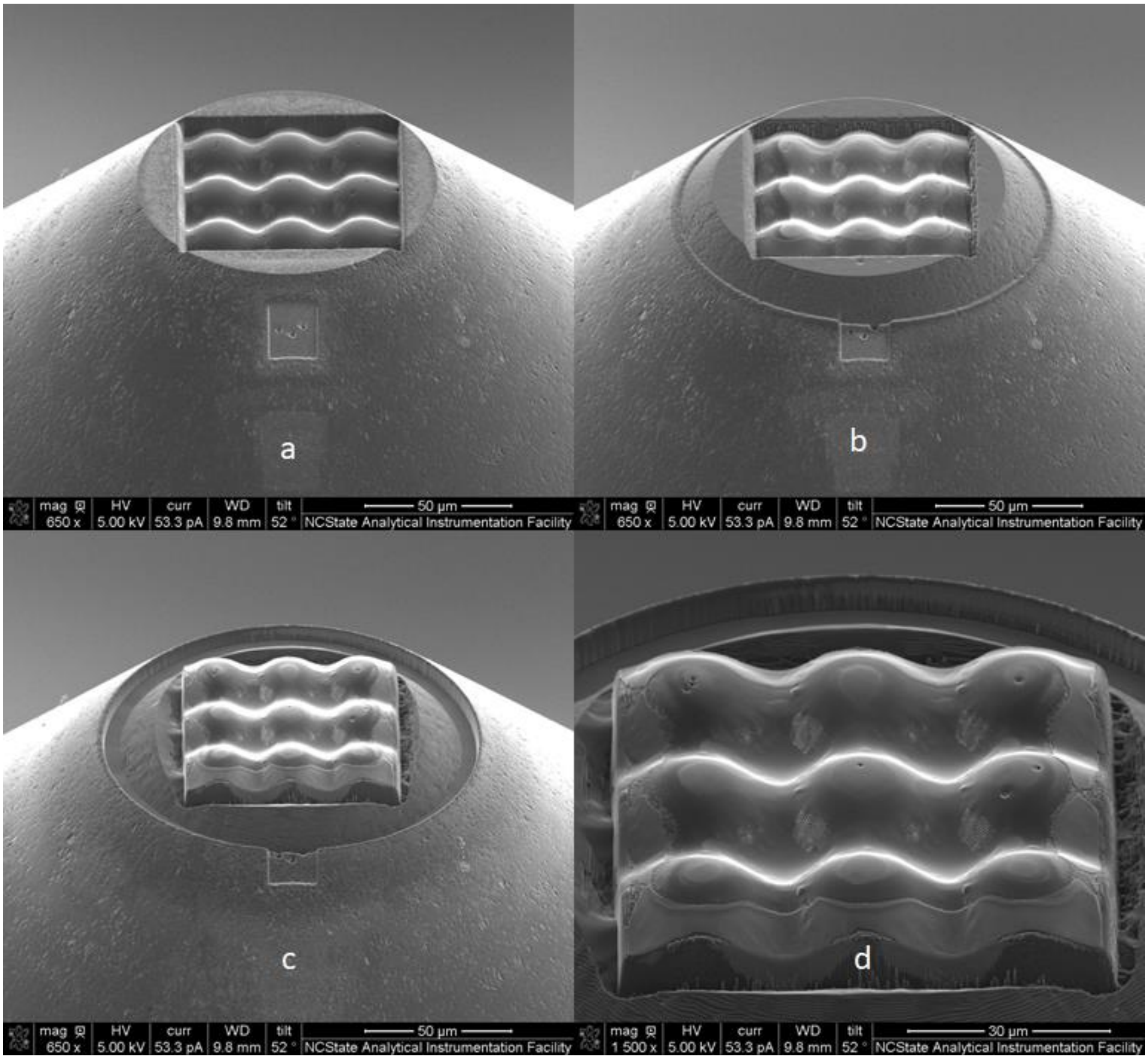

Figure 36. Completed FIB milled glassy carbon lens features (a), beginning of FIB milling the border (b), completed border (c, d)

Figure 36 shows the operation in the reverse order. Figure 36a shows the completed lens features. Figure 36b shows the border 25% complete. At this step in the process, a stain around the edges of the lens features is evident from the redeposition. Figure 36c and Figure 36d show the final lens features after the border is finished. This layer of redeposition is very thin and barely registers in the laser confocal microscope measurements. This feature appears in indents such as Figure 46, but due to the difficulty measuring it, the impact on the form or finish of the mold is unknown.

Ideally, the border would be FIB milled at the same time as the lens features. However, this presents a logistical problem of reserving the FIB for an extended period of time. Additionally, the lens features and border would be completed at the same time. If the reservation is not long enough or cut short for any reason, the glassy carbon would need to be precisely realigned to restart the FIB milling at a later time. Errors in alignment would likely cause errors in the lens features. Therefore, the dies in this project were made by first FIB milling the lens features and then the border as depicted in Figure 36. This method reduced the risk of needing to realign the glassy carbon in the FIB.

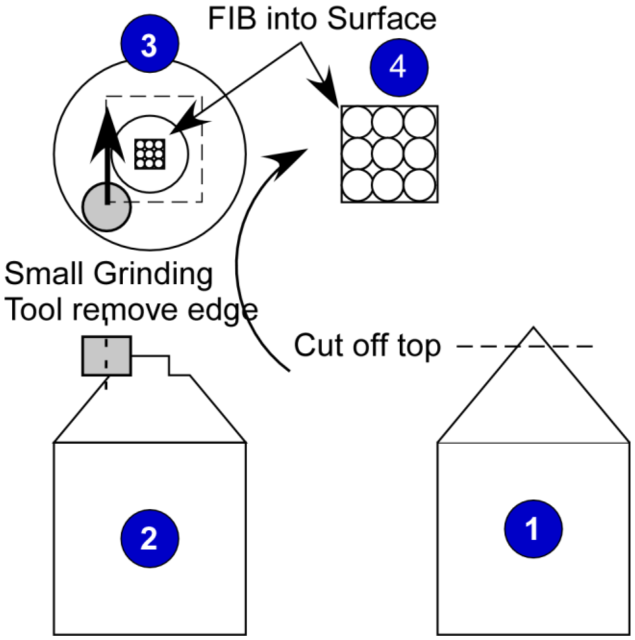

Figure 37. Proposed blank preparation process

Another way to address this issue is to mechanically remove the border prior to FIB milling. One possible process is shown in Figure 37. This process begins with a turned glassy carbon cone. The cone is fixtured in a high precision mill with a diamond end mill. The diamond end mill will then be used to mill a flat face onto the glassy carbon. Then the border will be removed either with the end mill or a grinding tool leaving a small raised area of the proper footprint to be FIB milled. This process is only in concept and has not been investigated. One challenge will be accurately locating the cone in the coordinate system of the mill. Also it is unknown what kind of surface finish is produced by milling glassy carbon.

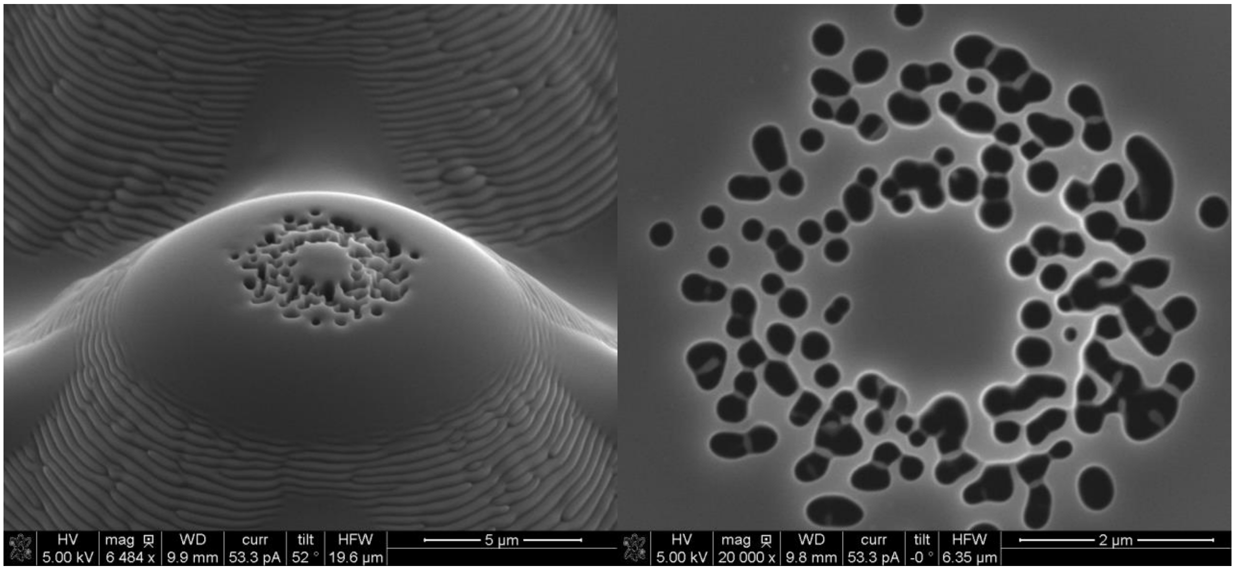

Figure 38. "Speckles" on the top of the glassy carbon lens features

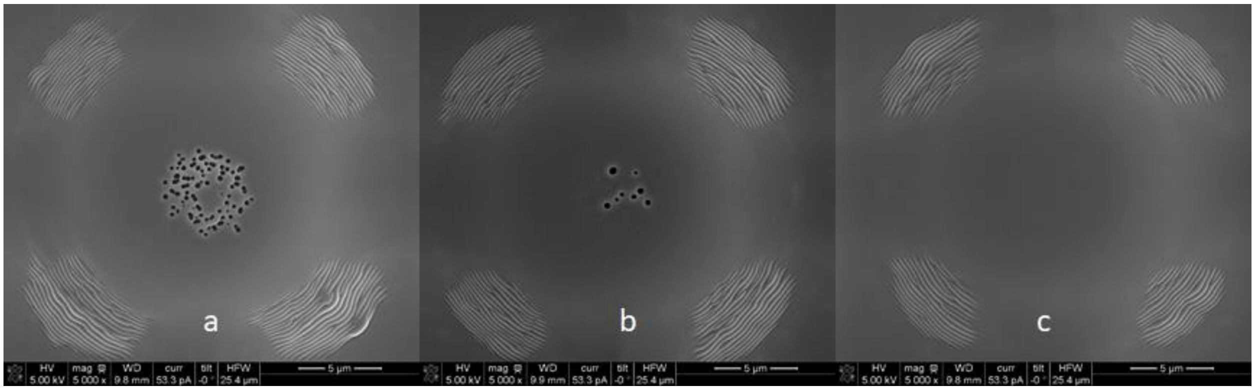

Figure 39. Plan view of glassy carbon lens features made by adjusting the minimum bitmap value

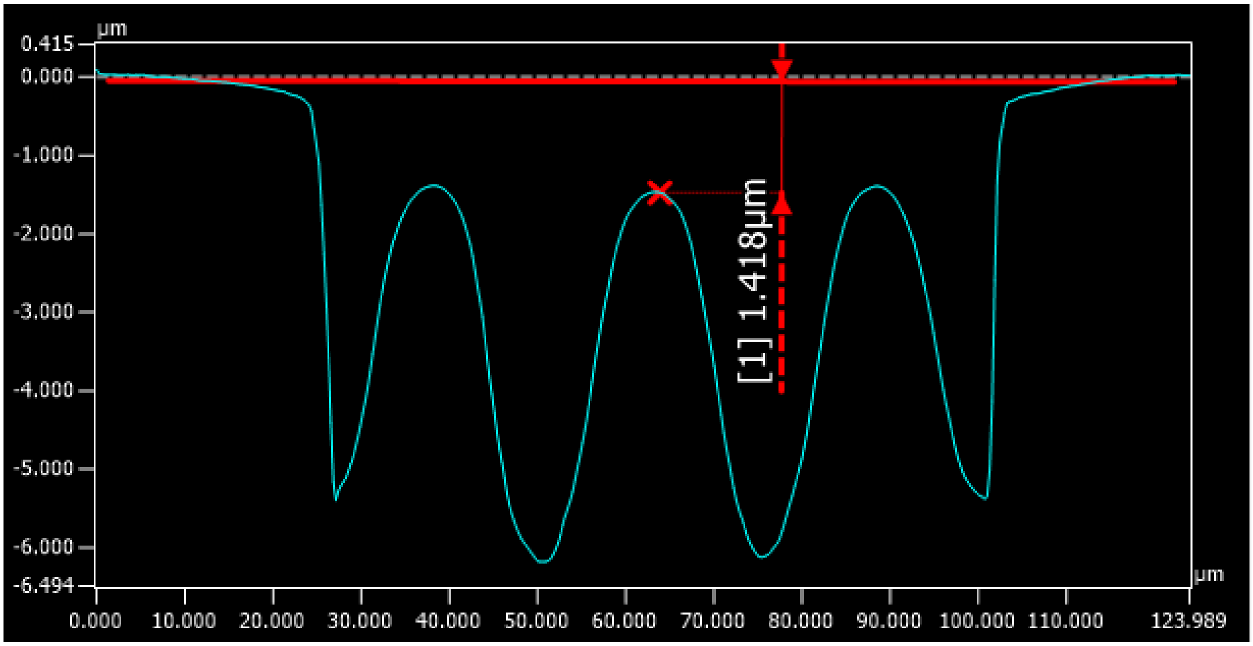

Figure 40. Profile of glassy carbon lens features made with a minimum bitmap value of 20

Another issue encountered with the FIB was the appearance of small depressions or “speckles” on the top of the lens features. Figure 38 shows an example of this. The speckles do not appear to be on a grid pattern indicating that it is unlikely to be related to the pixels in the bitmap. The speckles may be related to the minimum ion dose at the top of the lens features. When the minimum dose is very small, stray ions in the beam tails of the ion beam will have a large impact. In Figure 38 the beam was turned off at the apex of the lens features. Figure 39 shows a top view of a lens feature made with different minimum doses at the top of the feature. As described in Section 3.2, the bitmap values range from 0 to 255 and are linearly interpolated to a fixed table of 124 possible dwell times. For this experiment the maximum dwell time was 100 µs. In Figure 39a the minimum bitmap values was 1, in Figure 39b, 10, and in Figure 39c, 20. As the minimum dose is increased the speckles decrease and eventually disappear. One consequence of increasing the minimum dose is that the lens features are once again lowered below the uncut material surface. Figure 40 shows the profile of the bump shown in Figure 39c. The apex of the lens features are now 1.4 µm below the material surface. This less efficient FIB milling is a worthwhile trade off against the significantly worse finish caused by the speckles.

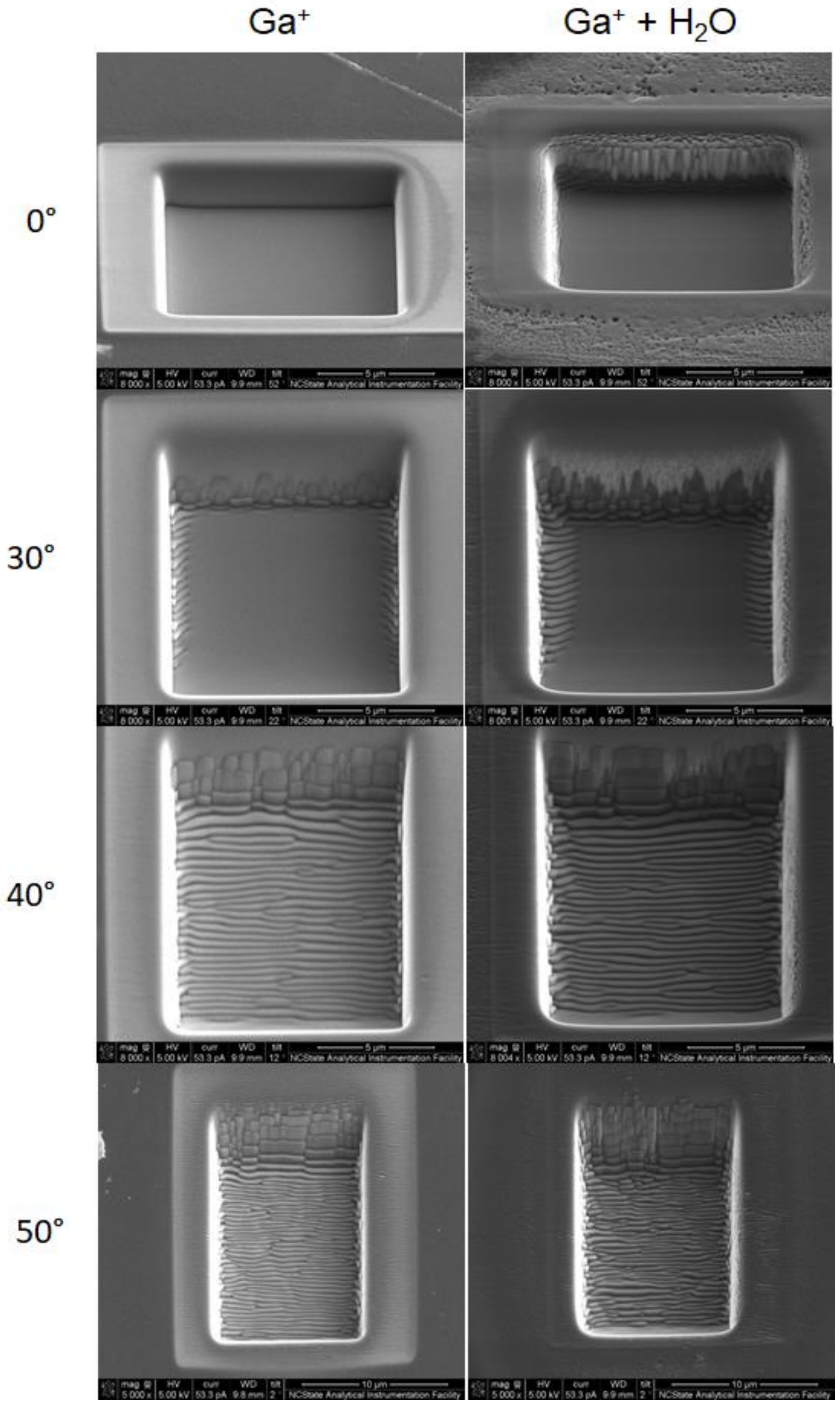

Figure 41. FIB milled glassy carbon squares at varying angles of incidence with a 5 nA beam with and without H_2O gas assist

Another issue evident from Figure 38 and Figure 39 is ripple in the sloped surfaces. The sides of the lens feature in the left image in Figure 38 shows this ripple. Figure 39 depicts a similar phenomenon from a top view. Literature reports that this is related to the angle of incidence, defined as the angle between the ion beam and the surface normal. Adams [6] reported degraded surface finish at angles of incidence above 40° in diamond. He postulates that this is caused by redeposition and ion reflection from the sloped surfaces. He also reports that the phenomenon is not evident in heavier mass elements such as gold and tungsten, both of which yield higher fidelity surfaces. Elsewhere Adams [9] reports that H_2O assist gas reduces the amplitude and wavelength of the ripple. Ding [10] also reported on this ripple effect in diamond grows faster at higher currents.

Angle of incidence experiments were conducted with glassy carbon which appears to be very similar to what was reported by Adams and Ding in diamond. Figure 41 shows the results of FIB milling a 10 µm square with a 5 nA beam. The stage of the FIB was tilted in 10° increments from 0° to 50°. For brevity, the results for 10° and 20° are not shown. Ripple begins to appear at 30°, and at 40° the surface is covered in ripple. Looking at the images though, it is hard to discern if the H_2O gas assist changes the ripple. The ripple is too low amplitude for the laser confocal to reliably measure, so quantitative measures of the surface roughness are not available. These results imply that in terms of ripple glassy carbon behaves similar to diamond. At this time there is not a method for avoiding ripple at angles of incidence greater than 40°.

Future work will focus on techniques for reducing this ripple. The effect of H_2O gas assist will be quantified. Also it may be beneficial to start with a 90° angle of incidence and mill the surface to 45°, instead of starting with a 0° surface and working up to 45°, as this will change the ion reflection. As an example, the 0°, Ga^+ FIB milled square in Figure 41, produced a very smooth 90° surface on the far wall. Finally, as described by Adams [6], alternative heavier molecular mass materials, can be investigated.

3.7 GLASSY CARBON DIE PREPARATION

As stated earlier, the previous experiments were conducted on a flat glassy carbon plate 25 x 25 x 3 mm. This geometry is not suitable for indentation. A Ø1 mm x 10 mm long glassy carbon rod (SPI-Glas 11) was purchased from the same supplier as the glassy carbon plate. The flat end face of the rod was FIB milled with a uniform dose, square pattern. As seen in Figure 42, the rough surface remains rough, as the same rough features are milled deeper into the surface. The surface finish of the rod end was measured by the New View 5000 to be 2 µm RMS. Given the amount of data dropouts, the actual roughness was likely higher. The glassy carbon plate used in the previous experiments had a surface finish of 3-5 nm RMS. After experimenting with cutting parameters, diamond turning was shown to achieve 5 nm RMS surface finish in glassy carbon. A

-30° rake angle tool with a 3mm nose radius, 5 mm/min cross feed, and 1000 RPM spindle speed were used to turn this quality surface.

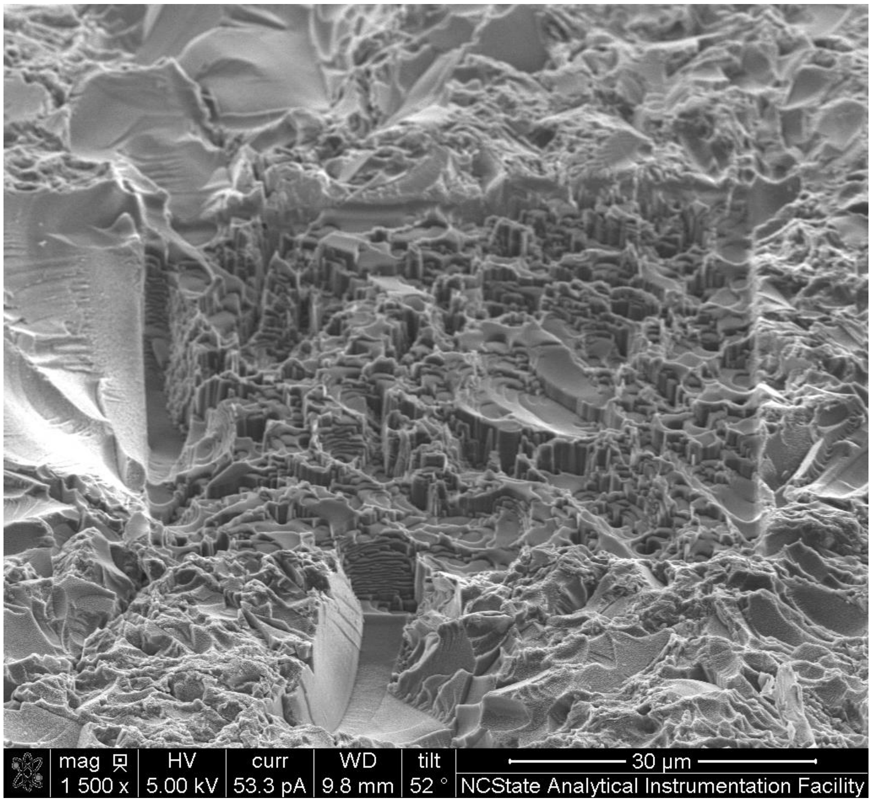

Figure 42. FIB milled rough glassy carbon surface

To make a glassy carbon geometry appropriate for indenting the Ø1 mm diameter glassy carbon rod (SPI-11) was cut to about a 2 mm length with a low speed diamond wheel saw (South Bay Technology Model 650). A holder was made of 0.25 inch diameter 6061 aluminum round stock. One end of the aluminum rod was turned to a 90º cone on a manual lathe. A hole was drilled into the tip of the cone to hold the glassy carbon piece. The glassy carbon was glued into the aluminum with a cyanoacrylate based adhesive (Gorilla Super Glue).

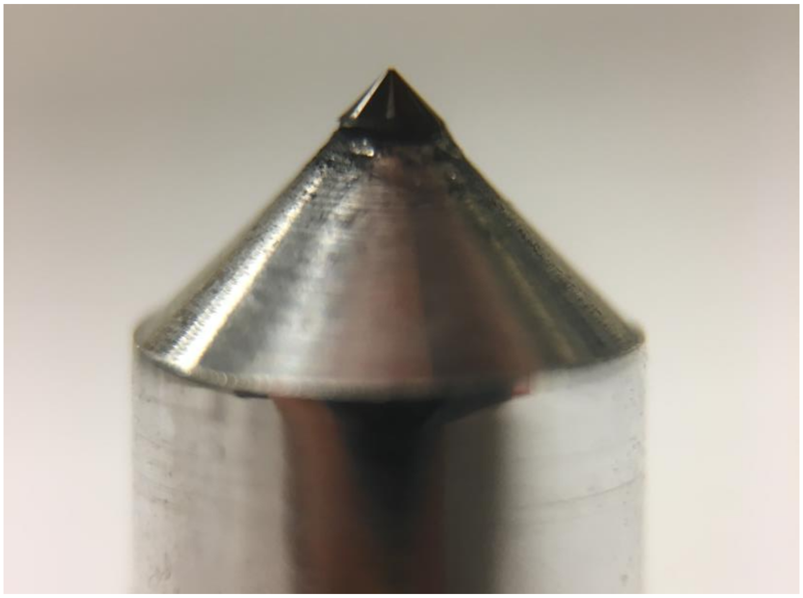

Figure 43. Diamond turned glassy carbon blank potted in an aluminum holder

The face of the glassy carbon rod was turned utilizing the previously described parameters with a -30º rake, 3 mm nose radius diamond tool in a Nanoform 600 diamond turning machine. Surfaces finishes of 4-8 nm RMS were achieved with a 5 µm/rev feed and 5 µm depth of cut. Next the cylindrical glassy carbon was turned with a 0º rake, 1 mm nose radius diamond tool to form a frustum with a 90º cone angle leaving a circular flat on the tip. Figure 43 shows an example of one of the glassy carbon blanks manufactured in this manner.

Figure 44. Custom FIB holder

Due to the height constraints of the FIB, a custom mount was fabricated to to hold the glassy carbon blank. The mount includes a 4-40 screw to securely clamp the 6061 round. A standard Ø12.7 mm sample stub with a 3.2 mm pin was adhered to the bottom of the mount to ensure compatibility with the FIB fixturing system. The custom mount is shown in Figure 44. A 2 by 2 array of convex features were FIB milled into the tip of the glassy carbon frustum. After FIB milling the features, a border was also FIB milled so the bumps would be higher than the surface around it. The final glassy carbon tip is shown in Figure 45.

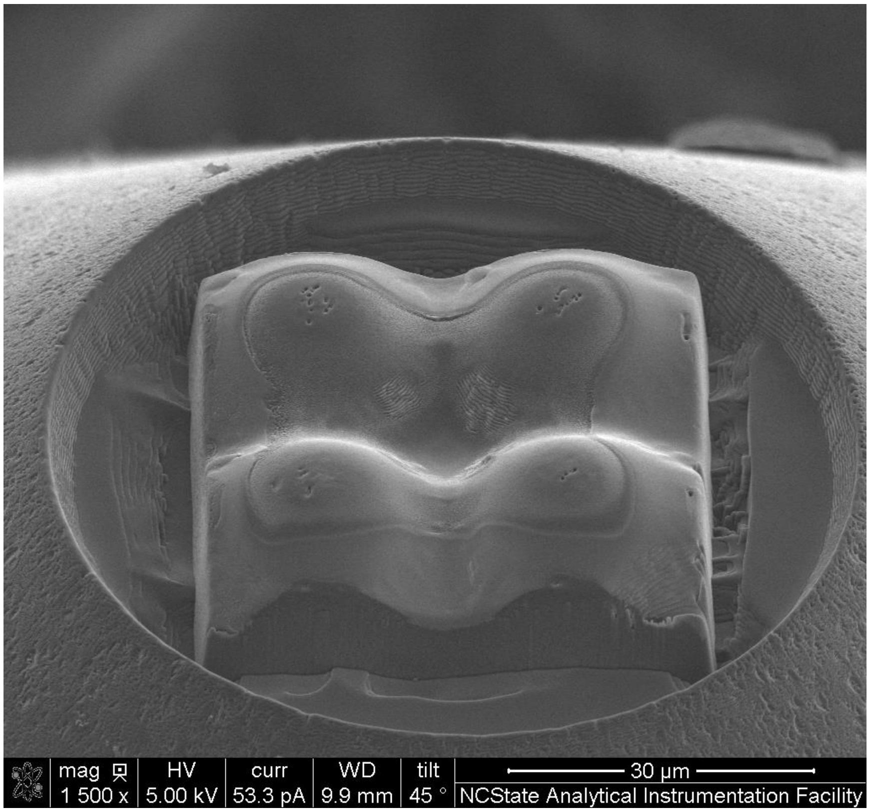

Figure 45. SEM image of the glassy carbon tip after FIB milling convex features and border

3.8 INDENTATION EXPERIMENTS

3.8.1 Indent Trial

An 1100 aluminum sample was prepared to be indented by diamond turning the face to 6 nm RMS. The glassy carbon and its aluminum holder were mounted in the tool post of the diamond turning machine. The axes of the diamond turning machine were then used to press the glassy carbon into the aluminum sample. 1100 aluminum, or 99.0% pure aluminum, was chosen because it is soft, diamond turnable and is well characterized in literature. 1100 aluminum specimens were material tested and the results are shown in Table 3. Figure 46 shows an image of aluminum indentation from the laser confocal microscope. The maximum depth of the indentation is about 11 µm. The aluminum appears to have replicated the glassy carbon features quite well.

Table 3. Measured properties of 1100 aluminum

Yield Strength	114 MPa
Young’s Modulus	76 GPa
Vickers Hardness with 0.2 kgf load	33

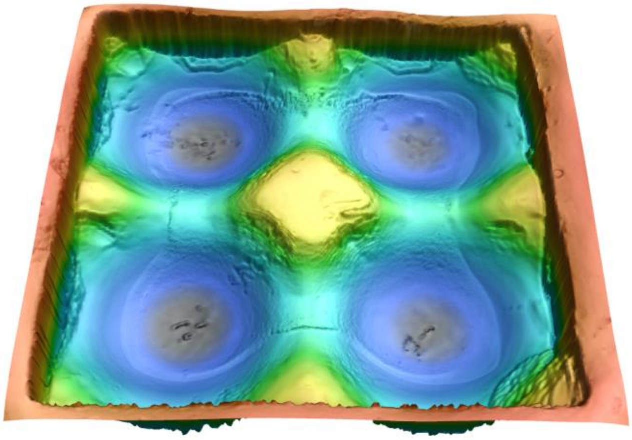

Figure 46. Laser confocal microscope image of an 1100 aluminum sample after it has been indented with the FIB milled glassy carbon

3.8.2 Slow Speed Indentation

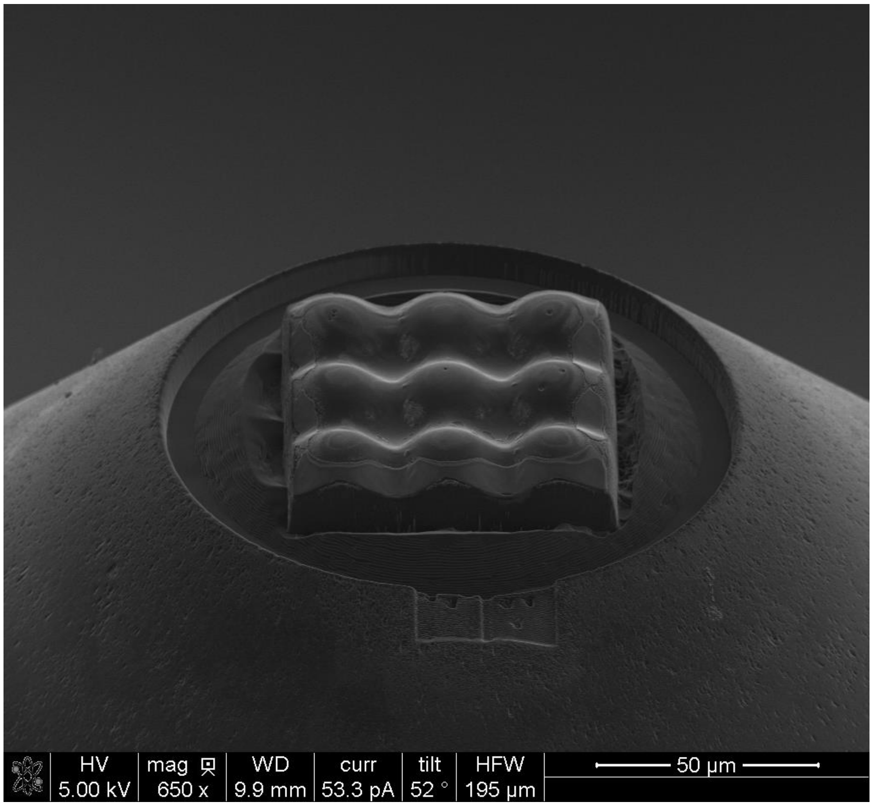

Figure 47. FIB milled 3x3 glassy carbon die

Another blank was made with a larger flat at the top of the frustum. A 3x3 array of lens features was FIB milled into the tip, as shown in Figure 47. A 3x3 array allows more lens features to be made at once. Alternatively, if the lens features need to be formed by multiple different shaped dies, similar to progressive stamping, the 3x3 would allow for more progressive steps.

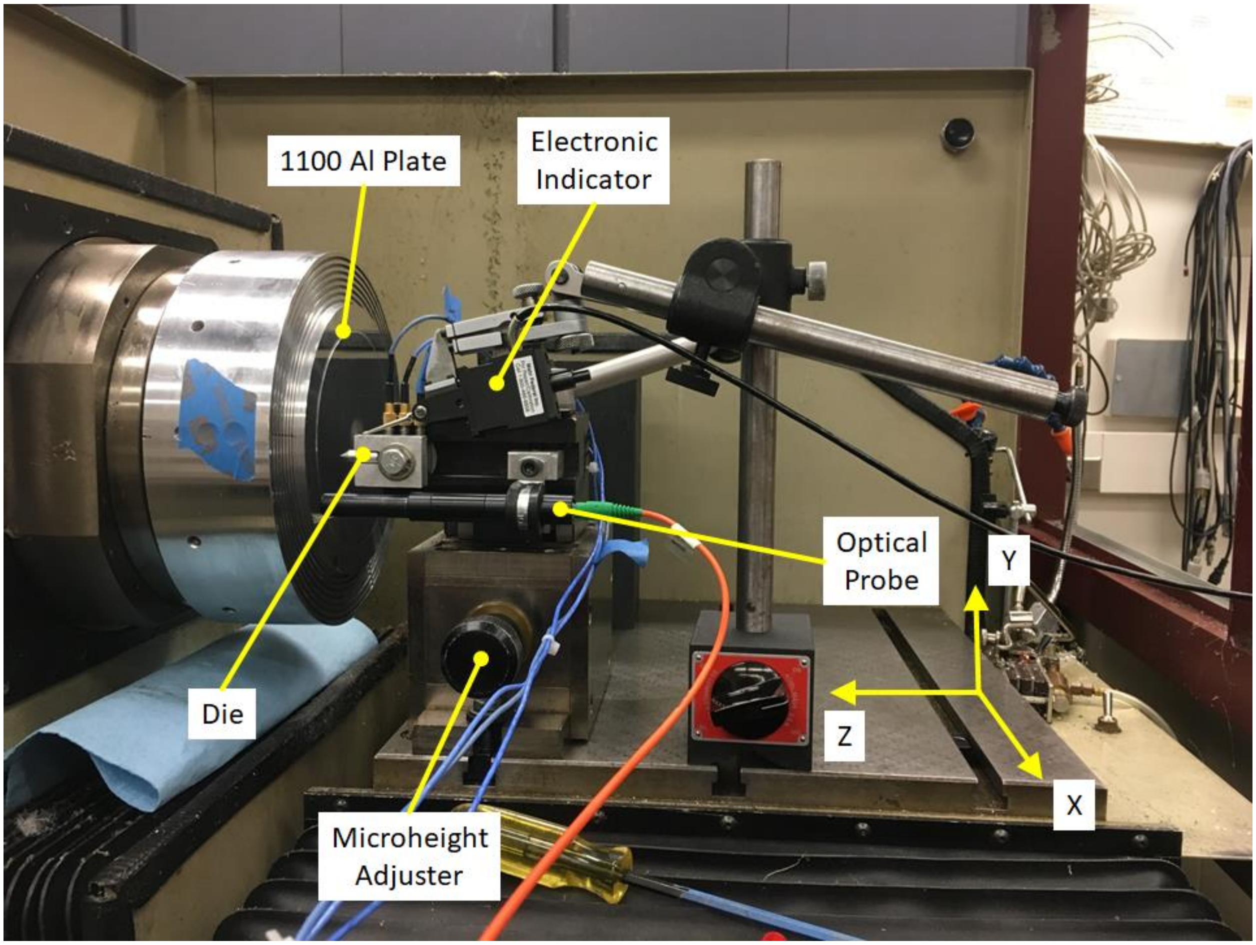

Figure 48. Test setup for the indentation experiments

The 3x3 die was attached to the tool post of an ASG diamond turning machine for the indenting experiments. Figure 48 shows the test setup as well as the axis directions. A second tool post was added to the machine to hold a diamond tool and turn a 6” diameter 1100 aluminum plate. The tool post was instrumented with a Kistler 9251A 3-axis load cell. The load cell was used to get a consistent touch off. The Z-axis was moved in 1 μm steps until an excursion was registered on the load cell. This coordinate was then set as the Z-zero.

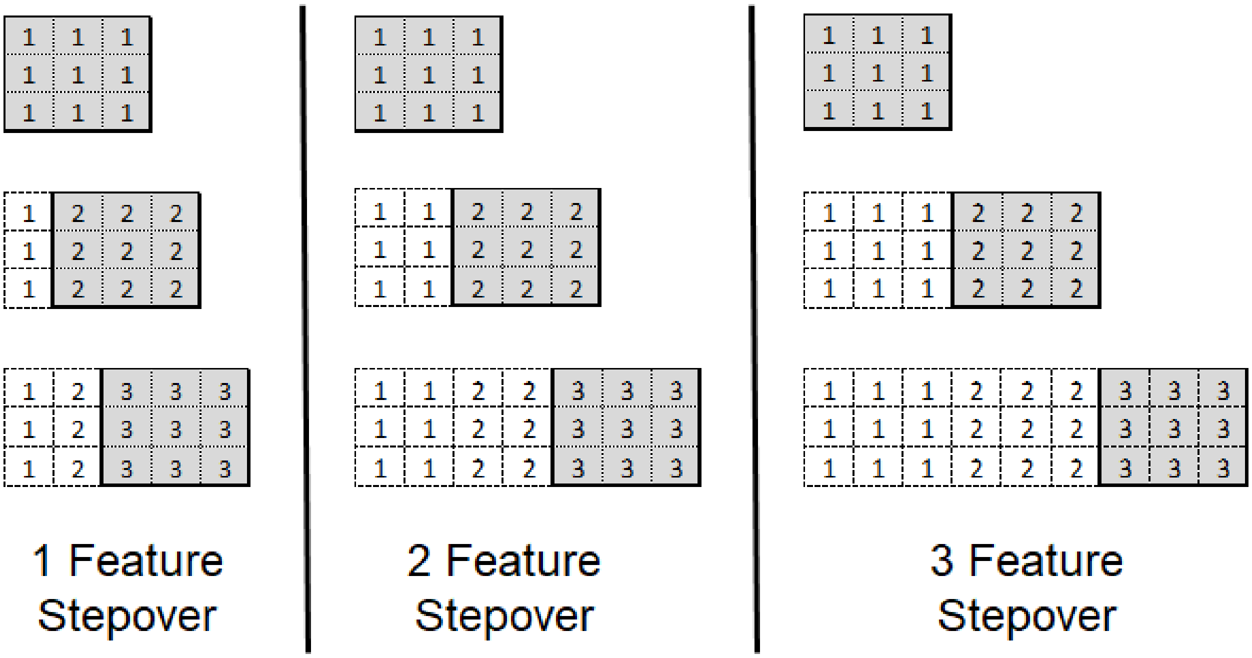

Figure 49. Stepover strategies

The plate was indented in a line in the machine's X-direction using various amounts of stepover. The machine's Z-axis was used to generate the indentation force, and the die was moved into the aluminum at a commanded velocity of 1 mm/min. Figure 49 shows these strategies, where each square represents one lens feature. The numbers represent the indent order, and the gray represents the current indent.

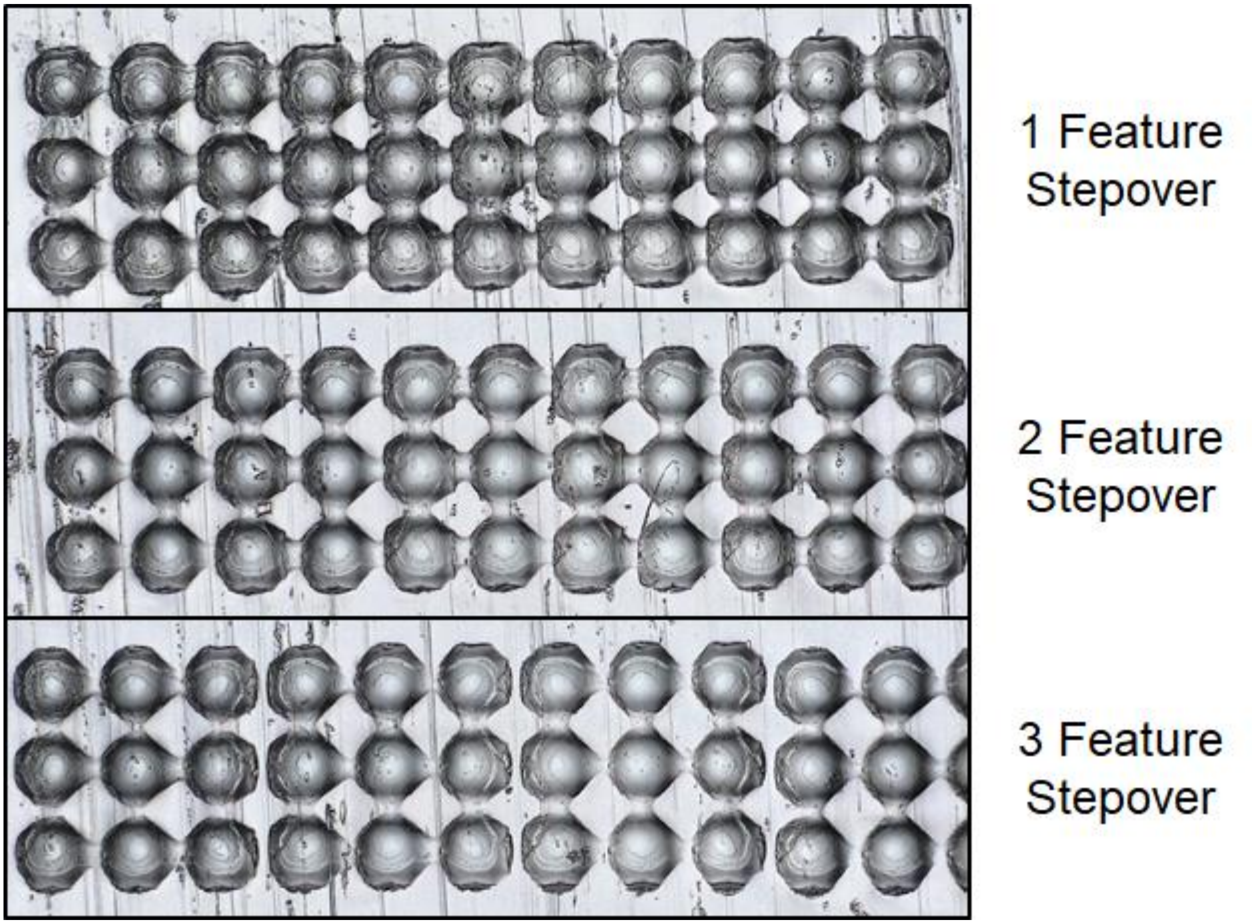

Figure 50. Indents with different amounts of stepover with a 3x3 die

Figure 50 shows the array of indents with the differing amounts of stepover. Qualitatively, the difference is subtle and hard to perceive in the optical images. Figure 51 shows profiles of each array of indents taken across the middle. The sectioning line is shown in Figure 52. In the 2 feature stepover profile, the bottom of the indents varies slightly every other indent. This is likely due to slight amount of die misalignment. The major issue is the 3 feature stepover, where every third peak is significantly taller. Upon inspection of Figure 52 which shows the profile aligned with the optical image of the indents, the taller peak appear to correspond to left edge of the die when a new set of 9 lenslets is created. This result suggests that some amount of overlap is necessary to prevent excessive material rise at the edge of the die.

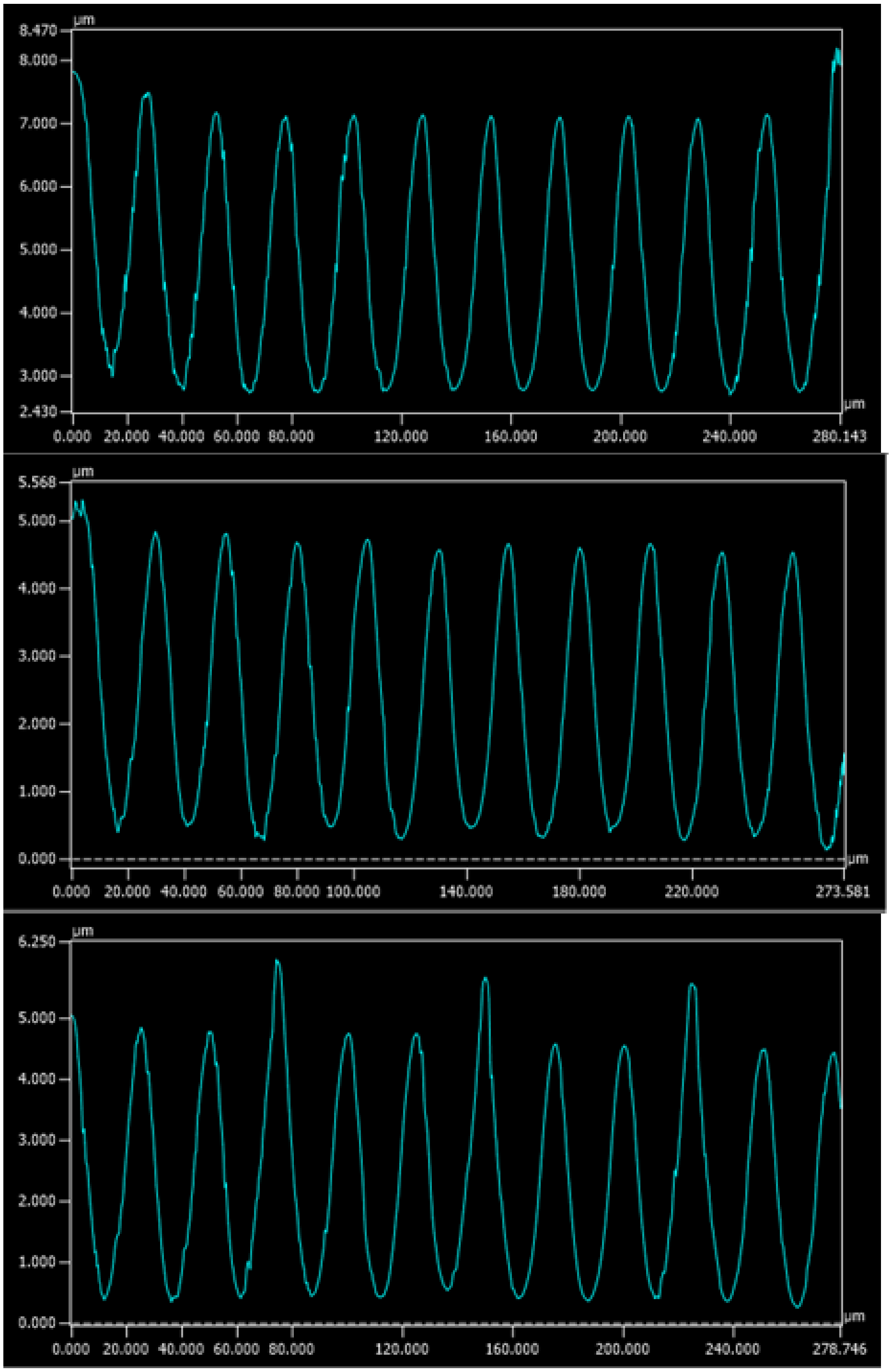

1 Feature Stepover

2 Feature Stepover

3 Feature Stepover

Figure 51. Measured profiles of the arrays of indents

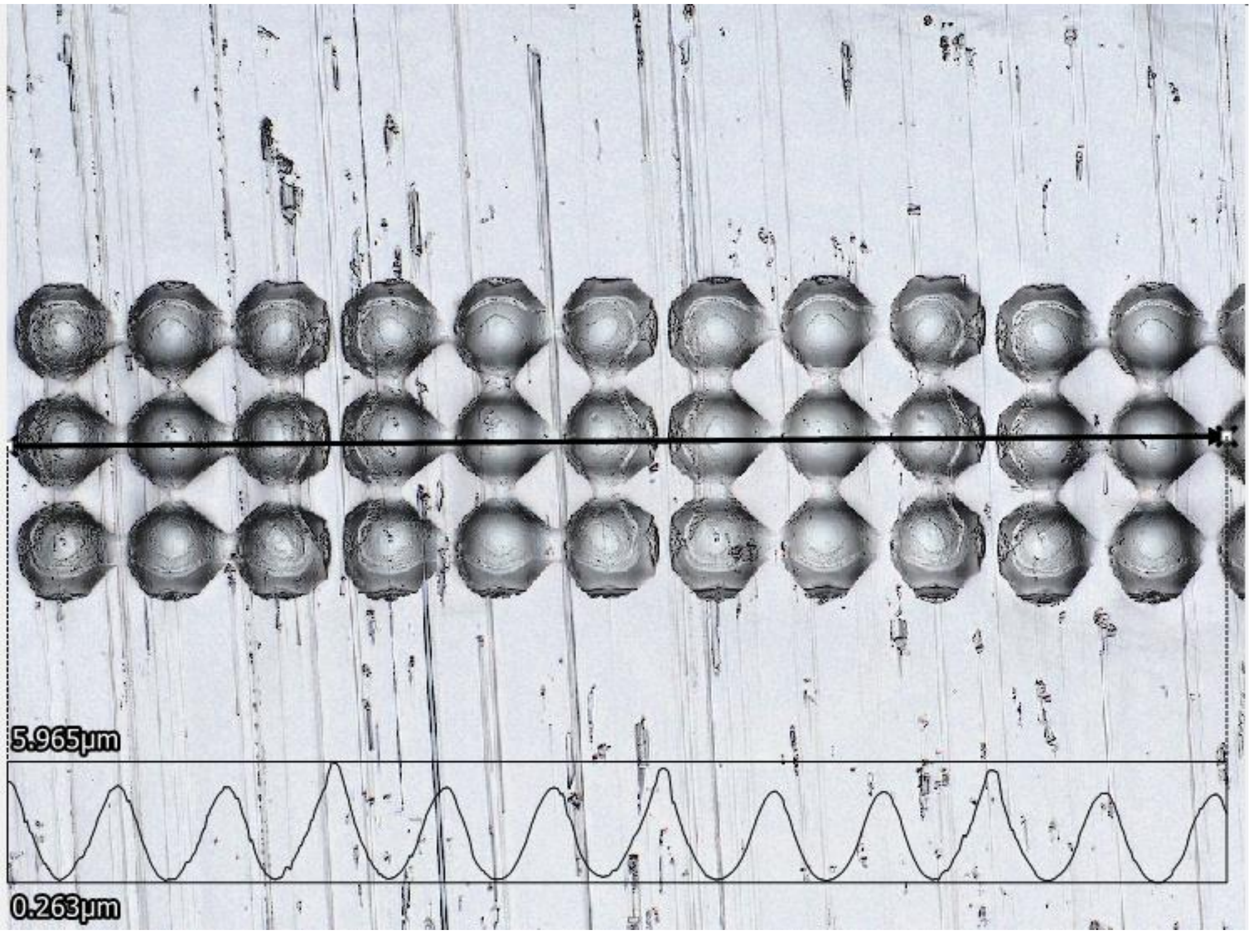

Figure 52. Profile of the array with a 3 feature stepover

Arrays in which the die is traversed along two axes were attempted by adjusting the microheight adjuster in the machine y-direction. However, it was determined that the microheight adjuster has significant error motion. In the setup shown in Figure 48, the electronic indicator measured the translation in the y-direction as the microheight adjuster is actuated. The microheight adjuster was moved to its lowest position, and then raised in 25 µm increments. The optical probe measured the relative motion in the z-direction between the tool post and the aluminum plate mounted on the spindle. This measurement was taken three times in the same location. Then the spindle was rotated 165° and another measurement was taken. Figure 53 shows the change in the z direction for each 25 µm step in the y direction. The single sample taken at the second location, labeled "Location 2-1", follows the same trend as the three samples taken at location 1. This indicates that the trend is not likely being caused by the form error of the aluminum plate and is the error motion of the microheight adjuster. The nonzero mean value in Figure 53 means the microheight adjuster could be aligned better. Alternatively, this z error can be compensated with the z slide of the diamond turning machine. Table 4 shows the average of the 4 measurements shown in Figure 53.

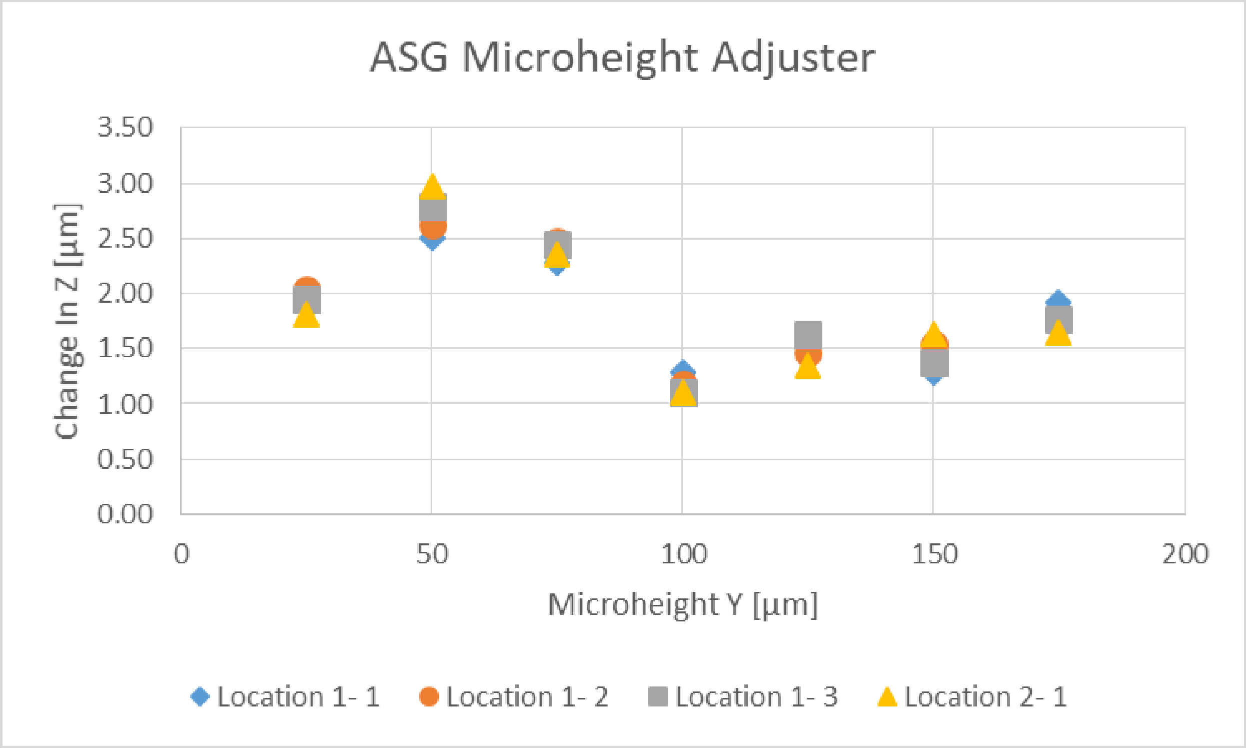

Figure 53. Measured Z error motion in the microheight adjuster

Table 4. Average Z error in the microheight adjuster

Height (µm)	Average ΔZ (µm)
25	1.96
50	2.72
75	2.39
100	1.17
125	1.52
150	1.46
175	1.77

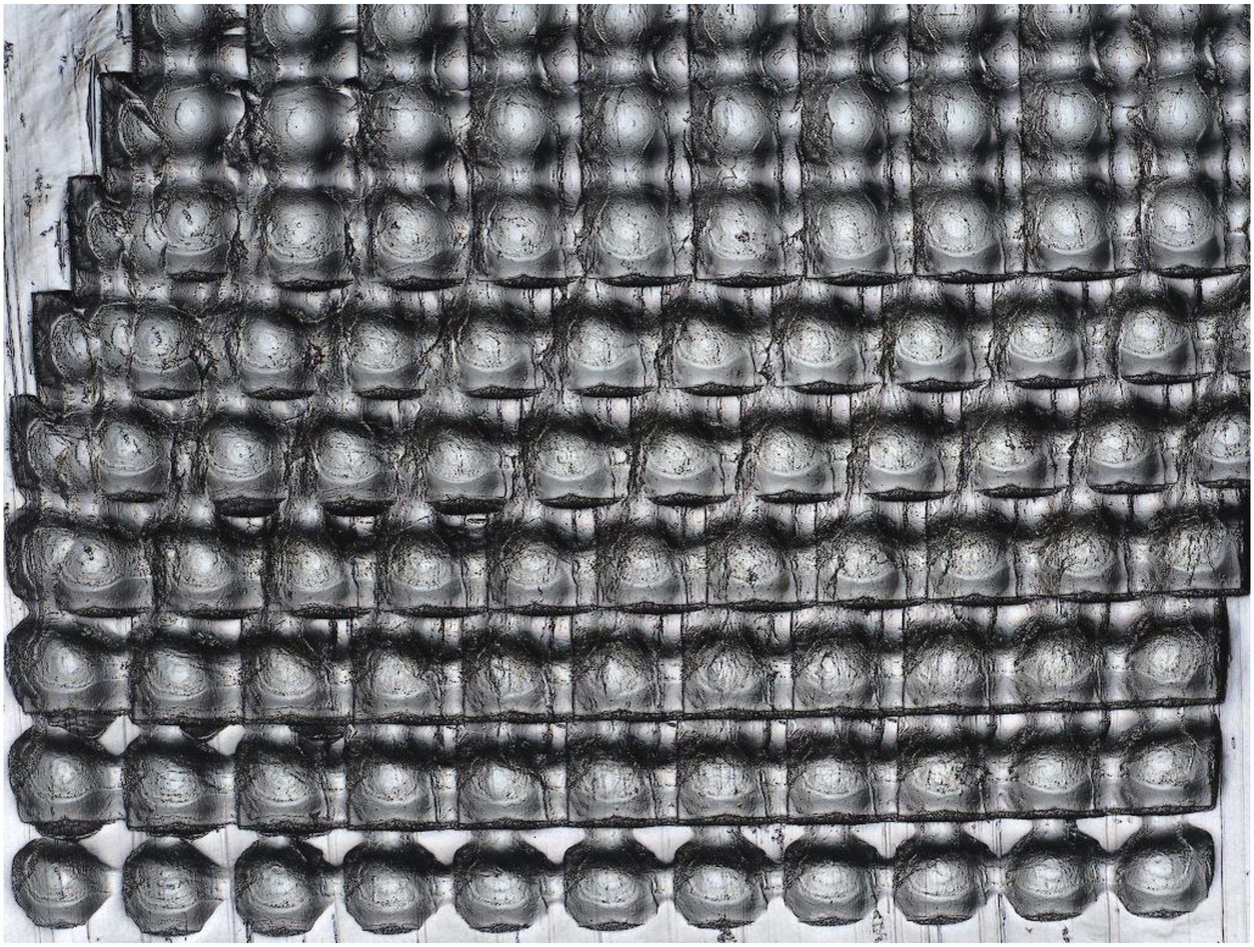

Figure 54. Array of indents actuated in the X (horizontal direction in the image) and Y (vertical direction in the image)

Figure 54 shows an array of indents created by rastering with a 1 feature stepover. At each step in Y the Z depth was adjusted based on the average value shown in Table 4. This Z correction was a little too aggressive and the indents become progressively deeper from bottom to top. Also there is a significant amount of X error in the microheight adjuster. By the final pass, the microheight adjuster has moved over 1 feature pitch in the x direction. These results indicate that the microheight adjuster is not adequate for creating these arrays. A different way to actuate in the y-direction needs to be found to study arrays that stepover in 2 directions.

3.8.3 High Speed Indentation

A lens array for a 3840 x 2160 4K display has approximately 8.3 million lenses spaced 25 µm center-to-center over a 96 by 54 mm area. The Nanoform 600 is capable of moving in 25 µm steps at a rate of about 2.4 Hz as shown in Figure 55. Although capable 50 mm/sec maximum velocity, only 7.26 mm/s is achieved before an axis has moved 25 µm when accelerating from a full stop. The axis is stationary for about 300 ms during which time a fast auxiliary actuator could make an indent.

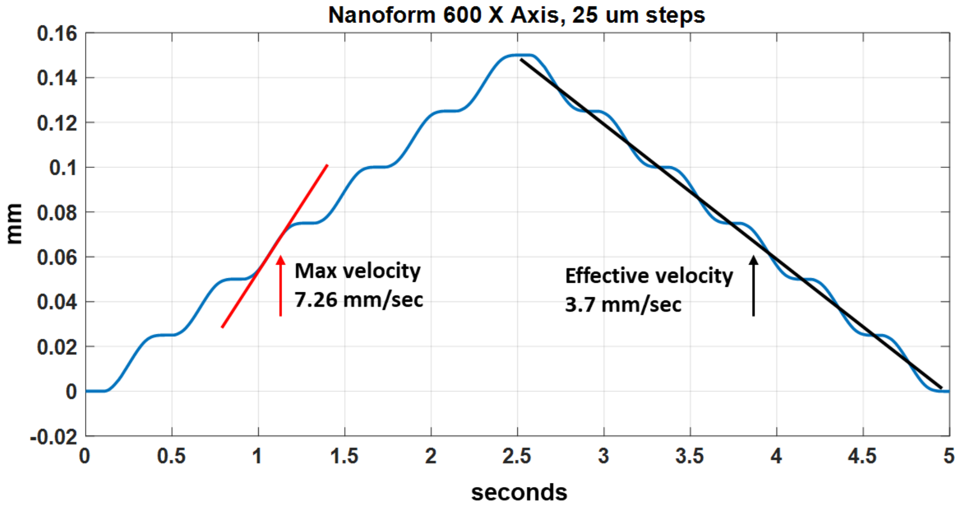

Figure 55. Step performance of the Nanoform 600

As shown in Figure 56, 48 days would be required to make a 4K lens array using the Nanoform. However at 200 Hz the process is a much more reasonable 12 hours. Higher acceleration planar XY stages capable of this step rate are available from Aerotech and ALIO Industries and are being proposed in the next phase of this project.

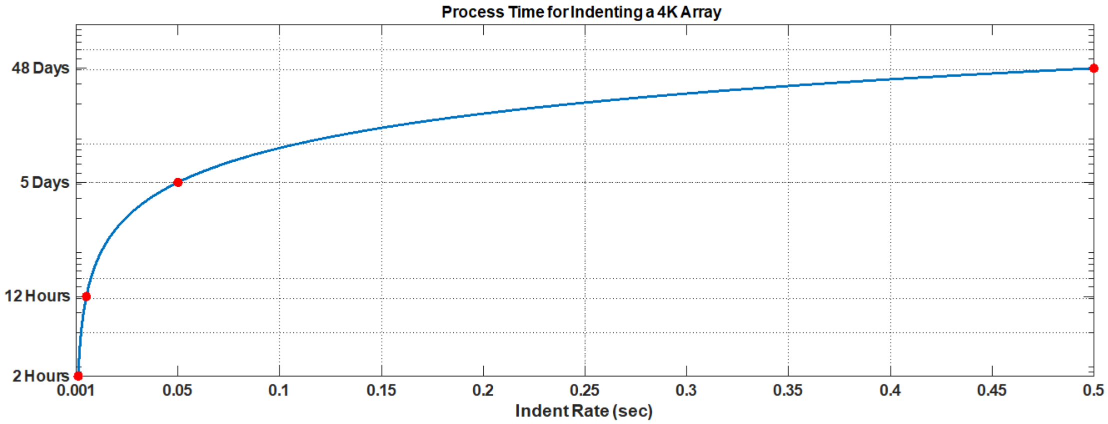

Figure 56. Process time vs indent rate for a 4K lens array. From left to right the red markers are 1 kHz, 200 Hz, 20 Hz and 2 Hz.

While the Nanoform 600 is not suitable for high speed indentation, a high speed actuator was investigated. The PEC built fast tool servo can provide the high speed actuation needed for each indent cycle. To test this concept a series of FTS motions were made with the servo mounted on the Nanoform Z axis. The servo was driven open-loop with a BK4050 arbitrary waveform generator. Modal commands were added to the Nanoform controller to trigger the BK4050 waveform at each step position. Figure 57 shows schematically how the FTS was commanded by the Nanoform 600. The wave used was the Lorentz function given in Equation 2.

$$L(x) = \frac{2}{\pi\,\Gamma\,(x-x_0)^2} \tag{2}$$

where x_0 is the abscissa of the peak value and the shape parameter Γ is the full width at half maximum. The FTS motion was measured with a capacitance gage. As shown in the plot in Figure 57, the FTS can move a small mass through a 14 µm excursion in less than 1 ms with good fidelity to this commanded waveform.

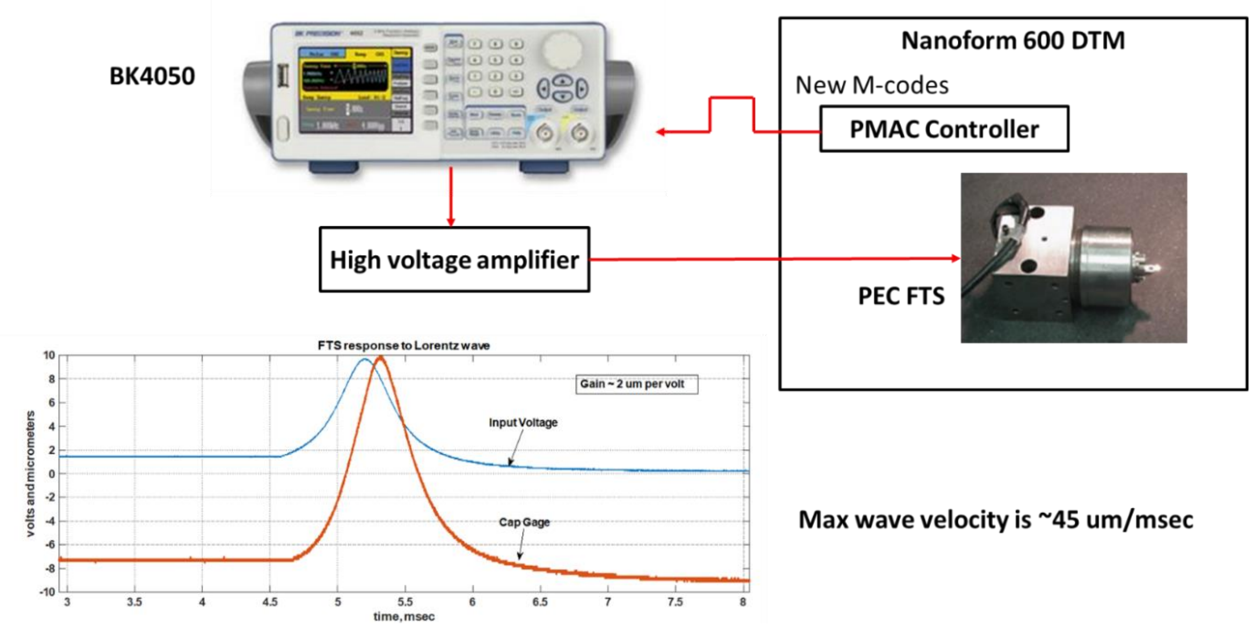

Figure 57. High velocity actuation using an arbitrary function generator and fast tool servo

After proving the motion of the FTS, a high speed indent test was performed with the ASG to test actual indentation. A glassy carbon 2x2 die was mounted in the FTS as shown in Figure 58. The FTS was commanded with a signal generator (BK Precision 4050) producing a single Lorentz wave. The period of the wave was set to 1000 ms, 20 ms, 10 ms, 6.7 ms and 5 ms (or 1 Hz, 50 Hz, 100 Hz, 150 Hz, and 200 Hz respectively). The motion of the FTS was measured with an internal capacitance gage. The measured displacement for the slowest and fastest indents are shown in Figure 59. As can be seen from the plot, the increased speed did not significantly attenuate the amplitude. Unfortunately, there was an issue with the touch off, so the surface comparison was difficult. However, the die did not appear to suffer any damage from indenting quickly.

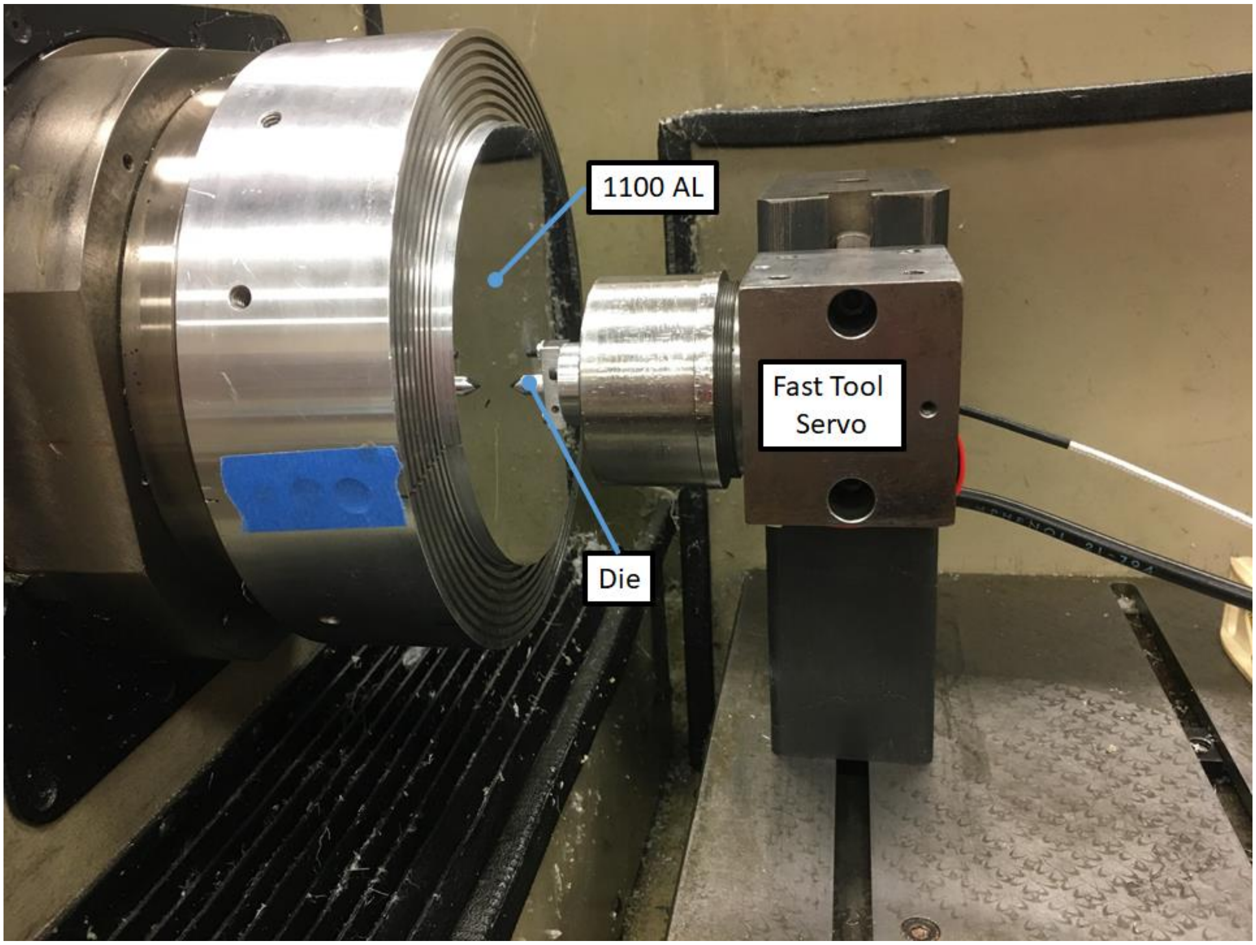

Figure 58. Indentation setup with a fast tool servo

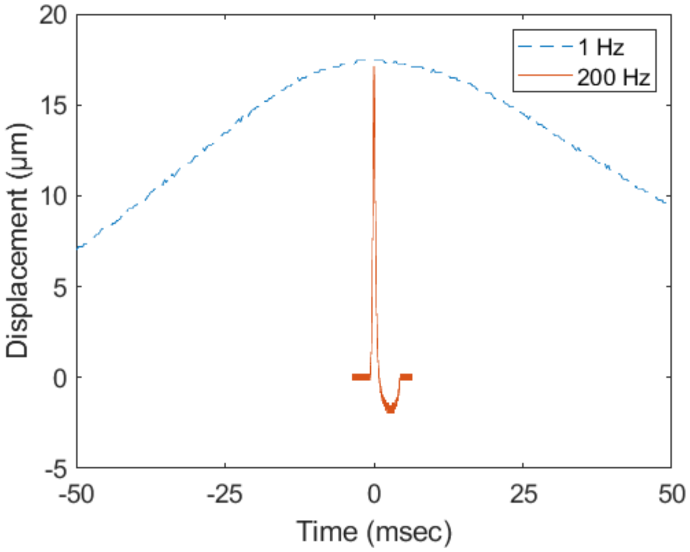

Figure 59. FTS displacement as measured by an internal capacitance gage

3.9 CONCLUSIONS

This work demonstrates the feasibility of creating a glassy carbon die with microscale features using focused ion beam milling. Spherical lens shapes were FIB milled into glassy carbon. A error correction method was implemented to improve the form. Spherical surfaces were FIB milled which were within 250 nm of the desired spherical radius over a 15 µm aperture. It was found that the border should not be FIB milled before the lens features to avoid degrading the surface with redeposition. Also the minimum amount of ion dose should be relatively high even at the apex of the lens features where little material is to be removed. This will prevent stray ions in the beam tails from significantly degrading the finish. In the bitmap patterns, the overlap should be approximately the same as the beam diameter. A maximum dwell time of 100 µs has been shown to produce good results. Low maximum dwell times such as 1 µs reduces the quality of the surfaces.

A method of preparing a glassy carbon indenter blanks suitable for indenting was developed. Parameters for diamond turning glassy carbon were found which could achieve 5 nm surface finish. The lens features were FIB milled into the glassy carbon indenter blanks. These features were then replicated in an aluminum workpiece by indenting. The indentation experiments showed that some amount of overlap is needed to prevent pile up from deteriorating previously made features.

Future work will focus on improving the form and finish of the FIB milled die and the indentations. Specifically, the ripple in the FIB milled glassy carbon will be investigated. Error compensation of the FIB milled lens features will continue to be developed. The Matlab simulation tool will be improved to run faster and assist in planning bitmaps. The indentation process will also continue to be explored. The transfer function of the indentation process will be quantified and error compensation for the indentation will be investigated.

REFERENCES

[1] E. Zdanowicz, Nanocoining Sub-Micron Features, Raleigh NC: North Carolina State University, 2013.

[2] T. A. Dow, E. Zdanowicz, A. Sohn, R. Scattergood and W. J. Nowak, "Method and System for Fast Imprinting of Nanometer Scale Features in a Workpiece". Patent 0141265 A1, 24 May 2018.

[3] Y. Yoshida, W. Okazaki and T. Uchida, "Laser and focused ion beam combined machining of micro dies," *Review of Scientific Instruments,* vol. 83, no. 02B901, 2012.

[4] M. Langridge, D. Cox, R. Webb and V. Stolojan, "The fabrication of aspherical microlenses using focused ion-beam techniques," *Micron,* vol. 57, pp. 56-66, 2014.

[5] S. W. Youn, M. Takahashi, H. Goto and R. Maeda, "A study on focused ion beam milling of glassy carbon molds for the thermal imprinting of quartz and borosilicate glasses," *Journal of Micromechanics and Microengineering,* vol. 16, pp. 2576-2584, 2006.

[6] D. Adams, M. Vasile and T. Mayer, "Focused ion beam sculpting curved shape cavities in crystalline and amorphous targets," *Journal of Vacuum Science & Technology B,* vol. 24, pp. 1766-1775, 2006.

[7] M. Shi, B. Lane, C. Mooney, T. Dow and R. Scattergood, "Diamond tool wear measurement by electron-beam-induced deposition," *Precision Engineering,* vol. 34, pp. 718-721, 2010.

[8] M. Vasile, R. Nassar, J. Xie and H. Guo, "Microfabrication techniques using focused ion beams and emergent applications," *Micron,* vol. 30, pp. 235-244, 1999.

[9] D. Adams, M. Vasile, T. Mayer and V. Hodges, "Focused ion beam milling of diamond: Effect of H2O on yield, surface morphology and microstructure," *Journal of Vacuum Science & Technology B,* vol. 21, no. 6, pp. 2334-2343, 2003.

[10] X. Ding, G. Lim, C. Cheng, D. Butler, K. Shaw, K. Liu and W. Fong, "Fabrication of a micro-size diamond tool using a focused ion beam," *J. micromech. Microeng.,* vol. 18, 2008.

4 MICROSCALE LENS ARRAY: MODELING OF THE MICROINDENTATION PROCESS

Sumit Gundyal
Graduate Student
Dr. Mark Pankow
Assistant Professor
Mechanical and Aerospace Engineering

ABSTRACT

This report addresses the design of multi-indenter die and development of indentation strategies to create the negative features of a microlens array on a mold. Initially, correlation of quasi-static nanoindentation results of FEA models to the experimental results is obtained to gain confidence in the models. A material parameter study is performed using commercial finite element analysis software Abaqus™ to understand the effects of different material properties on the spring back amount, pile-up and the maximum force required. Al 1100 is selected as the mold material based on this study. Glassy carbon is used as the die material. Possible drawbacks in the design of the multi-indenter die and the different indentation strategies are discussed.

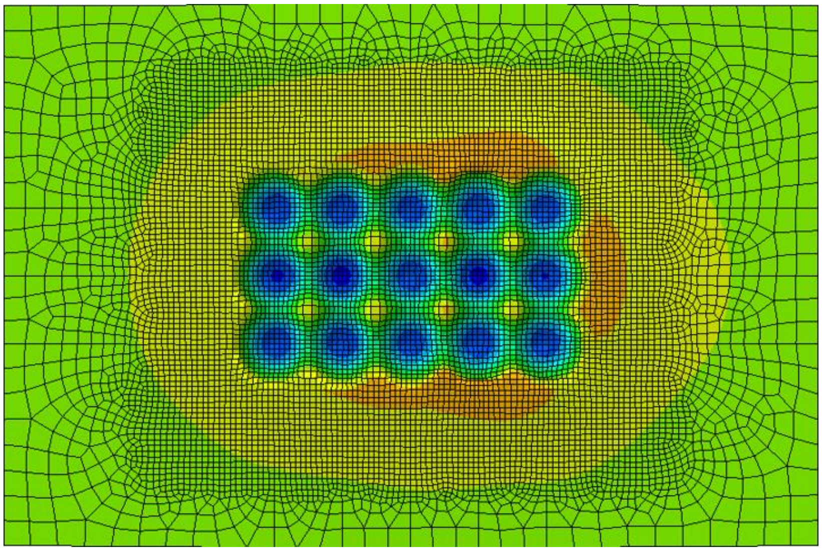

4.1 INTRODUCTION

Electronics in today's age with their continued reduction in size demand for small size optics. Digital projectors use micro-lens array to focus light to generate the image to be projected. Similarly, 3D displays free of 3D glasses also use the arrays of micro-lens to create the desired effect. Section 3.1 Figure 1 shows the cross-sectional view of a micro-lens array and a ray trace of a single lens. To create such a lens array, a male die made of a hard material with around 4-9 lens features shown in Section 3.1 Figure 2 needs to be pushed rapidly into a mold specimen by an actuator to plastically deform the surface and transfer the die features on to the mold. This mold will be used in a conventional compression or injection molding machine to create the final lens array that will be like as shown in Section 3.1 Figure 1.

The aim of this report is to develop a validated FEA model to understand this microindentation process to fabricate the microlens array. Glassy carbon is used as the die material owing to its high compressive yield stress and ease of carrying out focused ion beam milling process to create micron length features on it. This process involves problems: spring back of the indents; shape distortion of the surrounding indents due to plastic flow of successive indents; deformation of the die during the indentation; and pile-up of the mold material around the indents. These issues negatively affect the optical performance of the microlens array. This report attempts to study these issues in more detail and mitigate them by designing a die and developing indentation strategies.

To create around 4 million lenses quickly the indentations must be done fast. Strain rate dependency of the mold material must be accounted for to understand the effect of fast indentation. Currently, due to limitations in data acquisition from high-velocity indentation experiments, correlation of FEA models to fast indentation experiments is not addressed in this report. Although, the effect of dynamic indentation is presented.

4.2 MATERIAL PARAMETER STUDY

The microindentation process involves pressing a die with lens features on a relatively softer mold material. Material with high compressive yield stress is ideal for a die which helps prevent it from deforming plastically during indentation. Glassy carbon has a relatively very high yield stress of 700 MPa compared to any usual mold material. It is also conducive to use glassy carbon as a die material due to the ease of carrying out "focused ion beam milling" process on it. To understand the effect of material properties of mold on the final indent shape and the indention force required it is necessary to do a mold material parameter study. This would also aid in deciding a suitable mold material.

This study is conducted by developing a computational model of a quasi-static micro-indentation process of a rigid spherical die of radius 20 μm indenting into a rectangular cuboid. The material properties that would be varied are elastic modulus, yield stress, and tangent modulus. Elastic modulus is the slope of the stress-strain curve of the material during the initial elastic response. Yield stress is the stress at which the mold material starts deforming plastically. Tangent modulus is the slope of the stress-strain curve in the plastic region. These terms are shown in Figure 1. The effect of these parameters on spring back, pile-up of the mold material and the indentation force required is studied. Spring back is the elastic recovery that occurs after the indenter is unloaded. This results in the actual indent depth to reduce after the unloading. For softer mold materials, as the strain in the mold enters the plastic region the material is pushed out of the indent cavity which leads to pile-up around the periphery of the indent. Indentation force is the reaction force experienced by the indenter when the indentation is progressing. The role of friction on the indent shape and the indentation force required will be explored as well. Strain rate dependent behavior will also be addressed.

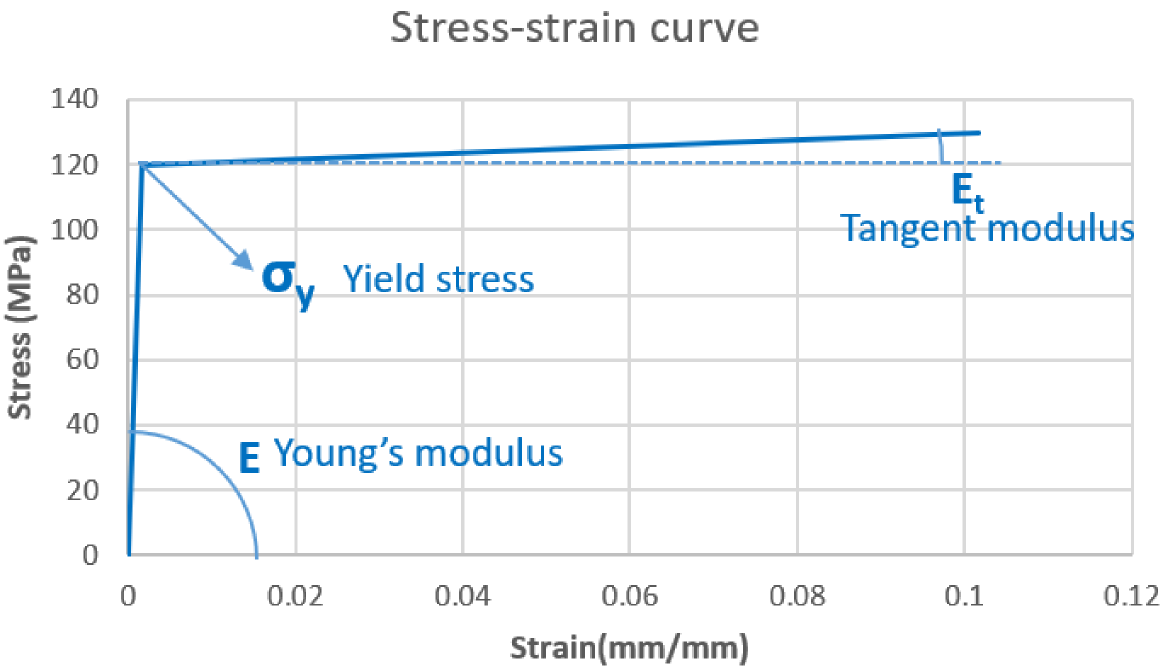

Figure 1. Stress-strain curve of a hypothetical bilinear elastic-plastic material

4.2.1 Finite element modeling

For the finite element modeling, Abaqus^{TM} commercial software was used. A 2D axisymmetric model was employed for the finite element modeling of the indentation process of a rigid spherical die on a mold specimen. The schematic representation of the model is shown in Figure 2. The indenter was meshed with RAX2 elements: 2 node linear axisymmetric rigid link elements and the mold specimen was meshed with CAX4R elements: 4 node bilinear axisymmetric quadrilateral, reduced integration, hourglass control elements as shown in Figure 3. The mold specimen was meshed with uniform density. Non-linear geometry option was used in the finite element simulation. Arbitrary Lagrangian Eulerian (ALE) adaptive mesh domains was defined for the mold specimen as it involved large deformations. Surface-to-surface contact condition was used with the Indenter as the master surface and the mold surface as the slave surface since a master surface can penetrate the slave surface. Frictionless contact was considered. Isotropic hardening material behavior was used to model the plasticity region of the material. Proper boundary condition was applied wherever necessary.

Abaqus/Explicit which implements the explicit solution method to solve the model was used for this simulation. Since a quasi-static process is, by definition, a long-time solution, it is often computationally expensive to simulate an event in its natural time scale. The advantage of using Abaqus/Explicit is that the event can be accelerated while keeping inertial forces very low leading to faster solution times. Also, explicit procedure solves contact problems with greater ease as compared to implicit procedure [1].

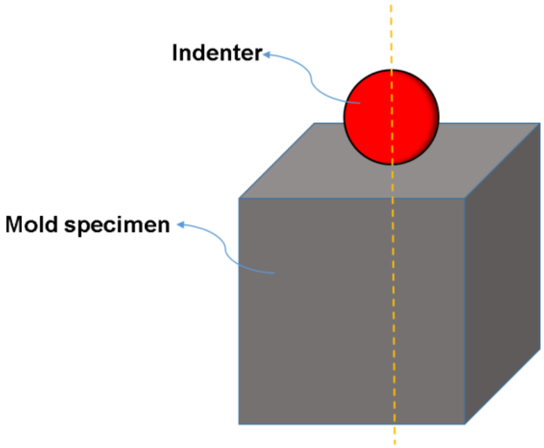

Figure 2. Schematic representation of the finite element model of the rigid spherical indenter and mold specimen

The simulations were performed by indenting the indenter of radius 20 μm to a depth of 10 μm from the mold surface and then unloading it back to the same position. The step time for the loading period is 1.2e-5 seconds which is very fast compared to a quasi-static process. The indenter is displaced at a constant velocity. Comparison of the kinetic energy and internal energy of the system obtained from the output results shows that the kinetic energy is less than 5% of the internal energy. This ensures the inertial effects are kept to the minimum.

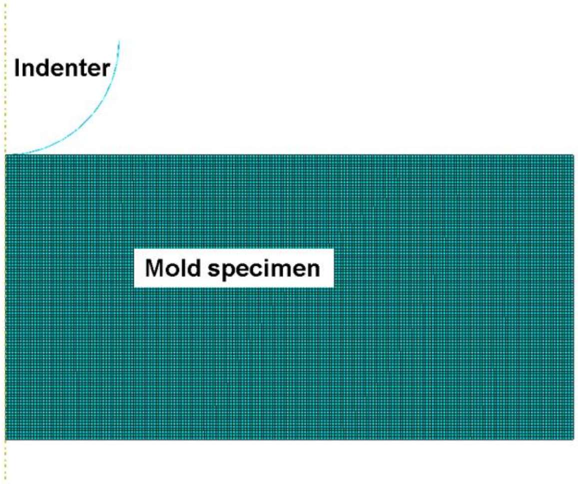

Figure 3. Mesh pattern used for the finite element model of the rigid spherical indenter and mold specimen

Young’s modulus as the input parameter

In the first study, the yield stress and the tangent modulus is kept constant at 120 MPa and 0.1 GPa respectively. The effect of varying Young’s modulus on the indent shape and the indentation force required is observed. The results can be anticipated in a bilinear stress-strain curve of a hypothetical material as shown in Figure 4

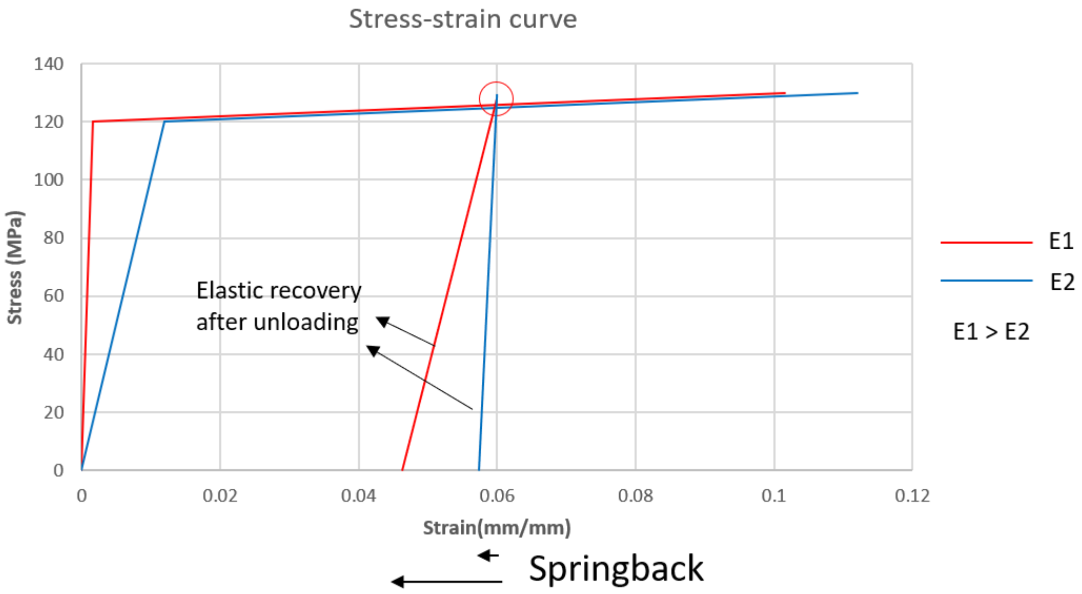

Figure 4. Effect of varying Young’s modulus on the spring back and indentation force required

As Young’s modulus is increased the spring back amount is expected to reduce considerably while the indentation force required is expected to increase by a negligible amount. Young’s modulus of 75 GPa, 60 GPa, and 45 GPa are used for the first study. As can be seen in Figure 5 spring back amount reduces with increasing Young's modulus while the force-displacement curves shown in Figure 6 shows that the force increases by a negligible amount. Figure 7 shows that the pile-up increases in height with increasing Young's modulus.

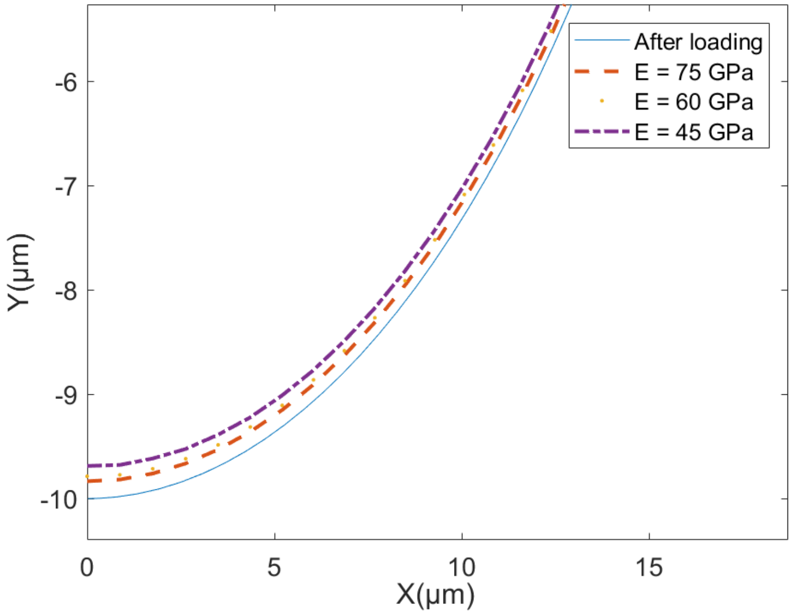

Figure 5. Spring back amount comparison for varying Young's modulus

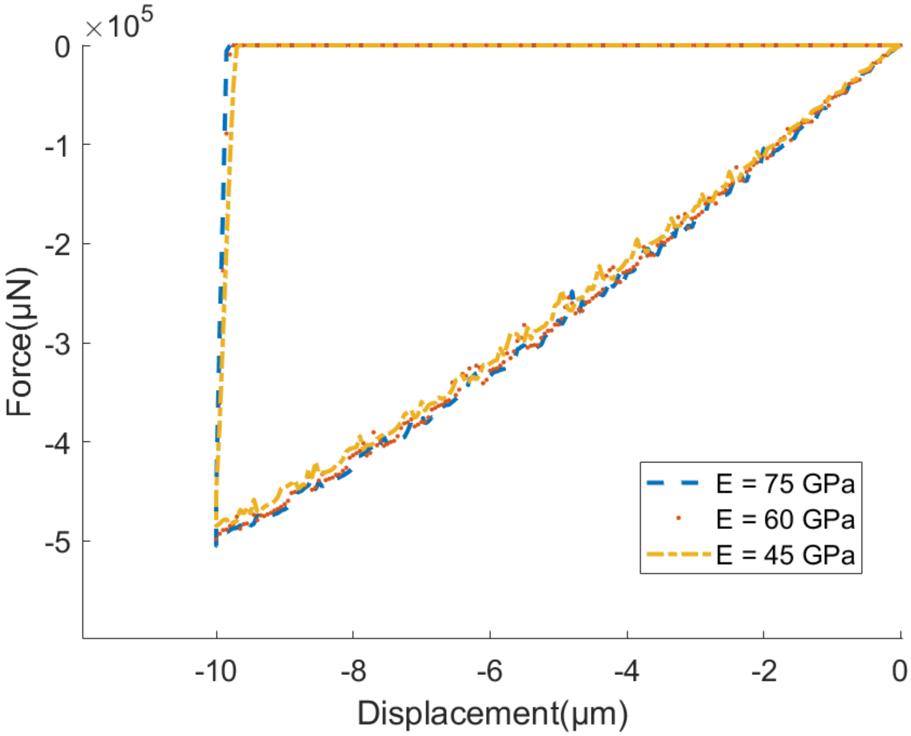

Figure 6. Force vs displacement curve comparison for varying Young's modulus

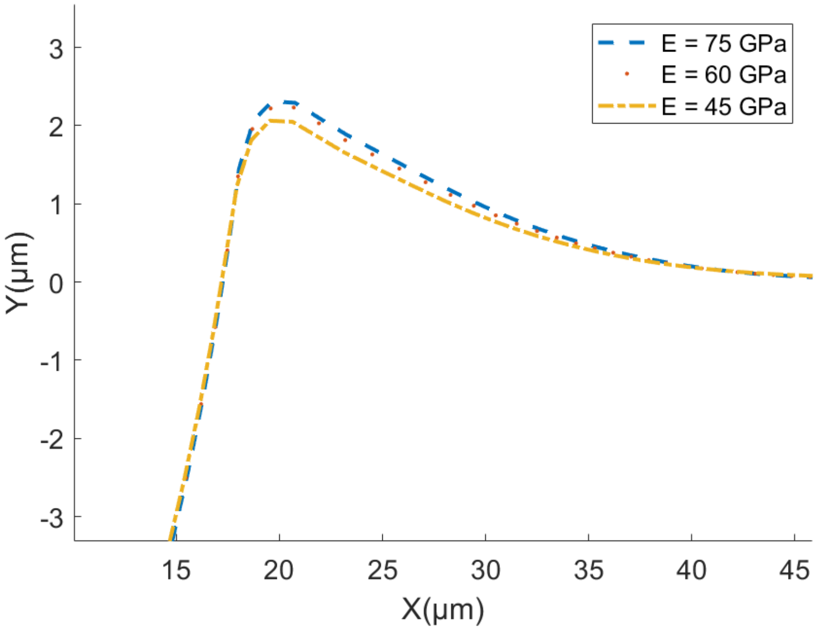

Figure 7. Pile-up comparison with increasing Young's modulus

Yield stress as the input parameter

In the second study, Young's modulus and the tangent modulus is kept constant at 75 GPa and 0.1 GPa respectively. The effect of varying yield stress on the indent shape and the indentation force required is observed. The results can be anticipated in a bilinear stress-strain curve of a hypothetical material as shown in Figure 8.

As the yield stress is increased the spring back amount and the indentation force is expected to increase considerably. The yield stress of 80 MPa, 120 MPa, and 200 MPa are used for the second study. As can be seen in Figure 9 spring back amount increases with increasing yield stress. Similarly, the pile-up height increases with increasing yield stress while the pile-up spread reduces with increasing yield stress. This is shown in Figure 11. The force-displacement curves shown in Figure 10 shows that the force increases by a considerable amount as well.

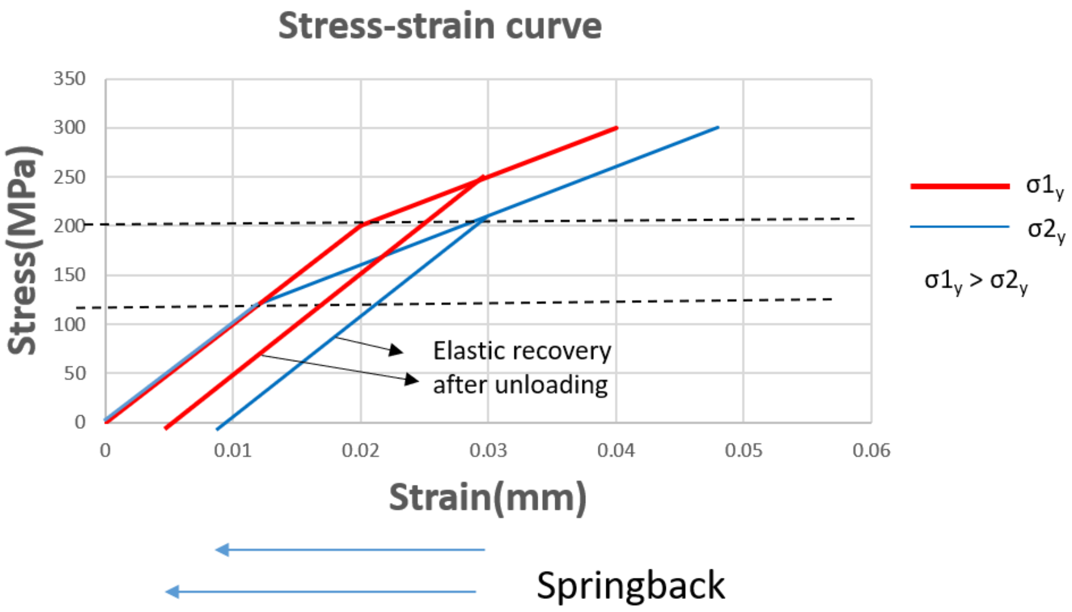

Figure 8. Effect of varying yield stress on the spring back and indentation force required

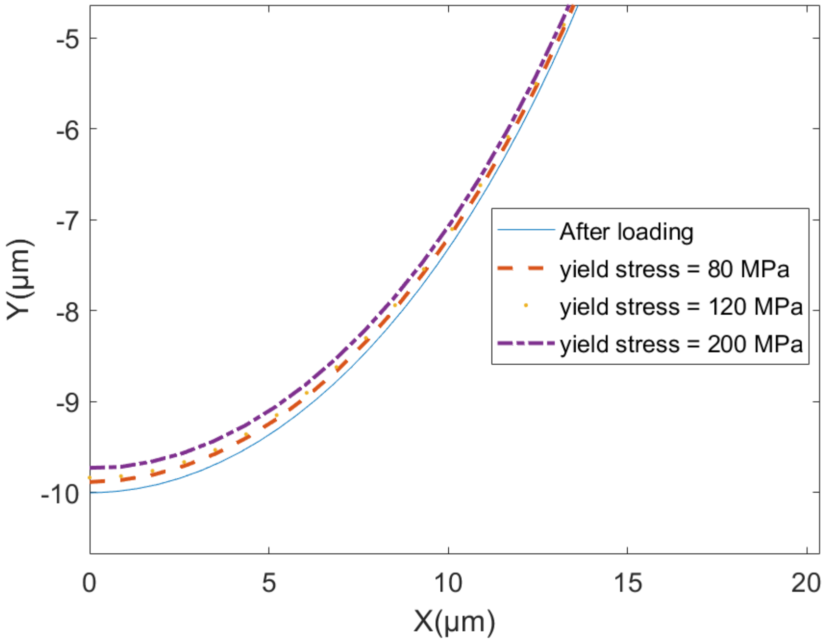

Figure 9. Spring back amount comparison for varying yield stress

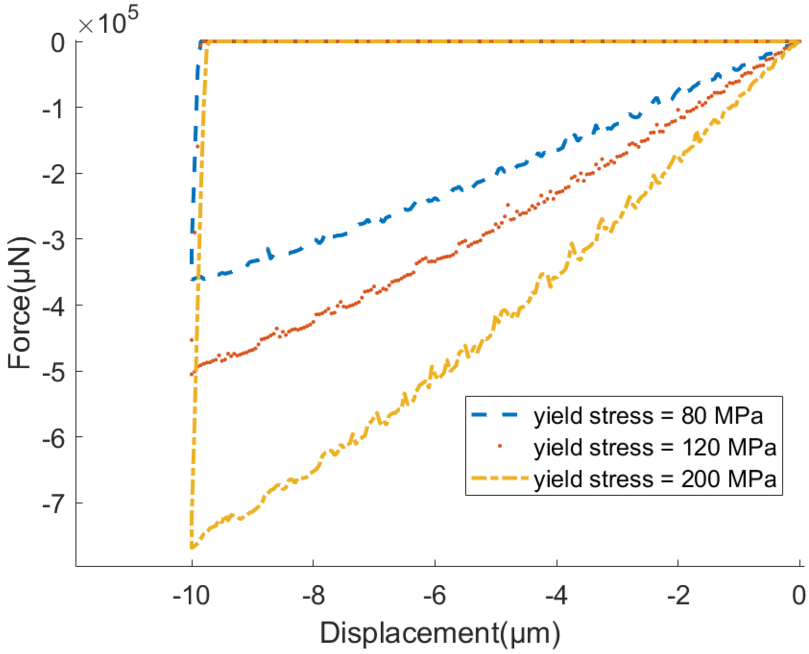

Figure 10. Force vs displacement curve comparison for varying yield stress

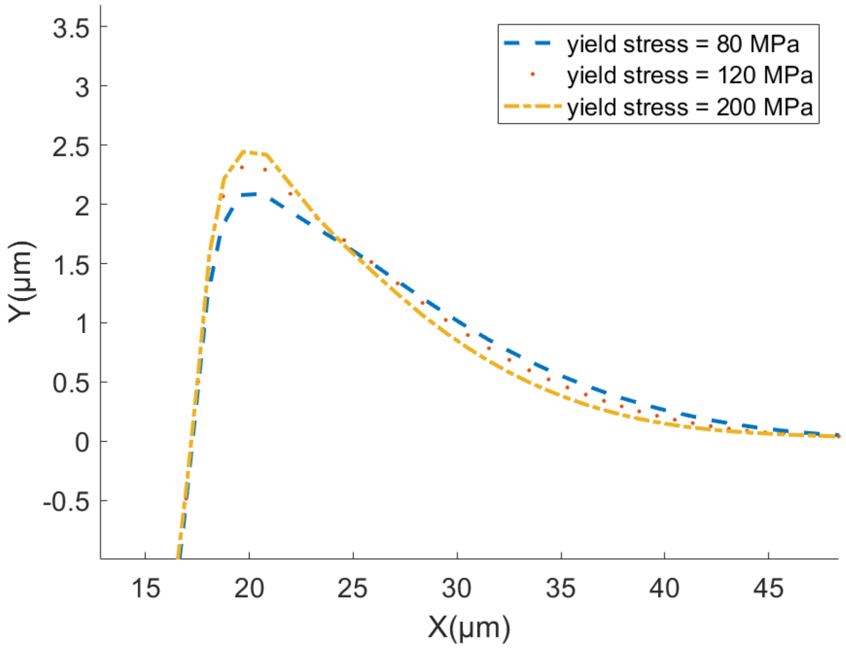

Figure 11. Pile-up height and spread comparison with increasing yield stress

Tangent modulus as the input parameter

In the third study, Young’s modulus and the yield stress is kept constant at 75 GPa and 120MPa respectively. The effect of varying the tangent modulus on the indent shape and the indentation force required is observed. The results can be anticipated in a bilinear stress-strain curve of a hypothetical material as shown in Figure 12

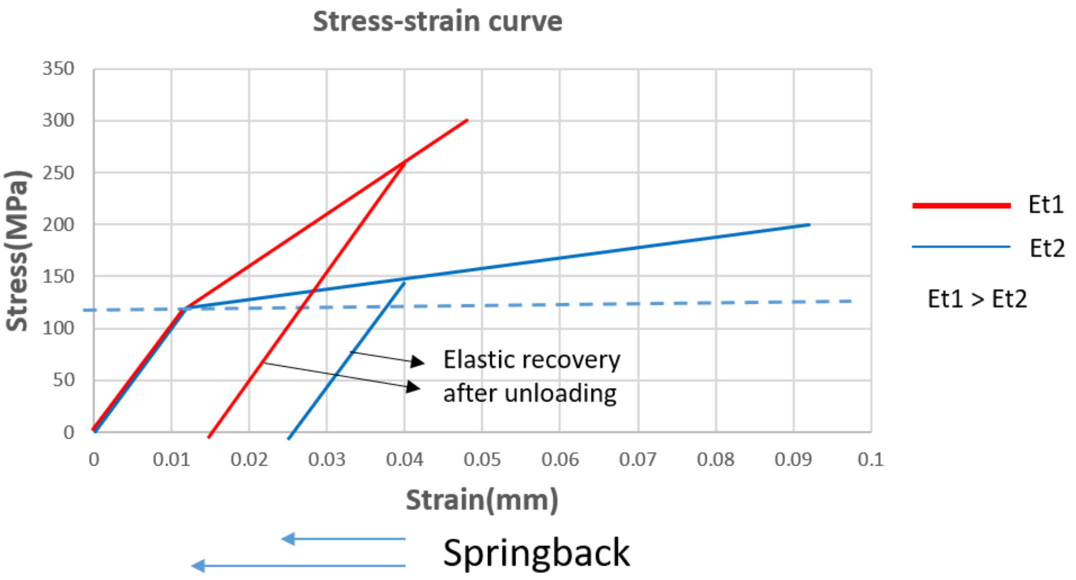

Figure 12. Effect of varying tangent modulus on the spring back and indentation force required

As the tangent modulus is increased the spring back amount and the indentation force is expected to increase. Tangent modulus of 0.1 GPa, 1 GPa, and 10 GPa are used for the third study. As can be seen in Figure 13 spring back amount increases with increasing yield stress. The pile-up height decreases with increasing tangent modulus while the pile-up spread increases with increasing tangent modulus. This is shown in Figure 15. The force-displacement curves shown in Figure 14 shows that the force increases by a considerable amount as well.

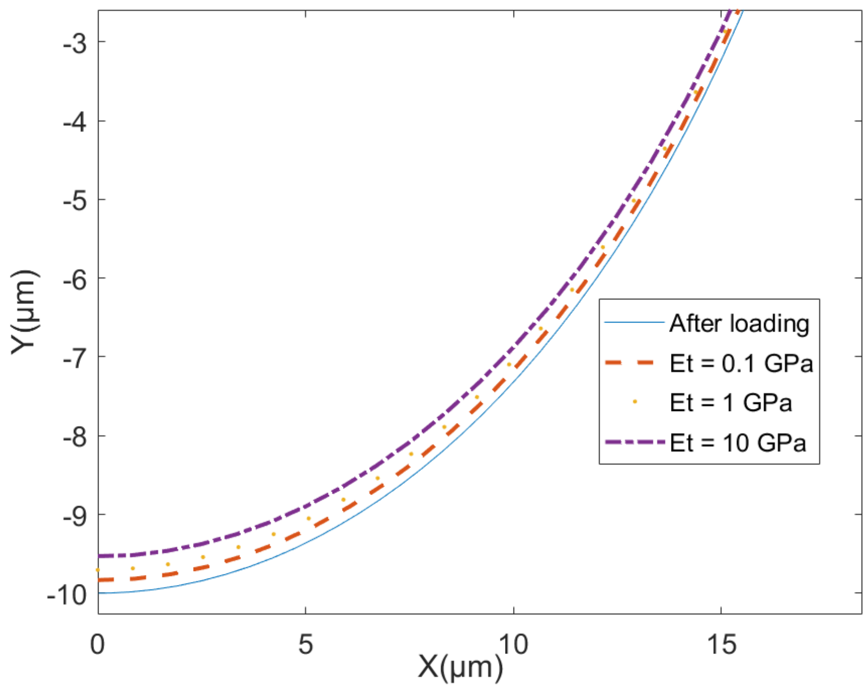

Figure 13. Spring back amount comparison for varying tangent modulus

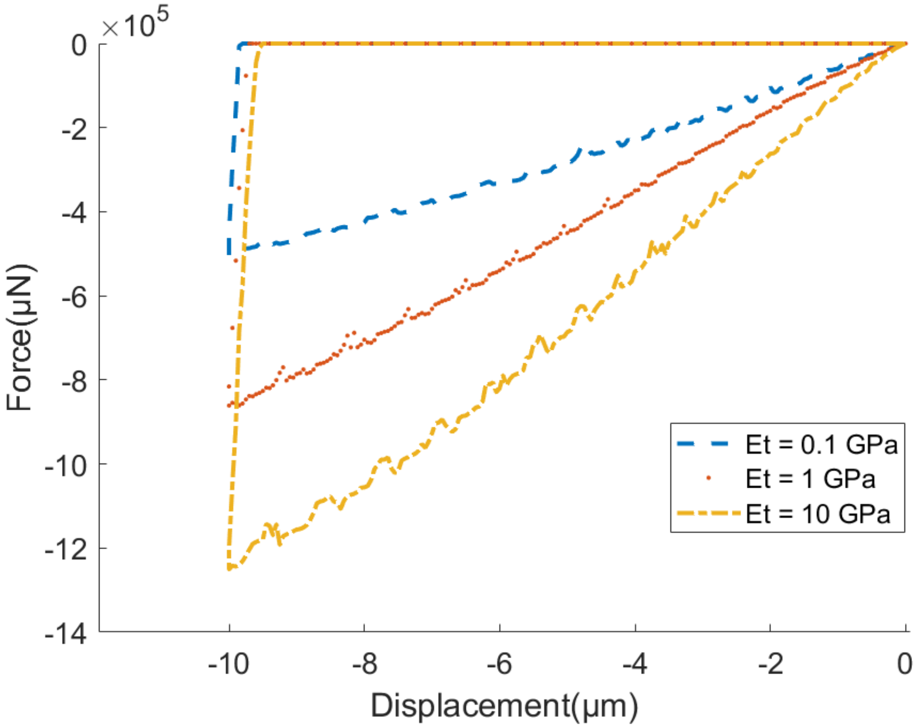

Figure 14. force vs displacement curve comparison for varying tangent modulus

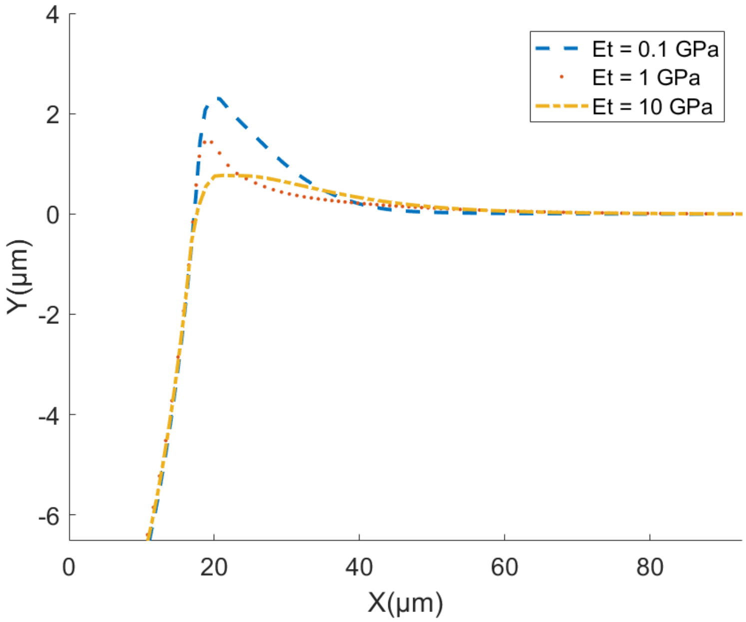

Figure 15. Pile-up height and spread comparison with increasing tangent modulus

Table. 1 shows the summary of the above studies. It shows how the output parameters: spring back, pileup, and indentation force required are related to the material properties of the mold. This study provides important insights into how the material flow behavior depends on various aspects of the material properties. This helps to select the most suitable mold material. For all the indentation experiments and simulation, Al 1100 - H14 is chosen as the mold material. Owing to its high Young's modulus and comparatively low yield stress the spring back amount experienced will be relatively very low. Figure 16 shows the results of the tensile test performed on Al 1100 - H14. The Young's modulus of the sample tested was 75.7 GPa and the yield stress was 114 MPa.

Table 1. Summary of the material parameter study

	Indentation Outputs		
Material parameters	Pile-up height	Spring back	Maximum force
Elastic modulus ↑	↑	↓	=
Tangent modulus ↑	↓	↑	↑
Yield stress ↑	↑	↑	↑

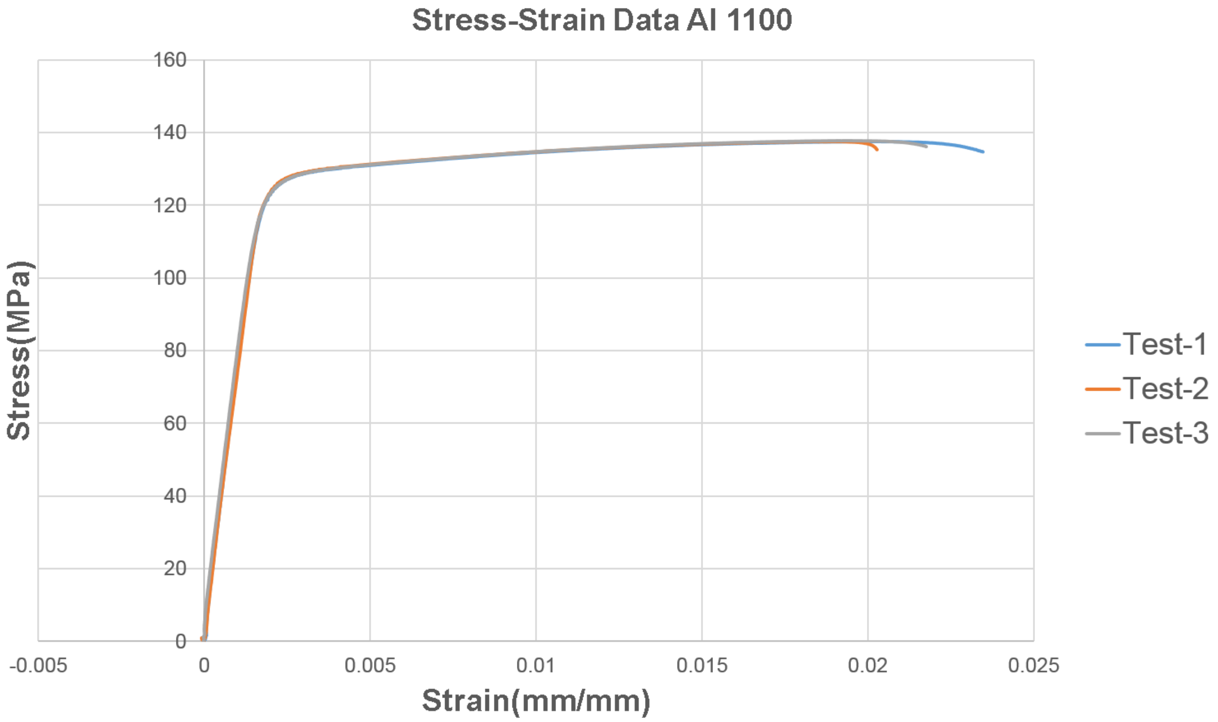

Figure 16. The stress-strain curve from a tensile test of Al 1100-H14

Effect of friction

Friction between the indenter and the mold specimen plays a major role in affecting the pile-up height and spread around the indenter whereas it has no significant effect on the indentation force required. Material properties obtained from the tensile test of Al 1100 were used for the material definition of Al 1100 in Abaqus. Isotropic hardening rule is employed to model the plasticity region of Al 1100. The same setup as shown in Figure 2 and Figure 3 is used for this study.

Models with friction coefficient of 0.1, 0.2, 0.3, and 0.4 are simulated and the results are compared with frictionless models. Penalty method is used for the friction formulation between the indenter surface and the mold surface. Figure 17 shows that as the friction coefficient is increased the pile-up height decreases and the pile-up spread increases. The force vs displacement curve comparison shows that friction does not have significant effect on the indentation force required as shown in Figure 18 with indentation forces varying only by 0.15 N for friction coefficient varying from 0 to 0.4.

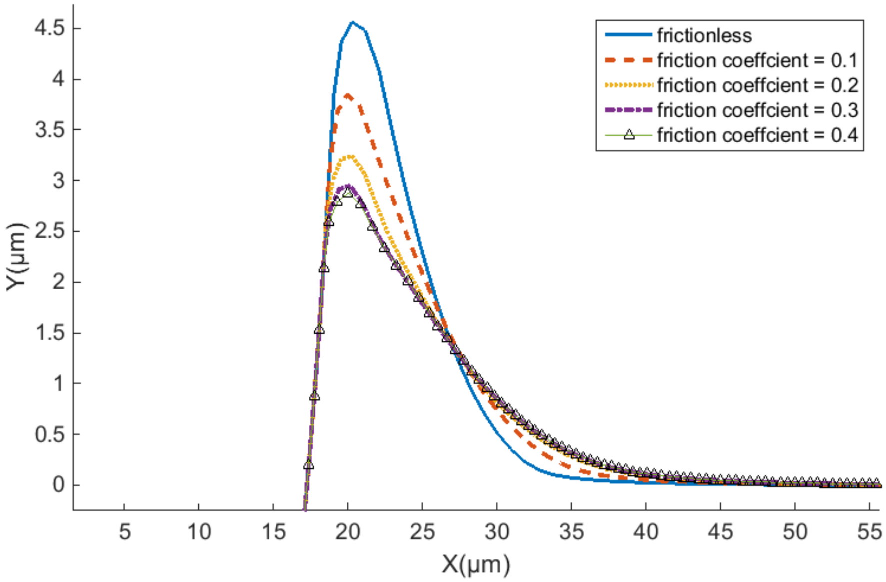

Figure 17. Pile-up height and spread comparison for varying friction coefficient

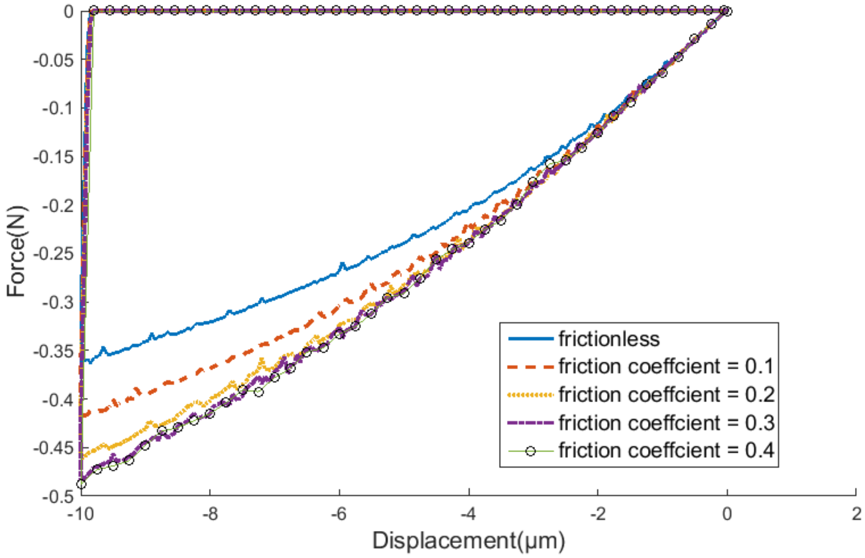

Figure 18. Force vs displacement curve comparison for varying friction coefficient

4.3 CORRELATION OF NANOINDENTATION EXPERIMENTS AND FINITE ELEMENT SIMULATIONS

Correlation of microindentation experiments and finite element simulations is important to gain confidence in the results from the models. Accurate prediction of the final indent shape and the force vs displacement curves will aid in designing the final die and developing indentation strategies. For this purpose, initially, nanoindentation experiments were conducted on Al-1100-H14 sample and glassy carbon sample using Hysitron TI-980 Nanoindenter provided by the Analytical Instrumentation Facility (AIF) at North Carolina State University and finite element models were developed to validate these experiments. This potentially helped in extracting the material properties of Al 1100 and glassy carbon.

4.3.1 Nanoindentation experiments

Nanoindentation tests use a standard diamond indenter tip which is driven into the different regions of the sample surface by increasing the normal load. Force-displacement data recorded during the test using high-resolution instruments are used to determine Young’s modulus, hardness, and the elastic-plastic deformation. For this study, a Berkovich diamond indenter tip is used. As glassy carbon is a hard material a Berkovich tip is a suitable geometry for an indenter to make an indentation deep enough to extract force-displacement data. The geometry of the Berkovich indenter is shown in Figure 19. Scratch tests were also performed to find the friction coefficient between diamond and Al 1100 sample which would later be used in the finite element simulations.

The tests are usually carried out using a load-controlled method. The normal load is increased at a certain rate and then held constant at the maximum load for a certain period before decreasing it back to zero at the same rate. The reduced elastic modulus of the sample is calculated from the unloading curve of the force-displacement curves obtained from the test. [2] The relationship between reduced elastic modulus and Young’s modulus is given by the Sneddon relationship Equation (1) where E and ν are the elastic modulus and Poisson's ratio of the test material, E_i and ν_i are the elastic modulus and Poisson's ratio of diamond indenter tip. The values of E_i and v_i are 1140 GPa and 0.07 respectively [3].

$$E = \frac{\left(1-\nu^2\right)}{\frac{1}{Er}-\frac{\left(1-\nu_i^2\right)}{E_i}} \tag{1}$$

These tests must be conducted carefully considering many factors to get reliable and accurate results. Creep is closely related with plastic deformation. This has influence on the slope of the loading and the initial part of the unloading curve which may affect the results. Proper loading rates and hold times must be maintained to minimize the effect of creep on the results [4]. Additionally, the roughness of the sample surface also plays a significant role in the results obtained from the tests. The recommended roughness of the indenting surface is less than 5% of the maximum indent depth. The loading rates, hold time, and surface roughness of Al 1100 and glassy carbon samples used for the tests are mentioned in the later section.

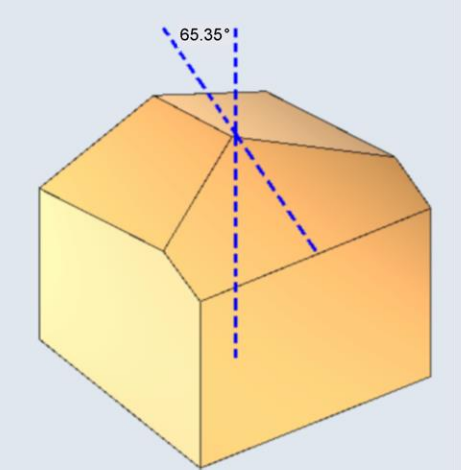

Figure 19. Schematic representation of Berkovich indenter

Nanoindentation and scratch test on Al 1100

Maximum load of 10 mN is applied by increasing the normal load from 0 mN to 10 mN in 30 seconds and bringing it back to zero at the same rate. A hold period of 187 seconds is chosen for aluminum alloy to minimize the creep effects during the unloading part of the curve [5]. Figure 20 shows the normal load vs time curve of the indentation procedure. The Al 1100 sample was diamond turned to get a surface finish of 15 nm Ra which is less than 5% of the maximum indentation depth, and, thus satisfying the roughness requirement for nanoindentation.

Two indents each were made at two different spots. Figure 21 a and b show the SPM images of the indents made. Figure 22 and Figure 23 shows the force vs displacement curves obtained from the four indents made. The reduced moduli obtained from the curves are converted to Young's modulus using Equation (1). The values of Young's modulus calculated are 75.0576 GPa, 69.1307 GPa, 62.1996 GPa, and 76.8899 GPa respectively. These values are close to Young's modulus value obtained from the tensile test of Al 1100 samples as shown in Figure 16.

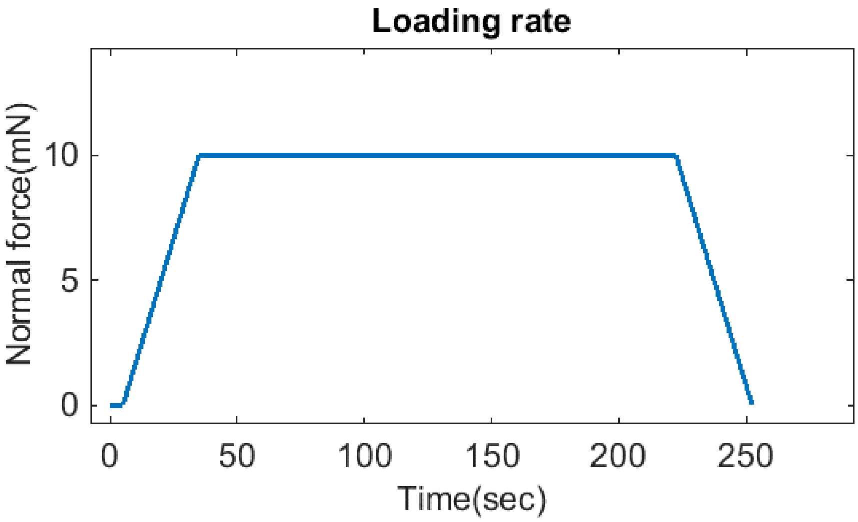

Figure 20. Loading, unloading and hold regime of the nanoindentation experiment on Al 1100 H14

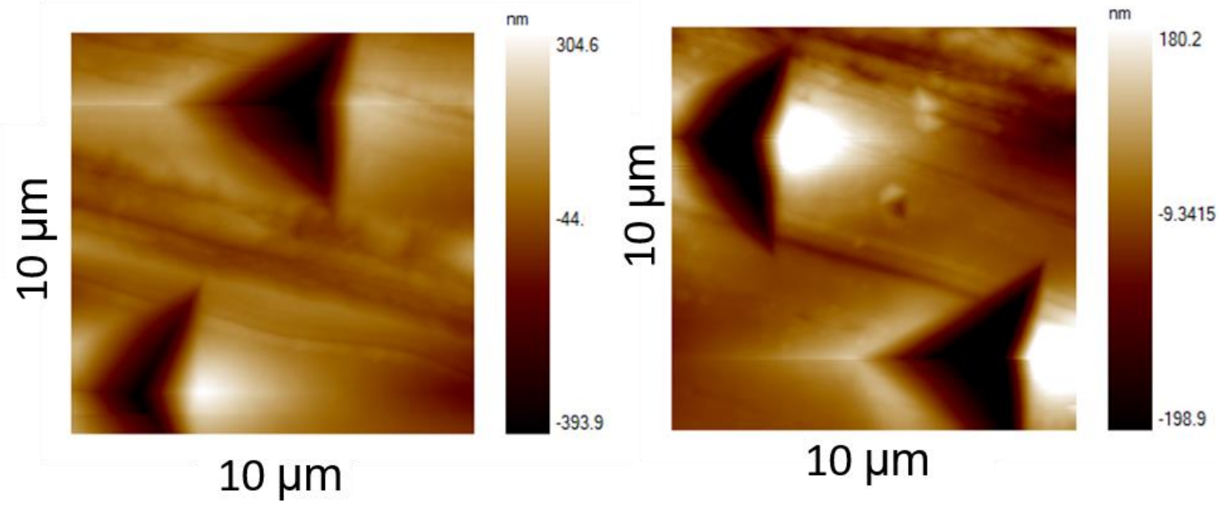

a b

Figure 21. Scanning probe microscopy images of nano indents

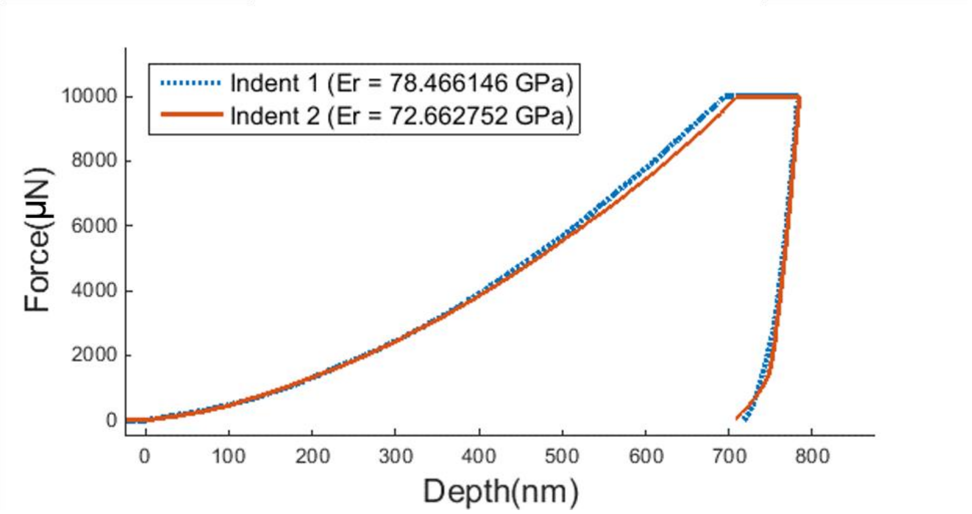

Figure 22. Set 1 indents-force vs displacement curves with measured reduced modulus values of Al 1100

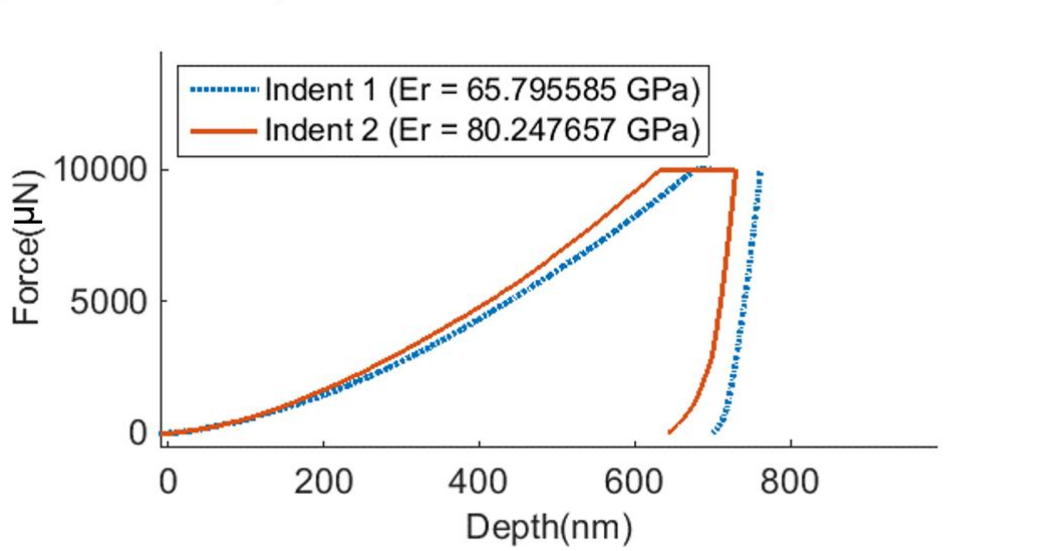

Figure 23. Set 2 indents-force vs displacement curve with measured reduced modulus values of Al 1100

As seen in section 4.2.1, friction between the indenter tip and the sample surface affects the pile-up height and spread of the indent. It is, therefore, important to measure the friction coefficient between the indenter tip and the sample surface. Scratch tests were performed to measure the friction coefficient. In the nano-scratch test, the diamond tip laterally scratches the sample surface under the vertically downward load from above. The tip displacement, vertical and lateral loads and frictional coefficient of the surface can be obtained. A schematic representation of the nano-scratch test operation is shown in Figure 24 Before the test a minor force is applied on the tip so that it scans the surface. Then the load is gradually applied to the moving tip. In the beginning, the surface deforms only elastically with no residual pattern on the surface. With increasing load, the surface starts to deform plastically and the residual scratch on the surface appears. Initially, a minor force of 4 μN is applied to scan the surface. The tip is then displaced laterally in one direction by 5 μm. Subsequently, the normal force is increased to 1 mN and the tip is displaced laterally in the opposite direction by 10 μm. The tip is brought back to 4 μN force and displaced laterally to its original position. This indenter tip movement and the normal force history is shown in Figure 25. Figure 26 shows the SPM image of the nano-scratch created on the Al 1100 sample surface.

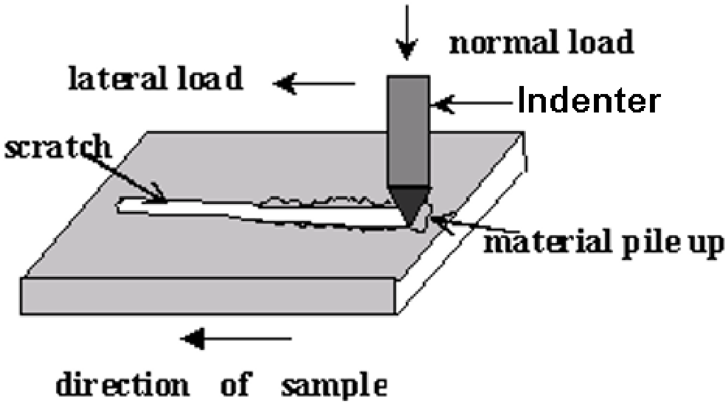

Figure 24. Schematic diagram of the general operation of the nano-scratch tester when taking a scratch measurement

Figure 26 shows the time history plot of the ratio of lateral force and normal force. The friction coefficient between the indenter tip and the Al 1100 sample surface is 0.6. This friction coefficient will be used later in the finite element model for correlation.

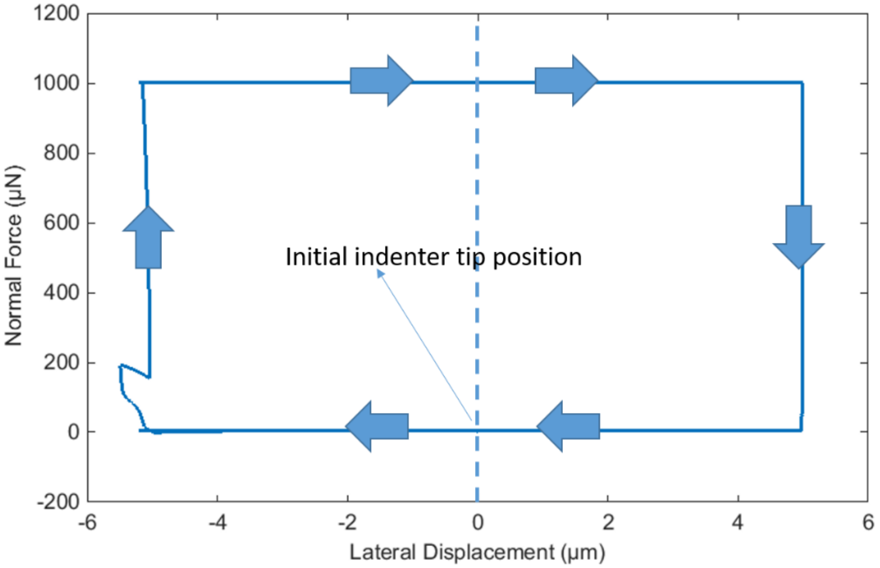

Figure 25. Normal force vs lateral displacement plot of the nano scratch procedure

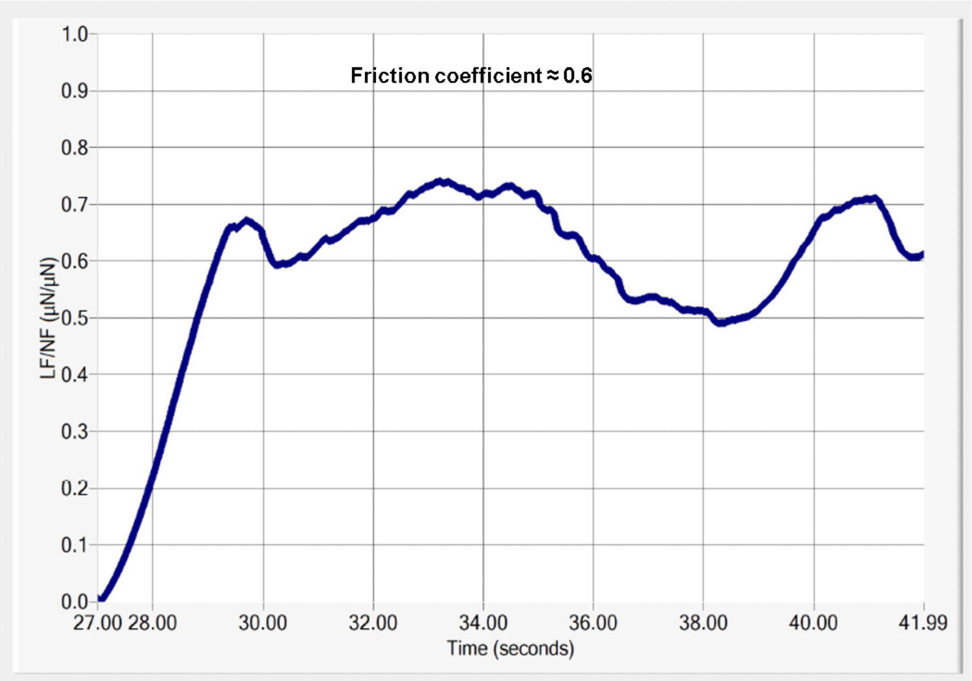

Figure 26. Time history plot of the ratio of lateral force and normal force on the indenter tip during the nano-scratch test

Nanoindentation test on glassy carbon

Maximum load of 10 mN is applied by increasing the normal load from 0 mN to 10 mN in 30 seconds and bringing it back to 0 mN at the same rate. A hold period of 20 seconds was applied between the loading and unloading as shown in Figure 27.

Three indents were made and the force-displacement curves were obtained as shown in Figure 28. The reduced modulus values derived from the experiment are converted to Young's modulus values by using Equation (1) and are found to be 28-29 GPa. SPM images of the glassy carbon surface before and after the indentation are shown in Figure 29. The green dots in Figure 29 (a) are the locations where the indents are made.

The elastic modulus of glassy carbon and compressive strength are 24-28 GPa and 700 MPa according to matweb website. If the material behaved as a purely linearly elastic material, then the unloading part of the force vs displacement curve should return back to zero displacement. No indent impressions should be visible in the SPM image. But, the unloading part of the curve doesn't return to zero displacement and indent impressions are visible as shown in Figure 28 (b) and Figure 29 respectively. This indicates that the glassy carbon sample did not behave as a pure linear elastic material and that there was some plastic deformation. This will be confirmed in the further section by looking at the stress distribution of the finite element model in the glassy carbon sample after the loading part of indentation.

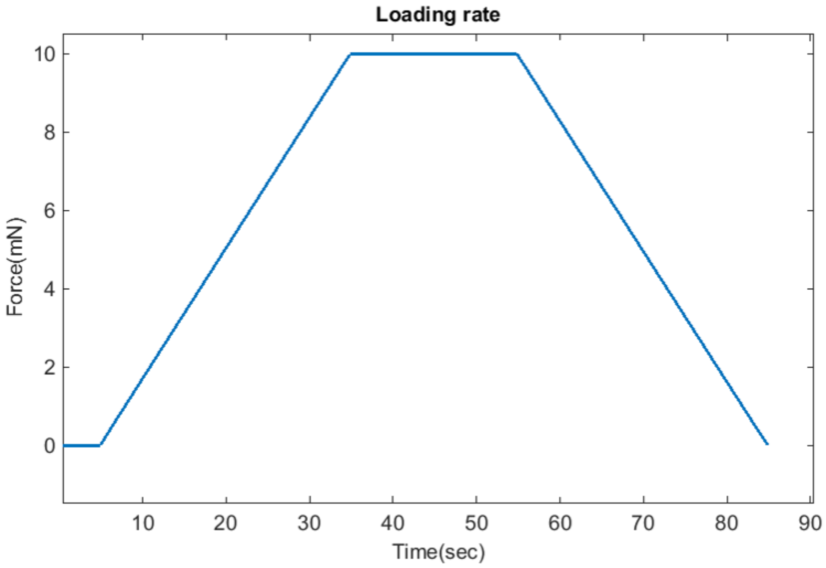

Figure 27. Loading, unloading and hold regime of the nanoindentation experiment on glassy carbon

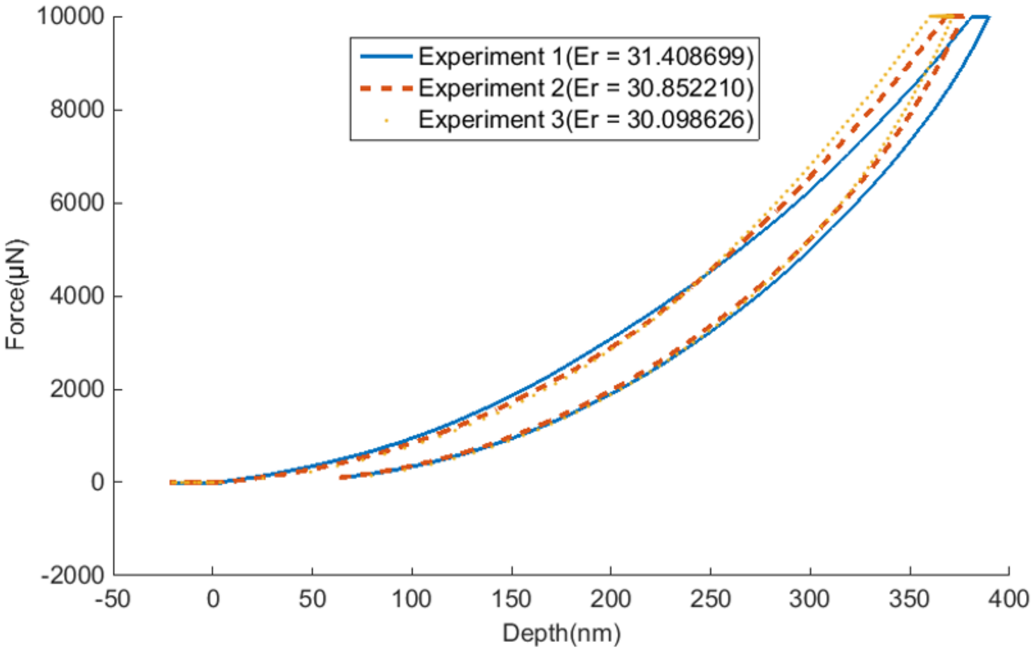

Figure 28. Force vs displacement curve with measured reduced modulus values of glassy carbon

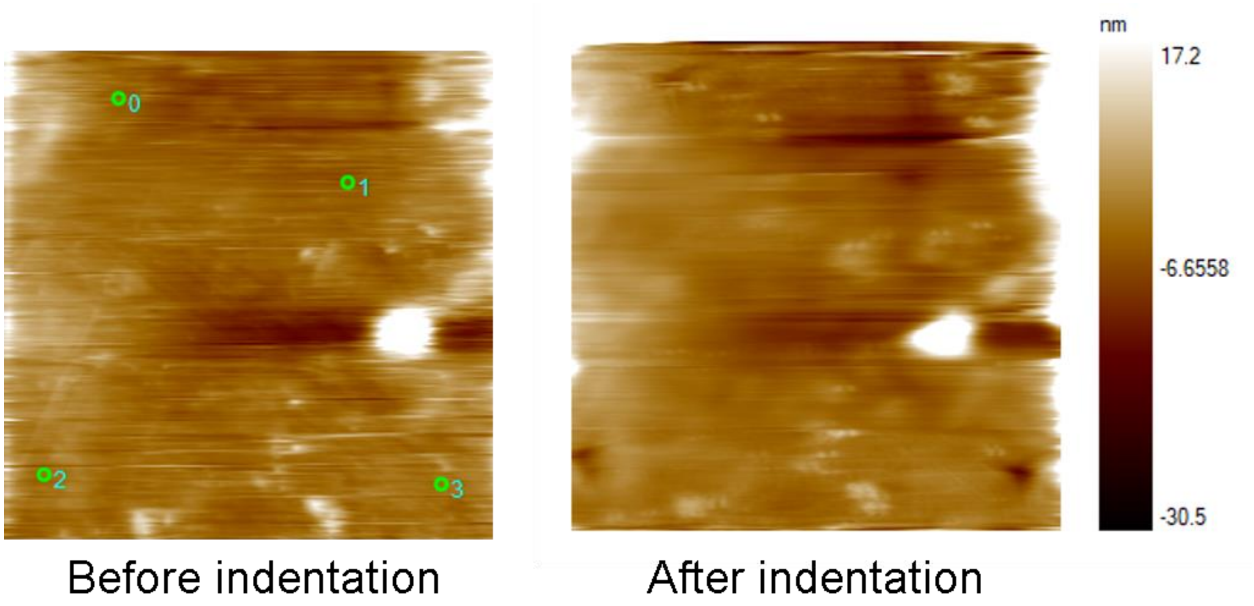

(a) (b)

Figure 29. SPM images of glassy carbon surface before and after indentation

4.3.2 Correlation of FEA model with nanoindentation experiments

Finite element model of the nanoindentation on Al 1100

A 2D axisymmetric model was used for the finite element simulation of the nanoindentation procedure. A conical rigid indenter with a half angle of 70.3° was employed in the axisymmetric model which has the same projected area to depth function as the standard Berkovich indenter [6]. Figure 30 shows the schematic representation of the finite element model used. An axisymmetric model was used initially as it requires less computational time and is more convenient than a 3D model. At first, the indenter is modeled as a sharp tip, although the actual Berkovich indenter tip has some roundness due to manufacturing limitations.

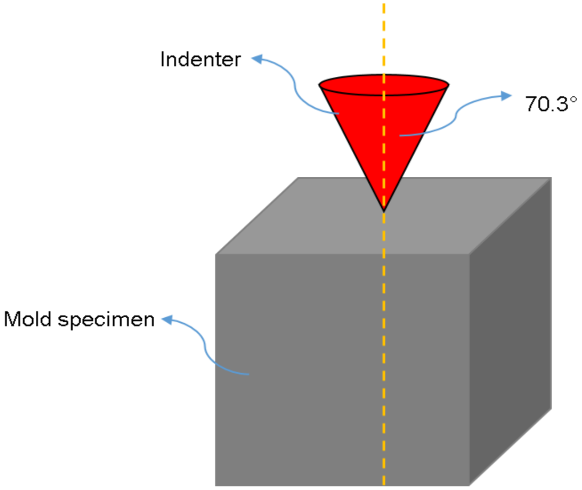

Figure 30. Schematic representation of the finite element model of the rigid axisymmetric indenter and mold specimen for nanoindentation using Berkovich indenter

The indenter was meshed with RAX2 elements: 2 node linear axisymmetric rigid link elements and the mold specimen was meshed with CAX4R elements:4 node bilinear axisymmetric quadrilateral, reduced integration, hourglass control elements. A finer mesh near the indenter tip and a coarser mesh away from the indenter tip was used for the mold specimen as shown in Figure 31. Non-linear geometry option was used in the finite element simulation. Arbitrary Lagrangian Eulerian (ALE) adaptive mesh domains was defined for the mold specimen as it involved large deformations. Proper boundary condition were applied wherever necessary. The creep observed during the hold period in the experiments is not modeled.

Surface-to-surface contact condition was used with the Indenter as the master surface and the mold surface as the slave surface since a master surface can penetrate the slave surface. At first, frictionless contact was considered. The mechanical properties of Al 1100 H14 obtained from the tensile test as shown in Figure 16 were used for the mold specimen. Isotropic hardening material behavior was employed to model the plasticity region of the material.

The force-displacement curve obtained from the simulation were compared with the experimental curves in Figure 32. The displacement of the node just below the sharp tip and the reaction force on the indenter is depicted in this plot. With the indenter modeled as a sharp tip, the curves are significantly different.

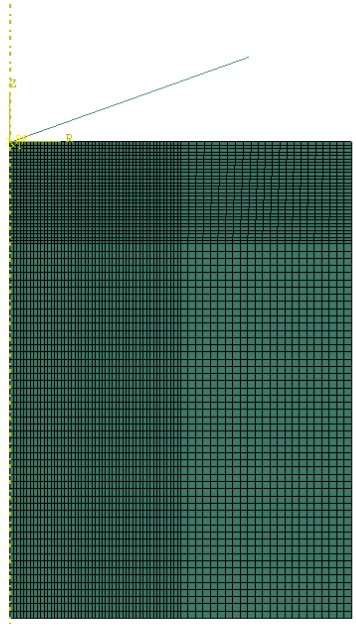

Figure 31. Mesh pattern used for the finite element model of the rigid spherical indenter and mold specimen

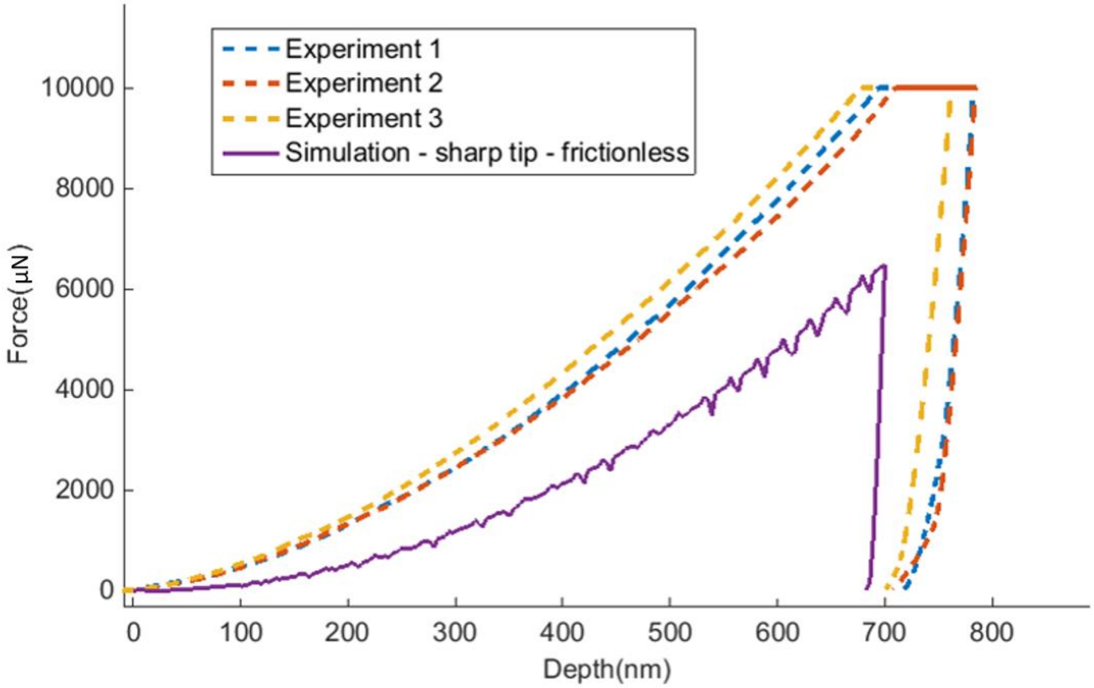

Figure 32. Comparison of force vs displacement curves obtained from the experiments and the simulation

In practice the indenter tip is not perfectly sharp and based on the ISO 14577 standard, the Berkovich indenter has an average radius of curvature about 150–200 nm. However, adding a radius of curvature of 200 nm to the tip, the force vs displacement curve of the simulation did not change as shown in Figure 33.

Penalty based friction formulation was employed as the interaction between the indenter surface and the mold surface to study the effect of friction on the force vs displacement curve. The friction coefficient of 0.6 measured from the scratch test in section 4.3.1 was used. Friction did not have any significant effect on the force-displacement curve as shown in Figure 33. However, friction would be important during the indent shape correlation as it has significant impact on the pile-up as explained in section 4.2.1.

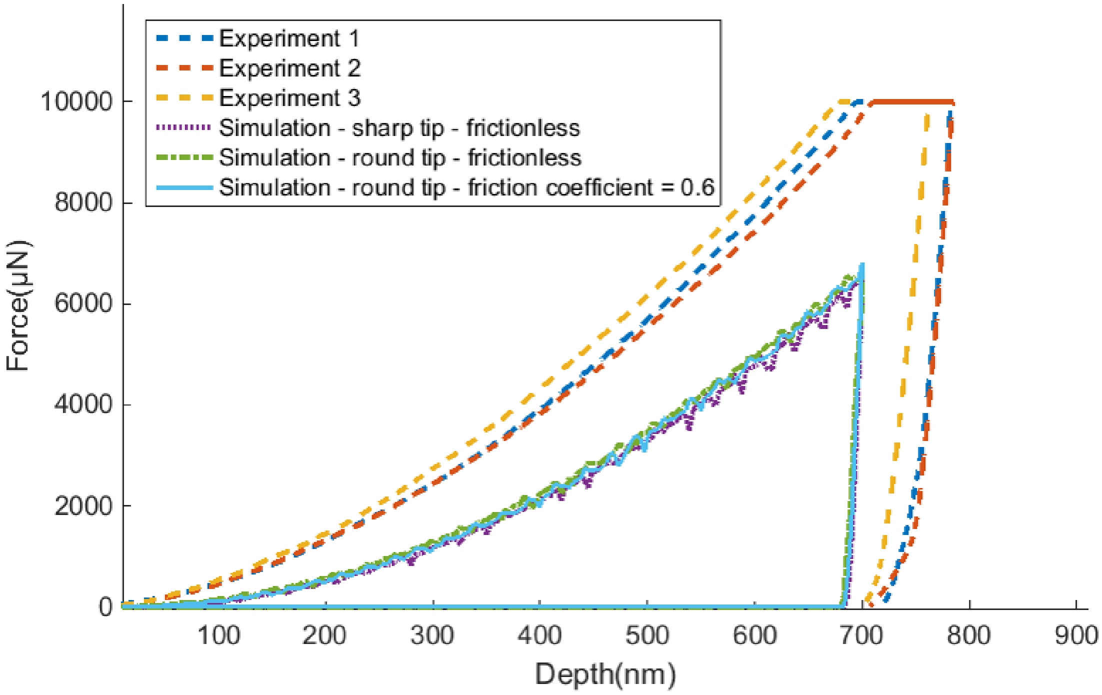

Figure 33. Comparison of force vs displacement curves obtained from the experiments and the simulations

To model the indenter tip imperfections accurately the Berkovich tip was scanned under the Keyence VKX1100 confocal microscope provided by the Analytical Instrumentation Facility (AIF) at North Carolina State University as shown in Figure 34. The scanned data was imported into Abaqus to be used as an indenter in the simulation. A 3D model was employed for this simulation. The mold was meshed with C3D8R: 8 node 3D reduced integration element. Figure 35 (a) and Figure 35 (b) shows the meshed indenter model and the mold specimen. The simulation was run with the same contact conditions as mentioned earlier with a friction coefficient of 0.6 between the Berkovich indenter and the mold specimen. The force vs displacement plot matches with the experiment curve as shown in Figure 36. Figure 37 and Figure 38 shows a curve fit of polynomial degree 2 of the loading curve of the experiment and simulation force vs displacement curves. The equations are a good fit.

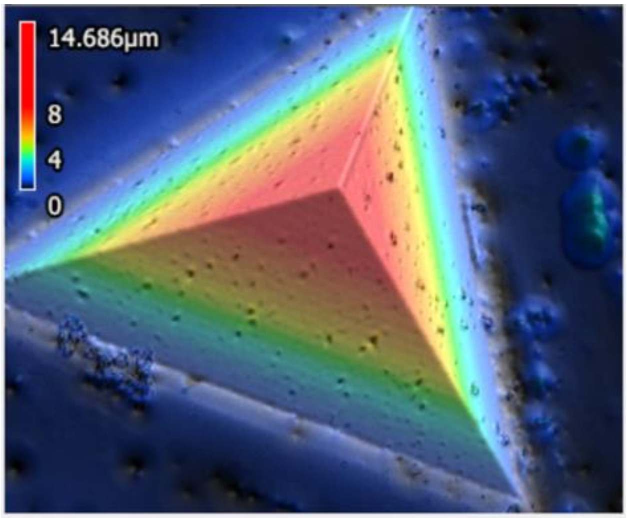

Figure 34. Height contour image of the Berkovich Indenter scanned under the Keyence confocal microscope

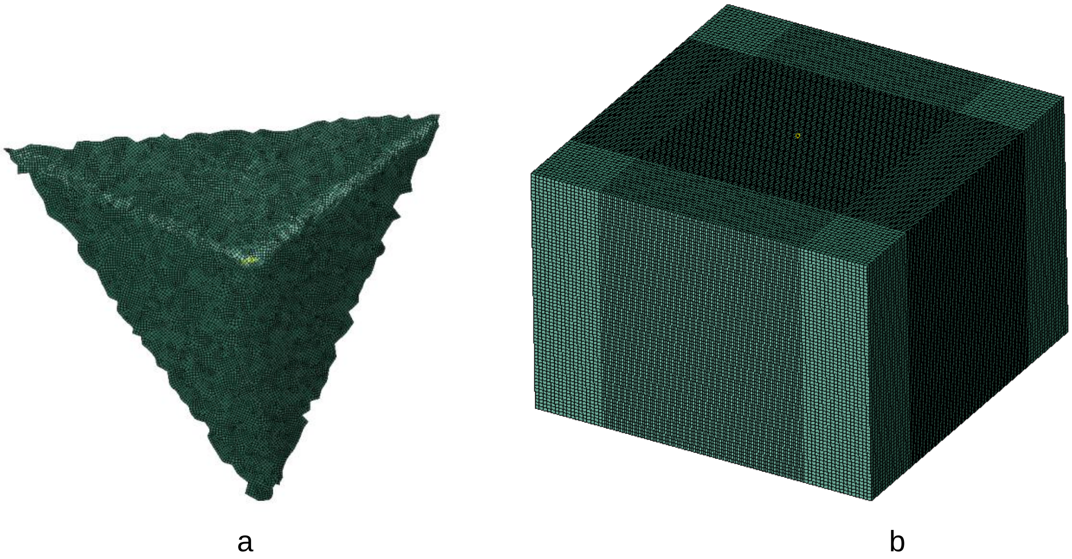

Figure 35. Mesh pattern of (a) Berkovich indenter and (b) Mold specimen

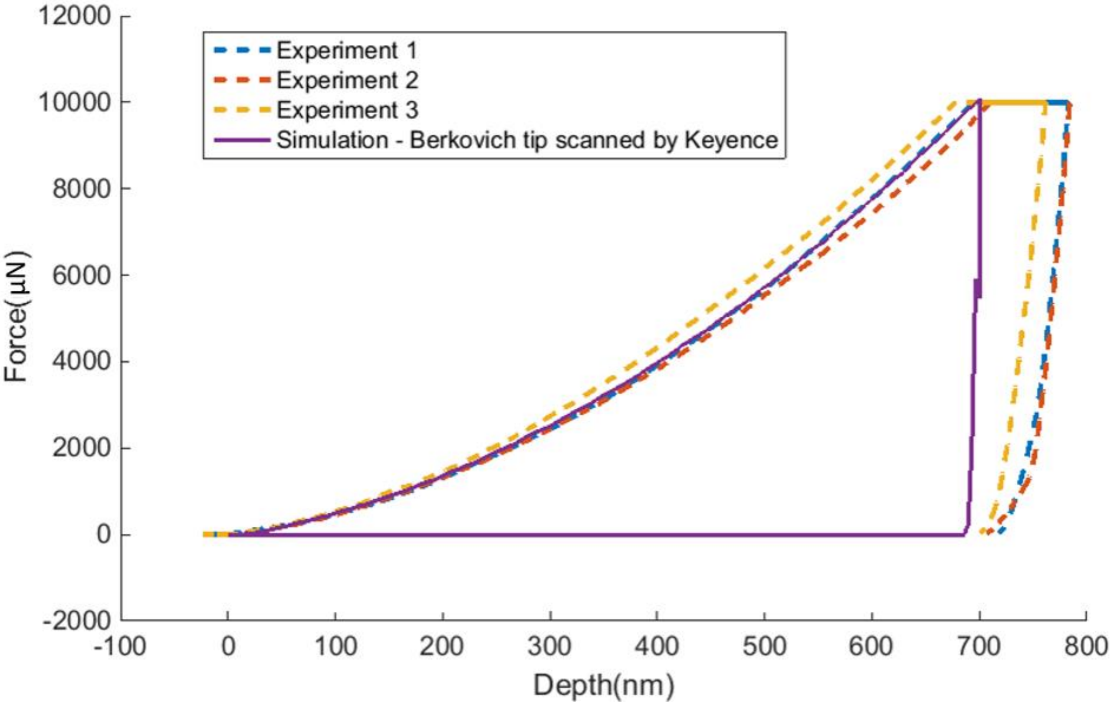

Figure 36. Comparison of force vs displacement curves obtained from the experiments and the simulation

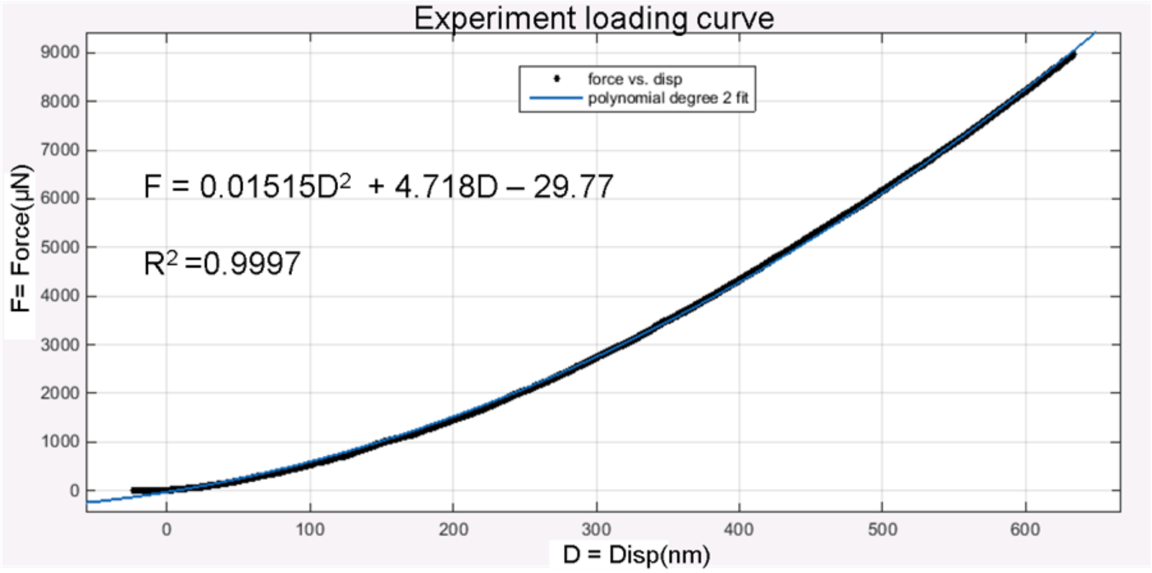

Figure 37. Polynomial degree 2 fit of the loading region of the experimental force vs displacement curve

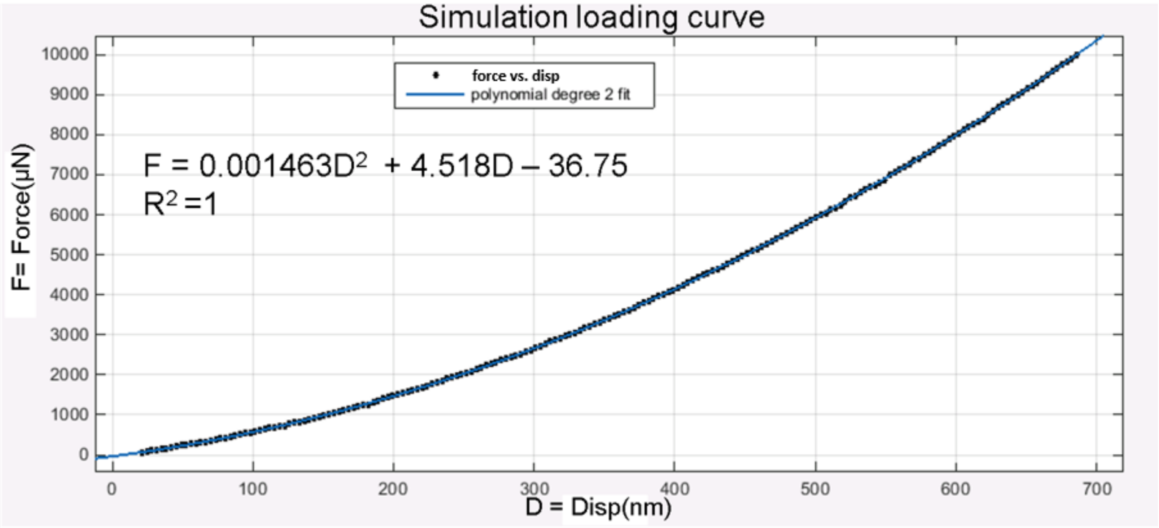

Figure 38. Polynomial degree 2 fit of the loading region of the simulation force vs displacement curve

To complete the correlation, comparison of the indent shapes obtained from simulation and experiment is important. Figure 39 shows the z contour plot of the experimental and simulation nano indents. Comparison of the cross-section passing through one vertex of the indent and the midpoint of the opposite side of the indent as shown in Figure 39 is presented in Figure 40. The slight deviation in the slopes of the indent could be due to a minor difference between the measurement of the indenter tip radius in the laser confocal microscope and the actual indenter tip radius. Although, the pile-up on either side of the indent match well for the experiment and the simulation indent profiles.

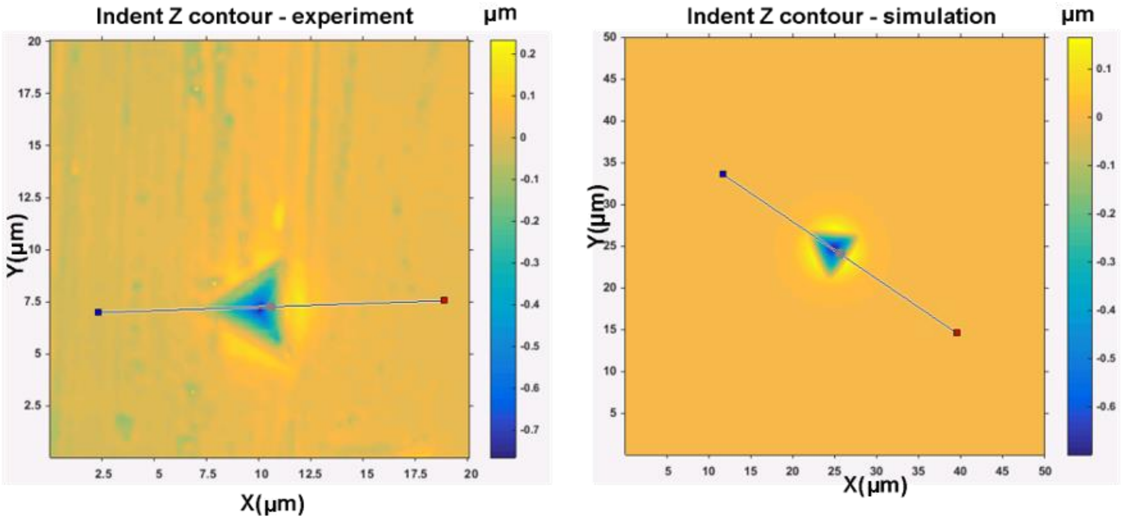

Figure 39. Z contour plot of the experimental and simulation nano indents using the Berkovich indenter

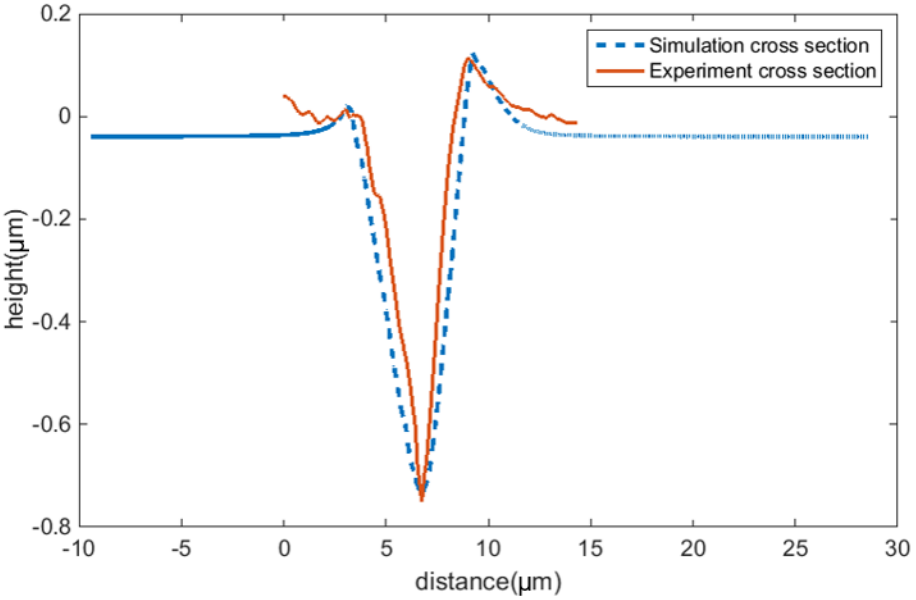

Figure 40. Cross section comparison of experiment and simulation indent profiles

Finite element model of the nanoindentation on glassy carbon

Similar 3D setup, as mentioned in the section 4.3.2 was used for the correlation of nanoindentation experiments on glassy carbon. A Young's modulus and Poisson's ratio of 30 GPa and 0.275 respectively was assigned as the material properties of glassy carbon. The mold specimen was modeled as a perfectly linear elastic material. The force vs displacement curve comparison of the experiment and simulation don't match as shown in Figure 41.

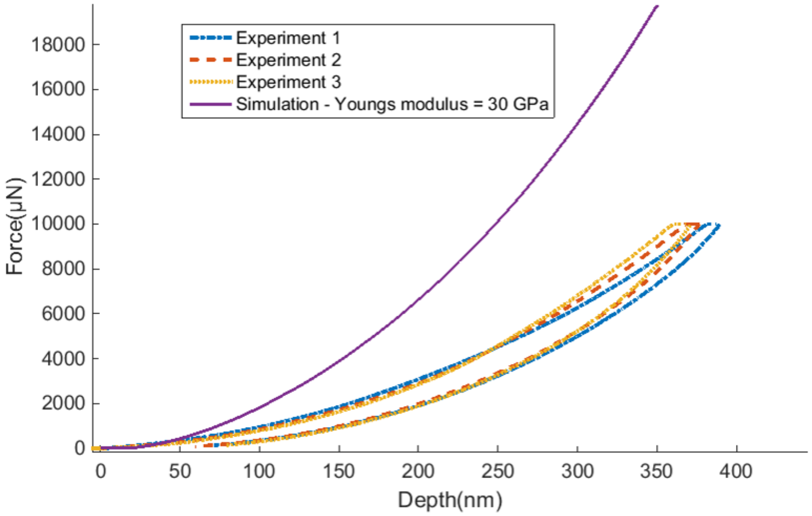

Figure 41. Comparison of force vs displacement curves obtained from the experiments and the simulation

Von Mises stress distribution of the indent at the end of the loading period is in the range of 2 GPa - 8 GPa which is well above the yield stress value 700 MPa of glassy carbon, which indicates that the mold specimen will go beyond the yield point during the indentation. Figure 42 shows the Von Mises stress distribution of the mold specimen at the end of the loading period. SPM images in Figure 29 clearly show the impressions of the indents made which depicts that the specimen might have undergone some plastic deformation. Henceforth, Young's modulus value of 30 GPa obtained from the nanoindentation experiments in section 4.3.1 and a Poisson's ratio of 0.275 would be used to model the glassy carbon die in the simulations.

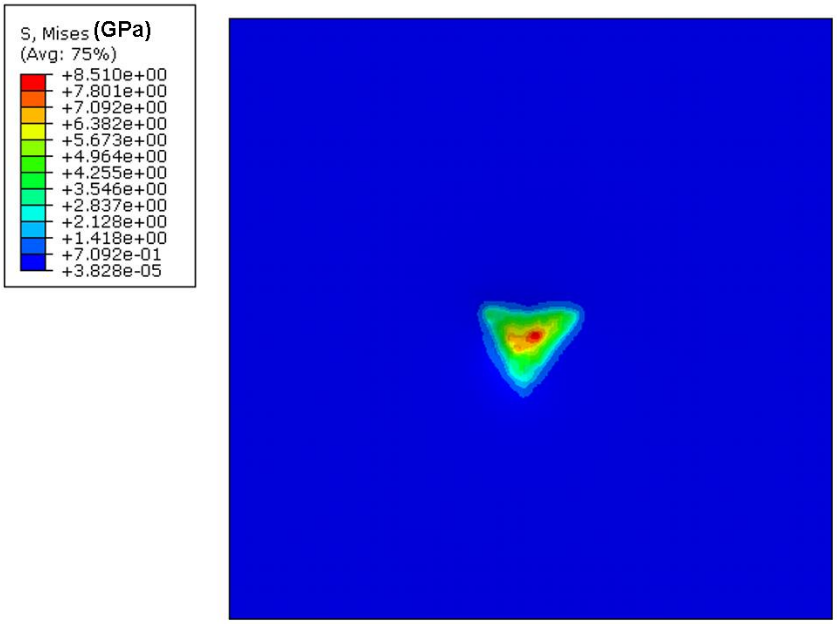

Figure 42. Von Mises stress distribution of the glassy carbon mold specimen at the end of the loading period of the simulation

4.4 EFFECT OF STRAIN RATE DEPENDENT BEHAVIOR OF AL 1100 H14 ON MICROINDENTATION

Al 1100 H14 is a positive strain rate sensitive material. A positive strain rate sensitive material experiences an increase in the yield stress as the strain rate increases. Johnson-Cook material model is generally used for computation analysis of impact and the penetration related problems involving ductile materials. For high-speed indentation process, this would be an ideal model. The Johnson-Cook elastoviscoplastic model is given by Equation (2) which involves an independent factor of strain hardening, strain rate hardening and thermal softening. A, B and C are material constants whereas n is a hardening exponent and m is a softening exponent. σ is equivalent Von Mises stress. ε^{pl} is the equivalent plastic strain. $\dot{\varepsilon}$ is the equivalent plastic strain rate. $\dot{\varepsilon}_0$ is reference strain rate which is equal to 1 s^{-1}. T is a non-dimensional temperature which is a function of room temperature.

$$\sigma(\varepsilon^{pl}, \dot{\varepsilon}, \hat{T}) = \underbrace{[A + B(\varepsilon^{pl})^n]}_{\text{Hardening factor}}\underbrace{[1 - \hat{T}^m]}_{\text{Thermal softening factor}}\underbrace{[1 + C\ln(\dot{\varepsilon}^{pl}/\dot{\varepsilon}_0)]}_{\text{Strain rate dependence factor}} \tag{2}$$

The values of these constants are obtained by a series of tensile test experiments conducted at various strain rates by Sonika Sahu et al [7]. These constants are presented in Table 2.

Table 2. Constant values in the Johnson cook viscoelastic model for Al 1100 H14

A	B	C	N	M	$\dot{\varepsilon}_0$
114	49.79	0.001	0.197	0.859	1

The same finite element setup was used as in Figure 2. Initially, only a single spherical indentation would be considered to study the effect of strain rate dependent mold behavior on indentation. Considering an indentation frequency of 1 KHz the loading time would be 0.005 seconds. Johnson cook hardening with rate dependent material model is used to model the plasticity of the Al 1100 mold. Figure 43 shows that there is no significant difference in the amount of spring back for quasi-static indentation and fast indentation. However, as the material is positive strain sensitive, the yield stress during high strain rate indentation is comparatively larger than that during quasi-static indentation and hence the pile-up experienced will be lesser. This phenomenon can be observed in Figure 43. Similarly, the force vs displacement plot in Figure 44 shows that faster indentation experiences higher indentation force.

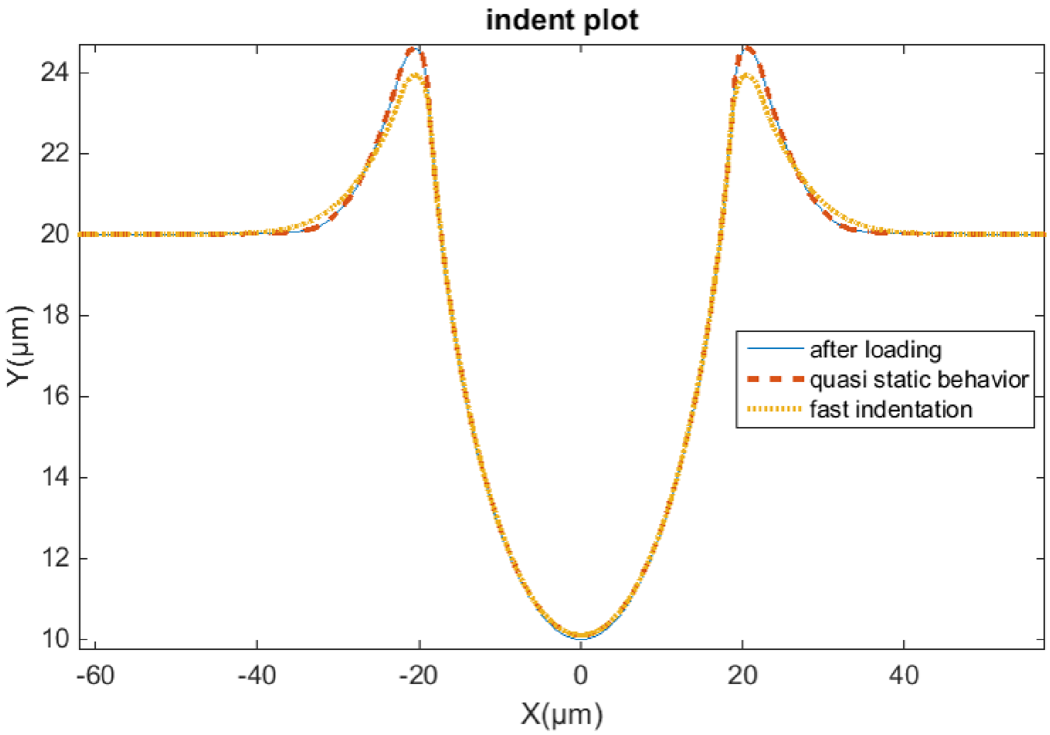

Figure 43. Indent profile comparison for quasi static and fast indentation

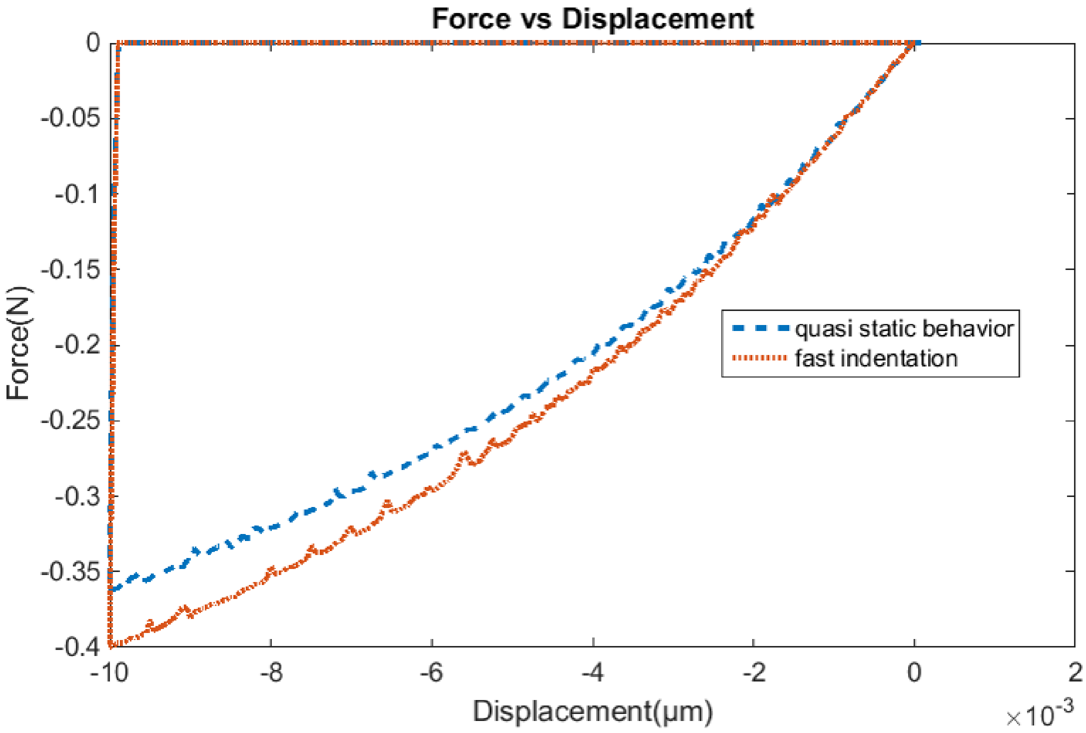

Figure 44. Comparison of the force vs displacement curves for quasi-static and fast indentation

4.5 FINITE ELEMENT MODELING OF MICROINDENTATION USING A MULTI INDENTER DIE

To fabricate a mold with millions of lens features on it the indentation process has to be done fast. Indenting with a die having multiple lens features on it helps to transfer the features on to the mold in a faster and efficient way. The specifications of the multi-lens array are shown in Figure 45. The radius of the spherical lens is 15.84μm, the pitch is 25μm and the indent depth is 15.84μm (radius of the sphere).

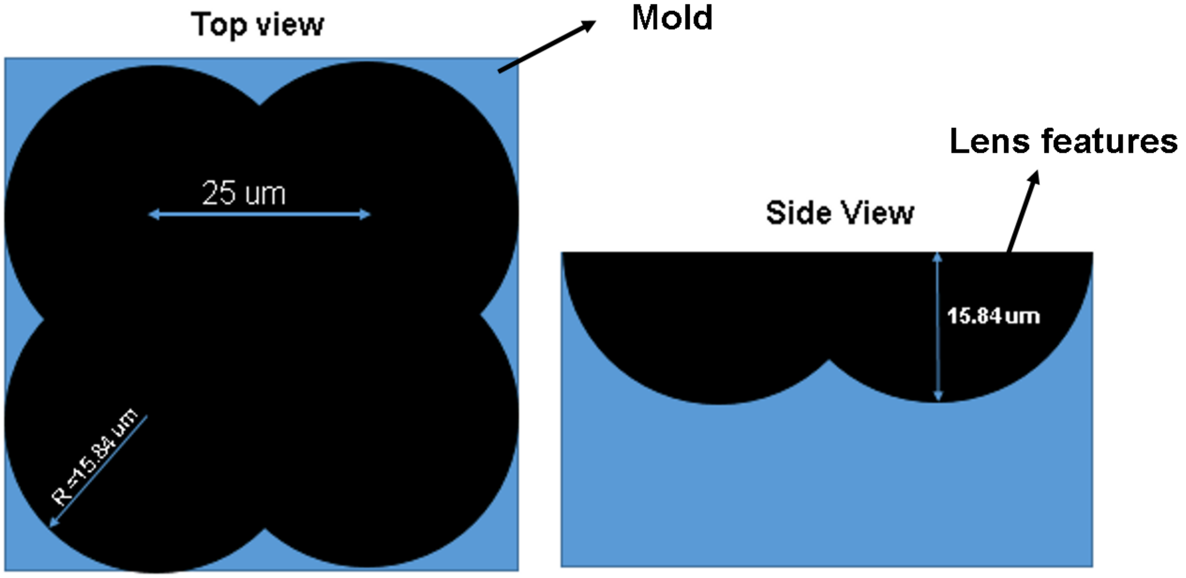

Figure 45. Specifications of the lens feature on the mold

A 3D model of the desired lens features on the mold is shown in Figure 47. To fabricate the desired lens features on to a mold a 3x3 indenter was designed as shown in Figure 48. Each hemisphere is of radius 15.84 μm with a pitch of 25 μm and a fillet of 5 μm at the intersection of the spheres.

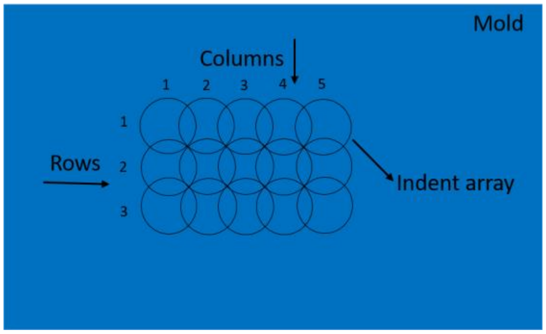

Figure 46. Schematic diagram explaining the terminologies of column and rows to refer to indent

Terminologies to refer to indents in an indent array is important to avoid any ambiguity. For this purpose, the vertical array of indents would be called 'columns' and the horizontal array would be called 'rows. The numbering of the columns and rows is shown in Figure 46. In this section, two indentation strategies will be discussed and analyzed. In the first indentation strategy, the 3x3 indenter indents at a spot in step 1 and then skips two columns to indent in step 2 with a single column overlap as shown in Figure 49. In this strategy, there is a single column overlap which helps mitigate the distortion of surrounding indents to some extent which will be discussed later. The final indent array would be a 5 by 3 array as shown in Figure 50.

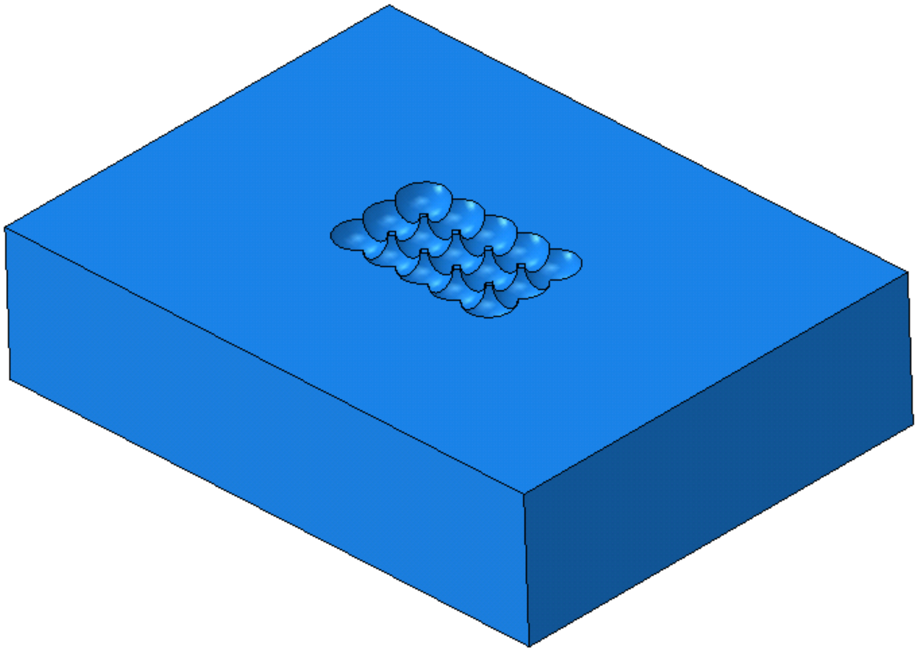

Figure 47. 3D model of the 5x3 lens array features on a mold. It satisfies the pitch and depth requirements specified in Figure 45

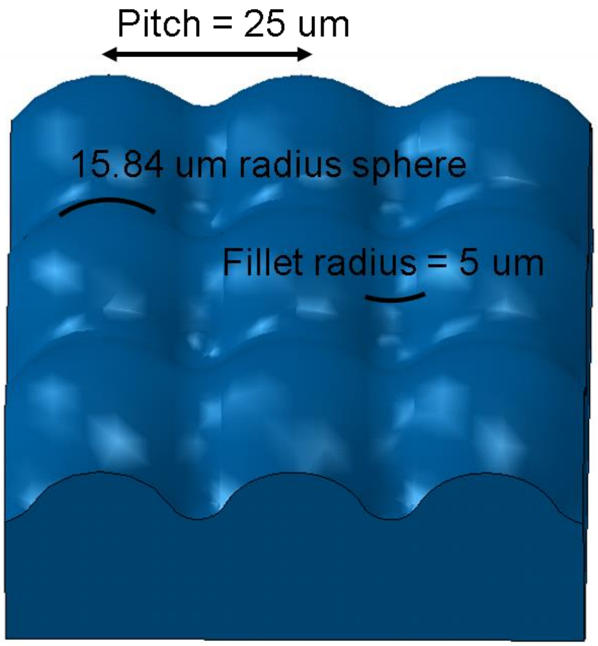

Figure 48. CAD model of the 3x3 indenter die

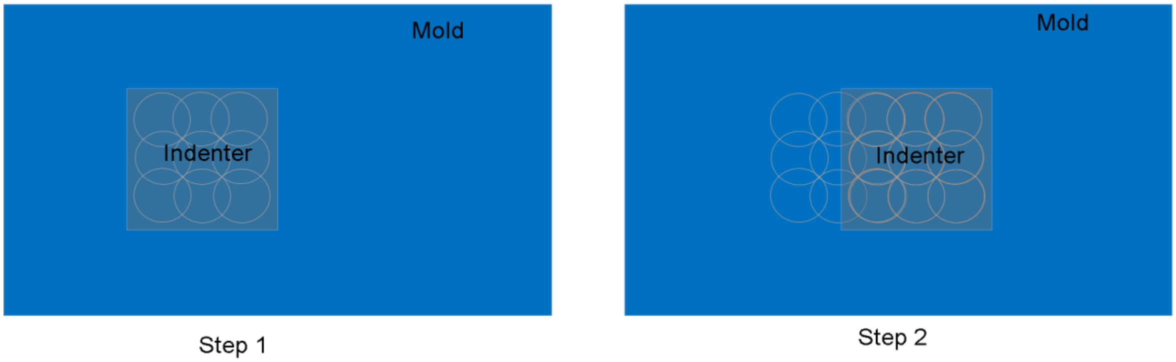

Figure 49. Indentation strategy 1: skip two columns and indent with a single-column overlap

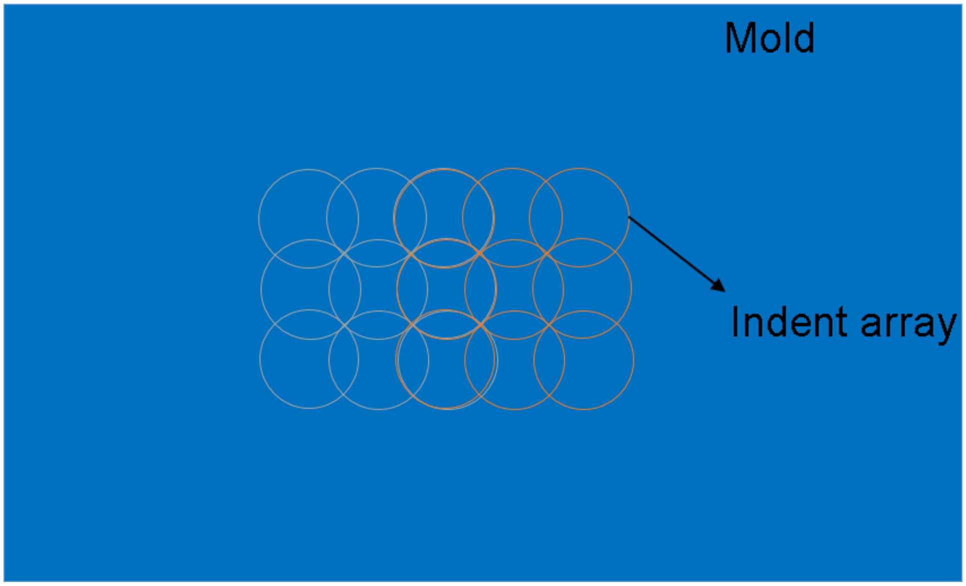

Figure 50. Final 5x3 indent array using indentation strategy 1

In the second indentation strategy, the 3x3 indenter indents at a spot in step 1 and then skips one column to indent in step 2 with a two column overlap as shown in Figure 51. In this strategy, there is a double column overlap which helps mitigate the distortion of surrounding indents to some extent which will be discussed later. The final indent array would be a 4 by 3 array as shown in Figure 52.

Figure 51. Indentation strategy 2: skip one column and indent with a two-column overlap

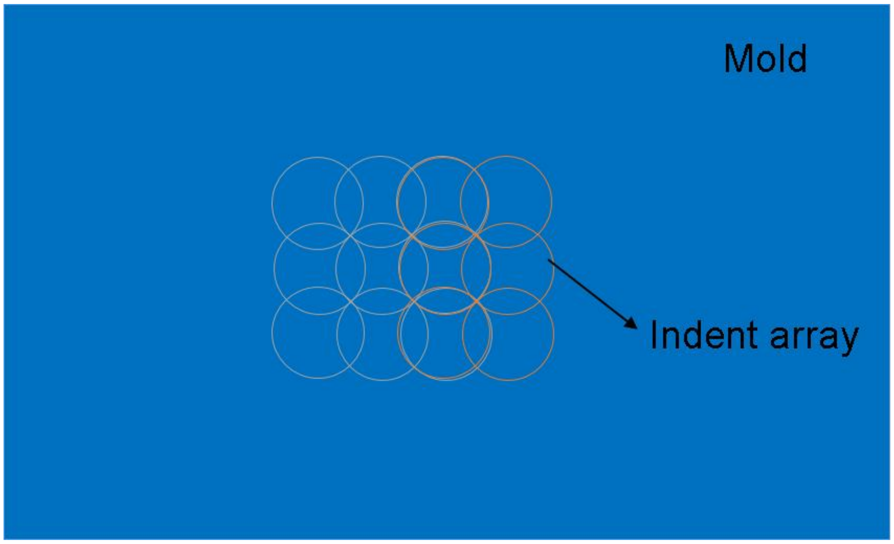

Figure 52. Final 4x3 indent array using indentation strategy 2

4.5.1 Finite element model specifications

A finite element model of the indentation procedure using a 3x3 indenter was developed. The indenter was meshed with C3D10M (10 noded tetrahedral quadratic elements) as this is the preferred element to model finite sliding surface to surface contact conditions to get accurate results [1]. The mold specimen was meshed with C3D8R: 3D continuum 8 noded reduced integration elements. Figure 53 shows the meshed 3x3 indenter and mold specimen. The mesh on the mold was made finer in the center region where the indentations would be made as compared to a coarser mesh in the remaining region to save some computational time.

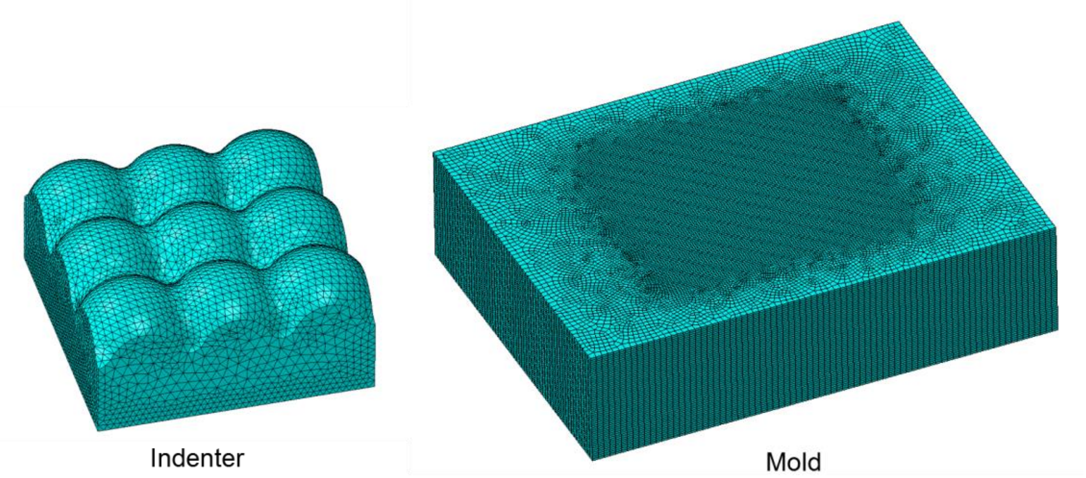

Figure 53. Mesh pattern of the 3x3 indenter and the mold specimen: Indenter meshed with C3D10M elements and Mold specimen meshed with C3D8R elements

Non-linear geometry option was used in the finite element simulation. Arbitrary Lagrangian Eulerian (ALE) adaptive mesh domains was defined for the mold specimen as it involved large deformations. Proper boundary conditions were applied wherever necessary.

Surface-to-surface contact condition was used with the indenter as the master surface and the mold surface as the slave surface since a master surface can penetrate the slave surface. The mechanical properties of Al 1100 H14 obtained from the tensile test as shown in Figure 16 were used for the mold specimen and the 3x3 indenter was modeled as a perfectly linear elastic material with glassy carbon properties obtained from the nanoindentation experiments in section 4.3. Isotropic hardening material behavior was employed to model the plasticity region of the mold material. As Abaqus / Explicit solver was used for the analysis, a load step and an unload step time of 1.2 e-5 seconds was employed. Mass scaling with a factor of 1000 was used to artificially decrease the computational time needed for the simulation. The loading rate and the mass scaling value chosen were suitable enough to ensure that the kinetic energy was always below 5% of the internal energy of the whole model during the simulation, thus satisfying the conditions for the simulation to remain quasi-static.

Four simulations with different friction coefficient values and indentation strategies were studied in this report:

A) Indent depth = 7.92 µm, friction coefficient = 0.4, indentation strategy 1
B) Indent depth = 7.92 µm, frictionless, indentation strategy 1
C) Indent depth = 7.92 µm, friction coefficient = 0.4, indentation strategy 2
D) Indent depth = 7.92 µm, frictionless, indentation strategy 2

For now, indent depths of 7.92µm is employed for all simulations. Higher indentation depths face the issue of element distortion causing the simulations to abort. This issue will be handled in future work. Penalty based friction formulation was employed as the interaction between the indenter surface and the mold surface in simulations A and C. The resulting indents formed are studied in terms of how good a fit are they to the desired indent array shown in Figure 54.

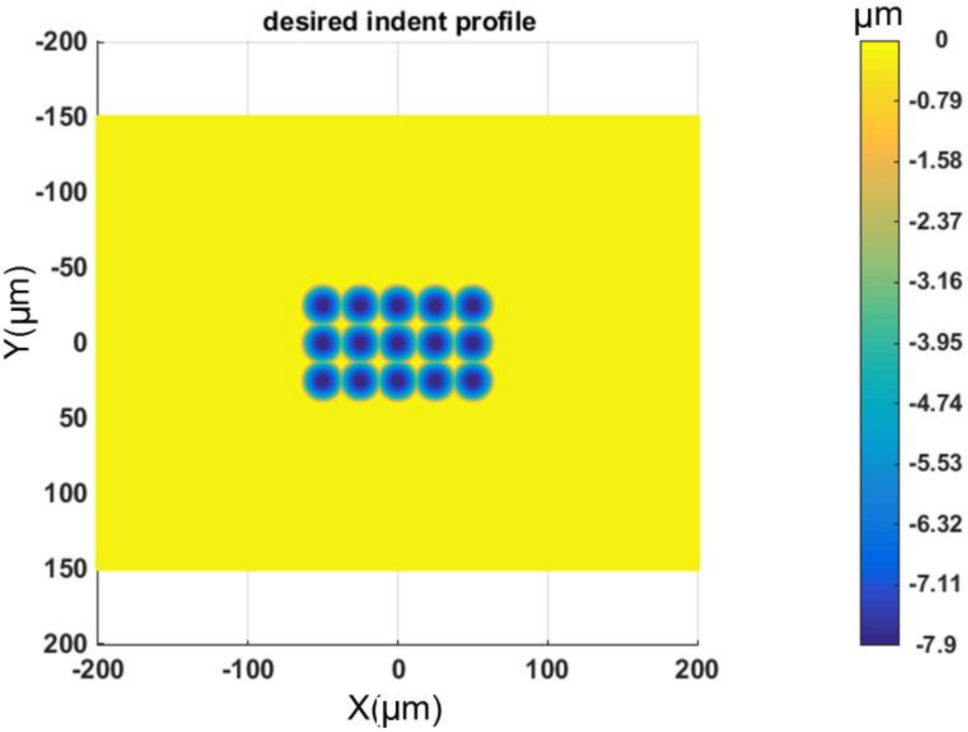

Figure 54. Z contour plot of the desired indents: radius of each spherical indent = 15.84 μm, pitch = 25 μm and an indent depth of 7.92 μm

A) Indent depth = 7.92 μm, friction coefficient = 0.4, indentation strategy 1

Figure 55 shows the Z contour plot of the indents formed in the simulation. The maximum depth from the color bar is 7.26 μm. Although the indenter was displaced to a full depth of 7.92 μm the maximum indent depth achieved was 7.26 μm. This difference is attributed to the deformation of the glassy carbon die and the spring back experienced by the Al 1100 mold after the indenter was unloaded. The second column of indents marked in red dashed box appears to be distorted in comparison to the other indents. Figure 56 depicts the Z contour error plot between the desired indent array and the simulation indent array in which the distortion in the second column of indents marked by the dashed red box is clearly visible. The Z contour errors at the intersection of adjacent indents are due to the presence of a 5 μm radius fillet at the intersection of adjacent spherical bumps on the die.

The cause of this distortion is because when the indenter is indenting in step 2 (indentation strategy 1) with a single column overlap, the second and third column of the indenter starts indenting and pushes the material disturbing the third column of indents. At this point, the first column of the indenter is not yet contacting the mold surface and thus does not prevent the disturbance of the third column of indents until later when the first column of indenter contacts the mold. When the loading of the indenter in step 2 is complete the third column of indents regains its original shape, but the second column gets distorted.

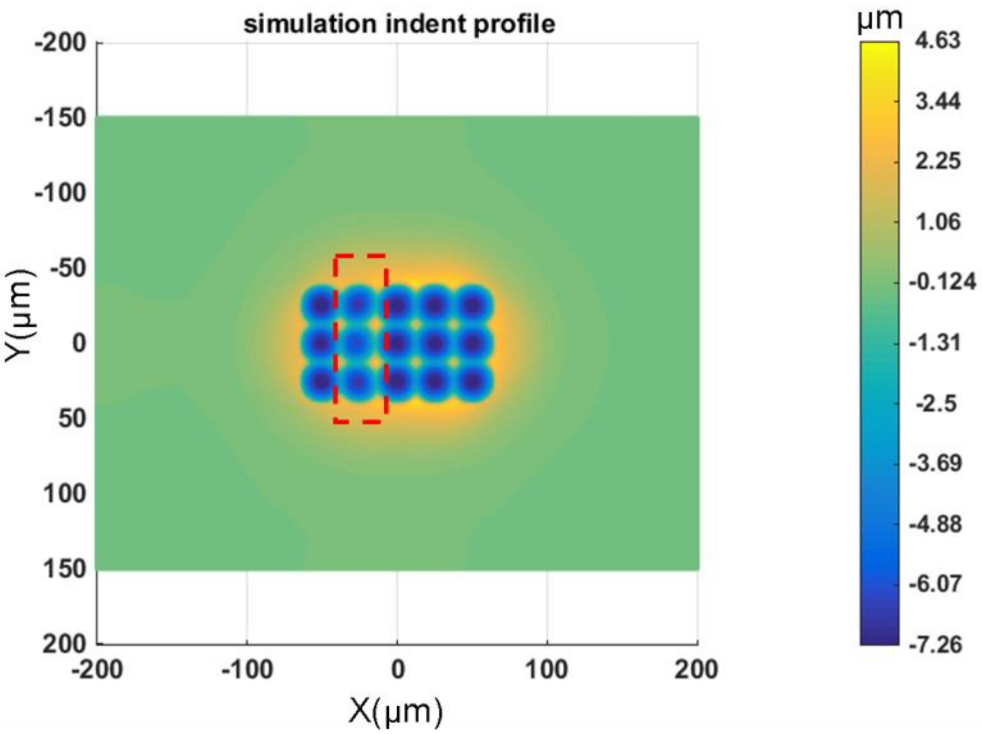

Figure 55. Z contour plot of the indents formed in the simulation: Indent depth = 7.92 μm, friction, indentation strategy 1

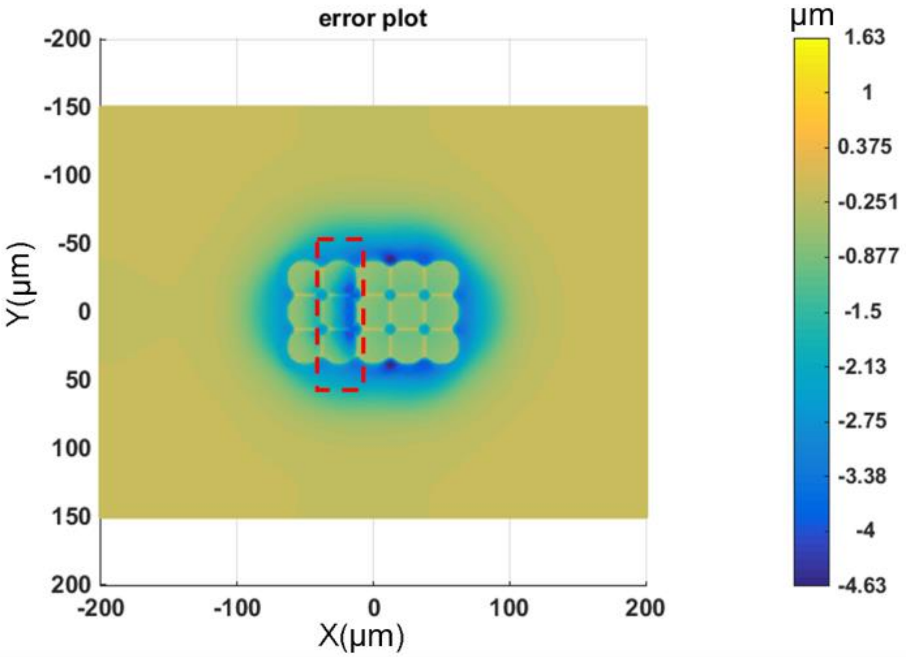

Figure 56. Z contour error plot between the desired indent array and the simulation indent array: Indent depth = 7.92 μm, friction, indentation strategy 1

Figure 57 shows the error plot of the cross section passing through the center of the middle row of indents. A comparison of the simulation profile and the desired profile along with the error between the two is presented in that plot. This gives a better visual understanding of the Z contour errors in the indents.

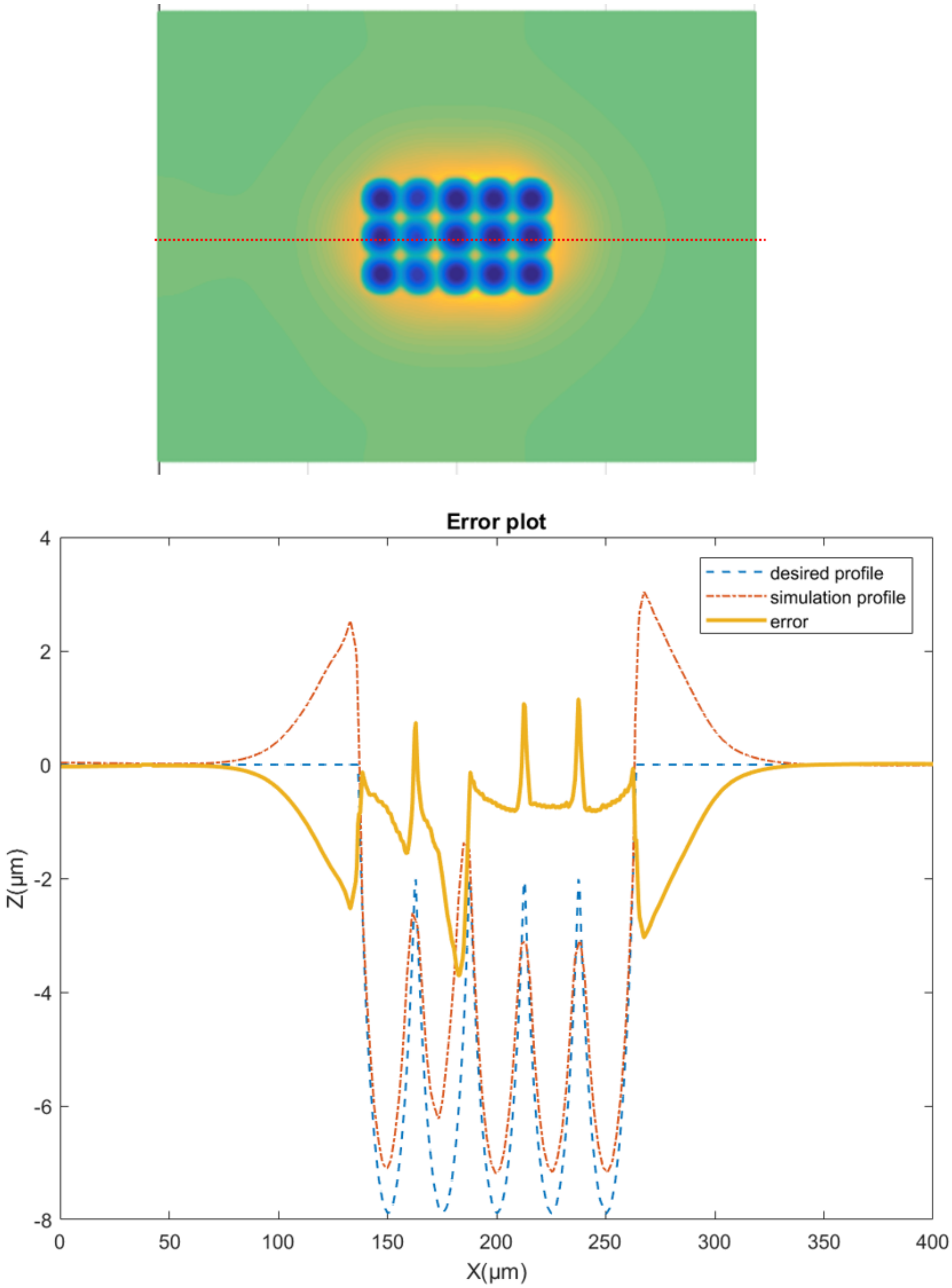

Figure 57. Error plot of the cross section passing through the center of the middle row: Indent depth = 7.92 μm, friction, indentation strategy 1

B) Indent depth = 7.92 µm, frictionless, indentation strategy 1

Similar results can be observed with frictionless contact as shown in Figure 58, Figure 59. However, Figure 60 shows that the error in the second column of indents is larger for a frictionless contact as compared to frictional contact.

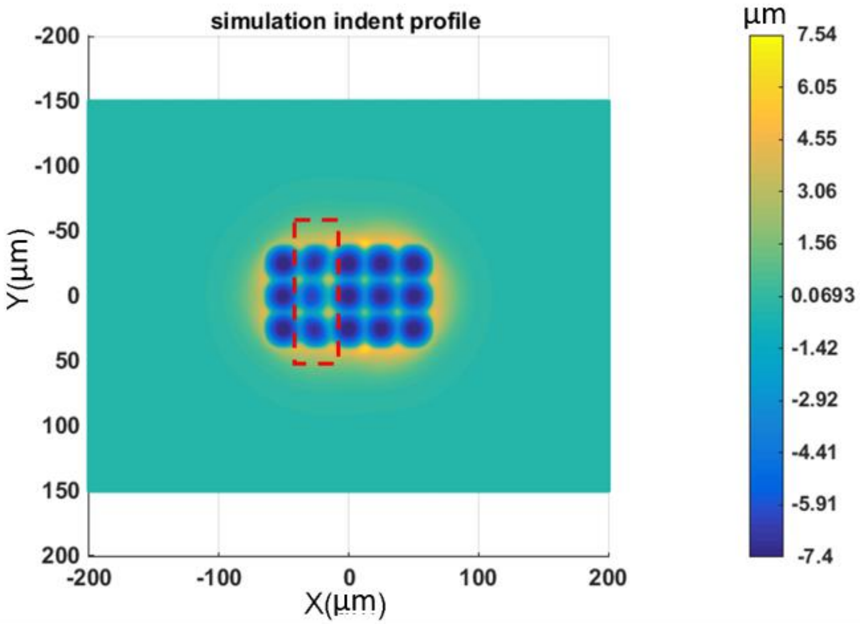

Figure 58. Z contour plot of the indents formed in the simulation: Indent depth = 7.92 µm, frictionless, indentation strategy 1

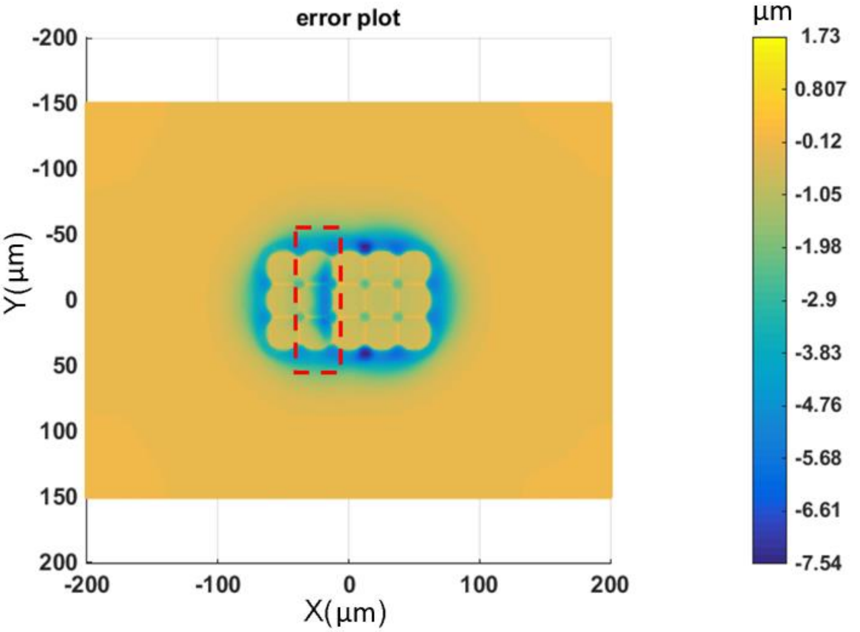

Figure 59. Z contour error plot between the desired indent array and the simulation indent array: Indent depth = 7.92 µm, frictionless, indentation strategy 1

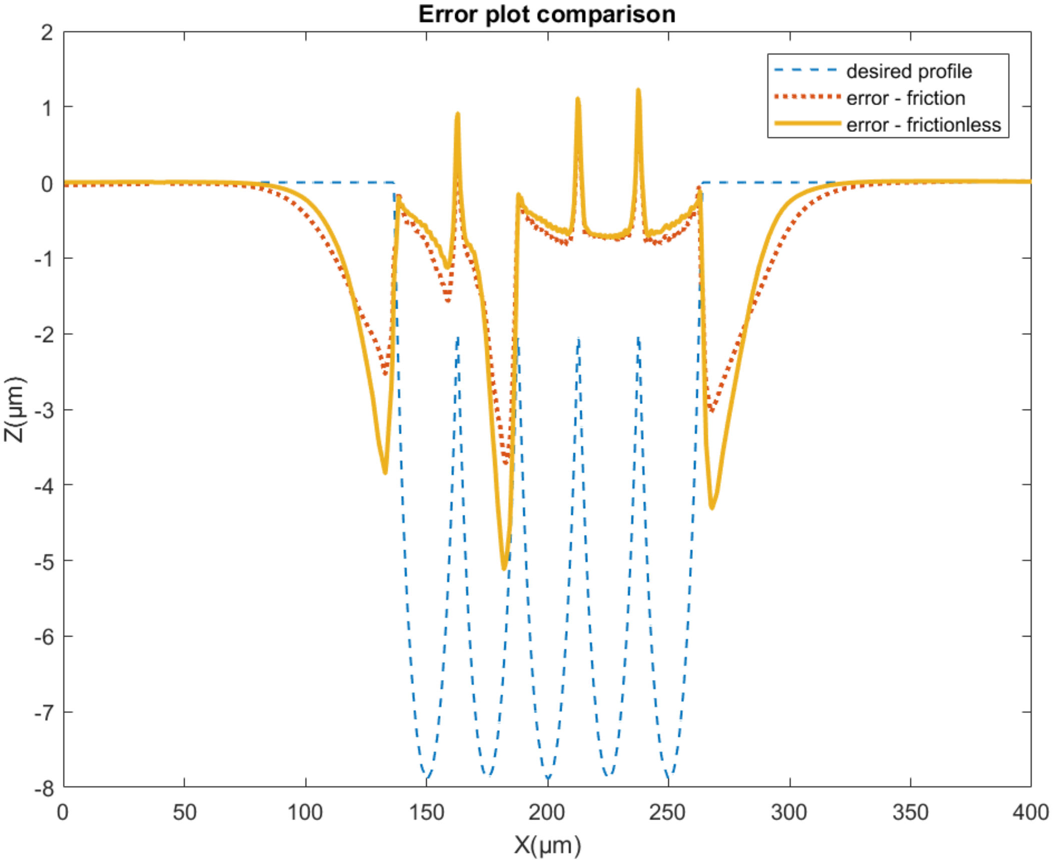

Figure 60. Error plot comparison for friction and frictionless contact, indentation strategy 1

C) Indent depth = 7.92 µm, friction coefficient = 0.4, indentation strategy 2

With the second indent strategy, the distortion in the second column of indents is eliminated as can be seen in Figure 61 and Figure 62. However, there appears to be some distortion in the first column of indents which is lesser compared to the first indentation strategy. Figure 63 demonstrates this error clearly. The second indentation strategy shows promising results when compared to that of the first in terms of the amount of distortion experienced by surrounding indents. However, it provides no advantage in the total indentation time required.

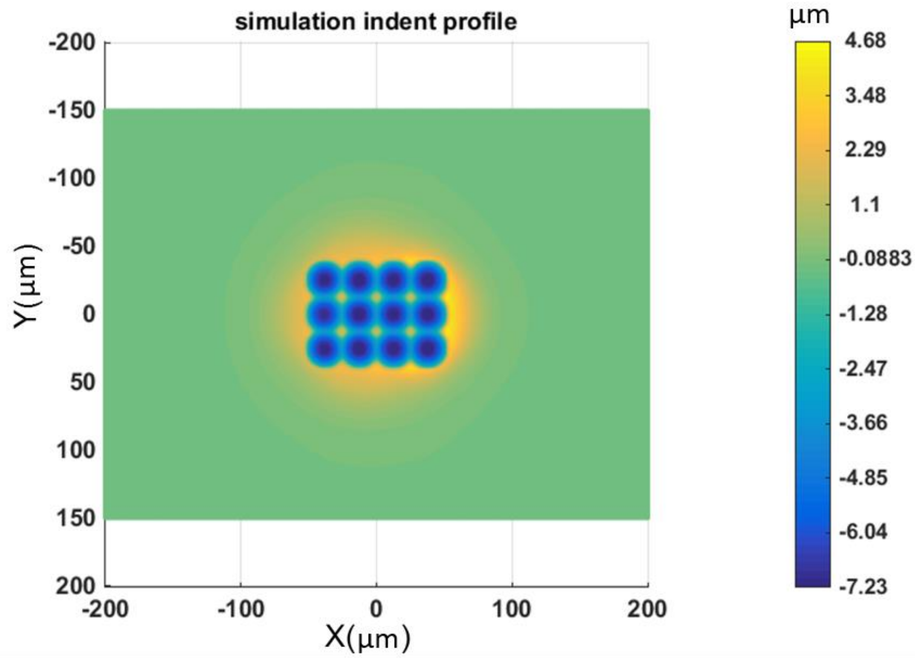

Figure 61. Z contour plot of the indents formed in the simulation: Indent depth = 7.92 µm, friction, indentation strategy 2

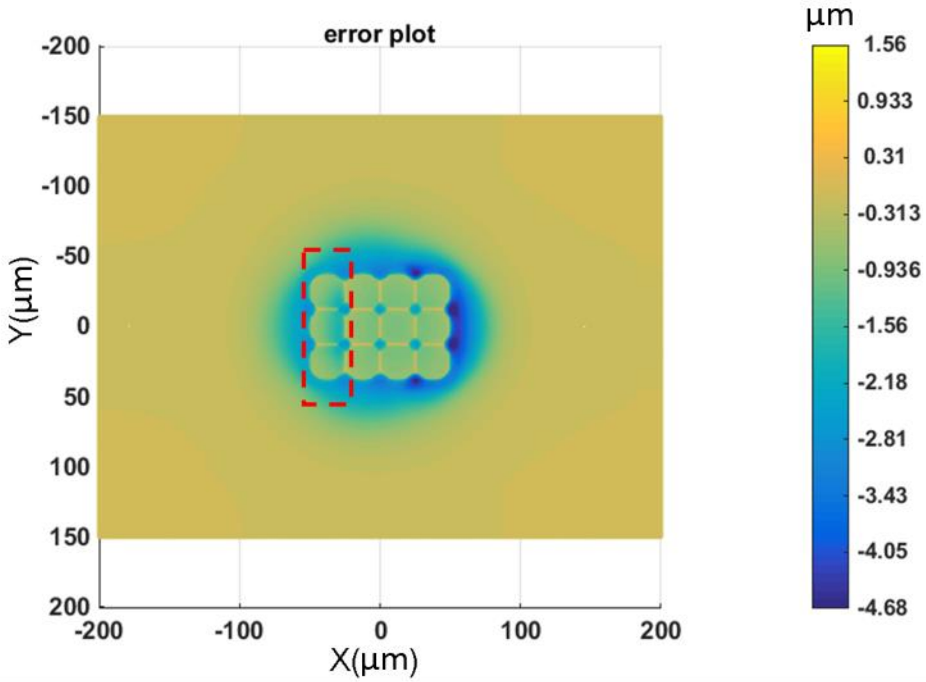

Figure 62. Z contour error plot between the desired indent array and the simulation indent array: Indent depth = 7.92 µm, friction, indentation strategy 2

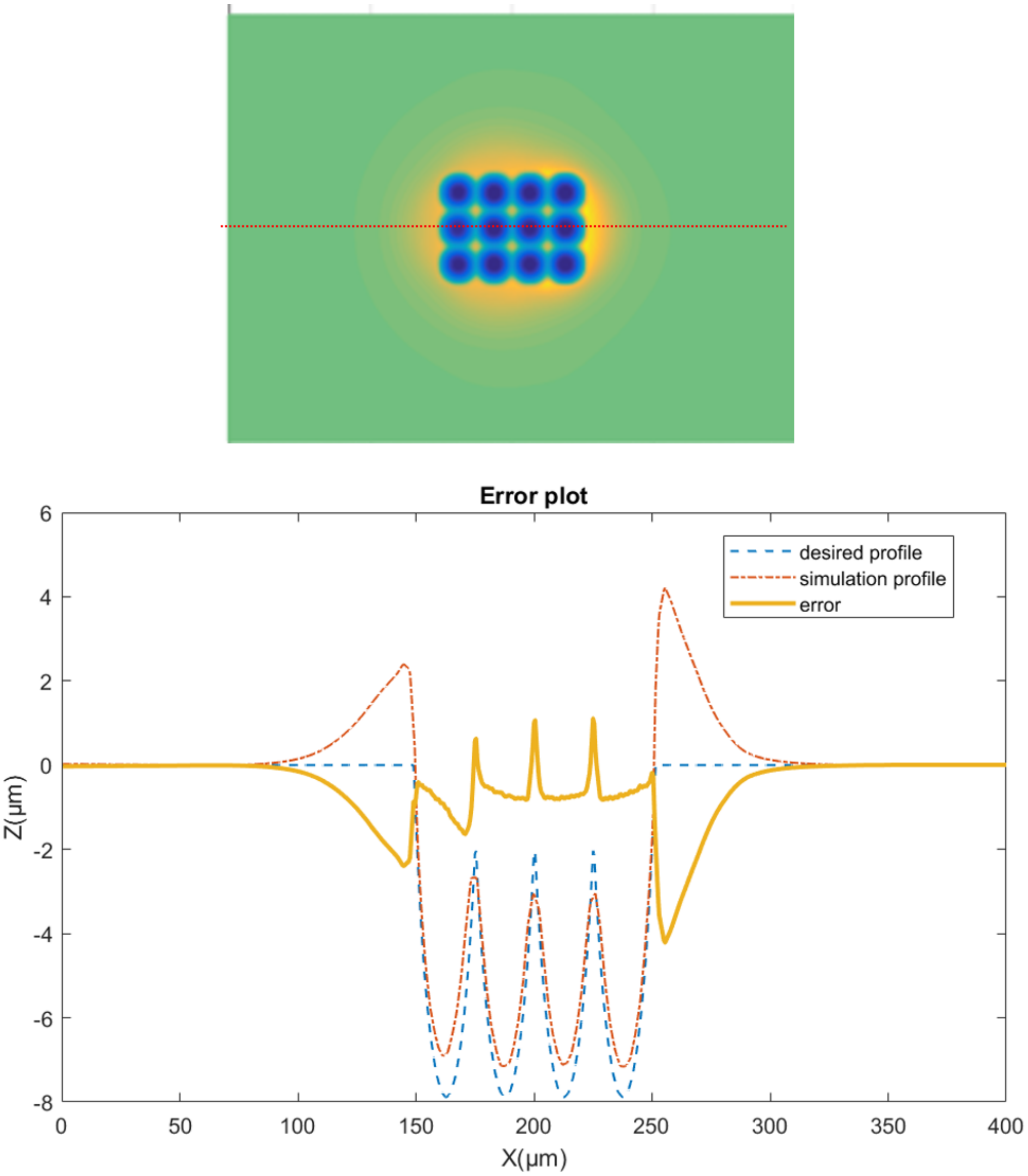

Figure 63. Error plot of the cross section passing through the center of the middle row: Indent depth = 7.92 μm, friction, indentation strategy 2

D) Indent depth = 7.92 μm, frictionless, indentation strategy 2

Figure 64 and Figure 65 shows the simulation indent profile and the error plot respectively for the second indent strategy with a frictionless contact. The difference between the error plot from a frictional contact and a frictionless contact is negligible as shown in Figure 66. Thus, with the second indentation strategy, friction does not affect the error plot of the indents significantly.

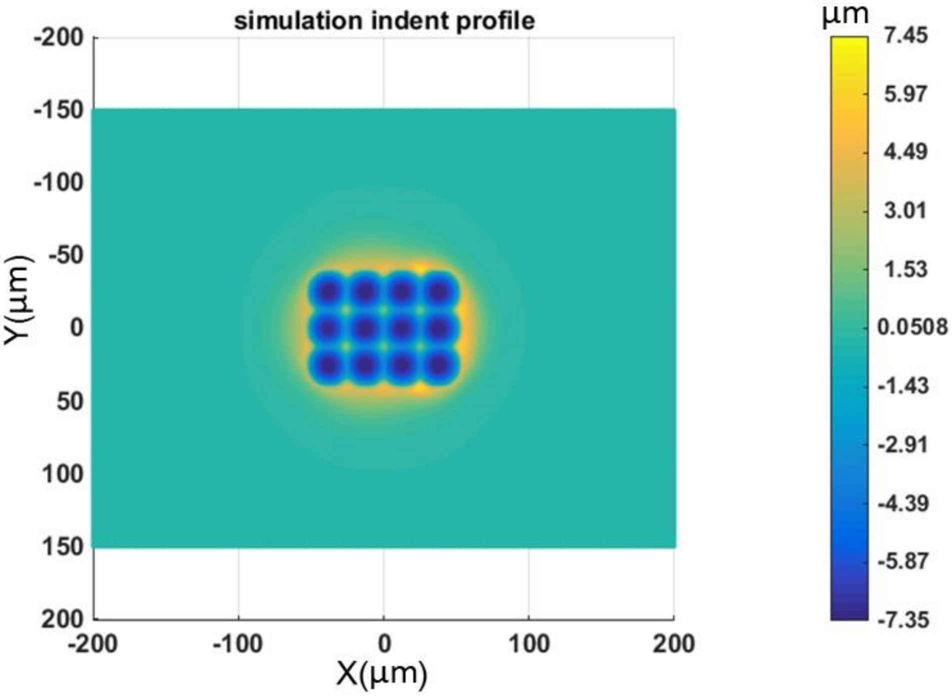

Figure 64. Z contour plot of the indents formed in the simulation: Indent depth = 7.92 μm, frictionless, indentation strategy 2

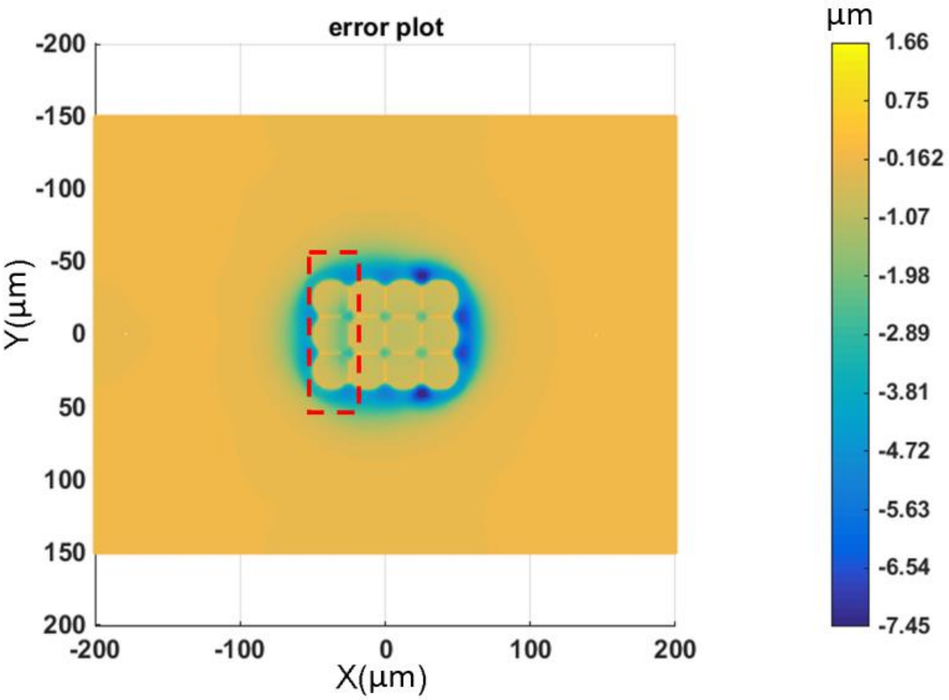

Figure 65. Z contour error plot between the desired indent array and the simulation indent array: Indent depth = 7.92 μm, frictionless, indentation strategy 2

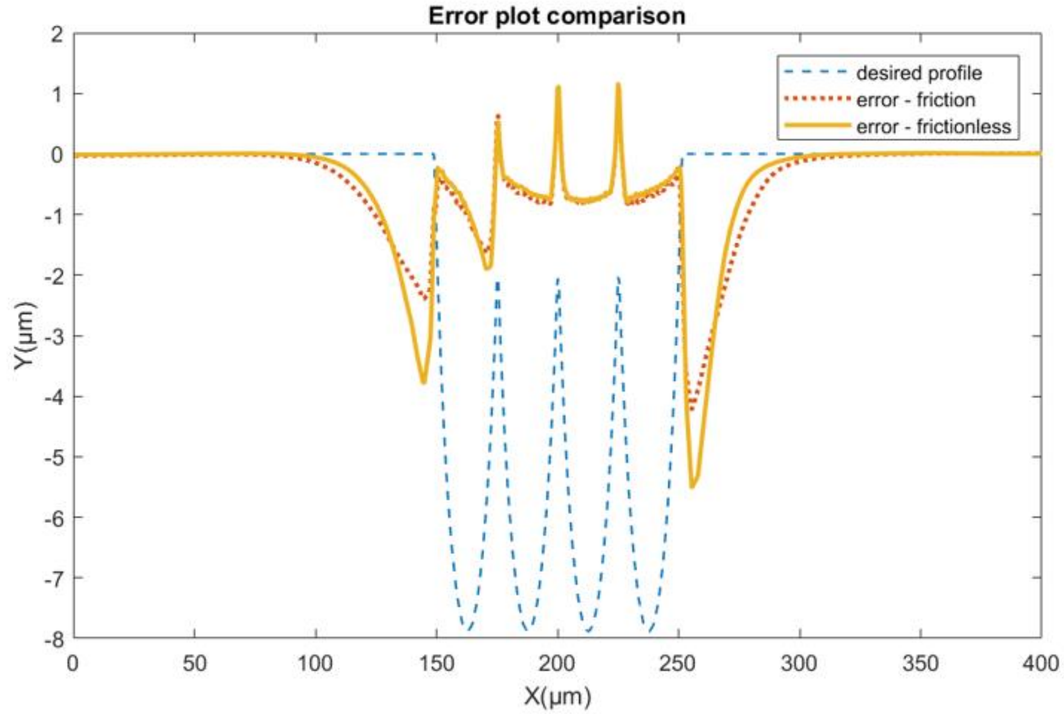

Figure 66. Error plot comparison for friction and frictionless contact, indentation strategy 2

Both the indentation strategies have a tradeoff between the quality of indents and the time taken to create the indents. The future work would be focused on developing the die shape correction and an indentation strategy so that the quality of indents would be increased, and the indentation time would be reduced as much as possible.

4.6 MULTI INDENTER DIE EXPERIMENTS AND ANALYSIS

Indentation experiments were conducted with a 2x2 indenter, fabricated using focused ion beam milling. Figure 67 shows the image of the indenter measured by a laser confocal microscope. In the first experiment, the 2x2 indenter was displaced to a depth of 8.03 μm to produce a single indent with no overlap and in the second experiment, the indenter was displaced to a depth of 8.17 μm with a single column overlap. Figure 68 and Figure 69 shows the laser confocal images of the indents produced by the first and the second experiment respectively.

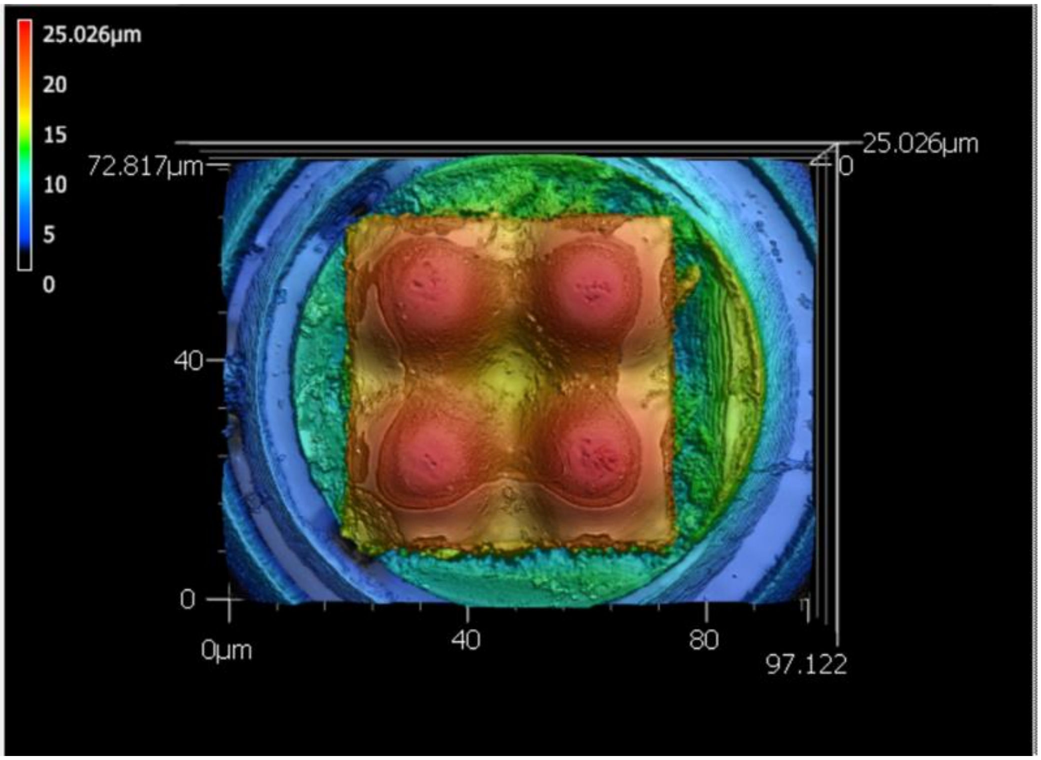

Figure 67. Laser confocal image of the 2x2 indenter

Force and displacement history during the indentation was collected using a piezoelectric load cell and optical probe respectively. The force vs displacement curve for the single indent with no overlap is shown in Figure 70. Measurement of the final indent depth is shown in Figure 71. The displacement at the end of the unloading curve is -7.03 µm which is in good agreement with the final indent depth measurement.

The force vs displacement curve for an indent with a single column overlap is shown in Figure 72. The curve for the first indent starts at 0 µm displacement but that for the second indent starts earlier than 0µm. The pile-up after the first indentation causes the indenter during the second indentation to contact the mold surface sooner than the first. This explains the unusual behavior of the curve. Measurement of the final indent depth is shown in Figure 73. The displacement at the end of the unloading curve is -7.25 µm which is in good agreement with the final indent depth measurement.

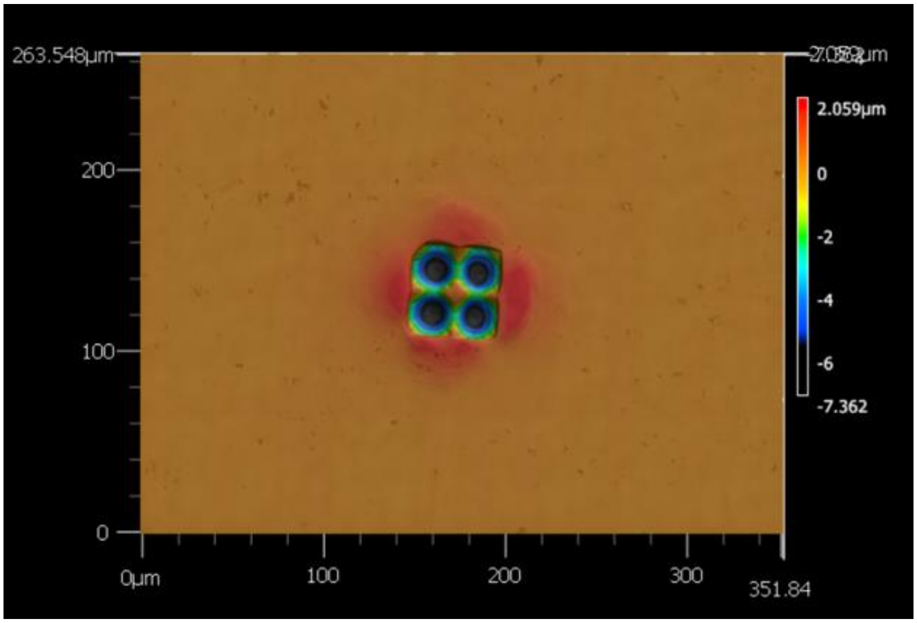

Figure 68. Laser confocal image of a single indent with no overlap

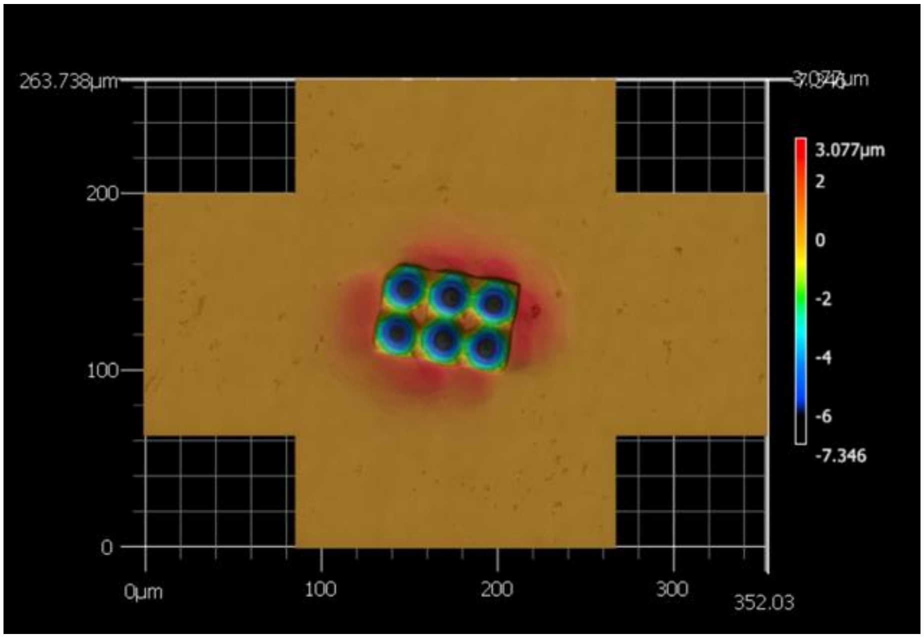

Figure 69. Laser confocal image of an indent with a single column overlap

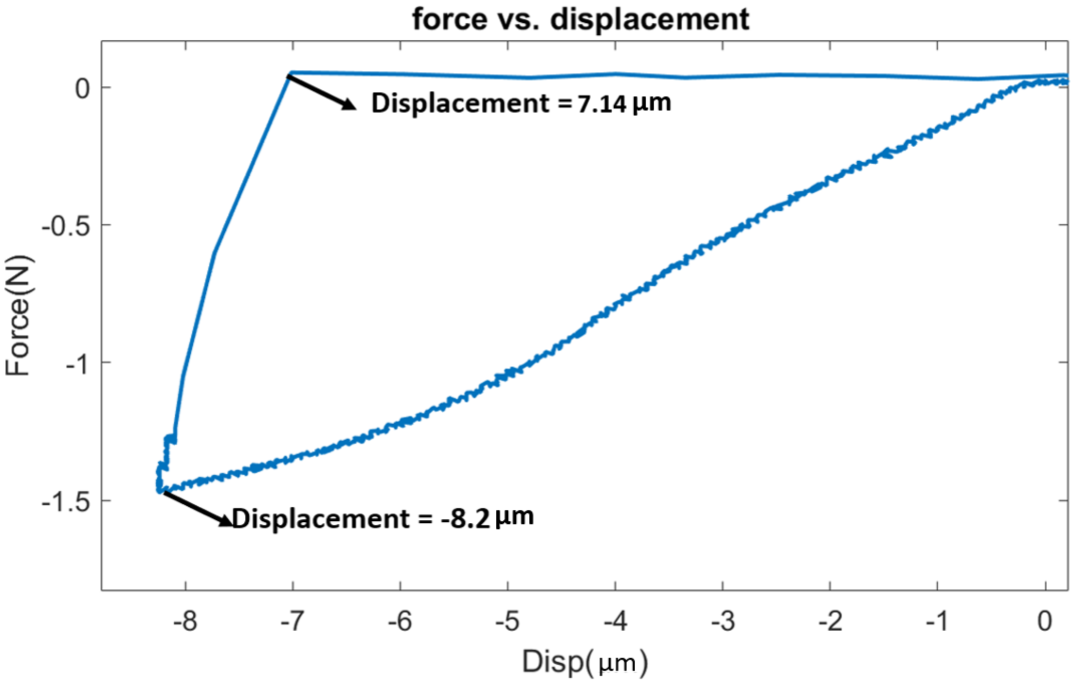

Figure 70. Force vs displacement curve for a single indent with no overlap

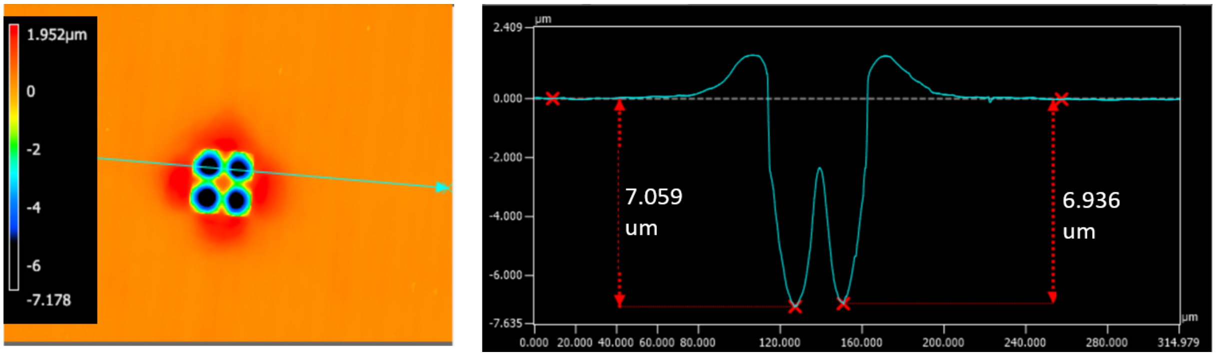

Figure 71. Final indent depth for a single indent with no overlap

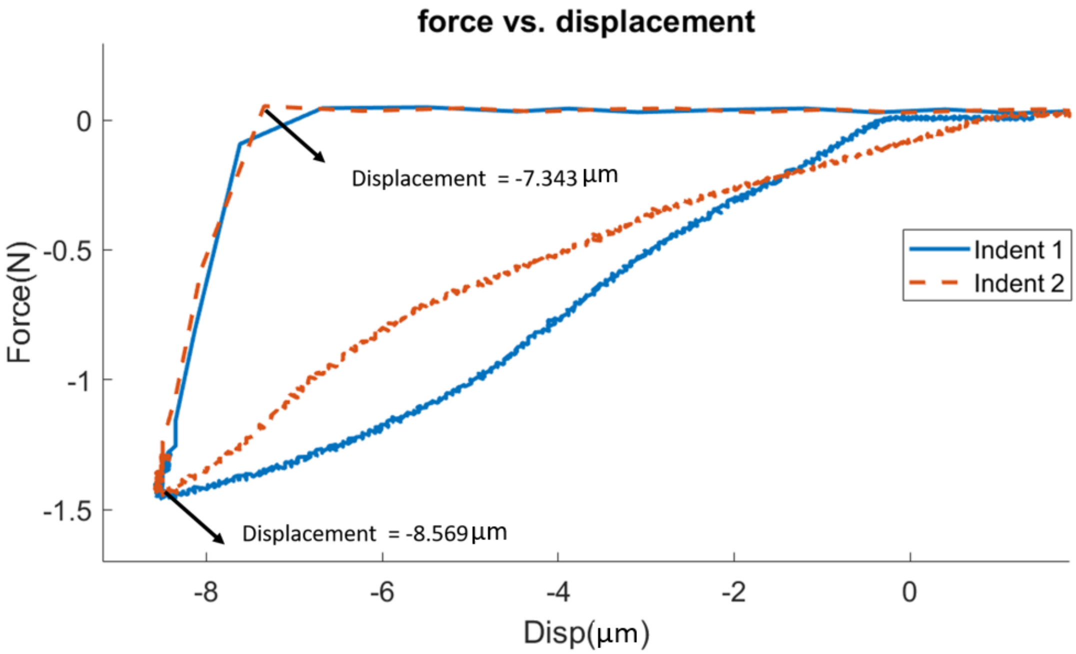

Figure 72. Force vs displacement curve for an indent with single column overlap

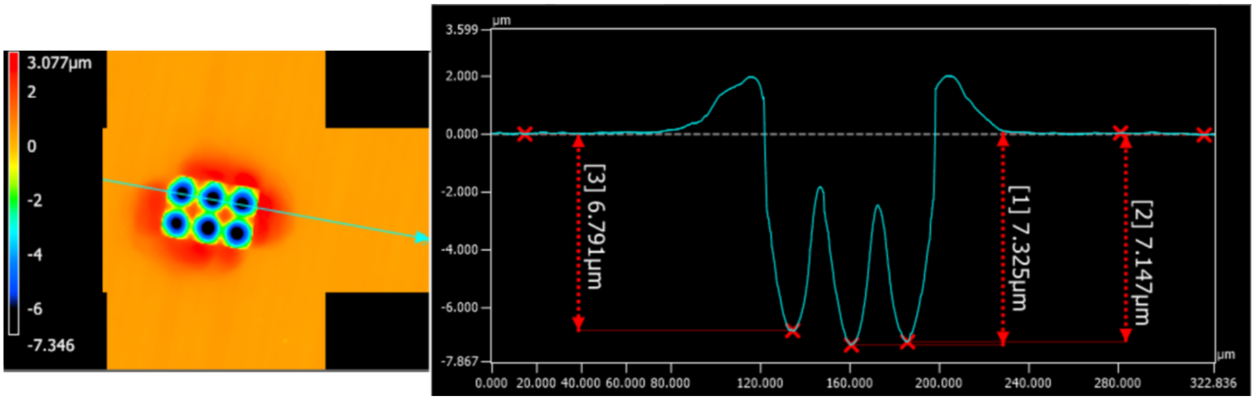

Figure 73. Final indent depth for an indent with single column overlap

Figure 74 shows the labeling of each indent using capital letters: A, B, C, D for the single indent with no overlap. These labels are used to refer to the indents. Similarly, Figure 75 shows the labeling of each indent using capital letters: A, B, C, D, E, F for the indent with single column overlap.

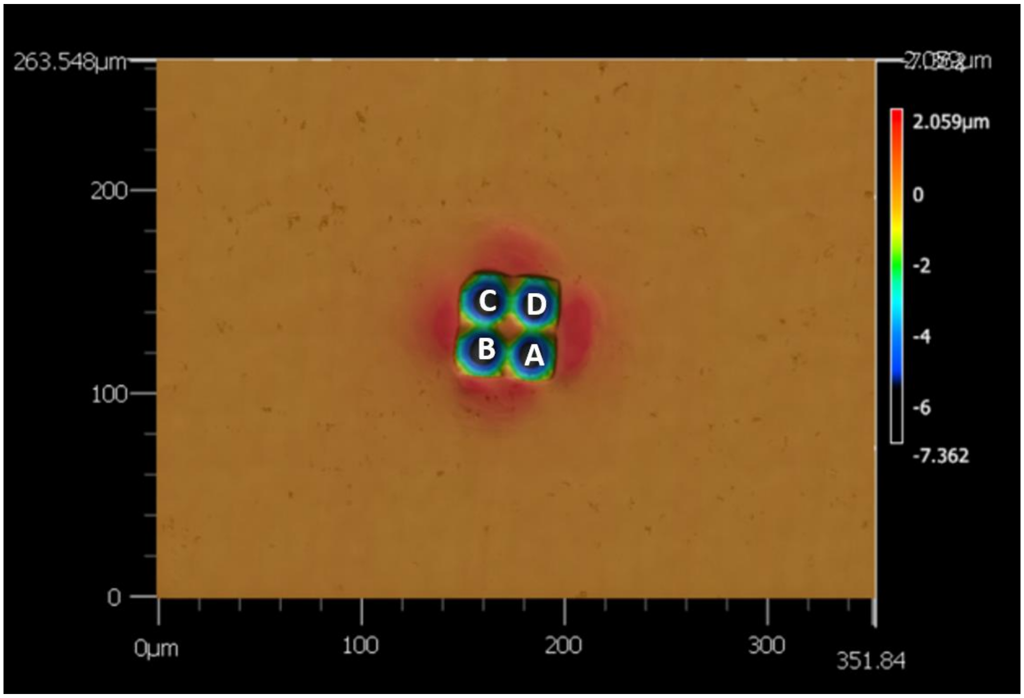

Figure 74. Labels of each indent for a single indent with no overlap

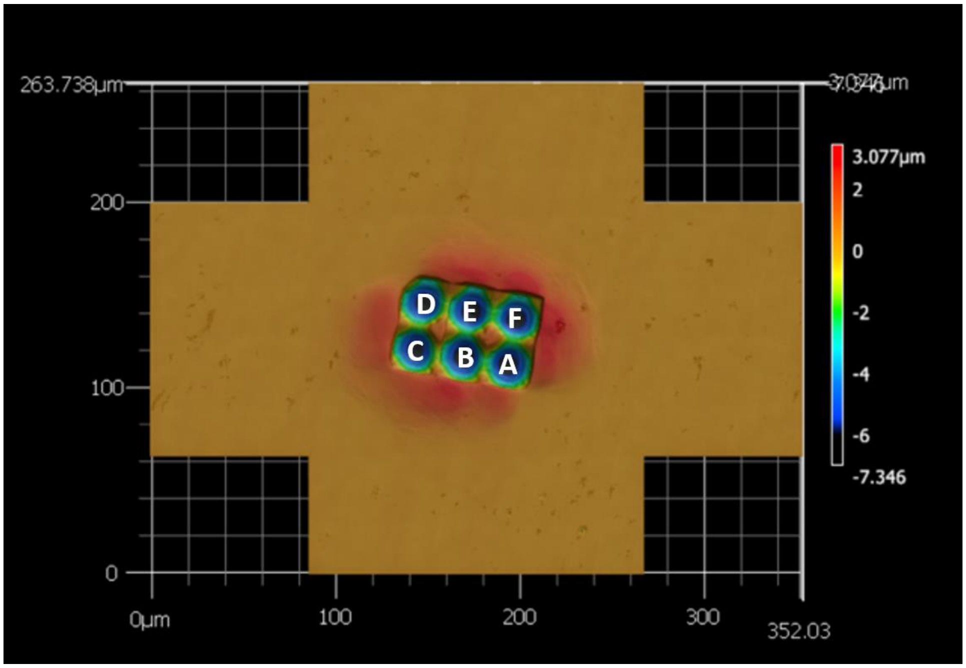

Figure 75. Labels of each indent for an indent with single column overlap

The data from the laser confocal microscope was first imported into Matlab, and a script was used to extract a user-defined region of interest containing each indent feature on the mold and some of the surrounding area. A sphere was fit to the data. The data was trimmed to a Ø24µm aperture centered on the best fit sphere center to remove data from the neighboring lens features which might have been included in the user-defined region of interest. The best fit sphere was calculated for the new trimmed data set. The data was adjusted once again to a Ø24 µm aperture centered on the new best fit sphere center. The best fit sphere center was then considered the center of the indent feature. The measured surface was then compared to the desired shape, which in this case was a hemisphere over a circular aperture. A spheroid of the desired radius was calculated for each (x,y) measured data point. The desired spheroid was shifted so that the apex of the spheroid matched the measured data at (x,y) = (0,0). This forces the error to be zero at the center of the lens feature. The z-direction difference between the desired and measured was calculated for each data point.

Figure 76 shows the desired spherical surface overlaid on the indent A of Figure 74. Figure 77, shows the deviation of the respective indents from the desired spherical surface converted to a percentage of the maximum indent depth. It also shows the deviation in terms of absolute errors. The percentage error plot in Figure 77 has a flat surface with zero percentage error around the center (x,y) = (0,0). The error increases away from the center. This includes the error that is propagated after the FIB process on the die and subsequent creation of the indents. Indents B, C, and D follow the same behavior.

For the indent with single column overlap, only Indent C is analyzed. Figure 78 shows the desired spherical surface overlaid on the indent C from Figure 75. Figure 79 shows the deviation of the indent C from the desired spherical surface converted to a percentage of the maximum indent depth. It also shows the deviation in terms of absolute error. The error plot for single column overlap tends to follow the same behavior as that wit no overlap. The final goal is to get the indent surfaces to perfectly match the desired spherical surface such that the percentage error plot has a flat surface of zero error percentage.

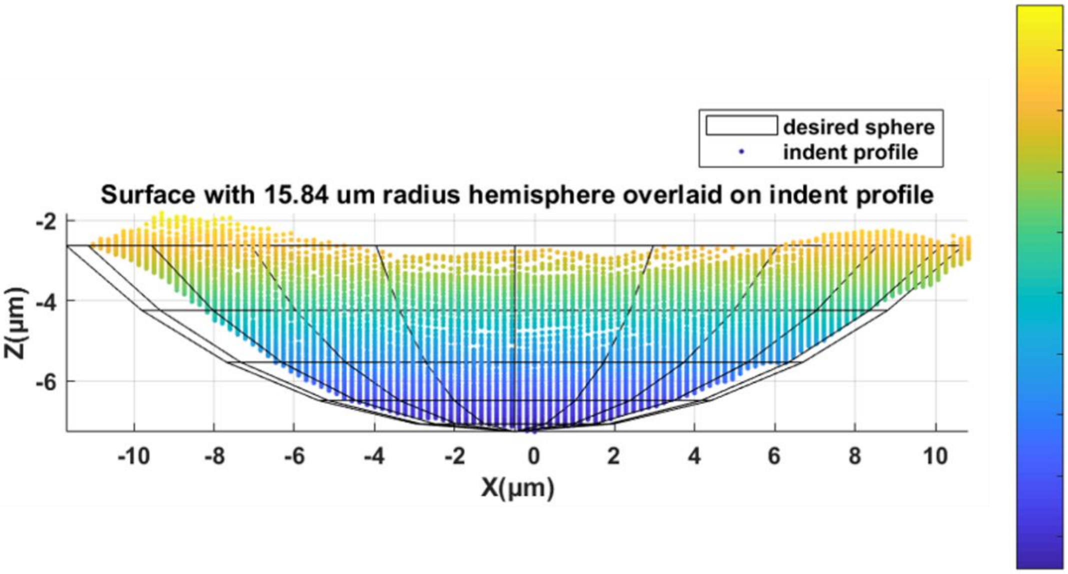

Figure 76. Indent A in Figure 74 with the desired spherical surface overlaid

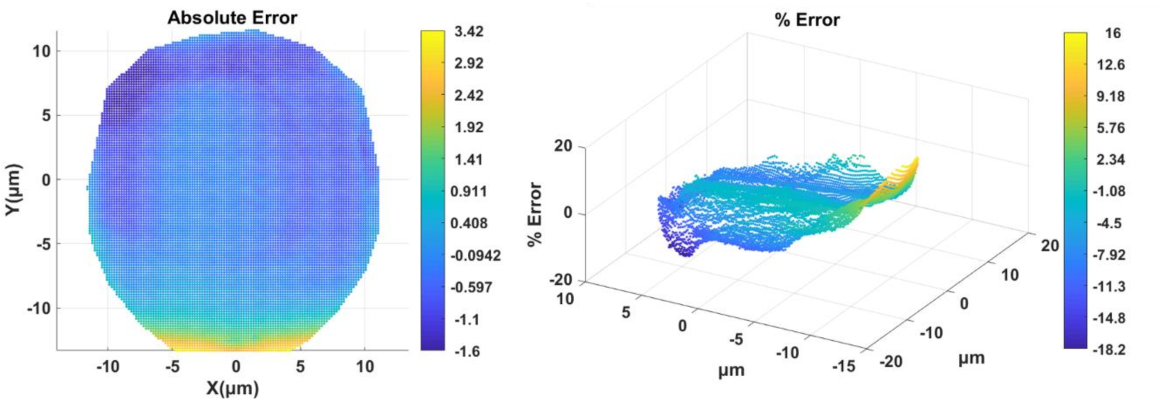

Figure 77. The deviation from the desired spherical surface in terms of absolute error and percentage error of the maximum indent depth of indent A in Figure 74

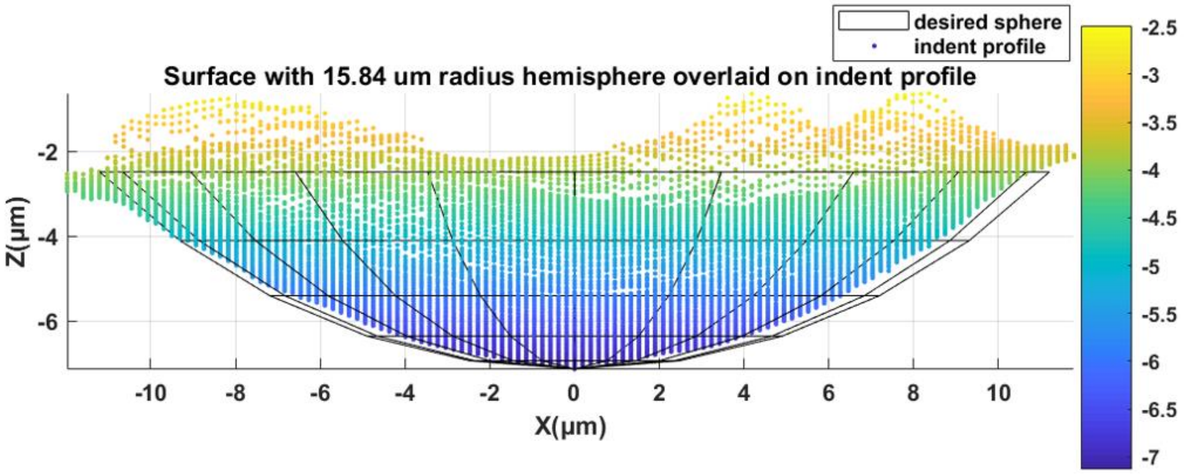

Figure 78. Indent D in Figure 75 with the desired spherical surface overlaid

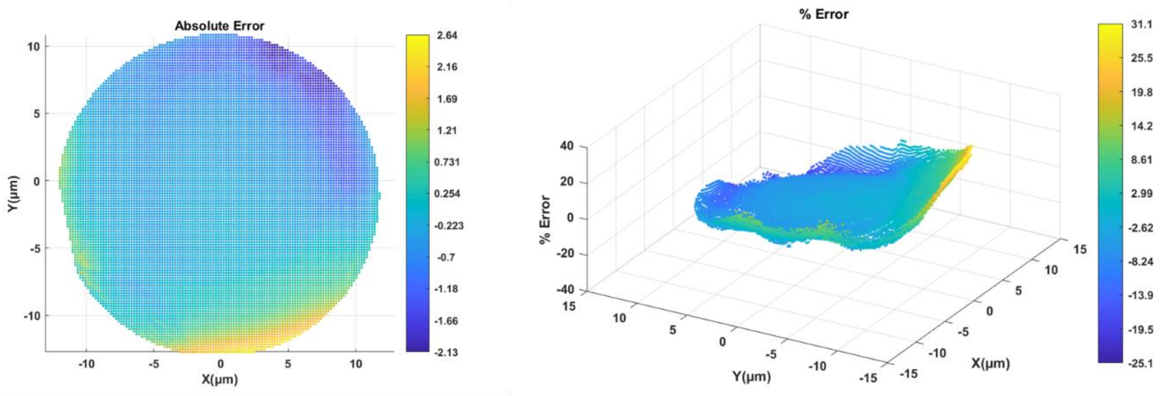

Figure 79. The deviation from the desired spherical surface in terms of absolute error and percentage error of the maximum indent depth of indent D in Figure 75

To further validate the correlation of the nanoindentation experiments in section 4.4 the indentation experiments conducted using the 2x2 indenter can be utilized. For this purpose, the measurement of the 2x2 indenter using the laser confocal microscope was first converted into a .stl file and imported to Materialise Magics software to repair. The repaired file was imported into Abaqus. Before using it in the simulation, it is important to mesh the indenter model properly. The repaired file has many small faces which had to be combined using virtual topology tool in Abaqus to make the model suitable for meshing. Figure 80 shows the final meshed 2x2 indenter in Abaqus. In the future work, correlation using this 2x2 indenter will be obtained.

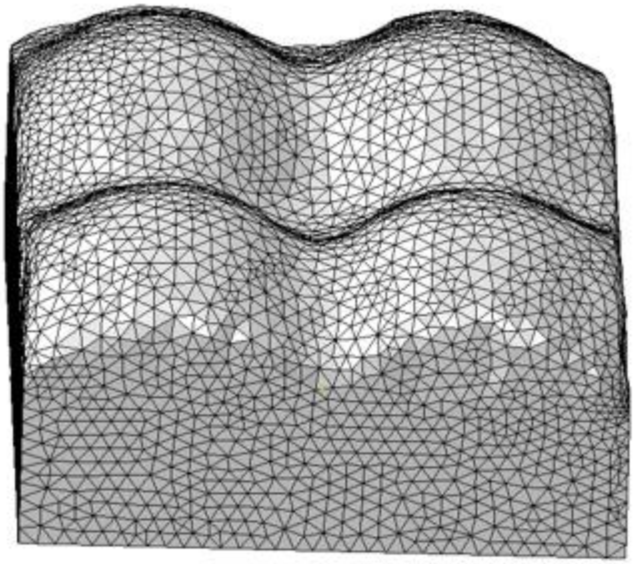

Figure 80. 2x2 indenter meshed in Abaqus

4.7 CONCLUSIONS

Successful correlation of the nanoindentation experiments and the corresponding FEA model shows that the macroscopic properties of Al 1100 measured from the tensile test can be used to assign the material properties to the mold specimen in the microindentation simulations to get reliable results. These same experiments also helped in extracting the elastic modulus of glassy carbon. The indentation strategies devised using the 3x3 indenter have their own drawbacks in terms of indent quality and the indentation time required. In the future work, the concept of die shape correction will be explored to account for the deviation of the indent shape from the desired spherical shape. Other indentation strategies like the progressive indentation which involves a multi indenter die with different sized individual features will also be explored. A tool was developed to compare the indent shape to the desired spherical shape to get the height error of the indents formed in the experiments. This tool helps in determining the goodness of fit of the lens features created on the mold. Once, a proper multi-indenter die is designed and a good indentation strategy is developed this tool will be used to verify the quality of the indents formed in the indentation experiments.

References

[1] Smith, Michael. ABAQUS/Standard User's Manual, Version 6.9. Providence, RI : Simulia, 2016." .

[2] Oliver, W. C., and Pharr, G. M., 1992, "An Improved Technique for Determining Hardness and Elastic Modulus using Load and Displacement Sensing Indentation Experiments," Journal of Materials Research, **7**(6) pp. 1564-1583.

[3] Sneddon, I. N., 1965, "The Relation between Load and Penetration in the Axisymmetric Boussinesq Problem for a Punch of Arbitrary Profile," International Journal of Engineering Science, **3**(1) pp. 47-57.

[4] Chudoba, T., and Richter, F., 2001, "Investigation of Creep Behaviour under Load during Indentation Experiments and its Influence on Hardness and Modulus Results," Surface and Coatings Technology, **148**(2) pp. 191-198.

[5] Chudoba, T., and Richter, F., 2001, "Investigation of Creep Behaviour under Load during Indentation Experiments and its Influence on Hardness and Modulus Results," Surface and Coatings Technology, **148**(2) pp. 191-198.

[6] Lichinchi, M., Lenardi, C., Haupt, J., 1998, "Simulation of Berkovich Nanoindentation Experiments on Thin Films using Finite Element Method," Thin Solid Films, **312**(1) pp. 240-248.

[7] Sahu, S., Pada Mondal, D., Dass Goel, M., 2018, "Finite Element Analysis of AA1100 Elasto-Plastic Behaviour using Johnson-Cook Model," Materials Today: Proceedings, **5**(2, Part 1) pp. 5349-5353.

5 EVALUATION OF DIGITAL IMAGE RECOGNITION METHODS FOR MASS SPECTROMETRY IMAGING DATA ANALYSIS

Kenneth P. Garrard[1,2]
Senior Research Scholar
Måns Ekelöf[2], **Rika Judd**[3], **De-Yu Xie**[3], **David C. Muddiman**[2,5]
Elias P. Rosen[4], **Angela D. M. Kashuba**[4]
[1]Precision Engineering Consortium, Mechanical and Aerospace Engineering
[2]FTMS Laboratory for Human Health Research, Department of Chemistry
[3]Department of Plant and Microbial Biology
[4]Division of Pharmacotherapy and Experimental Therapeutics
University of North Carolina at Chapel Hill
[5]Molecular Education, Technology, and Research Innovation Center (METRIC)
North Carolina State University

Analyzing mass spectrometry imaging data can be laborious and time consuming, and as the size and complexity of datasets grow, so does the need for robust automated processing methods. We here present a method for comprehensive, semi-targeted discovery of molecular distributions of interest from mass spectrometry imaging data, using widely available image similarity scoring algorithms to rank images by spatial correlation. A fast and powerful batch search method using a MATLAB implementation of structural similarity (SSIM) index scoring with a pre-selected reference distribution is demonstrated for two sample imaging datasets, a plant metabolite study using Artemisia annua leaf, and a drug distribution study using maraviroc-dosed macaque tissue.

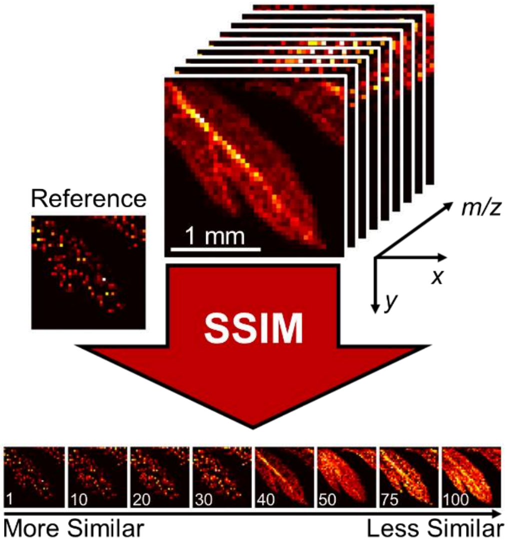

5.1 INTRODUCTION

Mass spectrometry imaging (MSI) datasets are highly complex, containing abundance and distribution information about hundreds of thousands of chemical species. As sample probes and ionization techniques have evolved, the information density of untargeted (discovery) MSI data has increased to the point where comprehensive manual interpretation is not practical. Some degree of automation must be employed to extract features of interest in a semi-targeted fashion. For untargeted analysis an automated technique is needed to find molecular images “similar” to a given reference image and rank them in a reasonable amount of time. With high resolving power instrumentation (RP=140,000) a small molecule data set (200 to 2000 Da) contains 2.5 x 10^8 potential images.

The desired outcome of discovery-type MSI experiments is typically the identification of molecular distributions correlated to some other feature such as a known region of the sample, or the distribution of some known compound such as a disease marker, isotopic label, or a drug. For this type of study, data interpretation comes down to finding images of *a particular appearance* from a limited search space. This is, in essence, an image recognition problem similar to those of facial recognition or compression quality evaluation in digital image processing [1].

Simple approaches that may be fast enough include pixel-by-pixel metrics such as subtracting images, calculating their ratios, the sum of absolute differences, mean squared error (MSE), and the peak signal to noise ratio (PSNR). However any Minkowski metric with the form of Equation 1 will fail to correlate structure in images because perceptual distance and molecular distance are not the same as Euclidean distance. For example, MSE and PSNR measure changes in luminance which is a relative measure that is independent of structure. Varying contrast, blurring and mean shifting do not change MSE but do change visual quality and may represent different molecular patterns.

$$E_p = \left(\sum_{i=1}^{N} |x_i - y_i|^{\,p}\right)^{1/p} \tag{1}$$

This can be seen in Figure 1 where the upper left photo is the reference and the other five distorted images have identical MSE values when compared to this reference image.

Figure 1. Deficiency of mean squared error for image comparison. The image in the red box (upper left) is the reference. The other images are clearly distorted but have identical MSE values.

5.2 STRUCTURAL SIMILARITY INDEX

The gold standard for calculating the perceived similarity of two given images is the structural similarity index metric (SSIM) [2, 3]. The SSIM algorithm arose from a need to automatically predict the perceived quality of digital images after compression or other processing. It is based on the human visual system and separates the luminance, contrast and structural elements as shown in Figure 2.

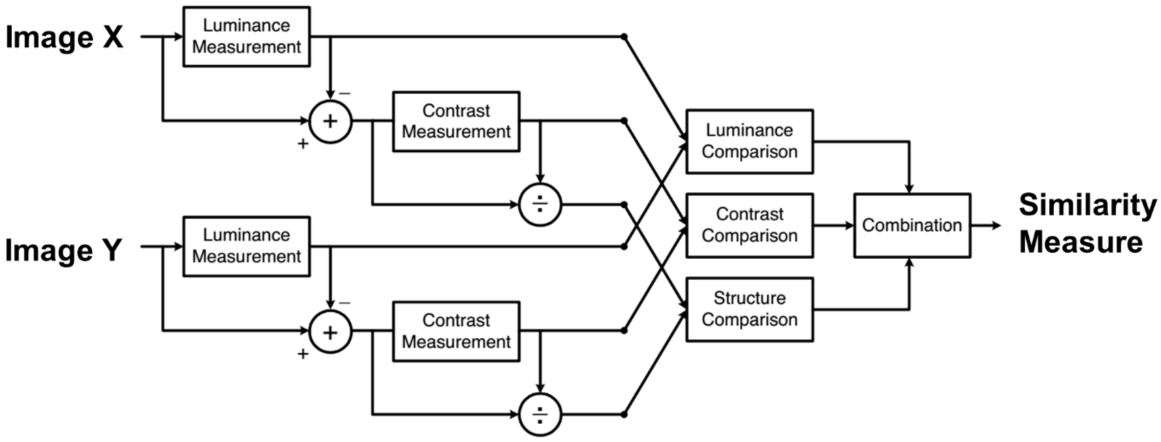

Figure 2. The structural similarity algorithm.

To calculate the SSIM index for a pair of images, each image is subdivided into smaller sub-images, typically by generating a small window around each pixel. For each aligned pair of sub-images x and y, the arithmetic mean (μ_x, μ_y), unbiased standard deviation (σ_x, σ_y) and Pearson's correlation coefficient ($\sigma_{xy}/\sigma_x\sigma_y$) are calculated. From these quantities the luminance, contrast, and structural differences can be calculated using Equations (2-4).

$$luminance = l(x_i, y_i) = \frac{2\mu_x\mu_y + c_1}{\mu_x^2 + \mu_y^2 + c_1} \tag{2}$$

$$contrast = c(x_i, y_i) = \frac{2\sigma_x\sigma_y + c_2}{\sigma_x^2 + \sigma_y^2 + c_2} \tag{3}$$

$$structure = s(x_i, y_i) = \frac{\sigma_{xy} + c_3}{\sigma_x\sigma_y + c_3} \tag{4}$$

The constants c_1, c_2, and c_3 are arbitrary small values that avoid numeric instability when the denominator would otherwise be close to zero. A score is obtained by combining luminance, contrast and structure as a product with exponential weighting factors as shown in Equation 5. The final result can be shown either as a map of local similarities, or as a mean SSIM (MSSIM) score for the whole image using Equation 6.

$$SSIM(x_i, y_i) = l(x_i, y_i)^{\alpha} * c(x_i, y_i)^{\beta} * s(x_i, y_i)^{\gamma} \tag{5}$$

$$MSSIM = \frac{\sum_{i=1}^{n} SSIM(x_i, y_i)}{n-1} \tag{6}$$

The SSIM algorithm has the following useful mathematical properties.

Symmetry	$SSIM(x,y) = SSIM(y,x)$
Boundedness	$SSIM(x,y) < 1$
Unique maximum	$SSIM(x,y) = 1$, iff $x = y$

5.3 MSIREADER IMPLEMENTATION

To apply image recognition methods to real MSI data, the batch processing function of MSiReader [4, 5] was modified to enable correlation scoring for a range of MS images with a given reference image. The SSIM algorithm is included in the MATLAB Image Processing Toolbox (The MathWorks, Inc., Natick, MA, USA) and was used without modification. The MATLAB implementation of SSIM calculates the index at each pixel by applying a circular gaussian weighting filter with adjustable radius. The combined score at each pixel is then calculated using Equations 5 and 6, where the weighting constants α, β and γ can be set by the user. Their default values are 1, giving equal weight to each component. An example SSIM calculation using 200x200 monochrome images is shown in **Figure 3**, illustrating both the individual components and final scoring (mean SSIM).

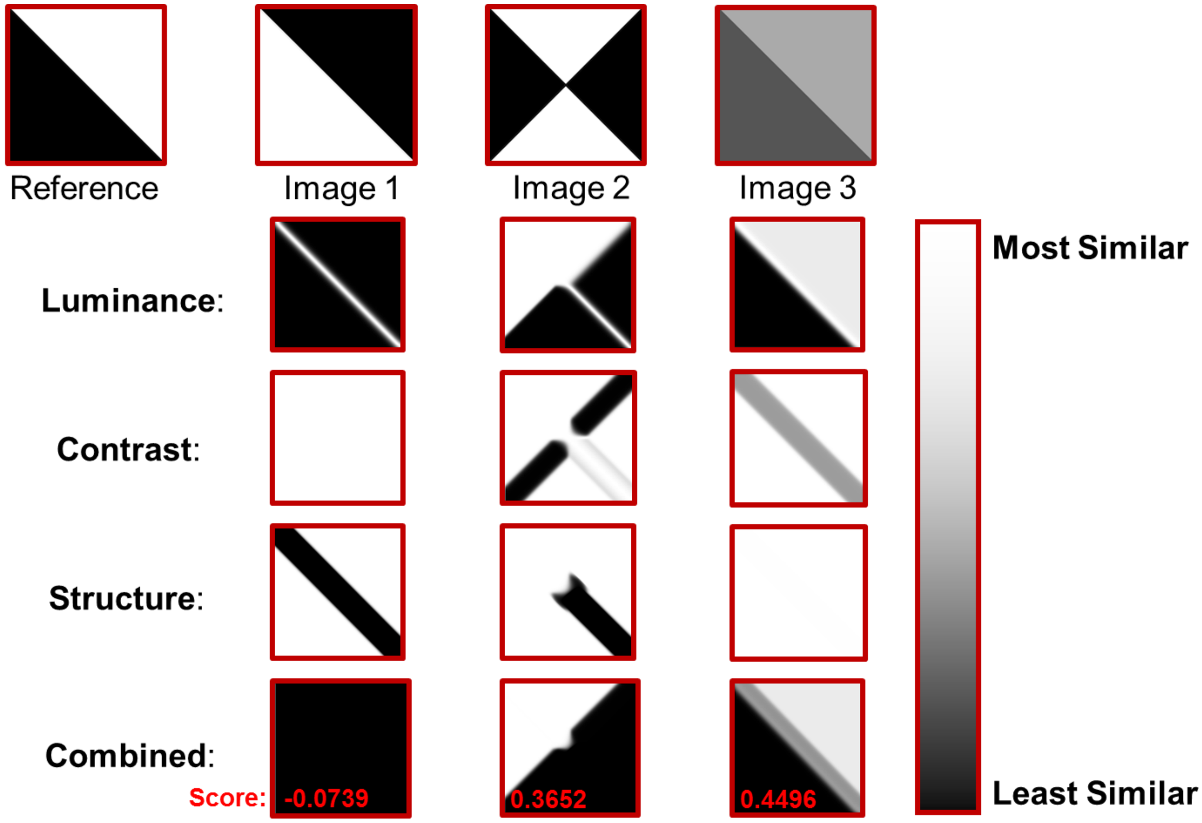

Figure 3. SSIM analysis of three example images for a given reference, with the separate components shown separately and combined into a numerical score (mean SSIM). The SSIM output shown was produced using the same MATLAB implementation as used for MSI evaluation, but with the Gaussian radius weighting set to a value of 6 for demonstration purposes.

The MSiReader SSIM correlation tool is very efficient. Execution scales linearly with the image size in pixels and the number of candidate images. The score for a pair of 1000 x 1000 pixel images is calculated in about 100 milliseconds on an ordinary laptop computer. In an hour 36,000 candidate images can be ranked. If parallel processing is used speedup is nearly linear in the number of processors since the image comparisons are independent and the final ranking is obtained by sorting the results from each processor. For the dosed drug study discussed below 280,000 images were generated and ranked in about 20 hours, or about 16 images per second. Less than 12 minutes were devoted to the SSIM algorithm with the remainder being used to generate the virtual images.

5.4 EVALUATION OF IMAGING DATASETS

To test the usefulness of image recognition for real problems, two imaging datasets were produced, selected to be representative of typical work done in our lab. Each image was acquired using IR-MALDESI ionization coupled to a Q Exactive Plus mass spectrometer operating at a nominal resolving power of 140,000 as previously described [6]. The raw data was converted to imzML using msconvert [7] and the imzmlconverter [8], and then loaded into MSiReader for analysis. Normalization to maximum abundance per image was used to ensure matching based on relative rather than absolute ion abundance for the luminance score. All heatmaps were generated using the perceptually linear “hot” colormap preset in MSiReader.

All raw data used are provided in mzML and imzML format in the electronic supplement. The image recognition tools used are included in the current open source and stand-alone versions of MSiReader (v. 1.01), available at http://www.msireader.com.

5.4.1 Imaging of *Artemisia annua* Leaf

The sweet wormwood (*Artemisia annua,* Chinese: *Qinghao*) native to China, is notable as the primary natural source of artemisinin, a powerful antimalarial compound, the discovery of which was awarded the 2015 Nobel medicine prize [9]. Artemisinin and other related metabolites (e.g. its precursors and derivatives) are accumulated in glandular trichomes on the leaf surface, the size and density of which depend on spatial positions of leaves and plant ages [10, 11]. The unique chemical composition and localization of glandular trichomes on the leaf surface makes it suitable as a validation system for MSI data analysis.

Leaves on the 15-17th nodes of two-month old *A. Annua* plants, grown in the NC State phytotron, were collected and affixed to a glass microscopy slide using double-adhesive tape. A 2x2 mm region of interest was imaged in negative mode at a spatial resolution of 50 µm (40x40 scans), in the mass range of *m/z* 100-400. The molecular ion of intact artemisinin $[M-H]^-$ observed at *m/z* 281.1395 was selected as reference for image scoring. The MSiPeakfinder tool was used to pregenerate a list of 332 masses with a 2x or higher abundance ratio in scans from leaf tissue compared to blank scans. This reduced dataset was used to evaluate the effect of the various SSIM parameters (*α, β, γ*, Gaussian filter radius).

5.4.2 Imaging of Drug-dosed Macaque Lymph Node

Combinations of antiretroviral therapies (ARVs) have radically improved health outcomes for persons living with HIV. Interruption of these regimens, however, leads to rapid viral rebound that may result from inadequate penetration of drug into tissues where virus primarily resides such as lymph nodes [12]. Tissue disposition of the viral entry-inhibitor maraviroc was investigated in the lymph node of a rhesus macaque, an animal model of infection, receiving 270 mg/kg maraviroc dosed twice daily. Since ARV tissue distribution can be highly heterogeneous [13], MSI analysis provides a useful tool in identifying ions accumulating in similar patterns to maraviroc that may participate in its trafficking and metabolism within the lymph node.

A 10 µm thick section of dosed lymph node was imaged in positive mode at 100 µm spatial resolution (75x90 scans, or 7.5x9 mm), in the mass range of *m/z* 200-800. Comprehensive SSIM analysis was performed by binning the entire mass range into evenly spaced non-overlapping bins of 5 ppm width (277259 bins), and subsequently comparing each bin against the reference distribution of maraviroc (*m/z* 514.3352) using default SSIM weightings. Duplicate hits resulting from the same peak being included in adjacent 5 ppm bins were removed, with only the highest ranked image at a given mass (10 ppm tolerance @ *m/z* 550) kept for analysis.

5.5 RESULTS AND DISCUSSION

5.5.1 Trichome-bound Metabolites in *A. annua*

To find suitable constant parameters for the SSIM algorithm, SSIM evaluation for the *A. annua* sample was performed repeatedly, with the weighting parameters (*α, β, γ*) varied between 0.5 and 4 individually and pairwise. While changes to the weightings did affect the numerical SSIM score, the rank order was largely unchanged, and so the default weight of 1 for each parameter was used for all data here presented. Similarly, evaluating the SSIM scores with the Gaussian filter radius parameter varying between 1 and 5 showed only minor effects on the final ranking. It was observed that a small increase in the radius parameter led to significantly lower ranking of images with visible noise, caused either by low absolute ion abundance (shot noise) or significant chemical background noise. We found that a value of 2.25, raised from the default 1.5, resulted in somewhat improved contrast between visually identified “good hits” and “bad hits”, while still assigning high similarity scores to images with moderate levels of chemical noise. These parameters ($\alpha = \beta = \gamma = 1$; *radius* = 2.25) were used for all subsequent processing.

The pre-selected set of 332 tissue-correlated peaks was evaluated against the reference *m/z* 281.1395 (artemisinin), and sorted by similarity as shown in **Figure 4**. The final ranking correctly identified the reference mass itself as a perfect correlation match, with its own first isotope as a close second. Known artemisinin derivatives including deoxyartemisinin (*m/z* 265.144, rank 13) and dihydroartemisinin (*m/z* 283.155, rank 22) were identified as visually similar distributions despite large variance in actual ion abundance. The peak set contained 31 ion masses with the characteristic distribution pattern of artemisinin, which were correctly assigned ranks of 1-31.

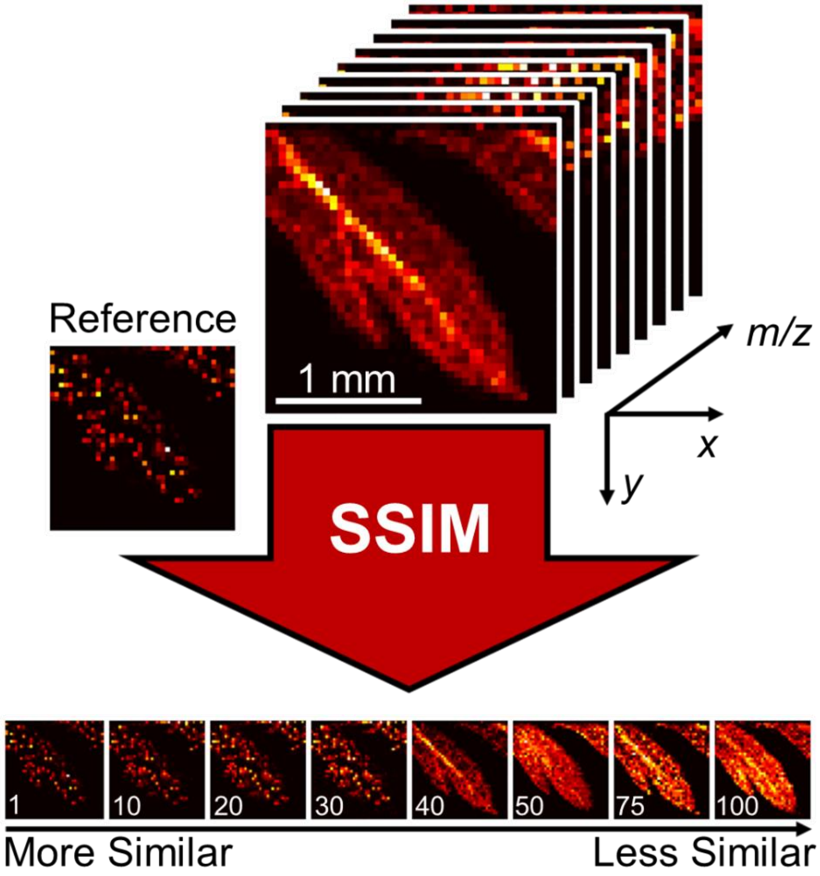

Figure 4. Illustration of the image recognition workflow applied to an MSI dataset acquired from IR-MALDESI imaging of *A. annua* leaf using a known metabolite (Artemisinin, *m/z* 281.1395) as a reference. All images were internally normalized to a 0-1 abundance scale before processing and visualization. Some selected masses taken from the top 100 best matches are shown with similarity rank.

5.5.2 Drug Distribution in ARV Dosed Tissue

For the drug dosed lymph node section, a comprehensive brute force search was performed, where the SSIM evaluation was performed separately for the mass image of each non-overlapping 5 ppm bin through the whole mass range of *m/z* 200-800. Performing the evaluation this way required a total of 20 hours of computation time. This represents the most thorough search possible with the method, providing a “worst case” example of computation requirements. The 500 best unique image matches were batch exported and inspected. The top 20 unique matches yielded images of very high visual similarity, with the top 10 almost indistinguishable from the reference. The exported images were all found to visually outline the tissue shape in part or whole, with lower ranked and partial images generally ranking lower. This is illustrated in **Figure 5**, showing a selection of images throughout the correlation range.

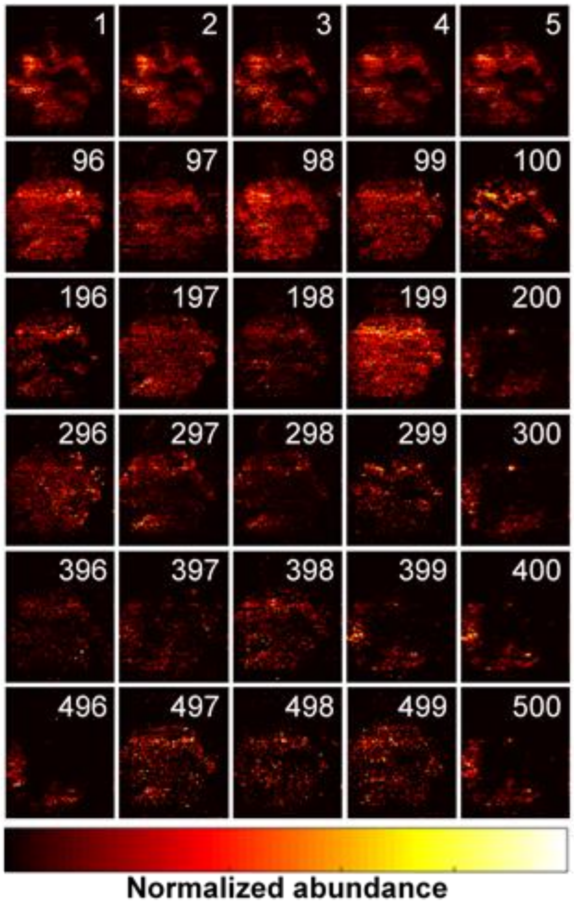

Figure 5. Selected output from a comprehensive SSIM search of drug dosed lymph node tissue. The images are shown on the normalized 0-1 abundance scale used for SSIM comparisons, with similarity rank shown in white. The image ranked 1 is that of maraviroc (*m/z* 514.3352), used as a reference.

We have found SSIM to be a very robust and useful noise filter for images that have background or off-sample data. Caution must however be taken not to include so much background data as to make the contrast between on and off sample dominate the correlation calculations. For images containing very large regions consisting exclusively of empty scans, or where matching to very localized distributions is desired, we recommend limiting the search to a pre-defined region of interest. Narrowing the search space this way has the additional effect of reducing processing times proportionately and can be applied for that purpose alone.

5.6 CONCLUSIONS

We have here described the implementation and use of an open-source tool using image similarity scoring to efficiently extract features of potential interest from high resolving power mass spectrometry imaging datasets. Using the SSIM method for image similarity scoring, the process of semi-targeted discovery can be performed in an automated fashion. Sorting or filtering data by structural similarity effectively reduces complex datasets down to a scale suitable for manual interpretation, and can be used as reproducible pre-processing step for methods where computation time and memory requirements are limiting factors, e.g., principal component analysis.

All the algorithms used have been incorporated into the latest public release of MSiReader through the batch processing interface. The code is distributed under the BSD 3 license [4] and can be freely adapted to other platforms for analyzing MSI data.

5.7 ACKNOWLEDGEMENTS

All mass spectrometry measurements were carried out in the Molecular Education, Technology, and Research Innovation Center (METRIC) at NC State University. The authors gratefully acknowledge the financial support received from the National Institutes of Health (R01AI111891, R01GM087964), and North Carolina State University.

All animal experiments were performed in accordance with locally-approved IACUC protocols.

REFERENCES

1. Wang, Z., Bovik, A.C. Morgan & Claypool Publishers, San Rafael, Calif. (2006)

2. Wang, Z., Bovik, A.C., Sheikh, H.R., Simoncelli, E.P.: Image quality assessment: From error visibility to structural similarity. Ieee T Image Process. **13**, 600-612 (2004)

3. Lin, W.S., Kuo, C.C.J.: Perceptual visual quality metrics: A survey. J Vis Commun Image R. **22**, 297-312 (2011)

4. Robichaud, G., Garrard, K.P., Barry, J.A., Muddiman, D.C.: MSiReader: An Open-Source Interface to View and Analyze High Resolving Power MS Imaging Files on Matlab Platform. J Am Soc Mass Spectr. **24**, 718-721 (2013)

5. Bokhart, M.T., Nazari, M., Garrard, K.P., Muddiman, D.C.: MSiReader v1.0: Evolving Open-Source Mass Spectrometry Imaging Software for Targeted and Untargeted Analyses. J Am Soc Mass Spectrom. (2017)

6. Robichaud, G., Barry, J.A., Muddiman, D.C.: IR-MALDESI Mass Spectrometry Imaging of Biological Tissue Sections Using Ice as a Matrix. J Am Soc Mass Spectr. **25**, 319-328 (2014)

7. Chambers, M.C., Maclean, B., Burke, R., Amodei, D., Ruderman, D.L., Neumann, S., et al.: A cross-platform toolkit for mass spectrometry and proteomics. Nat Biotechnol. **30**, 918-920 (2012)

8. Race, A.M., Styles, I.B., Bunch, J.: Inclusive sharing of mass spectrometry imaging data requires a converter for all. J Proteomics. **75**, 5111-5112 (2012)

9. Tu, Y.Y.: Artemisinin-A Gift from Traditional Chinese Medicine to the World (Nobel Lecture). Angew Chem Int Edit. **55**, 10210-10226 (2016)

10. Alejos-Gonzalez, F., Qu, G., Zhou, L.L., Saravitz, C.H., Shurtleff, J.L., Xie, D.Y.: Characterization of development and artemisinin biosynthesis in self-pollinated Artemisia annua plants. Planta. **234**, 685-697 (2011)

11. Xie, D.Y., Ma, D.M., Judd, R., Jones, A.L.: Artemisinin biosynthesis in Artemisia annua and metabolic engineering: questions, challenges, and perspectives. Phytochem Rev. **15**, 1093-1114 (2016)

12. Fletcher, C.V., Staskus, K., Wietgrefe, S.W., Rothenberger, M., Reilly, C., Chipman, J.G., et al.: Persistent HIV-1 replication is associated with lower antiretroviral drug concentrations in lymphatic tissues. Proc Natl Acad Sci U S A. **111**, 2307-2312 (2014)

13. Thompson, C.G., Bokhart, M.T., Sykes, C., Adamson, L., Fedoriw, Y., Luciw, P.A., et al.: Mass spectrometry imaging reveals heterogeneous efavirenz distribution within putative HIV reservoirs. Antimicrob Agents Chemother. **59**, 2944-2948 (2015)

FACULTY

THOMAS A. DOW

Director, Precision Engineering Center
Dean F. Duncan Distinguished University Professor in Mechanical Engineering
Professor, Department of Mechanical and Aerospace Engineering

BS, Mechanical Engineering, Virginia Polytechnical Institute, 1966
MS, Engineering Design, Case Institute of Technology, 1968
PhD, Mechanical Engineering, Northwestern University, 1972

After receiving his PhD degree from Northwestern University in 1972, Dr. Dow joined the Tribology Section of Battelle Columbus Laboratories and worked there for ten years. His research interests were in the areas of friction and wear and included studies on a wide variety of topics from lubrication of cold-rolling mills using oil-in-water emulsions to wet braking effectiveness of bicycle brakes to elastohydrodynamic lubricant film generation in ball and roller bearings. He developed experimental apparatuses, established analytical models, and corroborated those analyses with experimental measurements. Dr. Dow joined the faculty at North Carolina State University in 1982 and was instrumental in developing the academic and research program in precision engineering. His current research interests include precision machining, real-time control, metrology, micro-coining and nano-coining. He was one of the founders of the American Society for Precision Engineering and currently acts as the Executive Director.

VICTORIA M. MILLER

Assistant Professor, Department of Materials Science and Engineering

BSE, Materials Science and Engineering, University of Michigan, 2011
PhD, Materials, University of California Santa Barbara, 2016

Assistant Professor Victoria Miller joined the Department of Materials Science and Engineering at North Carolina State University in August 2017. Prior to NCSU, she worked as a research scientist at UES, Inc. onsite at the Materials and Manufacturing Directorate of the Air Force Research Laboratory in Dayton, Ohio. She completed her PhD in the Materials Department at the University of California Santa Barbara in 2016, and her BSE at the University of Michigan in 2011.

DAVID C. MUDDIMAN

Jacob and Betty Belin Distinguished Professor of Chemistry
Founder and Director of the W.M. Keck FTMS Laboratory for Human Health Research

B.S., Chemistry, Gannon University, 1990
Ph.D., Analytical Chemistry, University of Pittsburgh, 1995

Prior to moving his research group to North Carolina State University in 2006, David was a Professor of Biochemistry and Molecular Biology and Founder and Director of the Proteomics Research Center at the Mayo Clinic College of Medicine in Rochester, MN. Prior to this appointment, David was an Associate Professor of Chemistry at Virginia Commonwealth University. It was there that he began his professional career as an assistant professor with an adjunct appointment in the Department of Biochemistry and Molecular Biophysics and as a member of the Massey Cancer Center in 1997. These academic appointments followed a postdoctoral fellowship at Pacific Northwest National Laboratory in the Environmental Molecular Sciences Laboratory under Richard D. Smith from 1995-1997. David was born in Long Beach, CA in 1967 but spent most of his formative years in a small town in Pennsylvania. Dr. Muddiman is Editor of *Analytical and Biological Chemistry* and Associate Editor of the *Encyclopedia of Analytical Chemistry* as well as on the Editorial Advisory Board of *Mass Spectrometry Reviews*, *Molecular and Cellular Proteomics*, *Rapid Communications in Mass Spectrometry*, and the *Journal of Chromatography B*. He also serves on the advisory board of the NIH Funded Complex Carbohydrate Research Center, University of Georgia and the Yale/NIDA Neuroproteomics Center, Yale University. Dr. Muddiman has served as a member of the ASMS Board of Directors and Treasurer of US-HUPO, and he is currently the President of US HUPO. His group has presented over 500 invited lectures and presentations at national and international meetings including 20 plenary/keynote lectures. His group has published over 250 peer-reviewed papers and has received four US patents in addition to two patents pending. He is the recipient of the 2015 ACS Award in Chemical Instrumentation, 2010 Biemann Medal (American Society for Mass Spectrometry), 2009 NCSU Alumni Outstanding Research Award, the 2004 ACS Arthur F. Findeis Award, the 1999 American Society for Mass Spectrometry Research Award, and the 1990-1991 Safford Award for Excellence in Teaching (University of Pittsburgh). Dr. Muddiman's research is at the intersection of innovative mass spectrometry technologies, systems biology, and model organisms for diseases and bioenergy, and is funded by the National Institutes of Health, the National Science Foundation, the Department of Energy, and The United States Department of Agriculture.

BRENDAN T. O’CONNOR

Associate Professor
Department of Mechanical and Aerospace Engineering

BS, Mechanical Engineering, Marquette University, 2000
MS, Mechanical Engineering, University of Massachusetts, 2004
PhD, Mechanical Engineering, University of Michigan, 2009

After receiving his BS from Marquette University, Dr. O’Connor joined Norian/Siani Engineering, an engineering consulting firm in Boston MA. He then returned to the University of Massachusetts and joined the Industrial Assessment Center, conducting energy audits of industrial facilities. During his PhD, Dr. O’Connor turned his research towards solar power, with a focus on organic electronic materials processing. After his graduation, Dr. O’Connor joined the Polymers Division at the National Institute of Science and Technology as an NRC-NIST Postdoctoral Fellow. At NIST, Dr. O’Connor conducted research on processing and mechanical properties of organic electronic films, primarily for flexible transistor applications. He then joined NC State University in 2011. At NC State, Dr. O’Connor’s research interests are focused on polymer semiconductor device processing and characterization. His research efforts include developing plastic solar cells with unique optoelectronic characteristics, and developing mechanically robust flexible and stretchable electronic devices.

MARK R. PANKOW

Director, Ballistic Loading and Structural Testing Laboratory
Assistant Professor, Department of Mechanical and Aerospace Engineering

BS, Mechanical Engineering, California Polytechnic State University, San Luis Obispo, 2005
MS, Mechanical Engineering, University of Michigan, 2007
PhD, Mechanical Engineering, University of Michigan, 2010

After receiving his PhD degree from the University of Michigan in 2010, Dr. Pankow joined the Army Research Laboratories and worked there for two years. His research interests were in the areas of dynamic failure of composite materials. His work was both experimental and computational in nature. Dr. Pankow joined the faculty at North Carolina State University in 2012. His current research interests include dynamic testing (ballistic, blast, impact), computational modeling of composites, and deployable structures. He is the editor for the American Society for Composites.

RONALD O. SCATTERGOOD

Professor
Materials Science and Engineering Department

BS, Metallurgical Engineering, Lehigh University, 1961
MS, Metallurgy, Massachusetts Institute of Technology, 1963
PhD, Metallurgy, Massachusetts Institute of Technology, 1968

R.O. Scattergood is a Professor in the Department of Materials Science and Engineering. He received BS degrees in Mining Engineering and Metallurgical Engineering from Lehigh University. His MS and PhD degrees were obtained in Metallurgy from M.I.T. In 1968 he became a member of the basic research staff in the Materials Science Division at the Argonne National Laboratory. In 1981, he joined the faculty as a Professor of Materials Engineering at North Carolina State University.

Professor Scattergood's major research interests have been focused on the mechanical behavior of solids. He has worked in the areas of strengthening mechanisms in solids, mechanical testing, fracture and toughening in ceramics, tribology, processing, properties and thermal stability of nanocrystaline materials and precision machining processes. He has published over 250 papers.

STAFF

KENNETH P. GARRARD

Senior Research Scholar
Precision Engineering Consortium and
FTMS Laboratory for Human Health Research

BS, Computer Science, North Carolina State University, 1979
MS, Computer Studies, North Carolina State University, 1983

As a full-time researcher at the Precision Engineering Consortium for over 32 years, Mr. Garrard's interests and duties have included the development of high performance control systems for ultra-precision machines and software for custom, multiprocessor computer systems. He participated in the development of the original PEC fast tool servo as well as three other fast tool servo systems that have been delivered to commercial and government sponsors. One of these systems was built specifically for the machining of off-axis segments of conic surfaces of revolution and another was used for the fabrication of inertial confinement fusion targets. He has performed numerous prototype fabrication projects that required unique machine configurations and controller software. He is also co-inventor of the spherical coordinate measurement machine, *Polaris3D*, and was the developer of algorithms for its control and for the analysis of measurement data.

Since 2012 he has collaborated with the FTMS Laboratory for Human Health Research to assist with the implementation of video system directed sample stage motion control, region of interest selection, laser optics and instrument synchronization for IR-MALDESI imaging. This led to the development of the widely-used, open-source *MSiReader* software package for analysis and visualization of Mass Spectrometry Imaging data sets.

Mr. Garrard has a long-standing interest in the analysis of scientific data, computational geometry, signal processing, programming language structures, sorting and searching algorithms, multiprocessor computer architecture and the design and implementation of hard real-time systems. He is a regular contributor to the Mathworks user community web site.

ANTHONY R. WONG

Research Associate

BS, Mechanical Engineering, NC State University, 2005
MS, Mechanical Engineering, Massachusetts Institute of Technology, 2012

Mr. Wong joined the Precision Engineering Consortium in 2017 as a member of the technical staff. His current research interests include machine design and metrology. Prior to coming to the PEC, he had 7 years of industry experience including positions at Caterpillar, AKG of America, ShopBot Tools and Keystone Tower Systems.

GRADUATE STUDENTS

CHARAN BODLAPATI obtained his B.S. degree in Mechanical Engineering at Osmania University, Hyderabad, India. During undergrad, he had a variety of experiences, including working as the Design Lead for university motorsports team which participated in FSAE Italy (2015), and as an intern in the department of materials at Ashok Leyland, Hosur. He joined PEC in March 2017 as a research assistant. His current interests include precision machining, polymers and engineering design.

SUMIT GUNDYAL obtained his B.S. degree in Mechanical Engineering at University of Pune, Pune, India. He worked for 2 years at Dassault Systèmes, Pune, India before starting as a graduate student at NC State University. Sumit joined the BLAST lab in February 2018, working on the modeling and the simulation aspect of the micro-lens array project. He enjoys swimming, basketball, and tennis outside of the lab.

NOA MCNUTT obtained his B.S. in Mechanical Engineering at NC State in December 2017. Noa joined the PEC as an undergraduate researcher in January 2017, working on a Los Alamos National Laboratory funded project. He became a grad student at the PEC in January 2018, researching dry machining methods for ductile metals. Noa grew up in Raleigh and his interests outside of the lab include biking, skiing, golf and cars.

GRADUATES OF THE PRECISION ENGINEERING CONSORTIUM

2018
Charan Bodlapati

2016
Brandon Suit

2014
David Gebb
Sean Gunning
David Brehl
John Nowak

2012
Brandon Lane
Zachary Marston

2010
Meirong Shi

2009
Qunyi Chen
Erik Zdanowicz

2008
Lucas Lamonds
Stephen Furst

2006
Nadim Wanna
Robert Woodside

2005
Brett Brocato
Nathan Buescher
Karalyn Folkert

2004
Karl P. Freitag
Simon Halbur
Witoon Panusittikorn
Travis Randall

2003
Stuart Clayton
David Hood
Patrick Morrissey
Nobu Negishi
Tao Wu

2002
David Gill
David Kametz

2001
Markus Bauer
Matthew Cerniway
Matias Heinrich
Bryan Love

2000
Brad Austin
Byoung Loh
Michael Long
Edward Miller
Wonbo Shim

1999
Konrad Jarausch
Bradley Jared
Edward Marino

1998
Robert Day
John Fasick
Paul Minor
Keith Sharp

1997
Eugenio Decrescenzo
Hector Gutierrez
Ayodele Oyewole
John Richards
Robert Skolnick

1996
Chris Arcona
Christian Haeuber
Bradley Jared
Quan Ma
Alex Ruxton
Anthony Santavy
Brent Stancil
Anand Tanikella
Donna Thaus

1995
Konrad Jarausch
Charles Mooney
Keith Sharp
John Tyner

1994
Jeffrey Abler
William Allen
James Cuttino
Michele Miller
Ganesh Rao

1990
Scott Blackley
Byron Knight
John Pellerin
Mary Beth Smith

1989
Joseph Drescher
Karl Falter
David Grigg
Michael Luh
Hakan Ozisik
Denise Skroch
Elizabeth Smith

1988
Thomas Bifano
Peter Blake
Steven Fawcett
Michael Loewenthal

1987
John Carroll
Dan Luttrell
Gary Mitchum
Larry Mosley

1986
Mark Cagle
James Gleeson
Jerry Kannel
Mark Landy

1985
Damon Christenbury

ACADEMIC PROGRAMS

Problems and limitations associated with precision manufacturing can originate in the machine, the process, or the material. In fact, most problems will probably be caused by a combination of these factors. Therefore, improvement of current processes and development of new manufacturing methods will require knowledge of a multi-disciplinary array of subjects. The educational goal of the Precision Engineering Consortium is to develop an academic program which will educate scientists and engineers in metrology, control, materials, and the manufacturing methods of precision engineering.

The graduate students involved in the Precision Engineering Consortium have an annual stipend as research assistants. They can take up to 3 classes each semester while spending about 20 hours per week on their research projects. These students also work in the Consortium full-time during the summer months.

The Precision Engineering Consortium began in 1982 with an emphasis on the mechanical engineering problems associated with precision engineering. As a result, the original academic program proposed was biased toward courses related to mechanical design and analysis. However, as the research program has developed, the need for complementary research in sensors, materials, and computers has become obvious. A graduate student capable of making valuable contributions in the computer area, for example, will require a significantly different academic program than in mechanical engineering. For this reason, the Consortium faculty has set a core curriculum and each student in the program is required to take at least 2 of these core courses. The remainder of the courses for the MS or the PhD degree are determined by the university or department requirements and the faculty committee of the student.

The core courses are:

- MAE 545 Metrology in Precision Manufacturing
- PY 516 Physical Optics
- MSE 500 Modern Concepts in Materials Science
- CSC (ECE) 714 Real Time Computer Systems

PhD DEGREE PROGRAM

The PhD program in Precision Engineering has been set up as a multi-disciplinary program, drawing upon courses throughout the University to provide background and expertise for the students. It should contain required courses to insure solid grounding in the fundamentals plus electives to prepare the student in his area of specialization. Because Precision Engineering is concerned with an integrated manufacturing process, students interested in computer control, materials, machine structure, and measurement and actuation systems are involved in the program. Student research projects include the wide variety of topics addressed in this report. Each student's thesis should have an experimental component because Precision Engineering is basically a hands-on technology.

MS DEGREE PROGRAM

The Master of Science degree will have a higher percentage of application courses than the PhD degree. The emphasis will be to develop the foundation for involvement in precision engineering research and development. A total of 30 credits, including 6 credits for the MS thesis, are required. The thesis, while less comprehensive than the PhD dissertation, will be directed at important problems in Precision Engineering. Typically, the MS program will take four semesters plus one summer.

UNDERGRADUATE PROGRAM

The undergraduate degree broadly prepares an engineering student for industrial activities ranging from product design and engineering sales to production implementation. Because a large share of engineers only have the BS degree, these will be the people who must implement the new technology developed in research programs like the Precision Engineering Consortium. Therefore, a way must be found to acquaint engineers at the BS level with the techniques, problems, and potential of precision manufacturing.

In most undergraduate degree programs only limited time is available for technical electives. However, these electives offer the student the opportunity to expand his knowledge in many different directions. Beginning graduate courses (such as metrology) can be used as undergraduate electives.

FACT SHEET – PRECISION ENGINEERING CONSORTIUM (PEC)

History

1982-1985 ONR Selected Research Opportunity

Based on several years of evaluation of the state of the field known as precision engineering in Europe and Japan, the Office of Naval Research decided to ask for proposals in this area. Ralph Burton, the head of Mechanical and Aerospace Engineering at NC State, and Thomas Dow, who had just joined the University from the Battelle Research Labs, headed a proposal team consisting of faculty from NC State and the Research Triangle Institute. The proposal involved research in the areas of metrology, fabrication and controls. The proposal from NCSU was funded along with proposals from Purdue, Stanford and Maryland.

1985 PEC Affiliate Meeting

Buoyed by the success of the SRO project and interactions with precision engineering industries across the country, a meeting was held in Raleigh with 31 representatives from 26 potential industrial affiliates of the PEC. At the end of this meeting, the 5 original members - Kodak, Moore, General Motors, Texas Instruments and Livermore National Labs - signed up to provided $25K each to help support the Center. Support from these and other Affiliates, along with new projects funded by ONR, NSF and others, has allowed the PEC to educate a new generation of precision engineers and scientists. Our web site is www.pec.ncsu.edu

1986 ASPE Founded

The success of the PEC and the need to provide a forum for communication within this broad field led to the formation of the American Society for Precision Engineering in 1986. The impetus was a meeting held one year earlier in Raleigh that was jointly organized by Lawrence Livermore Labs and the PEC. There were about 60 attendees at that meeting and the question was posed - should a new society be created to serve the field? A majority of the attendees indicated “yes” and a not-for-profit corporation was chartered in North Carolina by Tom Dow, Ron Scattergood and John Strenkowski. The first meeting was held in Dallas, Texas in the fall of 1886 with Tom’s wife as a voluntary staff member. Currently the ASPE has offices in Raleigh and a worldwide membership of 800. ASPE headquarters will be relocating to Charlotte in 2019. The 2018 Annual Meeting was held in Las Vegas, Nevada and had more than 225 attendees and over 40 exhibiting companies. Web site: www.aspe.net

1986-1991 University Research Initiative

In 1986, a new DOD initiative was announced and NC State submitted a multi-disciplinary proposal with faculty from mechanical engineering, materials science, physics, computer science and electrical engineering. There were 35 proposals submitted in the manufacturing area and only the NC State concept was funded. This project was funded at $1M per year for 5 years.

1988 First Building on Centennial Campus

The $5M URI grant to the PEC was the largest single research grant received by the University up to that time. This grant came at a time when the University acquired a 1000 acre research campus from the state named Centennial Campus. Based on the space need for this program as well as the desire to begin development of the CC, a building for the PEC was started in April of 1987 and the Center was moved to Centennial Campus in February of 1988. This building was inaugurated in April of 1988 with Dr. Saalfeld, Technical Director of ONR, as one of the guest speakers.

PEC Affiliates

Numerous companies and government organizations have been members of the PEC and supported specific research projects with additional support. Membership fees partially support the administrative staff as well as the two research engineers.

1. Aerotech, Inc
2. Biomachines
3. Burleigh Instruments
4. Corning, Inc
5. Cummins Engine Co.
6. Department of Energy
7. Digital Instruments
8. Electro-Optics Center
9. General Motors
10. Hughes
11. IBM
12. Johnson & Johnson
13. Kodak
14. Lexmark
15. Livermore National Labs
16. Lockheed Martin
17. Los Alamos National Labs
18. 3M
19. Martin Marrietta
20. Materials Analytical Services
21. Missile Defense Agency
22. Moore Special Tool
23. NASA
24. National Institutes of Health
25. National Institute of Justice
26. National Institute of Standards and Technology
27. National Science Foundation
28. Oak Ridge National Labs
29. Optical Research Associates
30. Facebook VR
31. Office of Naval Research
32. Panasonic
33. Pneumo Precision Inc
34. Rank Taylor Hobson
35. Sandia National Labs
36. StorageTek
37. Teledyne, Inc.
38. Texas Instruments